THE EFFECTS OF HIGH INTENSITY ULTRASOUND ON THE ULTRASTRUCTURE OF MAMMALIAN CENTRAL NERVOUS TISSUE

Michael Jude Borrelli, Ph.D.
Department of Biophysics
University of Illinois at Urbana-Champaign, 1984

Tissue damage in the adult cat brain resulting from varying exposure times to focused 1 MHz, 300 W/cm^2 intensity ultrasound was examined with the electron microscope. Thermocouples were used to record the temperature changes produced by the absorption of acoustic energy by the brain tissue. Cultured cells were then heated at temperatures corresponding to the peak temperatures recorded by the brain-embedded thermocouples resulting from each of the ultrasonic dosages used. Electron microscope observations of the heated cells indicated that temperatures less than 57^oC required heating times significantly longer than the ultrasonic exposure times required to induce the identical temperature in the cat brain in order to produce changes in cellular morphology. These results suggested that tissue damage induced by exposure times shorter than 3 - 4 sec with 300 W/cm^2, 1 MHz ultrasound was not strictly the result of the ultrasonically induced hyperthermia.

Ultrasonically induced tissue damage, similar to that observed in the irradiated cat brains, was observed in the neonatal mouse spinal cord. Pressurizing the irradiation chamber to 16 atm raised the threshold dosage required to produce spinal cord damage. This observation, together with an observed decrease in the subharmonic signal within the pressurized irradiation chamber, suggested that acoustic cavitation played a role in producing the tissue damage.

Using the results of studies linking changes in tissue morphology to tissue function, it is suggested that the primary site of ultrasonic damages is to the selective permeability of the biological membranes. Freeze fracture replicas of the irradiated tissues revealed no initial changes in membrane ultrastructure, suggesting that any membrane damage occurred at the macromolecular level.

ACKNOWLEDGEMENT

I would like to thank my advisor, Dr. Floyd Dunn, for helping select the thesis topic and for his guidance and encouragement throughout the course of the research and writing of the thesis. Thanks are also due to the members of the Bioacoustics Research Laboratory staff, particularly: Charles Cain, Kay Carnes, Robert Cicone, Joseph Cobb, Wanda Elliott, Leon Frizzell, Ronald Johnston, Valerie Maynard, Billy McNeill, Robert Morimoto, and Philip Strom-Jensen.

More than just thanks are due to my parents for their constant support during my college career, even though they sometimes wondered why I stayed in school so long. Even though she had to put up with me on a daily basis for only three and one-half years, my wife Kathy deserves the lion's share of my appreciation, because those were the final and most difficult years of my graduate studies. Her support and love made the task much easier.

PREFACE

This thesis is divided into eleven chapters. Chapter 1 introduces the questions addressed by this thesis, and describes findings from earlier studies of ultrasonic interactions of biological tissue. The discussion centers around studies of whole tissue irradiation *in vivo*, particularly the earlier investigations performed at the University of Illinois. A brief outline of the experimental approach used for this study is also presented.

Chapter 2 is concerned with the physical properties of ultrasonic waves, how they are propagated through fluid and fluid-like media, and how the ultrasonic waves can interact with the propagating medium. Acoustic energy attenuations by means of reflection, scattering, and absorption are discussed, together with the manner in which these phenomena may be involved in producing ultrasonically-induced changes in the tissue morphology. The nonlinear acoustic phenomena of cavitation and radiation pressure are also presented.

Chapter 3 describes the materials and methods used to obtain the experimental data, which is presented in Chapters 4 through 9. Each chapter is devoted to presenting the results obtained from each of the different experiments described in Chapter 3. These results, and the conclusions drawn from them, are discussed in Chapter 10. Because the thesis is so long, Chapter 11 serves to briefly summarize Chapters 3 through 10.

TABLE OF CONTENTS

CHAPTER 1

INTRODUCTION

What physical properties of the ultrasonic wave are responsible for producing the changes in physiology and morphology observed in irradiated biological specimens? Where within the biological specimens does the ultrasound exert its initial effects? How do the initial changes affect subsequent physiological activities, resulting in the ultimate altered state observed in ultrasonically irradiated biological materials?

A series of painstakingly detailed experiments was initiated over 30 years ago at the University of Illinois in an attempt to answer these and other questions concerning the biological effects of ultrasound. The biological material chosen for these studies was mammalian central nervous tissue. Similar studies were also conducted at other institutions [Basauri and Lele, 1962; Robinson and Lele, 1972; Pond, 1968]. Because the present thesis can be considered an extension of the research begun at Illinois, these results are stressed during the following discussion. Data from the other studies will be included when it provides additional information or differs significantly from the results obtained at Illinois. Also, data from other studies not necessarily involving nervous tissue will be discussed when pertinent.

The adult female cat brain was chosen for essentially all of the morphological studies of ultrasonically irradiated central nervous tissue for the following reasons. The brain size and positions of the various anatomical structures vary little among

the adult female cat population, and atlases exist which permit the location of specific brain structures for ultrasonic irradiation when the animal is secured in an appropriate stereotaxic device [Snider and Neiman, 1964]. Neurophysiologists have long used the female cat brain for morphological and functional studies, and many of their findings were useful in interpreting the results from the ultrasonic experiments. Finally, the acoustic properties of the brain remain virtually unaltered in response to physiological and behavioral stimuli, providing a degree of stability not available with any other organ in the body. This last point was of added importance since the animals were obtained from commercial suppliers that secured them as strays, and did not breed them. Therefore, the prior medical history and living habits of a given animal were unknown.

In preparation for the irradiations, a portion of the skull was removed, but the meninges, the dura mater, arachnoid mater, etc., were undisturbed [W. Fry, 1958]. A headpan attached to the animal's head was filled with degassed physiological saline which served as an acoustic coupling medium between the transducer and the brain. Focused ultrasound in the frequency range of 0.8 to 10 MHz was used to irradiate selected regions of the brain. Intensities varied from several milliwatts per square centimeter to several thousand watts per square centimeter with exposure times ranging from tens of minutes down to microseconds. Plane wave propagation approximations were considered appropriate, and corrections were made for attenuation of the acoustic intensity as the wave propagated through the tissue using the following exponential relationship,

$$I_S = I_O \exp(- Ad), \tag{1.1}$$

where I_O is the intensity of the unattenuated focused wave, A is the acoustic attenuation coefficient of the medium expressed in nepers/cm (0.1 nepers/cm for brain at at 37°C and frequency of 1 MHz), d is the depth of the irradiated site from the surface of the brain, and I_S is the acoustic intensity at the focal point. The attenuation coefficient is a function of the acoustic frequency, f, and the relationship is expressed as,

$$A = \frac{f^B A_O}{10^6} \quad , \tag{1.2}$$

where A_O is the attenuation coefficient at 1 MHz, B is a numerical constant, and the frequency is expressed in megahertz. Therefore, the higher frequencies experience a greater degree of attenuation. The numerical constant B is so nearly equal to unity that it is usually approximated as such [Dunn et al., 1975].

The irradiations were spaced by measured time intervals in order to record the progression of the observed morphology changes as a function of post irradiation time. Fixation of the brain was accomplished by means of a heart-puncture perfusion which was either initiated immediately after the final irradiation or at some later time, in some cases up to several years later. Physiological saline was used to flush blood from the brain, followed by the fixative, 10% formalin in saline. After dehydration, paraffin embedding, sectioning and mounting on glass slides, the sections were stained in preparation for light microscopy, LM. Various staining techniques were used in order to

accentuate different aspects of the brain morphology, for example, nerve tracts [Barnard et al., 1955; W. J. Fry, 1955].

Following the examination of tissue from over 1,000 ultrasonically irradiated cat brains a threshold curve was established based on the minimum exposure time with a given intensity required to produce a LM visible lesion [F. J. Fry et al., 1970]. This curve is shown in Fig. 1.1. Each data point represents the root mean square, average of many specimen irradiations using that particular combination of intensity and exposure time. Therefore, irradiating the brain with a threshold exposure does not guarantee the production of a lesion, it can only be assumed that the formation of a lesion is statistically probable. The relationship,

$$It^{1/2} = 200 \qquad (1.3)$$

[Johnston and Dunn, 1976a], provides a good fit to the experimental data presented in Fig. 1.1.

The curve in Fig. 1.1 represents the threshold exposure data for lesions placed in the white matter, WM, of the brain. Exposure times had to be increased approximately 30% in order to produce a threshold lesion in the gray matter, GM, using any given intensity [F. J. Fry et al., 1970]. This was shown to be the result of the greater vascularization and blood perfusion within the GM [Basauri and Lele, 1962]. It was shown that the threshold curve is essentially independent of the acoustic frequency [Dunn et al., 1975], and that the volume of the lesion did depend upon the frequency, becoming smaller at the higher frequencies for a given set of exposure conditions [Johnston and Dunn, 1976a]. This

is due in part to the fact that the focal volume of a given transducer decreases with increasing frequency, a result of classical optics [Lerner et al., 1973]. Depending upon the irradiation parameters, viz., intensity and exposure time, the first signs of a lesion observable with LM appeared at varying time intervals after the irradiation. The larger the product of the intensity and the exposure time, the sooner the lesion became apparent. In the context of this thesis, the product of the attenuation-corrected acoustic intensity and the exposure time will be referred to as the dosage.

A detailed description of the ultrasonically induced morphology changes in irradiated brain tissue as a function of dosage and post irradiation time is given by Barnard et al. [1955]. It was reported by them, and all subsequent investigators at Illinois, that even with the largest dosages used, a post irradiation time, t_p, of 10 - 15 min was required before a lesion was detectable with LM. The lesion volume was observed to increase with the post irradiation time, reaching a maximum after approximately 24 hours [Lohnes, 1971]. Because of this observation, a t_p of 24 hr was routinely used to establish all the data points in Fig. 1.1. Lele [1978], however, claims that the lesion manifests itself immediately, and can be observed with LM directly following an irradiation. He irradiated tissue sites at, or just under the brain surface, and after quickly removing the acoustic coupling medium from around the brain, poured fixative onto the irradiated sites fixing them by diffusion. He has published at least two electron micrographs showing the altered morphology resulting from such an experiment [Lele and Pierce,

1971]. It must be pointed out however, that near the tissue-liquid interface violent processes such as acoustic cavitation may produce gross tissue damage, while such processes may be absent deeper in the tissue. Evidence and further discussion of possible cavitation-related effects will be presented later.

F. J. Fry et al. [1970] have divided their threshold curve into three distinct regions based on the mechanisms they believed were responsible for lesion production under different threshold exposure conditions. Lesions produced with intensities below 100 W/cm^2 were attributed to a thermal mechanism. That is, the heat generated by the acoustic absorption processes directly affected the tissue, e.g., by a denaturation of proteins which could result in the morphology changes observed within the lesion. Lesions resulting from exposure intensities greater than 1,500 W/cm^2 were believed to be the result of transient acoustic cavitation. This is a process whereby the ultrasound causes gas nuclei in the medium to oscillate in response to the time varying acoustic pressure. The ultrasound can also fracture the medium to create new cavities. In either case, the bubbles or cavities oscillate and then collapse violently to produce shock waves and extremely high localized temperature increases, both of which can substantially alter tissue morphology. Several LM micrographs were presented which substantiated this hypothesis.

Lesions within the middle threshold region, resulting from intensities between 100 to 1,500 W/cm^2, were assumed to be the result of some as yet unknown mechanical mechanisms. This opinion

mathematical model to calculate the temperature profiles produced by an ultrasonic irradiation in cat brain and methacrylate plastic as a function of the distance from the focal center of the acoustic beam. The resulting profiles depended upon the focusing geometry of the transducer and the thermal and acoustic properties of the two materials, all of which were measured by the investigators. Lesion boundary temperatures were also measured in both materials, and these were used together with the calculated temperature profiles to estimate the expected lesion size resulting from a given dosage of ultrasound. Good agreement was reported between the calculated and observed lesion sizes within the cat brain, while agreement for the methacrylate was not as good. Based on these results, it was concluded that focused ultrasonic lesions in brain tissue, for all regions in Fig. 1.1, with the possible exceptions of those lesions produced with intensities greater than 700 - 1,000 W/cm^2, were the result of only thermal mechanisms.

Further support of the proposed thermal mechanism for lesion production within this middle intensity range of the threshold curve came from Pond [1970]. He developed a method for calculating the temperature cycles produced at the focal center of the ultrasonic beam. The calculations were based on the measured beam profile at the focal region, and the thermal and acoustic properties of the medium. Predicted profiles were compared to those measured in ultrasonically irradiated rat brain, and good agreement with the data was obtained. Using these results as a guide, Pond attempted to determine whether the resultant heat from an ultrasonic exposure, in the absence of an acoustic wave, was

sufficient to produce a lesion in the tissue. Electric current was passed through high resistance wires positioned within rat brain tissue, resulting in the production of heat. The resulting temperature profiles were calculated as a function of time and distance from the wire surface, though they were not measured. The heated wire produced lesions in the brain that were similar in appearance to those produced by ultrasound. It must be pointed out, however, that the temperature distribution over the volume of the thermally produced lesion is not identical to that found in an ultrasonically produced lesion of an identical volume. This is because the acoustic beam is a broader heat source than the thin (0.125 mm diam.) resistance wire used by Pond. At some distance, r, from the wire surface, the temperature profile is identical to that present at the center of a given ultrasonic lesion, and because the tissue at this point r exhibited tissue damage similar to that present in an ultrasonically-induced lesion, it was concluded that the temperature change alone was sufficient to produce lesions in ultrasonically irradiated tissues.

The best evidence in support of a nonthermal mechanism for lesion production is provided by experimental results from ultrasonic irradiations of neonatal mouse spinal cords. W. J. Fry and Dunn [1956] chose the one day old neonatal mouse which is an essentially poikilothermic living system, permitting a wide range of animal temperatures, from nearly 0°C to be employed. An unfocused ultrasonic beam was centered on the specimen's third lumbar vertebra, the region of the spinal cord which contains the neurons and nerve fibers associated with the femoral, sciatic, and obdurator nerves [W. J. Fry and Dunn, 1956]. Damage to these

structures would impair the innervation of the hind limb muscles, and so hind limb paralysis was the functional endpoint chosen in determining the a threshold curve. Some of the tissue was also prepared for LM observation in order to determine any changes in morphology, and thermocouples were implanted in the spinal cord of some animals to record the temperature changes. At this stage in the mouse's development, ossification of the spinal column is incomplete. Therefore, the acoustic absorption of the spinal column would be more similar to that of the spinal cord and not 2-6 times larger, as would be the case with ossified bone [Goss et al., 1978]. This eliminated, or at least significantly reduced the presence of large temperature gradients at the spinal cord-spinal column interface.

The threshold region based on the hind limb paralysis endpoint is shown in Fig. 1.2. For a specific set of irradiation conditions, i.e., ambient temperature, and intensity, a sigmoidal relationship between the percentage of paralyzed mice and the inverse of exposure time was obtained, as seen in Fig. 1.3. A threshold range was defined from these results as the exposure range yielding 10 - 90% paralysis. Figure 1.4 shows the 50% paralysis curves obtained at several different ambient temperatures. The maximum recorded temperature rises for some of the irradiations are also indicated. It should be noted that although the animals were more sensitive to the ultrasound at the higher ambient temperatures, the maximum recorded temperature rises did not establish spinal cord temperatures in excess of 37^{o}C, the normal basal temperature of the adult animal. These experimental results suggested that the ultrasonically induced

paralysis was not the result of only a thermal mechanism, although temperature may in some way be involved as evidenced by the dependence of the threshold curves on the ambient temperature, i.e., the process, whatever its nature, may be a function of temperature.

The neonatal mouse experiments do not firmly established the involvement of nonthermal mechanisms in the production of ultrasonically induced lesions in biological tissues. Lele [1978] has suggested that it is the rate of temperature rise, not the peak temperature, that is important in lesion production. He has also speculated that localized "hot spots" may be present in the mouse spinal cord, and that they may produce damage in key structures giving rise to the observed functional and morphological changes. Another arguement that Lele has made together with Pierce [Lele and Pierce, 1971] is that the temperature increase within the spinal cord can produce a localized hypoxia. Their arguement is as follows. The metabolic rates of biological tissues are a function of the steady state temperature at which they are maintained, and change exponentially as a function of temperature. Changes in metabolism are reflected by the oxygen demands of the tissue, and in the case of animals, the heart rate and cardiac output are in turn affected because they are closely tied to the oxygen requirements of the organism. At any given temperature, the oxygen supply is just adequate to meet the animals metabolic requirements.

The oxygen requirement of central nervous tissue increases some 300 fold with a temperature rise from 10 - 20^{o}C [Lele and Pierce, 1971], and hence, if the oxygen supply is not increased to

compensate for the increased temperature, the tissue will be unable to sustain the increased metabolic activity. A localized temperature increase, such as that produced by ultrasonic irradiations, would increase the oxygen requirement for the heated region, but since the rest of the animal is still maintained at a lower temperature, there will be no corresponding increase in cardiac output or heart rate resulting in hypoxic conditions at the irradiated site.

Several experiments appear to support this hypothesis of an ultrasonically induced hypoxia. Taylor [1970] has irradiated rat spinal cord while the animals were breathing a hypoxic mixture of gases, 10% oxygen and 90% nitrogen. He observed a 40% decrease in the exposure times required to produce spinal cord damage using a given intensity of ultrasound. It has also been demonstrated that ultrasonic irradiation of the spinal cord was often accompanied by hemorrhaging [Taylor, 1970], which can further reduce the oxygen supply to the tissue and accelerate the degeneration process. Such hemorrhaging was not observed by W. J. Fry and Dunn [1956].

Light microscopic, histological studies of the irradiated mouse spinal cords did not reveal any indication of a lesion unless the post irradiation sacrifice time was greater than 10 - 15 min [Dunn, 1958]. This was consistent with the formation of lesions in the cat brain as described above. However, the functional endpoint of paralysis was observed instantaneously following the irradiation. This phenomenon of the functional change preceeding the morphological changes also occurred in the cat brain. F. J. Fry et al. [1958] were able to suppress temporarily the light stimulated evoked potentials in the visual

cortex immediately after irradiating the lateral geniculate nuclei, sites of synaptic stations along the visual pathway, with focused ultrasound. Reversible suppression was not accompanied by lesion production. However, when exposures sufficient to elicit lesions were used, lesion development occurred as described earlier for brain irradiations while the cortex potentials disappeared immediately [F. J. Fry, 1981].

To date, it appears that there are no complete answers to the questions raised at the beginning of this section. This is particularly true for the case of threshold lesion production in the intensity range of 100 to 1,500 W/cm^2. In order to identify the mechanisms(s) responsible for the production of ultrasonically induced lesions in biological tissue, a knowledge of the tissue structures initially affected by the irradiations, and the manner in which further morphological changes proceed is essential. The observation that functional changes precede the appearance of a light microscopically visible histological lesion in irradiated mammalian CNS tissue suggests that tissue structures smaller than the resolution limit of LM may be the sites where ultrasound exerts its initial effects [Dunn et al., 1975; Dunn, 1977]. A study using the higher resolution capabilities of electron microscopy, EM, may be able to identify these structures, and by varying the post exposure sacrifice time for the irradiated sites as was done in the earlier LM lesion studies, the progression of morphological changes can be investigated.

The approach of the present study was to use the adult female cat brain and the neonatal mouse spinal cord as experimental tissues for an EM study of the morphology changes induced by

ultrasound. These specimens were chosen for several reasons other than those cited to support their original choice as experimental animals for the earlier LM studies. The equipment for irradiating the animals was readily available, much of it used in the preceeding studies, and the well established surgical and irradiation procedures were used with only slight modifications. The already existing data provided a guideline for selecting ultrasonic dosages, and served as a reference for the new histological studies. For example, as the morphologic changes initially observed with EM become resolvable with LM, the further development of the lesion should parallel that described in detail by the earlier studies. Inconsistancies would be indicative of artifact, and, or poor experimental procedures.

Focused ultrasound with a frequency of 1 MHz and a spatial peak temporal average, SPTA, intensity of 300 W/cm^2 at the focus was used to irradiate selected sites in the cat brain, and unfocused 1 MHz ultrasound within the intensity range of 86 to 289 W/cm^2 was used on the neonatal mice. For both tissues the speed of sound is approximately 1,550 m/sec [Goss et al., 1980] with a wavelength of 1.55 mm.

Control, sham irradiated, and ultrasonically irradiated tissues were examined with transmission electron microscopy, TEM, in order to catalogue the induced changes in morphology as a function of dosage and post irradiation time. Tissue from many of the irradiated animals was also freeze-fractured and replicated with platinum and carbon [Rash, 1981; Hayat, 1974] in order to observe any effects of the ultrasound on the ultrastructure of the biological membranes. The replicas were observed with TEM, but

with a reduced resolution capability resulting from the size of the platinum crystals forming the replica, approximately 10 - 20 Å. High voltage electron microscopy, HVEM, was used to examine selected tissue specimens in order to record the effects of ultrasound on the cytoskeleton [Ris, 1981; Wolosewick and Porter, 1976; Heuser, 1981]. Preliminary TEM examination of the irradiated brain tissue demonstrated that the contours of some morphological features, e.g., synapses, were altered. It has been suggested that the cytoskeleton is involved in maintaining the shape of cells and cellular processes [Gulley and Reese, 1981], and so it was desirable to know whether any ultrasonically-induced cytoskeletal changes accompanied these structural changes. Although cytoskeletal elements such as microtubules and neurofilaments were visible in standard TEM sections, it was impossible to record their 3 dimensional structure because the sections were so thin, 400 - 700 Å thick. HVEM uses accelerating voltages of 1 MV, 10 times larger than for standard TEM, and sections 0.5 to 1 micron thick can be used. Stereo micrographic techniques can be used to exhibit the three dimensional nature of the cytoskeleton throughout these sections, as well as the structures of other tissue components.

Thermocouples were inserted into both the white and gray matter of the cat brain to record the temperature changes produced within the irradiated tissues. The thermocouple outputs were also used to measure the value of the absorption coefficient α, where α represents that fraction of the attenuation coefficient resulting from processes that produce a temperature rise in the tissue. Recordings were made in the presence and absence of blood

flow in order to determine its effect on the heating of the tissue. The thermocouples were also used to plot the acoustic field within the tissue, together with the temperature distribution throughout the irradiated volumes.

It was originally proposed that the heated wire experiments of Pond [1968] be repeated in order to determine the effects of heat alone on the tissue, and whether or not the temperature increases due to the ultrasound were sufficient to account for the ultrasonically-induced morphological changes. Initial experiments demonstrated that merely inserting the wire into the brain produced a localized edema around the wire which may have altered the thermal properties of the tissue and hence the thermal model used to predict the temperature gradient in the heated volume. In order to avoid this problem an <u>in vitro</u> model for investigating the effects of elevated temperatures and rapid heating rates on living tissues was used. Cultured cells were rapidly heated to temperatures identical to the peak temperatures recorded during the ultrasonic irradiations in order to observe the effects rapid heating can have on living cells in the absence of an acoustic wave. The cells were sacrificed at various post heating times similar to the t_p values used for the sonicated tissues, and then observed with TEM to record any changes in the cellular ultrastructure. Comparisons were then made to the cellular changes observed in the ultrasonically irradiated tissue in order to determine the role heat alone may play in producing the altered morphology observed in the central nervous tissue lesions.

Using the cultured cells presented the opportunity to observe the cytoskeleton and any heat-induced changes in its structure in

unsectioned cells. The cells were treated as a monolayer with a buffered, nonionic detergent solution (1% Tritox X-100) to extract the plasma membranes. After fixation, staining, and critical point drying, the entire cytoskeleton of the cells were observed with a standard transmission electron microscope.

CHAPTER 2

THE PHYSICAL PROPERTIES OF ULTRASOUND

2.1. Sound Waves in Fluids

It is pertinent to discuss the physics of ultrasonic propagation waves and the different ways it can interact with the medium through which it is being propagated. A solid medium can support both transverse (shear waves) and longitudinal acoustic waves, while pure fluid media can support only the latter. Frizzell et al. [1976] have measured the shear properties of mammalian soft tissues in the frequency range of 2 - 14 MHz and showed that the attenuation coefficient for transverse waves was extremely high. Since biological tissues cannot support transverse acoustic waves over any appreciable distance, they behave as fluid-like media in this respect. For this reason the following discussion will be restricted to the properties of ultrasound in fluid and fluid-like media. Significant deviations of the tissue from this fluid model will be discussed when appropriate.

Ultrasound is so named because the frequencies used are greater than 20 kHz which is the approximate upper limit of human audibility. The wave has a characteristic wavelength, λ, and frequency, f, with the two being inversely proportional to one another as is the case with any wave phenomenon,

$$\lambda = \frac{c}{f} \tag{2.1}$$

where c is the speed of the ultrasonic wave, and the numerical

value of c is determined by the propagation medium. In fluids, a theoretical prediction for the speed of sound is,

$$c = \frac{1}{\sqrt{\rho_o \beta_t}} \tag{2.2}$$

[Kinsler and Fry, 1962], where β_t is the adiabatic compressibility of the fluid ρ_o is the undisturbed density of the fluid.

The wave propagates by displacing successive elements, or particles, of the fluid medium from their equilibrium position while the elastic properties of the medium act to restore the elements to equilibrium. Because of this particle motion, regions of the medium experience localized condensations and rarefactions. P_o and ρ_o are, respectively, the ambient pressure and density of the medium. Deviations from these equilibrium values are expressed by the acoustic pressure, p,

$$p = P - P_o \tag{2.3a}$$

and the condensation, s,

$$s = \frac{\rho - \rho_o}{\rho_o} \tag{2.3b}$$

where P and ρ are, respectively, the instantaneous pressure and density for a given point in the medium.

The one dimensional acoustic wave equation, in a nonabsorbing fluid medium is

$$\frac{\partial^2 r}{\partial t^2} = \frac{c^2}{(1 + \frac{\partial r}{\partial x})^2} \frac{\partial^2 r}{\partial x^2} \tag{2.4}$$

(Beyer and Letcher, 1969), where r is the particle displacement from the equilibrium position, x is the distance coordinate in the

direction of propagation and t is time. Omitting $\partial r/\partial x$ from the term $1/(1 + \partial r/\partial x)^2$ would reduce Equation 2.4 to a more familiar form of the wave equation.

To understand under what conditions this omission, or linear approximation can be made, consider the case of a plane harmonic wave such that $r = R \cos(\omega t - kx)$, where $\omega = 2\pi f$ is the angular frequency, $k = 2\pi/\lambda$ is the wave number, and R is the amplitude of vibration. The maximum value for $\partial r/\partial x$ is then $|\partial r/\partial x|_{max} = Rk$, and if $\partial r/\partial x << 1$, then Rk must also be much less than 1. Equation 2.5 relates the acoustic pressure to the particle velocity of the fluid, u, where $u = dr/dt = - \omega R \sin(\omega t - kx)$, as

$$p = \rho_o c u = - \rho_o c R \sin(\omega t - kx) = P_p \sin(\omega t - kx) \qquad (2.5)$$

(Beyer and Letcher, 1969). Hence, the amplitude of the acoustic pressure, P_p, can be expressed in terms of the amplitude of particle displacement,

$$P_p = - \rho_o c R, \qquad (2.6a)$$

or

$$|R| = \left| \frac{P_p}{\rho_o c \omega} \right| \qquad (2.6b)$$

Now the condition $Rk << 1$ can be written as $P_p/\rho_o c^2 << 1$ since $k/\omega = 1/c$.

The pressure amplitude of the ultrasound used in this study is approximately 30 atm. The density of brain tissue, 1.02 g/cm^3 (Goss et al., 1978), and other soft biological tissue is very

nearly that of water, and this is also true for the speed of sound, 1,550 m/sec in brain tissue (Goss et al., 1978). Using these values for ρ_o and c, the corresponding value of Rk is on the order of 10^{-3}. This is significantly less than 1 suggesting that the linear approximation for the one dimensional ultrasonic wave equation, viz.,

$$\frac{\partial^2 r}{\partial t^2} = c^2 \frac{\partial^2 r}{\partial x^2} \quad , \tag{2.7}$$

is justified in the following discussion. It should be pointed out, however, that even this small value of $\partial r/\partial x$ may result in the development of nonlinearities in the propagating acoustic wave. The potential for nonlinearities developing within acoustic waves propagating through biological tissues and the effects they may produce will be discussed in Chapter 10.

The general solution to Equation 2.7 has the form,

$$r = Rb(kx + \omega t) + Rb(kx - \omega t) \quad , \tag{2.8}$$

where $b(kx \pm \omega t)$ is any continuous function with existing first and second derivatives. Ultrasound is usually produced by a sinusoidally oscillating source, and the wave equation solution is very conveniently expressed using complex notation,

$$r = R \exp[i(kx \pm \omega t)]. \tag{2.9}$$

The energy associated with the propagating acoustic wave is present as the kinetic energy of the oscillating particles and the potential energy stored within the compressed regions of the

fluid. The instantneous energy density of a given volume element is,

$$E = \frac{1}{2}\rho_o(U^2 + p^2/\rho_o^2 c^2) \tag{2.10}$$

[Kinsler and Fry, 1962], and using Equation 2.5 to relate p and u, Equation 2.10 reduces to

$$E = \rho_o U^2 \tag{2.11}$$

for a unidirectionally propagating, acoustic wave. For a harmonic wave where

$$u = U \exp[i(kx - \omega t), \tag{2.12a}$$

the time averaged energy density is,

$$\bar{E} = \frac{1}{T}\int_o^T E dt = \frac{\rho_o U^2}{2} \tag{2.12b}$$

The acoustic intensity, I, is defined as the average flow of energy through a unit area normal to the direction of wave propagation per unit time,

$$I = \bar{E}c \quad . \tag{2.13}$$

Other forms of this relationship are,

$$I = \bar{E}c = \frac{\rho_o c\omega^2 R^2}{2} = \frac{\rho_o c U^2}{2} = \frac{P_p^2}{2\rho_o c} = \frac{P_p U}{2} \tag{2.14}$$

2.2. Reflection

The intensity of the ultrasonic wave is attenuated as it propagates through the medium. Acoustic attenuation can be measured by placing a tissue slice of known thickness between two transducers. One transducer sends out an acoustic wave, and the other receives the signal after it passes through the tissue. The attenuation coefficient, A, is then calculated using Equation 1.1, and there is generally good agreement on the value of A in brain tissue, viz., 0.1 neper/cm (Johnston et al., 1979). Energy is removed from the acoustic wave through reflections at the boundaries between media with different acoustic properties, scattering by particles in the medium, and absorption which results in heat generation within the medium.

Reflection occurs when the sound wave encounters an interface between two materials with different acoustic properties. Consider an interface between two fluid-like media, 1 and 2; for example the interface between the saline coupling medium and the cat brain, with the wave incident on the interface from medium 1, the physiological saline. The fractions of the incident wave intensity, I_i, that are transmitted, I_t, and reflected, I_r are given by

$$\frac{I_t}{I_i} = \frac{4\rho_1 c_1 \rho_2 c_2 \cos\theta_i \cos\theta_t}{(\rho_2 c_2 \cos\theta_i + \rho_1 c_1 \cos\theta_t)^2} = \text{Transmission Coefficient} \quad (2.15)$$

and,

$$\frac{I_r}{I_i} = \left(\frac{\rho_2 c_2 \cos\theta_i - \rho_1 c_1 \cos\theta_t}{\rho_2 c_2 \cos\theta_i + \rho_1 c_1 \cos\theta_t}\right)^2 = \text{Reflection Coefficient} \quad (2.16)$$

[Kinsler and Fry, 1962], where Θ is the angle the incident wave makes with the normal to the interface. The subscripts r and t refer, respectively, to the reflected and transmitted waves, and the subscripts 1 and 2 refer, respectively, to the media 1 and 2. The product ρc is the characteristic impedence of the medium and has a value of 1.5×10^5 g/cm^{2}sec for saline, and an average value of 1.57×10^5 g/cm^{2}sec for brain tissue [Goss et al., 1978].

In experiments described herein, the ultrasound is applied to the cat brain at nearly a normal incidence. Therefore $\Theta_i = \Theta_t = 0$, and using the above values for the characteristic impedances of the saline and brain tissue, $I_t/I_i = 0.99$ and $I_r/I_i = 5.2 \times 10^{-4}$. Essentially all of the sound energy remains with the transmitted wave and reflection losses are minimal. However, the brain is not a homogeneous and isotropic medium. Johnston and Dunn [1976b] have studied the contribution of the meninges, and have shown that the transmitted wave intensity is significantly reduced, particularly near the brain sulci. This is due to the meninges forming a resonant structure at some frequencies in the lower megahertz range. Bone has a very high characteristic impedance, 7.4×10^5 g/cm^{2}sec, and reflections from the lower portion of the may also have to be considered.

2.3. Scattering

When inhomogeneities within the medium have dimensions on the order of the acoustic wavelength or smaller, the sound wave is scattered rather than reflected. Thus, the incident waveform is disturbed by the presence of the scattering particles. The standard mathematical procedure is to subtract the incident from

the disturbed waveform and to define this difference as the scattered wave. The scattered wave emmanates from the scattering particles, and its mathematical formulation depends on the geometry of the scattering particle and the nature of the incident wave. Even for scatterers having the simplest geometries, such as spheres and cylinders, a complicated mathematical treatment is required in order to describe the scattered wave.

The following is a brief discussion of the types of scatterers present in biological tissue, and the effect of scattering on the ultrasonic waves used in this study will be given. Using the value of 1,550 m/sec as the approximate speed of sound in brain tissue, Equation 2.1 gives an acoustic wavelength of 1.55 mm for a 1 MHz acoustic wave. Cells, connective tissue networks, small blood vessels, and multicellular aggregates, such as ganglia, are all dimensionally smaller than the acoustic wavelength and may act as scattering elements in the tissue [Reid and Shung, 1979; Waag et al., 1979]. As the frequency of the wave increases and the ratio of wavelength to scatterer dimension decreases, more of the incident wave will be scattered. Very few actual measurements have been made of this parameter, but according to Reid and Shung [1979], scattering accounts for approximately 28% of the total attenuation in liver at 10 MHz. Extrapolating their results to 1 MHz suggests that scattering would account for less than 7% of the total attenuation at this frequency. Freese and Lyons [1979] demonstrated that the amount of scattering is dependent upon the protein and lipid content of the tissue, with the scattering increasing with both protein and lipid content. Because the lipid content of brain tissue is high,

particularly in the white matter, the scattering in brain tissue may be greater than in other tissues, e.g., liver, for a given frequency.

2.4. Absorption

Absorption measurements of 1 MHz ultrasound in brain tissue range between 30% [Goss et al., 1979b] to 70% [Lele, 1982] of the attenuation. Absorption therefore represents the single most significant contribution to the acoustic attenuation.

2.4.1. The Thermoelectric Technique for Absorption Measurements

Absorption has traditionally been determined by placing a thermocouple in the irradiated tissue in order to record the ultrasonically induced temperature rise. The rate of the temperature rise, dT/dt, is used to calculate the value of the absorption coefficient α as,

$$\alpha = \frac{\rho_o C}{\partial I} \frac{dT}{dt} \qquad (2.17)$$

[Goss et al., 1977], where C is the heat capacity per unit volume of the tissue, 0.86 cal/^{o}Cg [Goss et al., 1978]. Equation 2.17 is only applicable when there is no conduction of heat away from the thermocouple junction, otherwise the calculated value for α will be too low. If a large volume of tissue surrounding the thermocouple junction is irradiated with an identical intensity of ultrasound, there would be no temperature gradients established within the absorbing tissue surrounding the junction, and hence, no decrease in dT/dt because of heat conduction. Such is not the

2.1 shows the typical shape of the thermocouple output from a tissue-embedded junction being irradiated with a focused ultrasonic beam. The region marked phase 3 shows a nonlinear temperature rise because of thermal conduction, and so is not suitable for calculating α. Phase 1 contains a viscoelastic contribution to the temperature rise because the thermocouple wires have a relative motion with respect to the tissue which is induced by the ultrasonic wave. Phase 2 displays an essentially linear temperature rise, and it is the slope of this region that is used to calculate α. Goss et al. [1977] calculated α from the slope of the thermocouple output at 0.5 sec into the irradiation because the effects of viscoelastic heating and thermal conduction were minimized.

The magnitude of the viscoelastic contribution to the thermocouple output increases with the diameter of the thermocouple junction, and it has been reported that the junction diameter significantly affects the recorded values of [Goss et al., 1977]. However, evidence supporting no effect of junction size also exists [Pond, 1968].

2.4.2. Viscous, Thermal Conduction, and Molecular Absorption

Absorption arises when ultrasound does work on the medium, losing some of its energy which is eventually converted into heat. This occurs when there is a time lag between the condensation of the medium relative to the varying acoustic pressure. Consider the pressure-volume diagram in Fig. 2.2. If condensation and acoustic pressure are in phase, the path of the compression cycle, 1-2-3, will be identical, but in the opposite direction of the

expansion cycle, 3-2-1. The work done on the medium during each cycle 1-2-3-2-1, represented by the area under each of these curves, is equal in magnitude and opposite in sign. Therefore, no absorption occurs and the ultrasound propagates in an energy conserving manner. However, if condensation lags pressure, the compression cycle 1-4-3 will differ from the expansion cycle 3-5-1, and the area circumscribed by the loop 1-4-3-5-1 represents the energy absorbed by the medium.

Absorption in isotropic fluids, such as water or castor oil, can be divided into three catagories, viz., viscous absorption, absorption resulting from heat conduction, and absorption associated with energy exchanges between the sound wave and molecules of the medium. The former two are commonly referred to as the classical absorption mechanisms. Viscous absorption occurs when there is relative motion between various portions of the medium during the condensation and expansion cycles in the propagating sound wave. The frictional forces between these portions retard their movement in response to the sound wave, and result in a phase lag of the condensation relative to the acoustic pressure.

The basic equations governing acoustic wave motion are derived assuming that the pressure changes occur adiabatically. Therefore, the temperature will rise in regions undergoing condensation and decrease during expansion. If the medium has a significant thermal conductivity, heat will then be conducted along the temperature gradient established between these two regions. This tends to reduce the pressure gradient, thus decreasing the pressure amplitude of the acoustic wave.

During condensation, some of the acoustic energy stored in the compressed medium may be transferred to the internal vibrational and rotational degrees of freedom of the molecules [Kinsler and Fry, 1962]. During the expansion stage, some of this energy in the internal molecular modes is returned to the sound wave, but because the energy transfer requires a finite period of time to occur, some of the energy remains within the internal modes and is transferred at a later time. This process is called molecular relaxation, and the time period required for the stored molecular energy to relax back to 1/e of its initial value is called the relaxation time. As long as the molecular relaxation times and time required for viscous interactions and condensation to occur are longer or on the order of the period of the acoustic wave, this mechanism contributes to the absorption of acoustic energy.

2.4.3. Relative Motion

W. J. Fry [1952] discussed the possibility that relative motions among the various components within the tissue, e.g., cytoplasm and nuclei, may contribute significantly to acoustic absorption. He presented the mathematical treatment of a hard spherical particle of mass M suspended in a viscous medium which is exposed to a sinusoidally oscillating acoustic wave. The resultant expression for the steady state velocity, v, of such a particle in a fluid of density ρ and viscosity η, irradiated with

an acoustic wave of angular frequency ω and pressure amplitude P_p is,

$$V = \frac{P_p}{c}\left[\frac{\omega^2(m_e/M_e) + (R/M_e)\sin(\omega t) + \omega(R/M_e - 1)\cos(\omega t)}{\omega^2 + (R/M_e)^2}\right] \quad (2.18)$$

where R is the frictional coefficient

$$R = 6\pi a\eta[1 + (\omega\rho/2\eta)^{1/2} a], \quad (2.19)$$

a is the particle radius, M_e is the effective mass of the suspended particle,

$$M_e = M + m[1/2 + (9/4a)(2\eta/\omega\rho)^{1/2}], \quad (2.20)$$

m is the mass of a fluid element having a volume equal to that of the particle, m_e is the effective mass of that fluid element,

$$m_e = m + m\,[1/2 + (9/4a)(2\eta/\omega\rho)^{1/2}] \quad (2.21)$$

and c is the speed of sound in the fluid. The particle velocity of the fluid element is $\dot{r}$,

$$\dot{r} = P_p/\rho c \sin(\omega t), \quad (2.22)$$

and the relative motion between the fluid and the suspended particle is obtained as the difference between Equations 2.18 and 2.22.

The expression for relative velocity can be differentiated with respect to time to obtain an equation for the relative acceleration between the particle and the medium. The amount of acoustic energy converted into heat per cycle of the acoustic wave

by the suspended particle is then,

$$\int_0^T R(v - \dot{r})^2 dt = \left(\frac{P}{\rho c}\right) \left(\frac{RT}{2}\right) \frac{\omega^2 (m_e/M_e - 1)^2}{\omega^2 + (R/M_e)^2} , \qquad (2.23)$$

where T is the oscillation period of the sound wave.

W. J. Fry [1952] presented the mathematical model, but did not make any sample calculations to estimate the contribution of such a mechanism to the absorption coefficient measured in biological tissue. The cell nucleus suspended in the cell cytoplasm may be considered the most likely source of any relative motion-related energy absorption in biological media since the nucleus is 35 - 60% denser than the cytoplasm [I. R. Johnston, 1972].

Both LM and TEM observations of the nonirradiated cat brain tissue have demonstrated that 12 μm is a typical diameter for neuronal nuclei. The neuronal nuclei appear very round in the tissue sections, and so assuming a spherical shape, the volume of the neuron nucleus is 9.05×10^{-10} cm^3. Using a density of 1.5 g/cm^3 [I. R. Johnston, 1972] gives a neuron mass of 1.36×10^{-9} g.

Although the cytoplasm is not a homogeneous fluid, as a first approximation it will be modeled as so with a density of 1.02 g/cm^3 [I. R. Johnston, 1973; Goss et al., 1978] and a viscosity of 0.05 poise [Haack et al., 1976]. The viscosity measurement of Haak et al. [1976] was made using an electron spin resonance, ESR, probe located in the axoplasm.

Using the irradiation parameters that were used for the cat brain experiments, viz., a 300 W/cm^2 acoustic intensity and 1 MHz

frequency, Equation 2.23 yields a value of 2.14×10^{-6} ergs per cycle per nucleus for the frictional energy being converted to heat resulting from relative motion between the nucleus and the cytoplasm. Greenough [1983] has determined that there are, on the average, 7.8×10^{4} neurons/cm^3 in the GM, which yeilds 1.67×10^{8} erg/sec cm^3 for the calculated heat energy generated by nuclear relative motion. The temperature rise $\Delta T/\Delta t$ is then 4.8^{o}C/sec. Inserting this value into Equation 2.17 yields an absorption coefficient of 0.029 np/cm. This is 100% of the absorption measured by Goss et al. [1978] and 41% of that measured by Lele [1982].

Note that these calculations were made using a value of 0.05 poise for the cytoplasm viscosity, i.e., the microviscosity measured by a macromolecular ESR probe. The effective viscosity acting on larger particles such as the nucleus may be much greater, because the number and relative size of other structures within the cell will affect the effective viscosity they experiened [Tanford, 1961].

Biological cells are filled with suspended organelles such as the endoplasmic reticulum, mitochondria, golgi, etc., and Fig. 2.3 suggests that the endoplasmic reticulum and golgi are even intimately associated with the nuclear membrane. The cytoplasm is also pervaded by a network of microtubules and other filaments which constitute the cytoskeleton (Fig. 2.4). The nuclei are large in comparison to the cytoskeletal filaments and other subcellular organelles, and so such structures will impede any motion imparted to the nuclei, thus increasing the effective

probe on the other hand would experience the lower effective viscosity of 0.05 poise since it is small enough to translate essentially unimpeded amongst the subcellular organelles and cytoskeletal matrix.

Direct evidence that the nucleus is subjected to a higher effective viscosity than 0.05 poise is provided by the position of the nucleus within the neuron. If there was nothing within the cell to impede it, the nucleus would sink to one side of the cell and rest against the cell membrane if the effective viscosity was only 0.05 poise. Observations of the neurons show that the nuclei occupy an essentially central location within the cell. One can almost picture the nuclei being suspended in the network of cytoskeletal filaments and endoplasmic reticulum, much like a spider in its web.

A more recent analysis by O'Donnell and Miller [1979] suggests that the viscous losses from the motions of scattering particles within biological tissues can account for nearly 60% of the measured attenuation within the frequency range of 1 - 10 MHz. They modeled the particles as spheres and computed the expected attenuation as a function of particle radius. It was determined that particles with radii much less than the acoustic wavelength, particularly those with radii near 1 micron, were most effective in producing the viscous attenuation. They suggested that molecular aggregates of proteins, such as collagen, were the principal structures in tissue that would contribute most to a viscosity related absorption mechanism. They did not specify the values used for the effective viscosity of the cell cytoplasm, but even the motions of particles with 1 μm radii would be hindered by

the cytoskeletal filaments, significantly increasing the effective viscosity and reducing any contribution of viscosity related attenuation.

2.4.4. Molecular Relaxation Processes

Pauly and Schwan [1971] measured the ultrasonic attenuation of whole, ground and homogenized liver. Two different homogenates were used. One had essentially all of the cells, nuclei and the majority of mitochondria, together with the other subcellular organelles destroyed. The other homogenate had more than 95% cell lysis, but the subscellular structures remained intact. The attenuation measured for both these homogenates was identical and only 30% less than that recorded for the whole and chopped liver. This study strongly suggests that 70% of the attenuation in intact biological tissue arises from a level of organization smaller in dimension than the mitochandria, 0.1 - 1 μm. This is in direct disagreement with the model proposed by O'Donnell and Miller [1979]. The 30% of the attenuation which may be related to larger structures and cellular organization within the tissue is similar to the attenuation contribution of scattering suggested by Reid and Shung [1979]. Therefore, homogenizing the tissue may have ruptured the scattering structures and eliminated that portion of the attenuation attributable to scattering phenomena.

Pauly and Schwan interpreted their results to mean that the majority of acoustic attenuation was absorption which occurred at the macromolecular level within the tissue. They suggested that the biological macromolecules of the tissue yielded a large number of different relaxation processes, having a wide range of

relaxation times. They also demonstrated that such a distribution of relaxation processes could account for the linear dependence of the attenuation coefficient on frequency that is observed in biological tissues.

An acoustic wave can also perturb the equilibrium state of chemical reactions as a result of the time varying acoustic pressure. Such equilibrium phenomena also fall into the catagory of relaxation processes. For example, Eigen and Hammes [1963] studied the acoustic absorption in solutions of the amino acid glycine at pH 10, as a function of frequency. Their data suggested the presence of a single relaxation process, specifically the transfer of a proton between the glycine molecules and the neighboring water molecules. At equilibrium, a certain fraction of the protons in solution are associated with the glycine molecules, and the remainder with the water molecules. As the acoustic pressure changes, the thermodynamic conditions change, and the equilibrium distribution of protons will shift in an attempt to reach an equilibrium at the new pressure. In the case of a sinusoidally varying acoustic wave, the equilibrium will change in an attempt to follow the time varying acoustic pressure.

The ultrasonic absorption from a single relaxation mechanism, at an acoustic frequency f can be expressed as,

$$\frac{\alpha}{f^2} = \frac{C\tau_r}{1 + (2\pi\tau f)} \qquad (2.24)$$

[White and Slutsky, 1972], where the relaxation time, τ, is a measure of the time required to achieve equilibrium following a small disturbance, and C is the amplitude of the relaxation

process. Using this notation, the model for a distribution of relaxation processes proposed by Pauly and Schwan [1971] can be expressed as,

$$\frac{\alpha}{f^2} = B + 2 \int_{\tau_1}^{\tau_2} \frac{C\tau}{1 + (\alpha\pi\tau f)} \, d\tau \qquad (2.25)$$

where τ_1 and τ_2 represent the lower and upper bounds of the relaxation times for contributing relaxation processes at the acoustic frequency f, and B represents the absorption from classical mechanisms and other relaxation processes occurring at frequencies much higher than $1/\tau$.

Although the model of multiple relaxation processes can describe the acoustic absorption and its linear dependence on frequency, it does not identify the physical and chemical nature of the relaxation processes. The following are some relaxation processes which have been suggested to account for the acoustic absorption in biological tissue.

Kato et al. [1979] measured the acoustic absorption for aqueous solutions of dextran as a function of temperature and frequency. They observed that the acoustic absorption and the relaxation amplitudes increased with decreasing temperature, i.e., increasing hydration [Nomura et al., 1964]. No dependence on molecular weight was observed for any of the dextran chains used. Their conclusion was that the ultrasonic relaxation processes were most likely associated with the exchange process of the water molecules within the hydration sphere of the polymer. The expression for the relaxation strength has both temperature and volume dependent terms, and the data for the dextran relaxations

demonstrated that the relaxation frequencies were essentially independant of temperature. With reference to the molecular structure of dextran, they concluded that the thermal relaxation resulting from the rotation of small molecular segments was insignificant. They considered the volume relaxation process to be predominant and speculated that the acoustic wave perturbs the segmental motion of the dextran chain in a manner which results in a rearrangement of the water molecules weakly interacting with the polymer chain.

Kessler and Dunn [1969] concluded that the observed distribution of relaxation times and the velocity dispersion from measurements made in aqueous bovine serum albumin (BSA) indicated a structural relaxation phenomenon was associated with acoustic absorption, and that the same mechanism was present in other aqueous biomacromolecular solutions. Since all macromolecules in aqueous solution have a surrounding hydration layer, it is possible that the structural rearrangement of the hydration sphere suggested by Kato et al. [1979] may play a significant role in the absorption of ultrasound in biological systems. O'Brien and Dunn [1972] measured the absorption properties of two distinct forms of hemoglobin and compared the frequency dependence to the absorption measurements made for several other proteins. Although the magnitudes of the absorption varied, the frequency dependencies were approximately the same. It was proposed that the mechanism of ultrasonic absorption in the different protein solutions was related to some common factor shared by these different protein molecules, viz., the surrounding hydration layer was perturbed by the acoustic wave. Differences in the magnitude

could be attributable to differing degrees of hydration, a supposition later supported by the findings of Kato et al. [1979] discussed above.

Other investigators contend that the absorption in aqueous biomacromolecular solutions results from a solvent-solute interaction similar to the protein transfer relaxation of Eigen and Hammes [1963]. Slutsky et al. [1980] have studied the absorption of the peptide bacitracin in aqueous solutions with and without a phosphate buffer being present, and found that the observed absorption increased with phosphate buffer concentration, and that the volume changes calculated from the data were close to the value expected for the protonation of the imidazole ring from the histadyl residue in bacitratcin. This information, together with the calculated rate constants, pointed to a proton transfer between the imidazole ring of bacitracin and inorganic phosphate, as the primary absorption mechanism. Analysis based on the intracellular concentrations of inorganic phosphate and concentrations of histadyl-like residues in biological tissue suggested that this proton transfer mechanism may significantly contribute to the absorption in tissues.

2.4.5. Hysteresis

Johnston and Dunn [1981] considered the effects of nonlinear stress-strain behavior for ultrasonic propagation in biological tissues during a high intensity ultrasonic irradiation and its relationship to the absorpton of acoustic energy. Yamada [1970] has measured the stress-strain relationships for many organs and tissues of the body. His findings indicate that for static

conditions, nearly all tissues exhibit a linear stress-strain relationship over a given range, and beyond this range nonlinear behavior prevails. Over a range of low acoustic intensities, below 50 W/cm^2, the tissue exhibits a linear relationship between stress, σ, and strain, ε,

$$\sigma = E\varepsilon \tag{2.26}$$

where E is the modulus of elasticity, reflecting the acoustical properties of the tissue [Johnston and Dunn, 1981]. With increasing acoustic intensity, and hence increasing stress, the relationship between stress and strain becomes nonlinear,

$$\sigma = K\varepsilon_i^n \tag{2.27}$$

where K is the strength coefficient, εi is the inelastic strain and n is the cyclic strain hardening exponent having a value between 0 and 1. When stress and strain are linearly related, the medium does not absorb any energy from the acoustic wave. Energy is lost only in the nonlinear portion of the stress-strain relationship, and the linear portion can be ignored. At a given point within the tissue, the energy absorbed by the medium during each acoustic cycle is constant. Therefore, the absorption will increase linearly with increasing acoustic frequency in agreement with the frequency dependence of absorption observed for biological tissues. This pheonomenon related to the nonlinear stress-strain properties of biological tissues has been termed ultrasonic hysteresis.

The empirical formula, $It^{1/2} = 200$ which described the threshold relationship between intensity and exposure time for lesion production in mammalian brain tissue can be written in terms of the acoustic stress and the number of acoustic cycles occurring during a threshold exposure. When this relaionship is applied to experimental data for lesion production in various tissues, the value for the cyclic strain hardening exponent, n, for that tissue can be calculated.

2.5. Acoustic Cavitation

The only concrete evidence suggesting non-thermal lesion producion was presented by Pond [1968] and F. J. Fry et al. [1970], using ultrasonic intensities in excess of 1,500 W/cm^2. The resulting tissue damage was very different in nature from that observed in lesions produced with the lower intensities. Tissue damage appeared immediately after the irradiation, it did not require any post-irradiation time to develop, and was not confined within the focal volume of the acoustic field. Instead, the damage had a tendency to occur near interfaces between the neural tissue and fluid filled regions such as blood vessels and ventricles, and there was no difference between the sensitivity of white and gray matter. Because of these facts, and because the temperature changes appeared inadequate to support thermal damage [Pond, 1968], acoustic cavitation was proposed as the mechanism most likely responsible for these high intensity lesions [F.J. Fry et al., 1970].

The term acoustic cavitation refers to the behavior of gas or vapor filled bubbles, or cavities, in response to an acoustic wave

within a fluid or fluid-like medium. If the negative pressure present during the rarefaction phase of the acoustic cycle is sufficient to overcome the tensile strenth of the medium it fractures, and cavities filled with the gaseous phase of the fluid medium are produced. These cavities oscillate in response to the acoustic wave. This process is referred to as true cavitation, and the term vapor is used to distinguish the gaseous phase of the fluid medium (water vapor in the case of biological tissues) from other dissolved gasses.

In the absence of cavity formation, cavitation activity requires the presence of proper sized nuclei such as gas bubbles within the medium. The bubble radius resulting in the maximum cavitation activity is referred to as the resonance radius, and it is a function of the acoustic frequency and the physical properties of the medium. In water, the resonant size has been determined experimentally to be 3.5 microns at a frequency of 1 MHz [Miller, 1977].

Cavitation nuclei need not be present at the resonant size, but may initially be smaller and then grow to resonant size by a process called rectified diffusion [Coakley and Nyborg, 1978; Crum, 1980a]. Therefore, a population of resonance sized bubbles or cavities can form from smaller nuclei under the influence of the acoustic wave.

Two distinct classes of cavitation have been discussed in the literature, viz., transient and stable. Transient cavitation is characterized by short lived bubbles or cavities that grow to an unstable size and then collapse violently upon themselves, usually within several cycles of the acoustic wave [Flynn, 1964; Crum,

1982]. Temperatures in excess of 3,500°K are believed to be achieved at the center of the collapsing bubbles [Repacholi, 1981], and may provide energy to accelerate chemical reactions, or initiate reactions unattainable at lower temperatures. Shock waves are also created during this violent collapse, and can cause massive destruction to biological material, as has been demonstrated on cells in suspension [Hughes, 1961; Sacks et al., 1982].

The cavitation that was observed in the cat brain by F. J. Fry et al. [1970] was of this transient type. Their results suggested that the fluid-filled regions of the brain, viz., the blood vessels and the ventricular system, may contain cavitation nuclei, or that the interfaces between these regions and the surrounding tissue are sites of structural weakness where *de novo* cavities may form.

Bubbles participating in stable cavitation oscillate for many acoustic cycles, usually in a nonlinear manner, and can produce secondary sound fields and streaming currents within the medium. The streaming, referred to as acoustic microstreaming, can cause damage to cells *in vitro* [Rooney, 1970; Miller et al., 1978], and to nervous tissue *in vivo* [El'Piner et al., 1965]. Stable, oscillating bubbles also generate heat, but are incapable of producing the extreme, localized temperatures which can accompany transient cavitation.

The acoustic thresholds required to induce cavitation decrease with both increasing gas content and temperature of the medium [Caokley and Nyborg, 1978; Crum, 1982b]. Hence, the temperature rise resulting from the sound energy absorption by the

tissue will increase the potential for cavitation to occur. Gas solubility decreases with increasing temperature [CRC Handbook, 1974], and so the free gas content within the irradiated volume will increase. This may promote the formation of cavitation nuclei or facilitate the growth of preexisting nuclei by rectified diffusion.

Evidence for the existence of lower intensity induced cavitation in vivo has recently been reported. Ter Haar et al. [1982] utilized an ultrasonic imaging system to observe echoes from what was interpreted to be gas bubbles within the tissue. Frizzell et al. [1983] observed half harmonic signals of the fundamental wave when they irradiated neonatal mice. The presence of a half harmonic signal is indicative of cavitation activity [Flynn, 1964; Beyer, 1974]. Frizzell et al. [1983] also pressurized their irradiation chamber and observed a decrease in the subharmonic signal, indicating that cavitation was being suppressed. They also noted an increase in the threshold dosage required to paralyze the neonatal mice under pressurized conditions, suggesting that cavitation is involved in producing the paralysis.

Cavitation may produce tissue damage in different ways besides the violent cell rupturing that can accompany transient bubble collapse. The additional heat generated by cavitation may increase the tissue temperature above that temperature which would have resulted from absorption processes alone, providing the additional heat required to kill cells. Cavitation activity can produce free radicals in the medium [Repacholi, 1981; Flynn, 1964]. Armour and Corry [1982] demonstrated that cells irradiated

with ultrasound *in vitro* were protected from ultrasonically induced death by introducing a cell membrane permeable, free radical quencher into the medium. Another free radical quencher incapable of crossing the cell membrane did not provide any protection. This suggested that the ultrasound induced cavitation within the system which produced free radicals that killed the cells from within.

2.6. Radiation Force

Because the propagating acoustic wave transports momentum, it exerts a time-independent force on the medium called radiation force. The radiation force on a steel sphere has been used as an absolute method for determining the intensity of acoustic sources [Dunn, et al., 1977; Stockdale and Hill, 1976]. Figure 2.5 illustrates the geometry of the steel ball radiometer, and from this, the radiation force, F, acting on the sphere can be expressed as,

$$F = mg \tan\theta = \frac{mgx}{(L^2 - x^2)^{1/2}} = \frac{YI\pi^2}{c} \qquad (2.28)$$

where m is the mass of the sphere, θ is the angular displacement of the sphere from the vertical, a is the radius of the sphere, x is the horizontal displacement of the sphere, Y is the acoustic radiation factor which depends upon the material and dimensions of the ball, g is the acceleration due to gravity, and L is the length of the string from which the ball is suspended. A similar pheomenon, called radiation torque, can impart a spinning motion to suspended particles exposed to an ultrasonic wave.

Dyson et al. [1974] observed an ultrasonically induced inhibition of blood flow in chick embryo blood vessels. The red blood cells redistributed into parallel bands one half wavelength apart within a standing ultrasonic wave. Although they themselves suggested that radiation forces may somehow be involved in producing this phenomenon, several calculations within their report indicated that this may not be true. Gould and Coakley [1974] have observed this phenomenon in vitro, and concluded that radiation forces were involved, but that the simple mathematical theory must be modified in order to fully describe the event. Church et al. [1982] have reached a similar conclusion.

If tubes, or tubelike structures exist in the medium, a gradient of radiation force across the tubes may produce a flow pattern. Gershoy and Nyborg [1973] suggested this may be the mechanism responsible for the cytoplasmic flow they observed in ultrasonicated plant tissue. The "tubes" in their model were the liquid filled spaces between the endoplasmic reticulum membranes, and other structures in the cell cytoplasm.

Dunn and Pond [1978] discussed several non-thermal, non-cavitation ultrasonic mechanisms, termed stress mechanisms, that may affect the structure and function of irradiated biological tissues. The stress mechanisms characteristically have a time-independent component, and are related to phenomena such as radiation force, radiation torque and acoustic microstreaming.

CHAPTER 3

MATERIAL AND METHODS

3.1. Cat Brain Irradiations

Adult, female cats were surgically prepared for ultrasonic irradiation of the brain in a manner similar to that described by W. J. Fry [1958]. Modifications in the procedure were made to permit a rapid perfusion of the brain following the irradiation without removing the animal from its stereotoxic apparatus. Provisions were also made for isolating those portions of the chemically fixed brain which contained the irradiated tissue.

Each animal was anesthetized with an intraperitoneal injection of sodium pentabarbitol at a dosage of 12 mg per pound of animal weight. An electric razor was used to remove fur from the animal's head, neck, and a region on the left side of the chest covering the fourth intercostal space. The animal was then properly aligned in a Horsley-Clark type stereotaxic apparatus [Snider and Neiman, 1964], and that portion of the skull covering the cerebrum was removed, taking care to ensure that the meninges remained intact. A bone flap was also removed in order to expose the cranial sinuses, which were then filled with bone wax. Gauze pads, soaked with physiological saline, were then placed over the exposed portion of the brain to keep the tissue moist.

A 0.5 cm^3, intramuscular injection of 1% lidocaine hydrochloride was placed in each side of the neck to suppress the presso receptors in the neck in order to inhibit the muscular walls of the neck arteries from contracting upon cannulation. Omitting the lidocaine hydrochloride injections did not result in

the collapse of the carotid arteries during perfusion, but since these injections did not affect the normal morphology of the brain or its response to the ultrasound, they were routinely administered as a precautionary measure. Using a cauterizing scalpel, a subcutaneous incision was made along the ventral midline of the neck, and blunt probes were used to manipulate the muscles and connective tissue in order to expose both common carotid arteries. Connective tissue was carefully removed from the region surrounding these arteries. A blunt probe was pushed through the carotid sheaths between the vagus nerves and the common carotid arteries, and the nerves and blood vessels were carefully teased apart. A piece of surgical thread was looped around each common carotid artery for subsequent relocation. Saline-soaked gauze was then used to pack the neck incision in order to keep the tissue moist. In earlier experiments, the right common carotid artery was cannulated at this point, and ligated immediately inferior to the point of cannulation [Borrelli et al., 1981]. In the later experiments cannulation was performed just prior to sacrificing the animal in order to maintain normal blood flow to the brain during the ultrasonic irradiations. A small hole was drilled through the skull, over the cerebelum, through which a thermistor probe was later inserted. The skin tissue from the cranial incision was used to form a watertight seal to a headpan that was attached to the stereotaxic device, and suspended over the exposed portion of the brain.

The transducer used for irradiating the cat brain consisted of a piezoelectric X-cut quartz crystal, mounted in a stainless steel housing. A plastic lens was placed in front of the

transducer to focus the ultrasonic beam, and the space between the quartz and the lens was filled with oil in order to minimize any internal losses of acoustic energy. The focused beam patterns for this transducer, showing the relative acoustic intensity as a function of position from the transducer face, as measured in water, are shown in Figs. 3.1 and 3.2. The beam pattern in the plane perpendicular to the beam axis has a half power beam width of approximately 3.0 mm. It must be pointed out however, that the actual beam pattern present in irradiated tissue may differ from that measured in water because of the differences in acoustic properties between the two media.

Before each experiment, the transducer output was calibrated using the thermocouple probe, a secondary standard that was previously calibrated against the steel ball radiometer discussed in Chapter 2 [W. J. Fry and Dunn, 1962]. A computer received the thermocouple output with the thermocouple located at the center of the focal volume, determined the slope at 0.5 seconds into the exposure (for reasons discussed earlier), and then calculated the acoustic intensity produced by the voltage applied to the transducer using Equation 2.17. Measurements were also made with the thermocouple located at other points within the focal volume in order to obtain a beam plot of the acoustic field.

After being calibrated, the transducer was attached to the stereotaxic system and a cap, containing a pointer, was placed over the transducer. The tip of the pointer represented the location of the focal volume center, and was brought to rest on the surface of the brain located above the sites selected for ultrasonic and sham irradiation. Since the stereotaxic

coordinates for these irradiation sites were known (from using the stereotaxic atlas), the difference between the vertical coordinate of the brain surface, and that for the desired site represented the depth of that site below the brain surface. The sites were selected such that they did not lie below the brain sulci in order to minimize the resonant effect on the sound attenuation introduced by the brain meninges discussed by Johnston and Dunn [1976b]. Equation 1.1 was then used to correct for the attenuation of the intervening tissue, and to determine the acoustic output of the transducer required to deliver the desired acoustic intensity when the focal volume of the acoustic beam was centered on each site. After all of the sites were measured, the pointer was removed from the transducer, the headpan was filled with physiologic saline (the acoustic coupling medium between the transducer and the brain), and the transducer was lowered into the saline, taking care that no air bubbles were trapped on the surface of the focusing lens. Because the attenuation coefficient of the saline is some 4.4×10^2 times smaller than that of the tissue [W. J. Fry and Dunn, 1962], any saline related attenuation was regarded as insignificant.

The saline and brain temperatures were regulated and maintained at $37^{\circ}C$. Four to eight selected sites were irradiated with 1 MHz ultrasound having a spatial peak temporal average (SPTA) intensity of 300 W/cm^2 at the focal center, and exposure times were in the range of 0.35 to 5.0 sec. Successive irradiations were made in alternate brain hemispheres, and the corresponding site in the unirradiated hemisphere was sham

irradiated. The exposures were delivered to each of the animals according to one of the following protocols.

1. The irradiations were delivered to sites that were similar with respect to their GM and WM constitution. Two different exposure times were used, and the irradiations were made in pairs, one of each exposure time, with a minimum elapsed time in between. The exposure pairs were separated by recorded time intervals.

2. Two classes of sites were chosen that differed with respect to their GM and WM constitutions, e.g., one class being a pure WM region and the other pure GM. The sites were irradiated in pairs, one from each class, with identical exposure times. The time between irradiating each member of a pair was minimized, and the elapsed time between irradiating pairs was recorded.

3. Two different exposure times, t_1 and t_2, were used, where t_1 was longer than t_2. Two classes of sites, differing in their GM and WM constitution, were irradiated in pairs, one from each class, with the site having the lower WM content receiving the longer exposure. Time between irradiating the sites from each pair was minimized, and the elapsed time between irradiating pairs was recorded.

4. All sites were of similar WM and GM constitution, and received identical exposures. The elapsed time between the exposures was recorded.

Protocol 1 was used to investigate the effect of different exposure times on the ultrasonically-induced tissue damage, protocol 2 was used to investgate the variations in tissue damage resulting from differences in the WM and GM constitution of the tissue sites, protocol 3 was an attempt to determine exposure times for WM and GM that would result in iso-effect lesions, and protocol 4 was used as the primary scheme for determining the temporal sequence of the ultrasonically-induced morphological changes resulting from the given exposure time. Protocol 4 was the most frequently used. It might be argued that animals irradiated with protocol 4 could have provided the information obtained from protocols 1 - 3. This would have been true except that it was discovered early in the study that there was considerable variation in the response of identical sites in different animals to the same ultrasonic exposures. Protocols 1 - 3 provided the desired information while eliminating the factor of specimen variability.

If the animal was to be sacrificed immediately following the last irradiation, the right carotid artery was cannulated just prior to making the exposure. Immediately following the last irradiation, a large scalpel was used to cut into the fourth intercostal space and remove the animal's heart. Simultaneously, perfusion with herparinized (500 units of pan heparin per liter of perfusate), physiological saline was initiated via the right carotid artery, and the saline was removed from the headpan. While the heart was being removed, the left carotid artery was canulated and so perfusion continued via both common carotid

the brain, because no blood could enter the brain to mix with or work against the perfusion solutions. If the animal was to be sacrificed at some later time, the right carotid artery was not cannulated until the scheduled time had elapsed, thus preserving normal blood flow to the brain during the lapse period.

Some animals were sacrificed following a 24 hr post irradiation period, and for these animals the following procedure was followed. After the last irradiation, the pointer was reattached to the transducer to relocate the points on the brain surface over the irradiated and sham irradiated sites, and these were marked with indelible ink. The scalp was sutured over the brain, and the animal was removed from the sterotaxic apparatus to a padded cage. After 24 hr, the animal was reanesthetized and relocated into the stereotaxic apparatus. The carotid arteries were cannulated and perfusion proceeded as described below.

Perfusion was accomplished by using a pump to maintain the fluid pressure between 115 - 120 mm Hg. The pump was used in place of the syringe-driven perfusion used earlier. The solutions could now be delivered at a constant pressure similar to the normal atrial pressure of the animal, thus eliminating the possibility of pressure-induced artifacts in the tissue morphology. Once both catheters were in place the perfusion could be completed by one person, whereas the syringe method required an additional person to fill the syringes. Draining perfusate was channeled to a collection bottle.

After aproximately 1 min of saline perfusion, the brain became paler in color, indicating that the blood had been flushed out. Perfusion was then continued with an aldehyde fixative

consisting of 2.5% gluteraldehyde, 2.0% paraformaldehyde in 0.1 M cacodylate buffer at a pH of 7.2, until 1.5 to 2 liters of the fixative had been perfused through the animal, or the brain became firm to the touch. The meninges were then carefully removed from over the surface of the irradiated portion of the brain and the pointer was reattached to the transducer to relocate the points on the surface of the brain directly over the irradiated and sham sites. The sites were then marked with a small indelible ink spot. A 5 mm diameter hollow tube with a razor sharp rim was attached to the pointer, centered over the marked regions, and slowly driven into the fixed tissue using the vertical control of the stereotaxic system. Thus, 5 mm diameter cores of tissue containing the irradiated or sham sites were separated from the rest of the brain.

In general, the cores remained in the brain when the tube was retracted. The entire brain was then removed from the animal, and the cores were isolated using a blunt probe. When the cores became lodged in the tube, a gentle stream of fixative applied with a syringe was sufficient to dislodge them. A very shallow groove was cut along the ventral side of the core for orientation purposes. Each core was then placed in a labeled vial filled with fixative, allowed to set 2 - 3 hr at room temperature, and then stored for a minimum of 24 hr at $4^{o}C$.

A tissue slicer with micrometer advance [Duffy and Tyler, 1975] was used to cut 0.25 mm thick disks from the sham and irradiated core samples, for a distance of 3 mm on either side of the tissue site centered in the focal volume. The pattern of gray and white matter on each disk was sketched so that it could later

be properly reoriented. If these tissue patterns were nondistinct, one or more nicks were placed on the disk for orientation purposes, in addition to the mark resulting from the groove placed on each core. These disks were stored an additional 24 hr in refrigerated fixative before further processing.

During the course of this study four animals were prepared as above, except that the brains were not irradiated with ultrasound. Two of these animals were perfused with the syringe perfusion used earlier in the study, and the other two were perfused using the perfusion pump. Tissue was examined from these animals with both LM and TEM and served as controls to which the irradiated and sham irradiated tissues could be compared. Random tissue samples were taken from the irradiated cat brains, from regions other than the tissue contained in the cores with the sham irradiated and irradiated sites. These along with the sham irradiated sites were used to determine whether tissue damage existed anywhere in the brain other than the irradiated volumes.

3.2. Thermocouple Experiments

The temperature profile recorded by a tissue embedded thermocouple results not only from the bulk heating of the tissue arising from acoustic absorption, but also from a viscous relative motion between the thermocouple wires and the surrounding tissue. Goss et al. [1977] demonstrated that this viscous heating increased with increasing wire diameter, and that it could be reduced to less than 10% of the absorption related heating by using a wire diameter of 13 μm or less. For this reason, thermocouple wires were acid etched before forming the junction to

ensure that the junction and wire within 4 mm of the junction had an approximate diameter of 13 μm.

Etched, chromel-constantan thermocouples were constructed according to the following scheme. Eight inch segments of each material were cut from stock spools of 76 μm diameter wire and gathered into bundles of ten. The constantan wire bundles were formed into a gentle loop and the loose ends were taped to a wooden tongue depressor. Chromel bundles were treated in a similar manner, but the tongue depressor was wrapped with aluminum foil along the region where the wires were attached. All wires were cleansed by rinsing the loops several times with 95% ethanol, followed by several rinses in distilled water.

Constantan wires were etched by dipping the wire loops into a 2:1 solution of concentrated nitric acid and water. The apex of the loop was submerged in the acid solution and then withdrawn slowly. This process was repeated until the wire at the apex of the loop etched away completely, resulting in two groups of 10, 4 inch wires. Etching was continued until the free, wire ends had a nice taper, with a diameter of approximately 6.5 μm at the tapered ends. Residual acid was then rinsed away with distilled water.

Chromel wires were etched by dipping the wire loops into a glass petri dish containing a 30% sulphuric acid solution, and an steel plate at its base. A potential difference of 3 to 4 V was maintained between the iron plate (cathode) and the aluminum foil (anode) to which the wires were attached. The potential difference was produced by a DC power source, and measured while the wire loop was in the acid. Etching was then performed in the

identical manner described for constantan wires. The DC potential provided the energy to drive the acid-etching process. Without it, the chromel wires would not have been affected by the sulfuric acid.

The etched ends of all wires were examined under a dissecting microscope to ensure that the tapered ends were approximately 6.5 μm in diameter, and did not exceed a diameter of 13 μm for a distance of 3 - 4 mm from the tip. If the tip was too narrow, it was salvaged by cutting back to the point where it was of the appropriate size. Wires with too wide a taper were reetched. Etched wires meeting the above requirements were cleansed in 95% ethanol and rinsed with distilled water. The etched ends were then dipped into a soldering flux, and tinned by repeated immersion into a molten solder pool. Twisting the wire between the thumb and forefinger as it was inserted into the solder pool aided the tip in breaking the surface tension of the solder. Repeated treatment with the flux was necessary when difficulty in tinning a wire was experienced. This was often the case with the chromel wires which were significantly more difficult to tin than the constantan. If solder beads formed on the wire, they were removed by returning the wire to the molten solder and then removing it again quickly. Tinned constantan and chromel wires were washed in 95% ethanol, rinsed in distilled water and then located in separate holders.

A tinned, constantan wire was located in a stationary holder while the chromel wire was held in a micromanipulator that was translatable in three orthogonal directions. Flux was drawn into a disposable, Pasteur pipet with a suction bulb, and the bulb was

adjusted such that a small drop of flux hung from the pipet tip. The tinned end of each wire was then, in turn, immersed in this drop for several seconds. The wires were positioned such that their tips overlapped by 0.05 - 0.1 mm, and the point of overlap was approximately 13 μm in width. More flux was applied to the overlapping region, and then a hot soldering iron was brought near the junction without touching the wires. All this was done while observing the wires under a dissecting microscope. When the solder began to melt, the soldering iron was retracted, and the junction was allowed to cool for approximately 45 sec. The strength of the junction was tested by seeing if the assembled thermocouple could drag a 15 g weight across a flat surface. Surviving junctions were cleansed with 95% ethanol, followed by distilled water, a 30 sec wash in a 1.0 N sodium hydroxide solution, and then soaked for 2 min in a distilled water bath at 63^{o}C, while constantly moving the junction through the water. The treatment with the sodium hydroxide solution and the heated water bath facilitated the removal of excess solder flux from the wires. Failure to do so often resulted in junctions that disintigrated spontaneously during storage. This was most likely caused by residual flux which, because of its acidic nature, corroded the wires.

Before being used, the thermocouples were marked with indelible ink, using very fine tipped, felt markers. Alternating red and black marks were made 2 mm apart, over a distance of 1.2 cm on either side of the junction. These marks were used to locate the junction once it had been inserted into the brain. A few thermocouples were randomly selected from measuring the

thermoelectric power of the chormel-constantan junctions. This was not done for every junction used because of the time involved in making these measurements. The measured junctions all gave thermoelectric power value close to the reported values of 62 $\mu V/^{o}C$.

After preparing the cat, and removing the skull from the brain for ultrasonic irradiation (as described above), indelible ink marks were placed on the dura mater over the desired positions for junction placement, and the stereotaxic coordinates of this surface point were recorded. For each site, two additional marks were made on the dura mater, both lying on a straight line that also contained the point within the tissue where the thermocouple was to be located. The coordinates for these colinear points were obtained by consulting the stereotaxic atlas. The parameteric equation for the line connecting these two points was calculated using the distance between the two points as the parameter (see Fig. 3.3). Using this equation, it was determined which ink marks on the thermocouple had to be located at one of the two points in order to position the junction at the desired site when the wire was inserted into the brain along the line between these points. A 26 gauge, or 30 gauge needle was inserted into the brain at one of these points, and at such an angle that it exited the brain at the other point.

A pair of watchmakers forceps was used to insert the chromel end of the thermocouple into the pointed end of the needle. The thermocouple was fed further into the needle until the chromel wire exited the needle's other end. The chromel wire was then used to pull the thermocouple through the needle until the markers

on the constantan wire indicated that the junction was within the tissue. With one hand firmly grasping the exposed portion of the constantan wire, the other hand pulled the needle from the end near the chromel wire until it was removed from the brain leaving the bare thermocouple behind. The thermocouple wire was then pulled through the tissue until the appropriate marker was at one of the two points where the thermocouple exited the brain, thus positioning the junction near the selected site. The stereotaxic coordinates of each point where the wires exited the brain was then recorded and used to recalculate the parametric equation of the line traversed by the wires. If this equation differed from the first calculation, the markers were repositioned such that the junction was as close as possible to the desired site. The new streotaxic position of the junction was calculated and the coordinates of the point on the brain surface directly over this site were measured. This procedure was repeated until the desired number of thermocouples was inserted into the brain. A drop of rapidly polymerizing adhesive was then placed at the two points where each wire exited the brain in order to prevent any movement of the junction.

Prior to adopting this method of thermocouple location, the insertion point and angle of the needle were estimated using an "eyeball approximation" method in order to place the junction properly. After the thermocuple was inserted, the cordinates of the two points where it exited the brain were measured, the parameteric equation of the line determined by these two points was calculated, and the thermocouple was moved until the junction was as close as possible to the desired position. This method

often resulted in inaccurate junction location and was abandoned in favor of the more involved, and more accurate procedure described above.

Once the thermocouples were glued into place, the headpan was attached to the animal, and the thermocouple wires were soldered to bus wires within the headpan, which in turn were connected to a high input impedance amplifier. After filling the headpan with degassed, physiological saline, a resistance bridge was used to determine whether the junctions survived the insertion procedure. An infinite resistance indicated that the junction had broken. For each surviving junction, 1 sec exposures with an intensity of 10 - 20 W/cm^2 were used to irradiate the region surrounding the calculated position of the junction. The thermocouple output was recorded on a chart recorder, and the position yielding the maximum output was assumed to be the location of the junction. This was never more than 0.2 mm away from the calculated position, and hence there was no reason to remeasure the coordinates of the brain surface above this point. Once the junctions were located Equation 1.1 was used to correct for the attenuation of the overlying tissue. One second exposures of 10 - 20 W/cm^2 were used to plot both the transverse and axial focused acoustic beam patterns within the tissue. The transducer was moved such that the focal point of the beam was located at the desired positions relative to the junction. For the transverse measurements, the transducer was translated along a direction perpendicular to the thermocouple axis. The thermocouple orientation was previously selected such that the vertical height of the brain surface varied little along this direction, hence minimizing any changes in

acoustic attenuation so that any differences in the thermocouple recordings could be ascribed to the transverse movement of the transducer. An exposure was made at each different point, and the slope of the of the output at 0.5 sec into the exposure was measured. The ratio of this slope to that obtained when the beam was centered directly on the junction gave the ratio of the acoustic intensities since α remained constant (see Equation 2.17). This intensity ratio was then plotted as a function of position relative to the junction location to obtain the beam plots.

In order to obtain the temperature profiles resulting from the various exposures used in the morphology study, the focal point of the beam was centered on the junctions, and they were irradiated with a series of 300 W/cm^2 exposures using exposure times of 0.1 to 3 seconds. The exposure series was always initiated using the shorter exposures first, and then progressing on to the higher values. Permanent records of the thermocouple responses were made with a chart recorder. The absorption coefficient was calculated from the slope of the thermocouple output at the 0.5 sec point of 1 sec or longer exposures using the procedure of Goss et al. [1977]. With the latter experiments, the thermocouple output was channeled to a computer where a program designed by Dr. Leon Frizzell calculated the absorption coefficient. The computer-generated values for α were identical to those calculated from measurements of strip chart recorded outputs from the same thermocouple. Additional exposures were also made with intensities of 10 - 600 W/cm^2 and exposure times of 0.1 to 2 sec to investigate any dependence of α on intensity.

When all irradiations were completed, the animal was removed from the stereotaxic apparatus and fixed by means of a heart puncture perfusion using physiological saline followed by 10% formalin in physiological saline. The thermocouples were carefully withdrawn from the brain only after completion of the fixation procedure. The diencephelon portion of the brain was then removed from the skull, dehydrated in a graded ethanol series, embedded with paraffin, and cut into 10 μm serial sections for light microscopy. Sections were mounted on glass slides, stained with toluidine blue [Humason, 1962], and protected with a permanently mounted glass coverlip. The tracks made by the thermocouple wires in the brain were easily found. Because the distance of the junctions from both points where the thermocouple wires exited the brain were known, the actual positions of the junctions were determined. Thus there was visual proof to confirm whether the junctions were in WM or GM, or whether the coordinates yielding maximum thermocouple responses corresponded to those of the junctions. A LM visible lesion was often present to confirm further the areas which were irradiated.

In all, 8 cats were irradiated for the thermocouple studies. On the average, three junctions per animal survived insertion and were used to record data. In some animals four junctions survived, while in one animal only one junction survived.

3.3. Neonatal Mouse Irradiations

ICR (HAP:(ICR)BR Harland Industries Inc., Indianapolis, IN) mouse neonates harvested within 24 hr postnatal and weighing between 1.5 and 1.8 g were anesthetized by placing them on ice for

several minutes until they became dormant. A small skin flap, approximately 2 mm wide, was removed from the dorsal side of the mouse directly over the region bordered by the pelvic girdle and the first lumbar vertebra. The animal was positioned in a special holding device and a high intensity light beam was transmitted through the mouse, incident on the ventral side, such that the spinal vertebrae were visible. The specimen was repositioned, while being observed with a dissecting microscope equipped with a calibrated crosshair, such that the third lumbar vertebra would be centered within the unfocused acoustic beam used for the irradiations [W. J. Fry and Dunn, 1956]. The muscle tissue directly over the third lumbar vertebra was then marked with a small dot of indelible ink for easy identification after the irradiation. Removing the dorsal skin flap permitted better visualization of the vertebrae, while having an apparently insignificant effect on the acoutic properties of the specimen.

A very detailed description of this specimen holder and irradiation chamber was given by W. J. Fry and Dunn [1956], and the identical equipment was used for this study. The irradiation chamber was mounted in the insulated storage compartment of a food freezer containing ethylene glycol antifreeze. Temperature sensing devices were located within the irradiation chamber which monitored the chamber temperature and controlled refrigeration and heating units that regulated the temperature of the ethylene glycol, and hence the irradiation chamber. All irradiations were performed using an ambient temperature of $10^{o}C$. As mentioned in Chapter 1, the one day old neonatal mouse behaves as an

essentially poikilothermic animal, and its body temperature can be maintained near $0^{o}C$ without adverse effects.

The irradiation chamber was filled with degassed, distilled water which acoustically coupled the transducer to the mouse. A chamber filled with castor oil, and separated from the irradiation chamber by a diaphram of acoustical impedance matching rubber, absorbed the acoustic energy transmitted through the specimen, reducing back-reflected acoustic energy to an insignificant level. The specimen holder permitted the mouse to breathe while submerged in the water during the irradiation procedure. The transducer itself was a 1 MHz fundamental, 3.18 cm diameter, X-cut quartz disk mounted in a stainless steel housing. At the location of the specimen (10 cm from the transducer face) the transverse width of the unfocused ultrasonic beam, to points of 95% of peak intensity, was approximately 3 mm, ensuring a spatial intensity variation of less than 5% across the third lumbar vertebra. The beam profile and spatial peak acoustic intensity were determined earlier using the same procedure for calibrating the transducer used for the cat brain irradiations. After allowing the mouse time to attain thermal equilibrium with the chamber, approximately 4 min, it was irradiated with 1 MHz ultrasound incident upon the animal's dorsal side. Irradiating intensities were in the range of 86 - 289 W/cm^2, and exposure times were varied in order to determine the exposure at each intensity required to produce hind limb paralysis in 10 - 90% of the irradiated mice [Frizzell et al., 1982]. Sham animals were identically treated, except that ultrasound was not delivered.

After the irradiation procedure was completed the specimen, still supported in the holder, was placed in a 37°C water bath for 4 minutes to facilitate the animal's recovery from the hypothermic anesthesia. The hind limbs were then tested for paralysis by lightly pinching each hind limb separately, and then the tail. In order not to confuse leg movement with movement of the animal's back, the mouse was held such that the back was immobilized, yet the hind limbs were unrestricted. A record was made of whether or not the animal was paralized, or had the ability to sense the stimulating pinch, indicated by the animal emitting a squeeking sound and moving the forelimbs when the stimulus was applied. A similar test was also performed on the front limbs to ensure that they were mobile, indicating that the mouse had indeed recovered from the anesthesia.

During some of the irradiations, a second transducer was used to record the frequency spectrum and relative intensity of each frequency component of the ultrasound within the chamber. A 0.5 MHz narrowband acoustic monitor was used to record the subharmonic frequencies and a broadband detector was used for the higher harmonics and anharmonic noise [Frizzell et al., 1982].

In order to determine whether or not cavitation was involved in producing hind limb paralysis, some of the mice were exposed at an increased ambient pressure of 15 Atm to increase the intensity threshold required to produce cavitation [Frizzell et al., 1982]. Compressed air was used to pressurize the sealed-off irradiation chamber.

Several thousand mice were used to establish the threshold curves for hind limb paralysis [Lee, 1982; Frizzell et al., 1982],

and a smaller number was used for the elevated pressure experiments [Aschenback, 1982; Frizzell et al., 1982]. Of these, the irradiated spinal cord segments from over 300 mice were examined with LM and TEM in order to describe the morphological changes accompanying hind limb paralysis under the various irradiation conditions used.

Following the initial test for paralysis, the mice were sacrificed at post irradiation times ranging from 4 min to 4 hr. The specimens were again tested for paralysis immediately before being sacrificed. The same tissue slicer used to cut the disks from the cat brain cores was used to cut the mouse in half, transverse to the body axis either superior or inferior to the second lumbar vertebra, using the black ink mark as a guide. The position where the animal was halved depended upon how far away from the beam center tissue samples were to be taken for examination. The lower half of the mouse was immediately placed into an ice cooled petri dish containing the same fixative used to perfuse the cat brains. After swirling the specimen in the fixative for 30 - 45 sec to facilitate the removal of blood, it was moved to an another cooled petri dish containing fresh fixative. Using a dissecting microscope to observe the specimen, a sharp razor blade was used to isolate the irradiated portion from the remainder of the spinal column, usually by cutting it inferior to the fourth lumbar vertebra, depending upon how much tissue was required for analysis. Microdissection procedures were used to remove the spinal cord segment from the surrounding spinal column, and the isolated spinal cord segment was stored in a labeled vial filled with fixative. The entire sacrifice and

dissection procedure could be performed in less than 3 min. Control and sham irradiated specimens were prepared in an identical manner.

Although the penetration of the fixative into the specimen was slowed by the cooling, the lower temperature apparently minimized the rate of cellular degeneration and resulted in a better tissue preservation than was obtained at room temperature. A heart-puncture perfusion was also attempted with these animals. The animals were anesthetized with chloroform, the chest cavity was opened, and a 27 gauge needle connected to a small perfusion pump was guided into the left heart ventricle using a micromanipulator. The right atrium was cut to provide an outlet for the perfusion solutions. Tissue preservation by the heart-puncture perfusion was not significantly better than that obtained using the cooled-fixative, diffusion method, and since the heart puncture method required over 9 minutes to perform, it was abandoned.

The labeled specimen vials were stored at $4^{o}C$ for an additional 24 hours. Spinal cord segments were then cut into serial transverse sections 0.25 mm thick using the tissue slicer. The relative position of each section was determined by its diameter, since the diameter of the spinal cord narrows significantly between the second and fourth lumbar vertebrae. The tissue slices were then used for TEM and freeze fracture studies.

3.4. Tissue Preparation For Transmission Electron Microscopy (TEM)

The 5 mm diameter brain tissue disks were cut into smaller pieces according to the following scheme (see Fig. 3.4) before being processed for TEM. A 2 mm diameter disk was removed from the main disk's center, and then asymmetrically cut into 2 pieces along a line parallel to the apex of the notch on the main disk, which resulted from the groove previously cut into the tissue core. One or more different shaped nicks or notches (or a combination thereof) were made in these two semicircles for orientation purposes. The remaining doughnut-shaped tissue pieces were subsectioned into 4 - 8 smaller pieces, each of which was also marked with different shaped cuts placed in such a way that these marks, together with the natural GM and WM patterns on the tissue, permitted proper orientation of a particular tissue piece relative to the others. Earlier attempts were made to prepare the entire 5 mm disk as an intact unit. However, the tissue showed signs of poor osmium penetration and incomplete infiltration of the embedding medium. The mouse spinal cord sections were only 0.6 - 1.2 mm in diameter, and so were prepared intact without introducing any artifacts.

Earlier attempts to embed the entire 5 mm disks of brain tissue did not produce acceptable results. There were regions within the disks that the osmium did not post-fix properly, most likely a result of inadequate osmium penetration into the large tissue sample. Another disadvantage with embedding the entire 5 mm disk was that too much of the tissue had to be trimmed away for ultramicrotomy, and this severely restricted the volume of tissue

that could be observed with TEM. Cutting the 5 mm disk into smaller pieces alleviated both of these problems, although there were now 8 - 10 pieces of tissue to handle, mark for orientation, embed, and then section, requiring a substantially longer preparation time.

For some selected brain cores and spinal cord segments only every other tissue slice was prepared for TEM, while the remaining tissue was stored in fixative for freeze-fracture replication once the TEM prepared tissue had been examined. In this way, the results of TEM for tissue from either side of the freeze fractured tissue could be used to help interpret the features observed in the replicas.

After returning the tissue to be prepared for TEM to their labeled vials, the tissue was washed three times in fresh 0.1 M cacodylate buffer (pH 7.2), treated in 1% osmium tetroxide (1.5 hr for the cat brain tissue and 30 min for the mouse spinal cord sections) in 0.1 M cacodylate buffer, and then rinsed three times in fresh buffer. A graded series of aqueous ethanol solutions, 25%, 50%, 75%, 85% and 95% were used to dehydrate the tissue, ending in three, 10 min washings with pure ethanol that had been treated with Linde 3A molecular sieve in order to remove all residual water from the ethanol. The ethanol was removed from the tissue with five, 10 min washings of propylene oxide because the embedding resins were insoluble in ethanol but mixed readily with the propylene oxide.

The embedding mixture consisted of 55 parts by volume of DDSA (Dodecenylsuccinic Anhydride), 25 parts Epon 812, 15 parts Araldite 502, 2.8 parts DBP (Dibutyl Phthalate) and 1.4 parts

DMP-30 (an accelerator). This mixture was prepared in large volume, placed in small, 75 ml containers and maintained in the freezer compartment of a refrigerator up to 1 month before use. Because Epon 812 was no longer available, the embedding mixture was tested using the Epon substitutes, polybed 812, Epok 812 and Embed 812 in the same porportions as Epon, with favorable results. The only difference being that the polymerized plastic tended to be slightly harder than that obtained using Epon.

The tissue was infiltrated for 1 hr in a 1:2 epoxy to propylene-oxide solution, followed by 1.0 hr in a 1:1 epoxy to propylene-oxide solution and then 15 - 18 hr in a 3:1 epoxy to propylene oxide solution. For this last infiltration phase, the lids on the vials were left ajar so that the propylene-oxide could evaporate. After the tissue pieces in each vial had been identified and oriented properly using a dissecting microscope to observe the markings, they were placed in labeled gelatin capsules which were then filled with epoxy and placed in a 62^{o}C oven and polymerized for 72 hours. The gelatin capsules were dissolved away, and the embedded tissue was sectioned on an ultramicrotome. In cases where the epoxy was too soft for good sectioning, the tissue blocks were returned to the oven for additional polymerization, until the desired hardness was attained.

3.5. Light Microscopy Epoxy Survey Sections

Excess epoxy was trimmed away from the tissue, and a 1 μm Thick survey section was cut from each tissue block for LM observation in order to determine the region to be sectioned for TEM. The sections were floated on a drop of distilled water on a

glass slide and heated to 72°C to remove wrinkles and to accelerate the evaporation of the water. Once dried, the section was stained with 0.5% Toluidine blue for approximately 5 - 30 sec at 72°C and then, after cooling, was differentiated in 95% ethanol for a period of 30 sec. A coverslip was not permanently mounted on each slide, but one was placed over the slide when it was being observed because most microscopes were corrected for the additional refraction of the coverslip. Resolution was noticeably deteriorated when the coverslip was not used.

3.6. Sectioning for TEM

A region of the embedded tissue, 1 - 1.5 mm on a side, was chosen for TEM observation, and the surrounding tissue was cut away to a depth of 4 - 8 μm. A series of 450 Å - 700 Å thick sections were cut from the selected region, and mounted on 3 mm diameter, 300 or 200 mesh copper grids. If the same structure was to be observed in serial sections of the tissue, the sections were mounted on a grid having a 1 x 2 mm slot which was covered by a thin support film of formvar plastic [Reid, 1976]. After air drying, the sections were stained for 1 hr in a saturated, aqueous, uranyl acetate solution, and then counterstained in lead citrate [Reynolds, 1963]. The cat brain tissue was stained for 1 min in the lead stain, and the less contrasty neonatal mouse spinal cord tissue was stained for 2.0 min.

3.7. Freeze Fracture

The TEM observations of the adjacent tissue disks from the cat brain core indicated which regions of those disks set aside for freeze fracture replication were to be fractured. Tissue from

these regions was microdissected into squares 0.5 - 0.75 mm on a side, rinsed three times in 0.1 M cacodylate buffer, and then stored very briefly in a fresh change of the buffer solution. Because of its small, size, there was no need to microdissect the transverse sections of the mouse spinal cord. The selected pieces were simply rinsed, and then stored in buffer as described for the cat tissue.

Before freezing, biological tissue must be cryoprotected against the ice crystals which can severely damage the tissue ultrastructure, rendering many structures unrecognizable [Hudson, 1979]. The only disadvantage of using a cryoprotectant was that the fractured tissue cannot be etched, because the cryoprotectants most commonly used, e.g., glycerol, DMSO (dimethoxysulfate) and sucrose, are nonsublimable substances [Hudson et al., 1979]. Etching was the term applied to the procedure of subliming away a portion of the frozen liquid phase of the tissue in order to reveal a greater portion of the membranous structures on the fractured tissue surface. Attempts to etch cryoprotected tissue were made, but always resulted in the cytosol portion of the tissue taking on a cratered appearance (see Fig. 3.5). Rash [1981] attributes this effect to a separation of the cryoprotectant from the water, followed by the sublimation of the water. The craters mark the position of the water while the nonsublimable cryoprotectant remains.

A 30% glycerol solution in 0.1 M cacodylate buffer was added one drop at a time to the vial containing the tissue in the buffer solution. Using continuous agitation, the glycerol solution was added slowly until the volume in the vial was doubled. Two-thirds

of this solution was removed, and the volume was again restored by adding multiple drops of the 30% glycerol solution. This last step was repeated one more time, after which all of the solution was removed and replaced with the 30% glycerol solution. The entire glycerol infiltration procedure was timed to take approximately 15 min, after which the tissue was allowed to equilibrate in the 30% glycerol solution for 40 - 50 min.

Following the incubation period, the tissue pieces were mounted onto labeled, gold-nickel alloy specimen holders purchased from Balzers Union. These specimen holders, referred to s planchettes, were available in several different sizes and shapes. The planchettes with the 0.8 mm high solid, flat plateau, without a machined depression, worked best for these experiments. After placing the tissue onto the planchette, filter paper was used to absorb excess fluid from the face to be fractured. An applicator stick was used to apply a small quantity of the cyroprotectant solution to the base of the tissue which served as a "glue" to hold the specimen onto the planchette after freezing. Solid Freon-12, maintained at liquid nitrogen temperature, was melted with a brass rod. Just before the last portion of the freon resolidified, the planchette was rapidly plunged into the liquid freon such that the tissue was near the interface between liquid and solid freon phases, thus yielding the maximum freezing rate for the tissue. After 3 - 4 sec in the freon, the planchettes were touched rapidly with a small piece of filter paper to remove excess freon, and then were quickly stored under liquid nitrogen in labeled storage compartments.

Frozen specimens were placed onto the multiple specimen stage of a Balzers 301 freeze fracture, freeze etching apparatus, which has been precooled to -150°C, and lightly sprayed with Freon-12 gas. The freon formed a thin frost on the specimen stage, and aided in establishing a good thermal contact between the specimens and the stage. After locking the specimens into place, the chamber was evacuated to a pressure of 1×10^{-6} torr, and the specimens were gradually warmed up to -105°C. A microtome knife, mantained at -150°C, was used to fracture the specimens, immediately after which the specimen stage was rotated, and the fractured surface was replicated with an approximately 20A thick layer of platinum and carbon evaporated from an electron gun source mounted at an angle of 30° from the horizontal. Because the stage was rotated during the replication process, the shadows characteristic of unidirectionally replicated specimens were absent. Since there were no shadows to obscure surface features, more of the ultrastructure was observable, and at a higher resolution [Margaretis et al., 1977]. Once the platinum layer had been established, it was stabilized by vacuum-evaporating a supporting layer of carbon onto the platinum surfaces.

After the specimens had been slowly warmed up to -25°C, they were removed from the Balzers apparatus, the planchettes were briefly placed onto a finger to warm them, and then replicated tissue pieces were floated free from the planchettes in a spot plate well filled with the 30% glycerol cryoprotection solution. The specimens were transferred using a platinum wire loop to other spot plate wells for 2 min washes each in a 20% glycerol solution, followed by a 10% glycerol solution. In order to reduce the

surface tension between the different solutions, several loops full of solution were exchanged between the succesive solutions before tranferring the specimen. This helped protect the replica against mechanical damage, especially in the later stages of this procedure.

At this point, Hudson et al. [1979] suggest rinsing the tissue in several changes of distilled water. However, this treatment often produced cracks in the replicas, particularly on those attached to white matter tissue. The cracking was most likely related to an osmotic imbalance, and substituting 0.1 M cacodylate buffer for the distilled water essentially eliminated any cracking at this stage. Tissue digestion was initiated using a 0.2% sodium hypochlorite solution, made by diluting household bleach to 20% strength with distilled water. Digestion times in this solution for the cat brain tissue varied from 1 to 2 hr for GM and 2 - 8 hr for WM. It was probably the higher lipid content of the WM that necessitated the longer digestion period. The neonatal mouse spinal cord samples required only 1 hr in this solution, probably because myelination had not yet started. The tissue was transferred to full strength household bleach 13 -24 hr, or until most of the tissue attached to the replicas has been digested away. The replicas were then briefly returned to the 20% bleach solution, and passed through three, 2 min rinses in distilled water.

Digestion was continued in a graded series of chromic acid solutions. The replicas were treated for 10 min in 10% aqueous chromic acid, 20 min in 20% chromic acid and then 3 - 10 hr in 40% chromic acid, with the WM again requiring the longer digestion

times. The sequence through the acid was reversed for brief rinses in the 20% and 10% acid solutions, followed by three, 2 min washings and 5 brief rinses in distilled water.

The replicas were now ready to be mounted on copper grids (usually 200 mesh). Better adhesion of the replicas was obtained if the grids were pretreated with "grid glue" [Hudson et al., 1979], a solution of diethylene chloride and cellophane tape adhesive. Before transferring the replicas to the final water rinse, a small amount of a 30% photo-flo (Kodak) solution was added to the rinse. This was usually accomplished by dipping the grid into the photo-flo solution and then into the water rinse. The photo-flo reduced the surface tension of the water and facilitated capturing the replicas on the grids.

3.8. Cultured Cell Experiments

3.8.1. Monolayer Preparation

A thin formvar film prepared from a 0.2% formvar in choloroform solution was floated onto distilled water. Several 200 mesh, gold, electron microscope specimen grids were placed onto the film, and this assembly was lifted from the water on a glass coverslip such that the grids were sandwiched between the formvar and the coverslip. A thin conducting layer of carbon was vacuum evaporated onto the formvar-covered grids, which remained attached to the coverslip for ease in handling. The grid-studded coverslips, together with several 3 x 5 mm pieces of 0.025 mm thick mylar, were sterilized for 5 min in 70% ethanol, rinsed twice with sterile phosphate buffered saline (PBS), and placed in one or more 60 x 15 mm sterile, plastic petri dishes. They were

covered with the growth medium and allowed to set 5 min before being seeded with baby hamster kidney (BHK) cells, at a concentration of 1 - 1.5 cells per ml. The cells were grown in Eagle's minimal essential medium (MEM) supplemented with 10% heat-inactivated fetal bovine serum (FBS), 100 U/ml penicillin, 100 g/ml streptomycin, 0.03% L-glutamine, 0.01 M HEPES buffer and 0.075% $NaHCO_3$ (complete MEM), and incubated at 37°C in a humid atmosphere containing 5% CO_2.

3.8.2. Cultured Cell Control Preparations: Monolayer Extractron and Mylar Grown Cell Fixation.

When the cells were approximately 60 - 80% confluent, the mylar strips and glass converslips were rinsed several times in PBS, and the mylar strips were chemically fixed with the same fixative solution described previously. The coverslips were incubated for 1 min in a buffered, 5 μM Taxol (NSC 125973, obtained from NIH) solution containing 10 mM PIPES, 100 mM potassium chloride, 3 mM magnesium chloride and 300 mM sucrose, at a pH of 6.8, in order to preserve the microtubules. The cell membranes were then extracted with 1% triton X-100 dissolved in the same buffered solution used for the Taxol incubation. At one time, PMSF (Phenylmethyl-Sulfonylfluoride) was also added to the extraction solution in order to suppress proteolysis, but since its presence or absence had no apparent effect upon the observed cytoskeletal morphology, and it is a very hazardous reagent, it was subsequently excluded from the procedure.

After 3 - 4 min in the extraction solution, enough 25% gluteraldehyde was added to yield a final concentration of 2%, and

the extracted cells were allowed to fix for 20 min. The coverslips were rinsed twice with PBS and then treated for 10 min in unbuffered, aqueous 0.1% osmium tetroxide. At one time, a 1% osmium solution was used, but was replaced with the lower concentration because it has been demonstrated that osmium concentrations greater than 0.2% degrade actin filaments [Small, 1981]. Following a brief rinse in distilled water, the cells were stained for 10 min in aqueous 1% uranyl acetate, and again rinsed with distilled water. The cells were then critical point dried in preparation for TEM observation.

3.8.3. Critical Point Drying (CPD) Of The Extracted Monolayers

A graded ethanol series was used to dehydrate the extracted cells, starting with a 50% ethanol solution, and terminating with three, 5 min rinses in absolute ethanol that had been treated with Linde 3A molecular sieve in order to remove residual water. The grids were removed from the coverslip, and then transferred to a holder specifically designed for critical point drying grid-mounted specimens, while at all times being submerged in the ethanol to prevent air drying of the cells. The specimen compartment of a commercially available CPD unit (Tousimis Co., Samdri - 7900 was filled with enough molecular sieve-treated ethanol to cover the grid holder, and the specimens were critical point dried. A filter (Tousimis Co., #8782A) was used to remove residual water from the carbon dioxide transition fluid, and the machine was gently agitated during the CPD process to facilitate the carbon dioxide-ethanol exchange.

3.8.4 Mylar Monolayers: Preparation For TEM

The mylar pieces were removed from the fixative, rinsed twice with PBS, and then treated for 20 min with 1% osmium tetroxide in 0.1 M cacodylate buffer, at a pH of 7.2. A graded ethanol series was used to dehydrate the cells, the ethnol was replaced with propylene oxide, and the specimens were then infiltrated with epoxy resins as described for the cat brain tissue. The cells were stored in the unpolymerized epoxy for 1 hr, after which the non-cell covered side of the mylar was wiped clean of epoxy, and the pieces were laid cell side-up on a square of silicone rubber. Sufficient epoxy was placed on the cell covered side of the mylar to completely cover it but not overrun its borders. The specimens were then polymerized for 72 - 90 hr at 62°C.

Once the resin polymerized, the mylar easily fell away from it, leaving the cells embedded within the epoxy. Small squares were cut from the cell-impregnated epoxy, which were then attached cell side up with a quick drying adhesive to an epoxy stub (molded in a gelatin capsule, with the rounded end filed flat) that fit into the specimen mount of an ultramicrotone. After trimming the square down to the desired size, the specimens were sectioned on the ultramicrotome with the first sections containing cellular material.

3.8.5. Hyperthermia Experiments

A closed vessel containing growth medium was heated in a temperature regulated water bath to a selected temperature within the range of 40 - 57°C. The grid studded coverslips and mylar pieces were exposed to the heated medium for periods ranging from

1 sec to 2 hr. Some of the specimens were processed immediately after heating according to the procedures described above. The remainder were returned to the 37°C incubator and processed at later times, up to 4 hr after heating.

An identical water bath system was maintained at 37°C for sham exposures. The sham cells were treated in a manner identical to those exposed to the hyperthermic temperatures.

3.9. Electron Microscopy

All ultrathin sections, freeze-fracture replicas and extracted cells were examined with a JEOL, JEM 100 -C transmission electron microscope, using accelerating voltages of 80 and 100 KV.

3.10. High Voltage Electron Microscopy (HVEM)

The selection of tissue to be examined with HVEM was based on the TEM observations of ultrathin sections taken from embedded cat brain specimens. A glass knife with attached water "boat" [Reid, 1976] was used to cut 0.5 micron thick sections from the trimmed block. The sections were cut at the slowest possible cutting speed in order to minimize the formation of compression lines on the section. A filter paper "arrow" soaked in xylene was waved several times over the floating sections in order to stretch them out. The sections were then picked up on 1 x 2 mm slotted grids covered with a formvar support film made from a 0.5% formvar in chloroform solution. Once the sections dried, they were stained for 1 hr with saturated uranyl acetate in 50% ethanol, at room temperature. After washing in 50% ethanol, the grids were stained for 20 min in lead citrate, and then a thin, conducting layer of carbon was vacuum evaporated into the grids. The sections were

observed with the AEI, EM-7 high voltage electron microscope at the University of Wisconsin campus, using an accelerating voltage of 1 million volts.

CHAPTER 4

THERMOCOUPLE EXPERIMENT RESULTS

4.1. Thermocouple Insertion

The "eyeball method" used to locate the thermocouple junctions in the cat brain for the initial thermocouple experiments often resulted in the junctions being nearly 3.0 mm away from the desired stereotaxic position as shown by the 10 m thick sections containing the thermocouple tracks. This inaccuracy was unacceptable, and so the more complicated insertion procedure described in the previous chapter was instituted and yielded inaccuracies in junction placement of 1.0 mm or less. Once the junctions were inserted into the brain, their positions were calculated to within an accuracy of 0.2 mm, using the parametric linear equation.

The rapid drying glue functioned well in immobilizing the junctions while the thermocouple wires were manipulated and soldered to the bus wires attached to the headpan. If the glue was too close to the brain surface directly over the junction's position, the thermocouple output became very irradic, and the glue turned from a white to a black color when intensities greater than 100 W/cm^2 were used. Also, if the beam focus was directly centered on the glue, the junctions recorded a temperature rise which appeared sometime following the completion of the ultrasonic irradiation, indicating that the heat absorbed by the glue was being conducted down the thermocouple wires to the junction. In order to eliminate this problem, the thermocouples were secured in such a manner that the glue was not in the acoustic field.

The thermocouple outputs from junctions located less than 1.5 mm below the brain surface did not have the classic shape of Fig. 2.1. The chart recorder pen fluctuated wildly during the exposure, occassionally going off scale. This activity may have been indicative of cavitation or some unknown phenomenon occurring at the saline-brain interface. In any event, thermocouples from which the data reported below were taken were never inserted less than 2.0 mm below the brain surface.

4.2. Intensity Distribution in the Cat Brain

Figure 4.1 is the transverse beam pattern in the plane containing the focal center, which was constructed with data from 24 brain-embedded thermocouples. Comparing this figure to the transverse beam plot recorded in water (Fig. 3.2) using the same transducer shows that the brain tissue apparently has the effect of broadening the acoustic field, particularly at the larger radial distances, and has a half power beam width of 3.6 mm compared to 3.0 mm shown in Fig. 3.2. The radial beam plots centered about axial positions at increasing distances from the focal point exhibited broader curves that were indicative of the defocusing of the beam. For a given axial distance from the focal point, the defocusing was greater for those plots centered about axial points down field from the focal point. Figure 3.2 shows that the half power beam width measured with a thermocouple is broader when the transducer is moved along the thermocouple axis rather than perpendicular to it. Therefore, some of the scattering of the measured points and broadening of the curve in

Fig. 4.1 may be attributable to errors in moving the transducer directly perpendicular to the thermocouple wires.

The axial beam plots in brain tissue and water, Figs. 4.2 and 3.2 respectively, are significantly different in the region between -3 mm and -7 mm. Note the almost sinusoidal pattern which was recorded to some degree with every thermocouple used in this study. As this was the only region on the axial plot that had any significant scattering of the data points, it is considered not to be an artifact. A dashed curve has been drawn in Fig. 4.2 which averages out this "sinusoidal" region, and which corresponds well with the same region of the axial plot in Fig. 3.2.

The cause of this variation in the axial beam plot is unknown. Perhaps some of the acoustic wave was reflected from the anterior surface of the skull, and set up a standing wave pattern. This seems unlikely as there was no other region in Fig. 4.2 to indicate the presence of standing waves. More likely, the brain-saline interface refracted the acoustic wave and caused the change in the beam pattern. The scattering of the measured points may have resulted from varying curvatures of the brain surface above the different thermocouple sites.

The transverse beam intensity plots made with the 1 sec, 300 W/cm^2 exposures agreed with the curve in Fig. 4.1. However, as can be seen in Fig. 4.3, a secondary temperature rise occurred after the acoustic power was terminated when the junction was no longer located at the focal center. Table 4.1 lists the initial and secondary peak temperatures as a function of radial distance from the beam axis for a WM embedded thermocouple. In some cases,

the secondary peak temperature exceeded the initial peak temperature rise, as is graphically illustrated in Fig. 4.3.

4.3. The Effect of Ultrasonically-Induced Tissue Damage upon the Thermocouple Responses to Subsequent Irradiations

Figure 4.4 shows a thermocouple track through a transverse section of a cat brain, with an arrow marking the junction's location. After performing the beam plotting procedure to locate the junction and map the intensity profiles, the specimen was treated to a series of irradiations using intensities of 50, 100, and 300 W/cm^2, for exposure times of 0.38 sec to 3 sec, as described in Chapter 3. At any time within this series of exposures, identical ultrasonic irradiations elicited thermocouple responses that were indistinguishable from each other. Exposures were again made until 1 hr later, just prior to sacrificing the animal. The earlier irradiation sequence was repeated, the animal was sacrificed, and the brain was perfused. Even though Fig. 4.4 shows that the tissue surrounding this junction had been damaged ultrasonically during the previous sequence of irradiations, the thermocouple responses were essentially identical to those of the corresponding, earlier exposures.

An identical series of exposures was delivered to the junction located in the brain section shown in Fig. 4.5 which came from a similar tissue environment within the same cat brain from which the section in Fig. 4.4 was taken. This junction was, however, located close to an interface of white and gray matter. Six hours elapsed between administering the first and second series of exposures to this site. The second exposure series was

administered immediately prior to the second exposure series that was administered the site pictured in Fig. 4.4, after which the animal was promptly sacrificed. It is evident that the tissue damage is much more extensive in Fig. 4.5 than that seen in Fig. 4.4. A comparison of the initial thermocouple responses with the corresponding ones delivered 6 hr later showed that, on the average, the peak temperature decreased by 30% in the latter recordings, and the value for α was down by 21%. The absorption properties of the tissue had changed as the tissue damage developed with increasing post irradiation time.

The properties of the thermocouple responses described for the two cases above were characteristic of those observed for every thermocouple used in this study, viz., identical exposures yielded indistinguishable thermocouple outputs as long as the ultrasonically induced morphological changes had not progressed much beyond that depicted in Fig. 4.4. When more significant tissue damage was present, both the peak recorded temperature and the absorption coefficient decreased, and the magnitude of these changes increased with the severity of the tissue damage.

4.4. Peak Temperatures, Decay Times, Absorption Coefficients, and their Dependence on the White and Gray Matter Content of the Tissue

The brain is by no means a homogeneous mass of tissue. Aside from the fluid filled ventricles, the brain basically consists of two types of tissue, the gray matter, GM, and the white matter, WM. These two tissue types stained very differently with the toluidene blue stain used on the paraffin embedded sections. As

can be seen in Figs. 4.4 and 4.5, the WM stained distinctly darker than the GM, because the myelin sheath surrounding the myelinated axons had a high affinity for the stain. There were regions of the brain that exhibited a stain density somewhere between the WM and GM, and closer examination of such tissue showed a mixture of myelinated and nonmyelinated structures. For easy reference, this tissue will be referred to as white-gray matter, or WGM.

The WM and the GM exhibited different responses to identical ultrasonic exposures with respect to the thermocouple recordings, as seen in the data of Tables 4.2 - 4.4, and the induced tissue damage, as described in Chapter 5. In all respects, the magnitude of the WM response to the ultrasound was greater than that of the GM, in agreement with the results of the earlier investigators [Barnard et al., 1955; Basauri and Lele, 1961]. The WGM exhibited a response in between that of the WM and GM, with the magnitude of the response increasing as the WM content of the WGM increased.

In order to report the thermocouple data, the tissue into which the junctions were located was divided into three classes, viz., WM, GM, and WGM. For this purpose, all tissue regions that contained less than approximately 25% GM were classified as WM, the converse was used to define the classification WM, and those regions containing between approximately 25% - 75% WM (or GM) fell into the catagory of WGM. No quantitative analysis, e.g., densitomitry, was used to catagorize a given tissue region. The tissue was assigned one of the three designations based on the author's examination of the tissue with LM using magnifications between 100 - 1,000X.

The response of the junctions located at the interface of a WM and GM region was very similar to that of the WGM tissue, hence such interface regions were also designated as WGM. When measuring the response of WM or GM, the junctions were located in large masses of WM or GM as far as possible from a WM-GM interface, e.g., the junction location in Fig. 4.4. This was done to provide the largest, homogeneous volume of tissue in order to record the thermal response of these two tissue types, and to minimize any influence of surrounding tissue from the other two classes.

The data reported in Tables 4.2 - 4.4 are given as the mean of the recorded parameter for each tissue classification plus and minus, respectively, the upper and lower bounds of the recorded data in order to illustrate the range over which the data were collected, and the variability encountered.

The mean peak temperatures recorded at the focal center of the acoustic beam, using an intensity of 300 W/cm^2, are presented in Table 4.2 for the various exposure times used. The corresponding times required for the thermocouple recorded temperature to fall to 1/e of these peak values are given in Table 4.3 and Table 4.4 lists the mean values for the absorption coefficients measured using 300 W/cm^2 irradiations delivered to the various tissue types. Five of the thermocouples used in this study were also irradiated with intensities of 10, 40, 100, 200, and 600 W/cm^2, and in no case did the resultant values for the absorption coefficient differ significantly from those obtained with 300 W/cm^2.

It is clear from the data in Tables 4.2 - 4.4 that the thermocouple responses for a given set of irradiation parameters were dependent upon the nature of the tissue surrounding the junction. Junctions in tissue with a higher white matter content, or lying in close proximity to white matter, yielded higher values for the peak temperature, t(1/e), and the absorption coefficient. In the past, this difference has been attributed to an accelerated rate of heat diffusion away from the irradiated volume resulting from the higher degree of vascularization in the gray matter [Basauri and Lele, 1961]. The variablity among the measurements from similar tissue regions in the same brain may also have been the result of differences in the circulation to these areas. Measurements from similar and even identical tissue sites from different animals exhibited even more variability. This may have been the result of differences in vascularization, blood flow rate, or even variations in the attenuation effect of the subarachnoid space [Johnston and Dunn, 1976b] among the different specimens.

4.5. Effects of Blood Flow

The experiments described in the previous chapter for measuring the effect of blood flow on the thermocouple responses met with limited success. Clamping both common carotid arteries had no effect on the thermocouple outputs. Electrical stimulation of the right vagus nerve did not stop the heart completely, but did significantly reduce the rate and amplitude of the heartbeat as monitored with a stethoscope, which resulted in a very small increase in the recorded peak temperatures in WGM (less than 4%),

but did increase the value of t(1/e) by almost 10%. After sacrificing the animals, and hence eliminating blood flow completely, the peak temperatures in cortical gray matter rose on the average by 15 - 25%, but with only a 5 - 10% increase in t(1/e). There was no significant change in the peak temperatures attained in WM or WGM; however, t(1/e) increased by 130 - 200%.

CHAPTER 5

RESULTS OF THE CAT BRAIN IRRADIATION STUDY: LIGHT AND ELECTRON MICROSCOPE OBSERVATIONS OF CONTROL, SHAM IRRADIATED, AND IRRADIATED TISSUE

5.1. Histological Observations of the Control and Sham Irradiated Tissue

Differences were not observed between morphology in the control and sham irradiated tissues, or the randomly selected sites from the nonirradiated regions of the brains for all the cats used in the study. Further, tissue from these three tissue groups was morphologically identical to that shown in atlases of central nervous tissue at both the light and electron microscope levels [Peters et al., 1970]. Therefore, the morpnology exhibited by the various tissue structures observed in the nonirradiated tissues will be referred to collectively as the normal morphology. A very small number of swollen mitochondria, and occasional fragments of membranous debris, were observed in the nonirradiated tissues. The myelin sheath surrounding some of the larger axons appeared frayed at points along the circumference, particularly in sections taken from large regions of solid white matter. These infrequent irregularities are common in normal, perfused nervous tissue [Pappas, 1982]. It is concluded therefore, that artifacts were not induced by the perfusion and the histological procedures employed, and that the abnormal morphology observed in the irradiated tissue resulted only from the ultrasonic exposure.

The LM appearance of the control and sham irradiated brain tissue has been presented and discussed in the reports from the

earlier ultrasonic studies of the cat brain conducted at the University of Illinois [Barnard et al., 1956; F. J. Fry et al. 1970]. Therefore, the following discussion will center on describing the ultrastructure of the nonirradiated tissues. The descriptions are brief, but will serve as a basis of comparison for the electron micrographs from the irradiated tissues presented later in this chapter.

5.1.1. White Matter (WM)

A low magnification micrograph of white matter is presented in Fig. 5.1. The field is covered with close packed, myelinated axons, Ma, and an oligodendrocyte cell, Od, is also present. These two structures were the major constituents of WM regions. Blood vessels, astrocyte cells, and occasionally synapses were also observed.

The myelinated axons were surrounded by the dark staining myeline sheath, My, and its multilayered nature is more easily seen in Figs. 5.2a and 5.2b. A repeating pattern is formed by two distinct lines, the lighter intraperiod line and the darker dense line. The intraperiod line is formed by the opposition of the outer leaflets of the plasma membrane from two different portions of the oligodendrocyte cell that repeatedly wrapped itself around the axon to form the myeline sheath. The dense lines are formed by the opposition of the inner leaflets from the same plasma membrane. Figures 5.1 and 5.2 show that localized unravelings of the myelin sheath, particularly on the larger axons

occur occasionally. As shown in Fig. 5.2b, the spearation of the myelin layers always occurred at the intraperiod line and never at the dense lines.

Figure 5.2 also shows the typical appearance of mitochondria in the axons, which had a dark staining central matrix surrounded by a double membrane. The inner membrane was highly convoluted and forms finger-like projections into the matrix called crista, crs. Mitochondria in other portions of the brain tissue also displayed these same morphological features. Within the mitochondrial matrix are the enzymes for the tricarboxylic acid cycle (Krebs cycle), and the inner membrane contains the components of the electron transport cycle.

The oligodendrocyte's nucleus and cytoplasm (Fig. 5.3) were characteristically darker staining than in other cells such as the neurons and astrocytes. Mitochondria, lysosomes, Ly, golgi, g, and ribosomes, r, were among the more prominent subcellular organelles present within the cytoplasm. Notice in Fig. 5.3 that the ribosomes are either attached to the endoplasmic reticulum or free within the cytoplasm. The free ribosomes are not randomly distributed throughout the cell, but form local patterns of spirals, rosettes, and rows [Peters et al., 1976]. The endpolasmic reticulum containing attached ribosomes is designated rough endoplasmic reticulum, rer, while that without attached ribosomes is termed smooth endoplasmic reticulum, ser.

5.1.2. Gray Matter (GM)

The gray matter displayed a greater diversity of structures than the white matter, as seen in Fig. 5.4. Myelinated axons

stood out against the other structures because of their dark staining myelin sheaths, but were present in small numbers, or totally absent in some GM regions. The remaining membrane-bound regions in Fig. 5.4 are synapses, Sy, nonmyelinated axons, Ax, dendrites, Dy, dendritic thorns, th, or small regions of a cell body, sans nucleus.

The neurons (Fig. 5.5) were large cells with a prominent nucleus and light staining cytoplasm and nucleoplasm. The neuronal cytoplasm did not stain uniformly but had a mottled texture. In general, the nucleoplasm stained lighter than the cytoplasm, and contained small condensations of chromatin, Cr, which were randomly distributed throughout the nucleus. The nucleolus, nu, was very electron dense and distinct, and absolutely identified the neurons when it was present in the section being viewed. Neurons have a complex network of smooth and rough endoplasmic reticulum throughout the cytoplasm. Both free and attached ribosomes abound, and Fig. 5.6 shows that the free ribosomes are not randomly distributed but form distinct patterns [Peters et al., 1976] similar to those found in the oligodindrocytes, but they are more elaborate and obvious against the lighter staining neuronal cytoplasm. The dense concentrations of free ribosomes and rough endoplasmic reticulum correspond to the Nissl bodies, Nb, observed in LM. Other prominent structures included the lysosomes, golgi, and multivesicular bodies, mvb. Figure 5.6 clearly shows the two nuclear membranes, and illustrates that the outer membrane was more irregular than the inner membrane. The nuclear pores, p, are points where the two

membranes come into opposition. A diffuse, electron dense material was associated with each pore.

Chemical synapses, the tight junctions formed between two communicating cells, were observed within GM in much larger numbers than in WM. In low magnification micrographs such as in Fig. 5.4 they are distinguishable by the dark staining regions where the two components meet.

The basic features of the synapses are better illustrated in Fig. 5.7. Each synapse consists of a presynaptic, Pre, and postsynaptic, Po, element separated by a cleft 200 - 400 Å wide. The electron dense region associated with the cleft is termed the junctional density, Jd, and it is either distributed symmetrically or asymmetrically across the cleft. The presynaptic region, or bouton, contains small, membrane-bound vesicles, Sv, which are believed to be filled with the chemical transmitters such as acetylcholine and norepinephrine. Some of the vesicles form a localized concentration near the cleft, and this association of vesicles and the junctional density is called the synaptic complex. In almost all chemical synapses, the remainder of the presynaptic element is filled with a random distribution of vesicles, as seen in Fig. 5.4 and 5.7. However, in very few cases, the vesicles remain more or less concentrated in a region about the synaptic complex. The synaptic elements also contain mitochondria, microtubules, neurofilaments, and smooth endoplasmic reticulum [Bradford, 1977]. The cytoplasm in both the pre- and postsynaptic elements had a mottled texture similar to that observed in the neuronal cytoplasm.

It can be observed in Figs. 5.4 and 5.7 that the curvature of the cleft region varies among the synapses, curving into either the pre- or postsynaptic elements, or remaining flat with respect to both elements. Synapses whose junctional region is convex into the presynaptic region are said to have positive curvature, a flat junctional region defines zero curvature, and one that is convex into the postsynaptic region has a negative curvature [S. E. Dyson and Jones, 1980]. S. E. Dyson and Jones [1980] studied the development and maturation of synapses within the molecular layer of the occipital cortex of rats between 15 - 22 days postnatal. With respect to synaptic curvature, they observed a statistical increase in the frequency of flat and positively curved junctions with increasing age. Because the increase in positive and flat junction curvatures paralleled increasing brain activity, it was postulated that these two curvatures represent functional synaptic junctions while the negatively curved junctions are nonfunctional. This supposition is supported by studies of the effects of anesthetics on synapses. Increasing anesthetic dosage induced an increase in negatively curved synapses while the nonanesthetized animals were characterized by a preponderance of flat and positively curved synapses [Cook et al., 1974; Jones and Devon, 1977; Jones and Devon, 1978]. This work with the anesthetics also demonstrates that the synaptic curvature is a dynamic morphological parameter that can change with environmental conditions. Whether the curvature changes when synapses are turned on and off during repetitive cycles has not been established.

5.1.3. Tissue Regions Consisting of Both White and Gray Matter

Tissue regions that contained a mixture of both the WM and GM were frequently irradiated, and in Chapter 4 the term WGM was adopted to identify such regions. The higher resolution of the electron microscope permitted a further subdivision of the WGM based on the relative amounts of WM and GM present. If the tissue was more than 50% WM and more than 10 - 20% of the structures common to GM it is referred to as WWGM (Fig. 5.8). In the opposite case the term GWGM (Fig. 5.9) will be used. Tissue that was approximately equal parts GM and WM is still designated as WGM. This terminology will also be used for the tissue at the borders between WM and GM. At these border regions the tissue did not exhibit an abrupt change from WM to GM. Instead there was a smooth and gradual transition from WM to WWGM, GWGM, and then to GM. The dimensions of this transition zone varied among the different WM and GM borders throughout the brain, sometimes extending over a span of almost a mm.

5.2. Factors Affecting the Tissue Response to the Ultrasonic Irradiation

The manner and degree to which the brain tissue was affected by the ultrasound depended upon the tissue's position within the focal volume, the WM and GM content of the irradiated region, the exposure time used, and the elapsed post irradiation time after which perfusion was initiated. Another variable that had to be dealt with was the animals themselves. There were cases where animals were treated identically with respect to lesion sites, exposure times and sacrifice times, and the tissue's response to

the ultrasound was very different. As a specific example, the same brain sites in three different cats were irradiated using identical suprathreshold exposure times, according to Equation 1.3, yet one animal exhibited no signs of ultrasonically induced damage, one animal had one lesion that was visible with LM, the rest required TEM for visualization, and the third animal had two LM visible lesions and two that required TEM to be observed.

5.2.1. The Variation in Tissue Damage Resulting From the Position of the Tissue Within the Focal Volume

When the focal point of the acoustic beam was centered within a tissue volume that was homogeneous with respect to its WM and GM content, the damaged tissue volume, or lesion, displayed the classic, ellipsoidal shape of the focused, ultrasonic lesion (see Fig. 4.3). The major axis of the ellipsoid was colinear with the beam axis, and the lesion volume was centered about the focal point of the transducer. It was at the focal point where the greatest degree of tissue damage was observed.

Tissue sections cut transverse to the beam axis showed circular cross-sections of the lesion volume (Fig. 5.10). In such sections, the degree of tissue damage was greatest along the beam axis, and decreased in a smooth and gradual manner with increasing radial distance from the beam axis (Fig. 5.10). In the transverse sections taken from planes above and below the focal point, both the circular cross-sectional area of the lesion volume and the degree of tissue damage decreased with increasing distance from the focal point. The gradient of the decrease in

the degree of tissue damage was steeper in the radial direction from the beam axis than along lines parallel to it.

The decrease in tissue damage observed with increasing distance from the focal point paralleled the manner in which the acoustic intensity decreases within the focal volume as demonstrated by the beam plots of Figs. 4.1 and 4.2. Since every point within the lesion was exposed to the ultrasound for the same time, this data indicates that both the exposure time and the acoustic intensity experienced by each point in the lesion was involved in determining the degree of the resultant tissue damage.

5.2.2. Effects of the WM and GM Content of the Tissue

For a given ultrasonic exposure and post irradiation sacrifice time, the resulting tissue damage was greater in degree and extent within WM than GM. This observation was in agreement with the results obtained in the earlier brain studies, as discussed in Chapter 1 [Barnard et al., 1956; Basauri and Lele, 1962].

When the focal point of the transducer was centered directly on an interface between a region of WM and GM, the lesion volume was no longer centered about the focal point as it was in lesions placed in homogeneous tissues (Section 5.2.1). Instead, the greatest degree of tissue damage was located on the WM side of the interface. The damaged volume was distributed asymmetrically about the point of greatest tissue damage because the gradient of decreasing damage was steeper going into the GM than the WM, and a greater volume of WM than GM was affected by the ultrasound. The decrease in damage into the GM was more gradual when there was

a substantial transition zone between the WM and GM, and more abrupt when this zone was smaller. In some cases the exposure produced damage only in the WM while the GM remained unaffected, making it appear as if the focal point was further displaced. This effect was enhanced when the focal point was located some distance into the GM, especially when the GM-WM interface was perpendicular to the beam axis, and hence the major axis of the focal volume. The focal point could then be located further into the GM from the interface and still have a substantial portion of the focal volume remaining in the WM to affect the tissue. The original records from the earlier studies at Illinois contained comments such as "lesion too high or low," or "lesion laterally displaced," in reference to lesions near WM and GM interfaces, indicating that this phenomenon was also observed by these investigators.

There were irradiated sites where a small region of GM was surrounded by a larger mass of WM, and vice versa. In the case of the GM surrounded by the WM, the damage observed in the GM was greater than if the focal point had been centered in a large mass of pure GM. The converse was true when a small WM region was surrounded by GM. As the size of the core tissue decreased in proportion to that surrounding it, the degree of the ultrasonically-induced tissue damage approached that which would have been observed in a region consisting purely of the surrounding tissue. The opposite was the case when the core tissue became larger.

The data presented in Chapter 4 clearly demonstrate that the ultrasonically-generated temperature rises from a given exposure

increased with increasing WM content of the tissue. This result was in agreement with the findings of Robinson and Lele [1972]. The measured intensity profiles of the focused transducer were identical in all the tissue types, viz., WM, GM, WGM, etc., including the tissue regions that contained an interface between WM and GM. The only asymmetry across the GM-WM border was the different absorption properties of the two tissue types. Hence, it appears that the resultant temperature difference between the GM and WM was the factor responsible for the asymmetrical distribution of the tissue damage. However, this does not necessarily mean that the additional heat was itself the sole and direct causal agent responsible for the increased tissue damage within the WM. The increased temperature may have increased the activity of some acoustically induced process that had a functional dependence on temperature, e.g., acoustic cavitation.

5.2.3. The Effects of Exposure Time and Post Irradiation Time on the Ultrasonically-Induced Damage

The shortest exposure time that resulted in LM observable, ultrasonically-induced damage was 0.5 sec in WM and 0.8 sec in GM. In both cases the lesions were visible only following a 24 hr post irradiation time while identical exposures did not produce any observable damage after eight hours post irradiation. Electron microscopy revealed that changes in the tissue ultrastructure were induced with slightly shorter exposures, 0.42 sec in WM and 0.7 sec in GM, again requiring a 24 hr post irradiated for the induced damage to develop. Lohnes [1971] determined that both the maximum volume of the lesion and the maximum degree of tissue damage

volume of the lesion and the maximum degree of tissue damage therein had developed by 24 hr post irradiated, and so the 24 hr sacrifice time was routinely used to assess the irradiation animals used in constructing the threshold curve of Fig. 1.1. It may therefore be assumed that the above reported exposure times represent the threshold exposures at 300 W/cm^2 required to produce LM and TEM observable lesions in the WM and GM.

Exposure times of 0.42 - 3.0 sec never resulted in LM observable damage immediately following the irradiation. A minimum of 5-12 min elapsed, post irradiation time was required before tissue damage resulted from a 3.0 sec exposure in WM was detectable with LM using oil immersion and a magnification of 1,000X. The irradiated tissue stained just a shade lighter than the surrounding tissue and some of the myelin sheaths appeared to be mildly swollen. Shorter exposures required progressively longer post irradiation periods before LM was able to detect any tissue changes. Barnard et al. [1956] reported that a minimum of 10 min post irradiation was required before tissue damage was observable following any of the exposures used in their studies. The earlier detection of ultrasonically-induced damage with LM in this study may be the result of several factors. The earlier studies used paraffin embedded tissue for their histological studies while epoxy embedded tissue was used in the present one. Epoxy embedding preserves the the finer details of the tissue and allows for higher resolution of the tissue structures, making it possible to detect more subtle tissue abnormalities. The TEM observations also helped in detecting more subtle damage with LM. By working backwards from higher TEM magnifications to 1,000X, the

observer becomes attuned to detecting milder tissue damage at 1,000X which had first been observed using higher magnifications.

The tissue near the focal point of some WM and WWGM irradiated for 3.5 to 4.5 sec and longer appeared abnormal immediately following the exposures. Portions of the tissue were often friable and crumbled upon handling and during processing. Light microscope examinations of the friable tissue revealed normal morphology at the lower magnifications, but the tissue features appeared fuzzy and had a grainy texture when magnified 400X or more. With post irradiation times approaching 10 - 15 min, the tissue surrounding the friable regions exhibited tissue damage identical to that observed at a similar post irradiation time in tissue irradiated with shorter exposure times. Such lesions appeared identical to the island-moat lesions described by Barnard et al. [1956]. It is believed that the central island portion of the lesion was heat-fixed by the ultrasonically-induced temperature rise (in excess of 22^{o}C according to the data in Chapter 4), thus preventing any further changes in tissue morphology. This would also explain the friable quality of the tissue because heat-fixed brain tissue also has a friable consistency. An exposure of 4.0 - 5.0 sec was required to produce an island-moat lesion in GM. An exposure longer than 5.0 sec in WM or WWGM altered the irradiated tissue to the point where it crumbled into a powder-like consistency as the core containing the lesion was removed from the brain.

Data from animals receiving identical, temporally spaced exposures delivered to similar tissue regions of the brain (protocols 3 and 4, Chapter 3) demonstrated that both the lesion

volume and the degree of tissue damage observed within the lesion increased with increasing post irradiation time. Comparing the results from animals irradiated in this same manner, but with different exposure times, together with those animals having multiple irradiated sites but different duration exposures (protocol 1, Chapter 3), showed that increasing the exposure time increased the degree of damage and the lesion volume observed following a given post irradiation time, as well as increasing the rate at which further damage developed with increasing post irradiation time. For a given exposure time, the tissue damage developed at a faster rate in the tissue with a higher WM content. However, at sites that contained both myelinated and nonmyelinated structures, altered morphology appeared first in the nonmyelinated structures and further degeneration progressed at a faster rate than in the myelinated structures. This last point will be discussed further later in this chapter.

5.2.4. Specimen Variability

Since the transducer was calibrated to produce the same acoustic intensity for all exposures, the variable responsible for the different tissue responses among identically irradiated animals was the animals themselves. The WM and GM content, and the vascularization of identical sites in different cat brains can vary significantly, as observed in this study, and as discussed in Section 5.2.1, these factors can substantially affect the tissue's response to the ultrasound. The observed variability in tissue response to the ultrasound was most pronounced with the shorter exposures, and became less so with increasing exposure times.

As mentioned in Chapter 1, the brain meninges and subarachnoid space may be a cause for the variable responses among different but identically irradiated animals. Johnston and Dunn [1976b] suggested that the weak frequency dependence of the ultrasonic threshold dose for the production of lesions in cat brains observed by Dunn et al. [1975] was the result of an acoustic impedance mismatch between the collagen trabeculae of the subarachnoid space and the material on either side of its bounding membranes, the arachnoid and the pia mater. They also suggested that the increased acoustic velocity in he collagen fibers over that of the cerebrospinal fluid within the subarachnoid space induced a progressively increasing phase difference across the subarachnoid space. Both of these factors would increase the attenuation of the acoustic intensity. This is supported by the observation that removal of the meninges increased the lesion volume resulting from a given ultrasonic exposure [Johnston, 1982].

Dunn et al. [1975] demonstrated that the threshold intercept function, C(f), in the equation describing the threshold response of the tissue,

$$It^{1/2} = C\ (f) \qquad (5.1)$$

has a weak frequency dependence. Johnston and Dunn attributed this dependence to the brain meninges and the subarachnoid space. They modeled the irradiation conditions by assuming the acoustic waves were planar in nature and were propogating through a three layered media, viz., the saline coupling medium, the subarachnoid space and the brain tissue itself. The three media were treated

as having plane parallel boundaries which were maintained by the brain meninges, and the media differed with respect to their densities, sound velocities and acoustic impedances. The saline and brain tissue were assumed to have similar acoustic impedences which differed from that of the subarachnoid space.

For this physical model, the ratio of the incident ultrasonic intensity to that transmitted into the third medium (the brain) was given as,

$$1 + [1/4(Z_s/Z_a + Z_a/Z_s)^2 - 1] \sin 2kl, \qquad (5.2)$$

where k is the wave number, l is the thickness of the subarachnoid space, and Z_s and Z_a are respectively the acoustic impedences of the saline and brain tissue, and the subarachnoid space. This function was fitted to the data of Dunn et al. [1975] and the fit provided values for the average thickness of the subarachnoid space, 250 μm, the speed of sound through the subarachnoid space, 1800 m/sec, and the frequency independent value for C(f), $W \cdot sec^{1/2}/cm^2$. This value for C(f) sets Equation 5.1 equal to Equation 1.3, as reported in Chapter 1.

Assuming Z_s and Z_a are constants, Equation 5.2 is a function of k and l, where k determines the frequency dependence for a constant l. If the frequency is held constant, as it was in the present study, then any variation in Equation 5.2, and hence in C(f), is due to variations in the thickness of the subarachnoid space among the irradiated animals. That such a variation exists is demonstrated by the range of threshold intercept values reported at each frequency by Dunn et al. [1975]. At 1 MHz the range of C(f) is 190 - 410. Using Equation 5.1, this gives a

threshold exposure range of 0.69 - 1.87 sec for an intensity of 300 W/cm^2 in WM, with a mean value of 1.1 sec. Therefore, variations in the thickness of the subarachnoid space among the population of irradiated animals can give rise to a significant variability in the response of identically irradiated animals to the ultrasound.

5.3. Defining a System for Scoring the Ultrasonically-Induced Morphological Changes

Observations of the irradiated tissue from 38 animals exhibited varying degrees of tissue damage ranging from lesions that required TEM to detect subtle changes in the tissue ultrastructure to those where all that remained of the tissue were fragments of membranous structures within an electron transparent volume. In order to make comparisons between the tissue damage induced by the various treatments a scheme for scoring qualitatively the resultant morphological changes was devised, in which the observed range of tissue damage is divided into 9 stages, each of which was assigned a numerical value of 1 through 9 with the larger numbers indicating a greater degree of damage.

The scoring stages 1 through 9 were also the sequence in which the tissue damage appeared in the irradiated sites with increasing post irradiation time, as determined by the observations of the temporally spaced lesions in the cat brain. Since the nature of the tissue damage depended on the tissue's position within the focal volume, comparisons were made between identical positions within each of the temporally spaced, irradiated sites.

Data from all of the animals used in this study demonstrated that the same temporal sequence of ultrasonically-induced morphological changes occurred in every animal, irrespective of the exposure times used. More specifically, the order in which alterations first appeared within the populations of a given morphological structure, viz., synapses, mitochondria neurons, etc., relative to their appearance in all other structures remained constant, together with the manner in which the altered morphology changed for that structure as a function of increasing post irradiation time. For example, changes in the ultrastructure of synapses always preceeded their occurrence in mitochondria. This does not mean that every synapse in the region under consideration exhibited altered morphology before any mitochondria did, only that abnormalities were observed in the synaptic population before appearing within the mitochondrial population. Once the ultrastructure in a given synapse was affected, subsequent morphological changes progressed through a series of stages that was universal for all altered synapses. As new altered synaptic states appeared in the tissues with longer post irradiation times, and a larger portion of the altered synaptic population occupied these states, it was assumed that the order in which these states appeared represented the sequence by which all synapses evolved once they were altered as a result of the ultrasonic exposure. This same reasoning was applied to all the other morphological structures.

By stating that the temporal sequence was the same irrespective of the exposure time used does not imply that the ultrasonically-induced damage from every exposure eventually

developed into stage 9. It does mean that if, following a given post irradiation time, the tissue damage was scored as stage n, the series of irradiated sites having shorter post irradiation times exhibited a progression in the degree of damage from stages 1 through n - 1. Increasing the exposure time did increase the rate at which the irradiated tissue progressed through the temporal sequence, without affecting the nature of the morphological changes or the order in which they occurred. The tissue always progressed more rapidly through the earlier stages of the sequence, after which the rate of change decreased as the later stages were reached.

It was found that the spatial variation of the tissue damage within a lesion was identical to the temporal sequence of stages 1 through 9. For example, a lesion in WM with a 2.0 sec exposure and a post irradiation time of 3 hr exhibited stage 9 damage at its center and stage 1 damage at its outer boundary. The intervening tissue exhibited stages 2 through 8 in such a manner that the degree of damage increased gradually in moving from the lesion's outer boundary to its center. With increasing post irradiation time, the tissue at the lesion center progressed through the temporal sequence faster than that at the lesion boundary. As the lesion center reached the latter stages of the sequence, further changes occurred more slowly and the degree of damage in the lesion periphery advanced to it with increasing post irradiation time. The spatial gradient of damage across the irradiated volume degenerated, and the tissue damage became more homogeneous throughout the lesion.

Each of the nine stages is characterized by the appearance of specific changes in the morphology exhibited within the populations of one or more of the tissue structures, e.g., axons, myelin, neurons, mitochondria, etc. At any given stage, the different morphological structures exhibited a range of altered states within their populations. This range included normal appearing structures, the altered states described for the previous stages, as well as the altered states characteristic of the stage for which the tissue was scored. The distribution of the altered structures among the different altered states varied considerably when comparing different tissue regions that were scored as the same stage. Factors affecting the distribution of altered states exhibited by the different structures were the exposure time, the tissue's position within the focal volume, the WM and GM content of the tissue, and the specimen variability. For any given stage, tissue that received a longer exposure, was located closer to the lesion center or had a higher WM content, had a higher percentage of the morphological structures exhibiting altered morphology, and the distribution over the altered states was shifted towards the more altered end of the range.

Herein lies the weakness of this scoring scheme. Two tissue regions would be scored as the same stage when one had, for example, 40% more of its morphological structures affected than the other. This is because the stages are defined on the basis of the type of morphological damage present and not on the percent of the structures that showed this damage. In an effort to express the variability of the damage within the tissue scored as a given stage in a more quantitative manner, the detailed descriptions of

each stage include a percentage range for the populations of some of the morphological structures that exhibited altered morphology at that stage. These numbers were generated as follows. At least ten different tissue regions scored as a given stage were selected such that they covered the damage range exhibited by the various tissues scored as that stage. A minimum of five electron micrographs were taken from each region and the number of affected structures was counted. Random counts of electron micrographs taken from other tissue regions scored as the same stage, together with numerical estimates made while observing the tissue with the electron microscope agreed with the reported ranges.

The ideal situation would be to subclassify each stage according to the degree to which the population of each morphological structure was affected by the ultrasound. These sub-classifications could then be used to compare the response of tissue receiving different exposure times, and differing in WM content and position within the focal volume. Establishing such a system was beyond the scope of this thesis. In order to obtain statistically significant data for each of the variables mentioned above, over 100 animals would have to be irradiated. This is because of the wide range of tissue responses to identical irradiations delivered to the same sites in different cats, as described earlier.

Detailed descriptions of the altered morphology for each stage is presented below in a separate section of this chapter. The discussion centers on the TEM observations; however, some LM observations of the tissue are also included. Each section begins with a brief summary of the tissue damage representative of each

stage followed by a detailed discussion of the altered morphology exhibited by the different tissue structures. The subsection headings are self-explanatory except for the one entitled, "nonmyelinated structures," which includes the following nonmyelinated, membrane-bound structures; nonmyelinated axons, dendrites, and dendritic thorns. Because of their importance in nervous functions, the synapses are discussed under a separate heading.

If a given structure is not mentioned within the discussion of a given stage, then its population still exhibited the morphology described for the previous stage. Unless otherwise stated, all comparative remarks, e.g., more electron dense, decreased numbers, etc., are made with reference to the previous stage.

Most of the stages are defined by the altered, morphological states exhibited by several different structures. If a small percentage of one of these structures displayed the altered state characteristic of a later stage, this did not warrant reclassifying the tissue or establishing a new stage.

5.4. Stage 1

The degree of ultrasonically-induced damage present represents the lower limit of detectability using TEM. Microscope magnifications of 3,000X or better were required to identify the abnormalities. Even LM micrographs enlarged to provide effective magnifications in excess of 3,000X could not show any differences

between stage 1 and nonirradiated tissue. Stage 1 tissue was found at the center of lesions that were just beginning to develop and at the periphery of already established lesions.

At the low TEM magnifications, the overall appearance of the tissue was less crisp and sharp than the nonirradiated tissue, almost as if the microscope was ever so slightly overfocused. Continual sweeps from over to under focus demonstrated that the loss of crispness was not due to poor focusing. This effect was hardly noticeable with magnifications in excess of 5,000X.

Altered morphology was only observed within the nonmyelinated structures of the tissue, and most notably within the chemical synapses. Upon closer examination, the cytoplasm in all nonmyelinated structures, with the exception of the neuron and glial cell bodies, appeared slightly less electron dense than their counterparts in the nonirradiated tissue. The axoplasm and other contents of the myelinated axons were unaffected.

5.4.1. Synapses

The most pronounced deviation was a change in both the number and distribution of vesicles within the presynaptic elements, as can be seen in Fig. 5.11. Most of the remaining vesicles tended to form aggregates, *, within the presynaptic element. In many instances, a diffuse, electron dense material was associated with these vesicle aggregates. A vesicle aggregate was always observed in association with the junctional density, and this aggregate usually contained the largest number of vesicles. Serial sectioning demonstrated that most of the larger vesicle aggregate that were not associated with a junctional density in one section

were in fact associated with one located in another plane of the tissue. However, nonassociated aggregates were also observed, together with nonaggregated vesicles. From 10 - 90% of the synapses in the stage 1 tissue exhibited some degree of synaptic vesicle aggregation and depletion. The remaining synapses displayed a morphological appearance indistinguishable from those in the nonirradiated tissues. The 10% figure was observed in the tissue sacrificed 24 hr post irradiation of a 0.42 sec exposure, and also in the outer boundary regions of lesions whose central regions displayed tissue damage characteristic of a latter stage. Typically, 20 - 70% of the synapses exhibited these effects at the lesion center in WGM irradiated for 1.2 - 2.0 sec and sacrificed immediately following the exposure, while a 3.0 sec exposure affected as much as 90% of the synapses.

Membranous debris, Md, was frequently observed within the affected presynaptic element, and less frequently within the postsynaptic element. Most of the debris was amorphous in nature, but a small fraction was suggestive of swollen, misshapen vesicles (brackets in Fig. 5.11).

There were no perceptible changes in the electron density and distribution of the junctional densities, or in the width of the synaptic clefts. However, over 95% of the altered synapses had junctions with either zero or positive curvatures, with the latter being more commonly observed. Unaltered synapses displayed a normal distribution of junctional curvatures. The cytoplasm in some of the altered presynaptic elements appeared to have a reduced electron density. This effect may have been enhanced by the reduced number of synaptic vesicles. However, observations of

vesicle-free regions of presynaptic elements from the nonirradiated tissues indicated that the density decrease was real. Mitochondria appeared normal both in the pre- and postsynaptic elements of the altered synapses. Very few neurofilaments were observed in the presynaptic elements and there were fewer observations of microtubules and smooth endoplasmic reticulum. Remaining neurofilaments and microtubules tended to be found in the portion of the presynaptic elements nearest the junctional densities. Much of the smooth endoplasmic reticulum was mildly swollen, and more swollen fragments may have given rise to some of the amorphous debris. The postsynaptic elements appeared relatively unaffected.

5.4.2. Nonmyelinated Structures

Membraneous debris was observed within nonmyelinated structures other than the synapses (Fig. 5.11), particularly the dendrites and dendritic thorns, and was generally amorphous, though there were rare instances where its shape suggested that of a deformed mitochondrian (double arrow heads in Fig 5.11). The increase in membranous debris was accompanied by a decrease in the occurrence of smooth endoplasmic reticulum in these structures, suggesting that the reticulum gave rise to some of the debris.

5.4.3. Myelinated Axons

A mild demyelination was observed in a small number of the myelinated axons, only within the WWGM and WM. This was more noticeable in the larger axons, and practically nonexistent within the population of axons with transverse or oblique section diameters less than approximately 5 μm. In WWGM and WM regions

where few or no synapses were observed, the demyelination of the axons and the increase of membranous debris in the nonmyelinated structures were the only indicators of ultrasonically-induced abnormalities. This made the scoring of some irradiated, WM sites as stage 1 difficult when no nonmyelinated structures were present. The close packing of the myelinated axons often masked the mild demylination.

5.5. Stage 2

The low magnification, electron micrograph of Fig. 5.12 illustrates that other structures besides the synapses were now significantly altered as a result of the ultrasonic irradiation, though the irradiated tissue still appeared normal when examined with LM, with the possible exception of the WM. Using an oil immersion objective, the myelin surrounding the largest axons in the WM appeared to stain a lighter color with the toluidine blue, and the boundaries of the axons appeared less distinct. This effect was enhanced by differentiating the stain with ethanol as described in Chapter 3.

Altered morphology appeared within the polulation of mitochondria, though the distribution of altered mitochondria was nonuniform throughout the irradiated region. Altered morphology was essentially nonexistent within the mitochondria located within the myelinated axons, while a significant number of those mitochondria within adjacent, nonmyelinated structures clearly displayed altered morphology (Figs. 5.12 and 5.13).

5.5.1. Synapses

A larger percentage of the synapse population exhibited some degree of altered morphology, sometimes by a factor of 2 or 3 for those tissue regions which received exposures that produced less than 30% affected synapses during stage 1. There was a tendency towards a further reduction in the total number of synaptic vesicles within the presynaptic elements, as illustrated in Figs. 5.12 and 5.13. Almost all of the remaining vesicles were found in aggregates. All the affected synapses still had a vesicle aggregation at the synaptic cleft, but in many synapses this cleft aggregate was less prominent than what was common for stage 1. There were also synapses where vesicles were only observed in the cleft aggregates. The vesicle aggregates still had some electron dense material associated with them, but this too had become less evident.

A comparison of Figs. 5.12 and 5.13 to Fig. 5.11 shows that the cytoplasm of the presynaptic elements was now less electron dense, and that their delineating membranes displayed significantly more rounded contours, giving the presynaptic elements a more turgid appearance. Both of these observations suggested that some swelling had taken place. As the fluid volume increased, the concentration of the cytoplasmic substances that took up the stain would decrease and result in a lower density staining of the cytoplasm. Any swelling would also stress the delineating membrane, and more rounded contours would result as the membranes were forced to contain an increased fluid volume.

The smooth endoplasmic reticulum and microtubules were still observed within the presynaptic elements, but in reduced numbers.

The remaining smooth endoplasmic reticulae were swollen and distorted, and were often observed to be continous with the membranous debris, demonstrating that some of the debris was overswollen reticulum. Most of the microtubules were found in the vicinity of the synaptic cleft. No neurofilaments were observed within the more damaged synapses.

The synapses still displayed a dichotomous response to the ultrasound with respect to the pre- and postsynaptic elements. Although some of the postsynaptic elements displayed a mild degree of swelling, it was nowhere near the magnitude of the effect seen in the presynaptic elements. The different responses may reflect some difference in the function of the two components or some inherent differences in the selective permeability of their membranes.

5.5.2. Mitochondria

Altered mitochondria were observed within the nonmyelinated structures, including the synapses. Both Figs. 5.12 and 5.13 show electron transparent regions within the affected mitochondria, while the higher magnification of Fig. 5.13 reveals that these transparent regions were swollen intracristal spaces (arrowhead). Most of the mitochondria having the swollen intracristal spaces exhibited a mild increase in the electron density of their matrices. This may have been the result of a reduction in the matrix volume resulting from the increased volume of the intracristal space, or a slight decrease in the total volume of the affected mictochondria. There were also mitochondria that had the swollen intracristal spaces and matrices

of a normal or slightly lower electron density. Some 10 - 50% of the mitochondria within the nonmyelinated structures exhibited these effects, whereas they were never observed in more than 2% of the mitochondria within the myelinated axons. The number of altered mitochondria within the myelinated axons was not significantly different than that observed within the nonirradiated tissue.

5.5.3. Nonmyelinated Structures

There was a very mild decrease in the electron density of the cytoplasm within the dendrites and nonmyelinated axons having cross sectional diameters less than approximately 4 μm (Figs. 5.12 and 5.13). This effect was more pronounced in the axons than the dendrites. There was also an increase in the occurrence of membranous debris in these structures.

A mild decrease in the electron density of the cytoplasm in the dendritic thorns was observed, but it was not easily detected, particularly at those points functioning as postsynaptic elements, as mentioned in Section 5.5.1. The cytoplasm itself may have truly been less electron dense, however, the electron dense filamentous network which was near the synaptic cleft in the postsynaptic elements may have masked it.

5.5.4. Myelinated Axons

Demyelination of the axons was now much more pronounced and prevalent, and was even observed in the 5 μm and smaller diameter axons (Figs. 5.12 and 5.13) within the WM, WGM and WGM. The demyelination was nearly absent in the GWGM and GM. No changes

were observed for the axoplasm and other, internal components of the myelinated axons.

The electron micrographs showed that there was a considerable spacing between the frayed layers of myelin from the larger axons. Since the fluid-filled space would not take up much of the toluidine blue stain, this may explain the suspected lighter staining and fuzzy borders observed in some of the larger axons using LM.

5.6. Stage 3

Tissue damage was now discernable with LM in both WM and GM when using magnifications of 400X or more. In the WM, the demyelination of the larger axons had progressed to the point where there was no doubt that the tissue was indeed staining lighter than the nonirradiated WM, and the margins of these axons were less sharply defined. When there were WM regions that had few or no very large axons, the confirmation of tissue damage using LM was more difficult and uncertain. It was the neurons that signaled the presence of tissue damage in the GM. Both the nuclei and the cell bodies appeared mildly swollen and lighter staining. Dark staining condensations were observed within the nucleus, which tended to occupy the central regions of the nucleus, particularly the area surrounding the nucleolus. In the cytoplasm, the Nissl bodies were either significantly diminished in numbers or totally absent. A small number of neurons had an accumulation of dark staining material surrounding the nucleus, while the area near the cell periphery was transparent. This phenomenon was best observed in the neurons having a large cross

sectional area in the tissue section. Evidence of ultrasonically-induced damage observable with LM only appeared when neurons were present in the section.

5.6.1. Synapses

The postsynaptic elements exhibited a more noticeable loss of electron density.

5.6.2. Mitochondria

There was a slight increase in the number of mitochondria displaying the altered morphology described for stage 2. Some of the mitochondria within the nonmyelinated structures exhibited lighter staining matrices; compare the mitochondria in Figs. 5.5, 5.14 and 5.16. Also note in Fig. 5.5 that the mitochondria within the neuron have slightly lighter staining matrices than those within the myelinated and nonmyelinated structures, save the dendrites. The mitochondria within the neurons appear more similar to those in the nonmyelinated structures) (Figs. 5.14 and 5.16).

5.6.3. Neurons

Figures 5.14 through 5.17 illustrate the TEM appearance of the altered neurons showing the LM observable changes described above. The most prominent feature in the low magnification micrographs is the condensation of the chromatin into electron dense clumps and the decreased electron density of the nucleoplasm; compared to the typical, more homogeneous chromatin distribution seen in Fig. 5.5. As in the LM observations, the

chromatin condensations tended to occupy the central regions of the nuclei.

Changes were also noted in the nucleoli of the affected neurons. As seen in Fig. 5.16, the nucleolus is more compacted and electron dense than that of Fig. 5.5. The electron transparent regions within the nucleolus became less apparent and smaller at this stage, adding to the impression that the nucleolus, like the chromatin, had condensed. The nculeolus in Fig. 5.5 shows ribosome-like granules amongst the more dense staining material, which is composed of fine, but tightly condensed filaments [Peters et al., 1970]. In the altered nucleoli, the granules were extremely difficult to see. There seemed to be no observable changes in the morphology of the nuclear pores (Fig. 5.17). However, the outer nuclear membranes were slightly less irregular than in the nonirradiated neurons, as can be seen by comparing Figs. 5.6 and 5.17. If the decreased electron density of the nucleoplasm truely reflected a swelling of the nuclear membrane, then the increased nuclear volume would stress the nuclear membranes. Such a stress may have been responsible for stretching and smoothing out the outer nuclear membrane. Figure 5.17 shows an absence of Nissl bodies. Both the rough and smooth endoplasmic reticulum were swollen into ring-like structures whereas they were more like parallel rails in Figs. 5.5 and 5.6. Ribosomes were still attached to the rough endoplasmic reticulum, but Fig. 5.17 illustrates that there was an apparent decrease in their numbers. It may be that the ribosomes actually detached from the rough endoplasmic reticulum. However, the lower density of attached ribosomes may be the result

of the reticulum swelling and increasing the membrane area. Although Fig. 5.17 shows that some of the free ribosomes still form the distinct patterns illustrated in Fig. 5.6 a significant fraction of the ribosomes were found as single, unassociated organelles. These unassociated ribosomes appeared less electron dense than the ribosomes remaining in the pattern formations.

Figures 5.14 - 5.17 show that portions of the golgi were also swollen and distended (as indicated by the asterisks). This was not surprising since, as shown by Fig. 2.3, the endoplasmic reticulum is continuous with the golgi. Most of the golgi within the altered neurons exhibited some degree of swelling and distortion, but some still appeared normal within many of these cells.

In Fig. 5.15, no significant swelling of the endoplasmic reticulum is observed, but it and the other subcellular organelles are concentrated in the region about the nucleus. The region near the cell periphery was distinctly more electron transparent, and there was a marked decrease in the observed number of neurofilaments and microtubles in this part of the cell. The decrease in the number of neurofilaments was greater than observed for the microtubules. Both neurofilaments and microtubules were present within the region surrounding the nucleus, but even here the neurofilaments appeared less numerous. A mild decrease in the neurofilament population was also observed within the altered neurons that did not exhibit the juxtanuclear concentration of subcellular organelles. The juxtanuclear organelle condensation was only observed in those neurons displaying a large cross sectional area in the tissue sections.

There was a noticeable decrease in the number of multivesicular bodies observed in the affected neurons. Many of the remaining multivesicular bodies were in various stages of swelling, as indicated by the double arrowheads in Figs. 5.14 and 5.15. These structures still contain some vesicles, and so can be positively identified as swollen multivesicular bodies. Some of the membranous debris within the altered neurons may have resulted from superswollen or ruptured multivesicular bodies. The structure indicated by a question mark in Fig. 5.17 may also be an altered multivesicular body; it is single membrane bound and contains several rounded structures that may be swollen vesicles.

In the tissue scored as stage 2, from 30 - 100% of the neurons displayed the above effects to some degree. It was not uncommon to see two adjacent neurons where one appeared as those in Figs. 5.14 and 5.15 while the other was as that in Fig. 5.5 and exhibited no altered morphology.

5.6.4. Nonmyelinated Structures

The dendrites exhibited the morphological changes described for the neuronal, subcellular organelles (Fig. 5.16). Dendritic thorns exhibited a mild, decrease in their cytoplasmic electron density.

5.6.5. Myelinated Axons

The internal structure of the axons themselves remained unaltered. Demyelination was severe enough that the WM tissue could easily be scored as stage 3 in the absence of any nonmyelinated structures, with both LM and TEM.

5.7. Stage 4

The mitochondria within the nonmylinated structures exhibited a wide range in altered morphological states. Similar mitochondrial changes were also observed within the neurons and many of the glial cells. Although an increased number of mitochondria within the myelinated axons displayed the altered morphological state described in stage 2, in general, the mitochondria and other internal structures within the myelinated axons remained unaffected.

A decrease in the electron density of the nonmyelinated structures bordering some of the blood vessels was observed using TEM. This decrease was greater than that observed for similar structures located further away from the blood vessels. There was a slight decrease in electron density of the cytoplasm within the endothelial cells of the blood vessels, but the greater effect was in the surrounding structures.

5.7.1. Mitochondria

Fewer mitochondria within the nonmyelinated structures, including the synapses, displayed the altered state described for stage 2. Instead, they exhibited a range of altered morphological states indicating that the affected mitochondria were in the process of swelling. The diversity of the altered mitochondrial states is illustrated in Fig. 5.18 by the mitochondria numbered 1 - 4. The first indication of swelling was the presence of small electron transparent regions located within the mitochondrial matrix giving it a mottled appearance. In the more affected mitochondria these electron transparent regions became larger, 2,

and as they further increased in size, they merged to form a single, large, electron transparent region within the center of the mitochondrion, 3. Remaining electron dense portions of the matrices in these mitochondria were restricted to the peripheral regions together with most of the cristae. The cross sectional diameters of these mitochondria were as much as four times larger than those presented by the unaltered mitochondria. In the most altered state displayed at this stage, there were no remnants of the electron dense matrix 4, and most of the cristae were found near the periphery. Despite the increased mitrochondrial volume, both membranes remained intact, but the space between the inner and outer membranes was decreased. There were still mitochondria that exhibited normal morphology. Figure 5.18 illustrates another aspect of the mitochondrial swelling. With the exception of the cell bodies, the mitochondria within the same membrane-bound structure generally exhibited similar degrees of altered morphology. However, altered mitochondria displaying markedly different degrees of swelling did exist within some of the membrane-bound structures.

5.7.2. Neurons

More neurons exhibited the altered morphology described in stage 3, many of which were more swollen. This was most noticeable when the tissue was examined with LM. The cytoplasm and nucleoplasm of the most swollen neurons were very transparent and in some cases did not seem to take up any of the toluidine blue stain. Mitochondria in many of the neurons displayed the altered states described for stage 3, and this was most prevalent

in the more swollen neurons. Aside from the increased, neuronal swelling and mitochondrial alterations, there were no other significant changes observed in the neuron population.

5.7.3. Glial Cells

All of the glial cells appeared to respond in a similar manner to the ultrasound, and for this reason one of these cell types, the oligodendrocyte, was chosen as the example for illustrating the altered morphology observed.

The damage observed in the glial cells at this stage were very similar to that described for the neuron in stage 3, as seen in Fig. 5.19. Both the cytoplasm and nucleoplasm were less electron dense (compare Figs. 5.1 and 5.19). There was no chromatin condensation as observed in the neuron nuclei, but the electron transparent regions of the nucleoplasm observed in the nonirradiated cells were now larger. Swollen rough and smooth endoplasmic reticulae were observed together with a decrease in the number of ribosomes attached to the swollen rough endoplasmic reticulum. The free ribosome patterns were markedly reduced, more so than in the neurons, and in some cases were totally absent from the glial cell cytoplasm. Like the neurons, the nonassociated ribosomes appeared less electron dense than their associated counterparts. Unlike the neurons, the mitochondria within the glial cells displaying this earliest stage of altered cell morphology showed altered states beyond those described for stage 2.

5.7.4. Blood Vessels

A capillary from the nonirradiated tissue is shown in Fig. 5.20. Note the membrane-bound structures bordering the endothelial wall, EW, of the capillary, and the ultrastructure of the endothelial wall itself and compare to the same structures in Fig. 5.21. In the latter, the membrane-bound structures immediately surrounding the capillary appear less electron dense and more swollen than those in Fig. 5.20. The swelling in these structures was significantly greater than that observed in the nonmyelinated structures located at further distances from the blood vessels. Fewer recognizable, ultrastructural features were found within the swollen tissue, while the amount of membranous debris was increased. A less noticeable decrease in electron density was observed within the endothelial cells forming the vessel walls. There was also an increase in the occurrence of small, electron transparent vacuoles within the endothelial cells.

The swelling observed in Fig. 5.21 is distributed rather uniformly about the blood vessel, forming a cuff of less electron dense material, because the surrounding tissue is of a similar nature with respect to myelination. If, for example, half the vessel was bordered by myelinated structures and the other half by nonmyelinated structures, the swelling was only present in the nonmyelinated structures, forming an asymmetrical cuff about the vessel. Such asymmetrical cuffing was also observed about blood vessels surrounding purely nonmyelinated structures, but the asymmetry was less obvious.

Both Figs. 5.20 and 5.21 are transverse sections through the blood vessels. More oblique and longitudinal sections

demonstrated that the degree of swelling, or cuffing, was nonuniform along the length of the blood vessels. There were segments along a given vessel where no cuffing was observed, but the segments on either side exhibited very distinct cuffing. This asymmetry existed even though the tissue surrounding each of these segments was very similar.

5.7.5. Myelinated Axons

The asymmetry between the morphology displayed by the mitochondria in the nonmyelinated structures and the myelinated axons is vividly demonstrated in Fig. 5.18. Less than 10% of the mitochondria within the myelinated axons exhibited the altered state of stage 2 (Figs. 5.18 and 5.19). More advanced stages of damage were rarely observed.

Whorls of membranous debris, some almost cloud-like in appearance, were observed in the WGM, WWGM and WM (* in Fig. 5.18). The arrowheads in Fig. 5.18 indicate where one of these whorls is continuous with the myelin sheath, suggesting that such structures were highly unraveled segments of myelin. It appears in this figure the whorl is within the bounds of a nonmyelinated structure; in actuality, it is resting on the membrane of this structure and appeared inside since the section was taken tangential to the membrane. In other instances the myelin whorls distorted the shape of other membrane-bound structures forming indentations that made it appear that the whorl invaded the central portions of these structures.

5.8. Stage 5

The transparent cuffs surrounding many of the blood vessels were now visible with LM. Electron microscopy showed that many of the membrane-bound structures surrounding the vessels had ruptured. The larger blood vessels did not have a cuff completely circumscribing them when observed with LM, but instead had transparent, bubble-like regions at points along their periphery. As with the cuffs about the smaller vessels, the membrane-bound structures near these bubble regions had ruptured.

The cell bodies of many glial cells and neurons were distinctly more damaged as observed with LM, yet a small number still remained normal in appearance. Transparent vacuoles now became apparent in the oligodendrocyte cytoplasm giving it a mottled appearance in the more damaged cells. Some neurons now appeared to have a grainy texture to both the cytoplasm and nucleoplasm. Such cells appeared to be less swollen than those described in stages 3 and 4.

A greater fraction of the mitochondria in the nonmyelinated structures were now observed in the more altered states. In the most damaged tissue that was scored as stage 5, less than 10% of the mitochondria in the nonmyelinated structures displayed normal morphology. Some mitochondria were swollen to the point where their outer membranes ruptured, and began to fall away from the inner membrane. This permitted a further expansion of the inner membrane and a reduction in observable cristae. Single membrane-bound, ring-like structures were now observed in the sections. These ring structures were most likely the remmants of mitochondria that had lost their outer membranes and the inner

membrane had unfolded, resulting in the loss of the cristae. Fewer altered mitochondria were still observed in the myelinated axons in comparison to those observed in the nonmyelinated structures, and the degree of mitochondrial damage was less.

Membrane degeneration was observed in the population of nonmyelinated structures, particularly the presynaptic elements of the synapses. The membranes appeared swollen and less electron dense. In some regions the membrane was so diffuse that it essentially blended into the background. A similar type of membrane degeneration was also observed in the most swollen mitochondria and the ring-like structures mentioned above.

5.8.1. Synapses

Many synapses exhibited what appeared to be a degeneration or dissolution of their delimiting membranes; most notable in the presynaptic elements, as illustrated in Fig. 5.22. The arrowheads in this figure indicate where the delimiting membrane apparently became swollen and distended. At one point the membrane is so distended that it nearly blends into the electron transparent background. A good deal of debris was observed in these synapses, but much of it, like the synaptic membrane, was distended and light staining.

The cytoplasm within both the presynaptic and postsynaptic elements appeared less electron dense and the presynaptic elements contained very few synaptic vesicles. In some cases the synaptic elements appeared so swollen that the only means of identifying them as synapses was the presence of the junctional density and a few associated vesicles. The junctional density itself was less

electron dense in such synapses, and the synaptic cleft was often 20-40% wider than normal. No endoplasmic reticulum was observed, no neurofilaments were present and microtubules were less frequently observed. When microtubules were present, they appeared to be very light staining (Fig. 5.22). Mitochondria were also less frequently observed.

Although the population of synapses was markedly shifted into displaying the more damaged states, there were still a small number of synapses (5 - 15%) displaying normal morphology, which were never found in clusters, but were randomly distributed throughout the tissue. Such synapses were frequently surrounded by several synapses displaying altered morphology as severe as the that shown in Fig. 5.22.

5.8.2. Mitochondria

Like the synapses, the population of mitochondria in the nonmyelinated structures was shifted towards the more altered morphological states, but some 5 - 20% of the mitochondria still appeared normal in appearance. Some of the more swollen ones had partially or completely lost their outer membranes (double arrowheads in Fig. 5.22). In such structures there was very little, if any, evidence of cristae structure. It is believed that as the inner membrane expanded further, the cristae unfolded since they were simply infolded segments of this membrane.

Membrane-bound, ring-like structures having no internal features, were first observed during this stage. They were found throughout the nonmyelinated structures, but not in the myelinated axons. Figure 5.23 shows that the membranes of these ring

structures which were often irregular and exhibited the same type of membrane degeneration observed in the synapses. Increasing degrees of this apparent degeneration are presented in Fig. 5.23 by the structures labeled 1 - 4.

It is very likely that the ring structures were either the discarded, outer mitochondrial membranes or the swollen, cristae-free inner membranes. Besides the trend of increasing mitochondrial swelling, there was further evidence for the origin of the ring structures. Low magnification micrographs of the tissue scored as stage 5 showed a decrease in the number of structures identifiable as mitochondria when compared to the comparable sections from stage 4 and earlier stage tissue. The number of ring-like structures observed in the stage 5 tissue was of the order of which would be expected if they were the remnants of the missing mitochondria.

5.8.3. Neurons

Figure 5.24 shows that small condensations of electron dense material were now present in the nucleoplasm and cytoplasm. These electron dense condensations were also observed in many of the dendrites (Fig. 5.22). It was these condensations that gave the neurons their grainy appearance when observed with LM and the lower magnifications with TEM. These grainy neurons appeared less swollen than those exhibiting the morphological states described in stages 3 and 4, indicating that these once swollen cells were now in the process of shrinking. The fact that these neurons were indeed in the process of shrinking is substantiated by the observation of the neurons described later in state 6.

There were no longer any structures that displayed the lamellar morphology so characteristic of the golgi. Instead, clusters of membranous vesicles within the cytoplasm that were present in the same quantity that the golgi were observed in the nonirradiated cells and in neurons at the earlier stages (Fig. 5.24). There were also golgi observed during the earlier stages which exhibited morphology that was intermediate between the vesicle clusters in Fig. 5.24 and the mildly distorted golgi in Fig. 5.17. This confirmed that the vesicle clusters were indeed the end product of ultrasonically-altered golgi.

Some ribosomes were still attached to the rough endoplasmic reticulum which itself appeared less swollen and distorted than in Fig. 5.17. The free ribosome patterns so prominent in the nonirradiated neurons were now all but completely obliterated. Some of the free ribosomes were associated with an electron dense material that exhibited a filamentous structure, with the filament diameter being approximately 6 mm. Figures 5.6 and 5.17 also reveal the filamentous nature of the ribosome-associated material. This material was more plentiful in Figs. 5.6 and 5.17 and contributed significantly to the overall density of the cytoplasm such that its filamentous nature was masked. Fewer neurofilaments were also observed in the cytoplasm while the number of microtubules observed appeared unchanged.

The mitochondria displayed the same range of swollen states described for this stage and stage 4, including the ring-like structures. No multivesicular bodies or any structure resembling them was observed. Most of thee lysosomes appeared unaffected

while the contents of a small number of lysosomes were slightly less electron dense.

Electron dense materials, ribosomes and fragments of endoplasmic reticulum were accumulating on the surface of the outer nuclear membrane. This debris often obscured observations of the outer nuclear membrane and the nuclear pores. When the pores could be observed it appeared that the electron dense material associated with them was more dense. As mentioned above, the number of condensed chromatin particles with the nucleoplasm was increased, and it was distributed more equally throughout the nucleus than seen in Figs. 5.14 through 5.16.

5.8.4. Glial Cells

Both the mitochondria and endoplasmic reticulum exhibited increased degrees of swelling and were responsible for the transparent vacuoles observed within the oligodendrocyte cytoplasm with LM. In most cases the swollen endoplasmic reticulum and the swollen mitochondria were distinguishable because most of the mitochondria were still double membrane bound (double arrowheads in Fig. 5.25) whereas the endoplasmic reticulum had a single deliminting membrane (arrowheads in Fig. 5.25). The ring form of the swollen mitochondria was not as prevalent in the glial cells as in the neurons and nonmyelinated structures. It was distinguished from the swollen endoplasmic reticulum because the reticulum still had some ribosomes attached to it.

The free ribosomal patterns were not completely absent in the glial cells. The denser staining of the oligodendrocyte cytoplasm made it difficult to see any cytoplasmic filaments other than the

microtubules. However, the oligodendrocytes and other glial cells showed a decrease in the population of filaments with diameters smaller than the microtubules, but no significant change in the population of microtubules.

No significant changes were observed in the nucleus of the glial cells. The cytoplasm of the oligodendrocytes was now less electron dense. Lysosomes remained unaffected with the exception of a small number that appeared less electron dense.

5.8.5. Blood Vessels

The membrane-bound, nonmyelinated structures surrounding the blood vessels had now swollen to the point where most had ruptured (Fig. 5.26). A true electron-transparent void now formed the cuff about the smaller vessels. Sub-cellular organelles, fragments of subcellular organelles, and membranous debris were observed in the cuff. The cytoplasm of the endothelial tissue was now less electron dense, and the subcellular organelles exhibited morphological changes similar to those described for the neurons and glial cells. Unlike the small capillary in Fig. 5.26, the larger blood vessels were not circumscribed by a cuff. Instead, there were transparent, bubble-like regions located at various points along the periphery of these vessels. The TEM observations demonstrated that these bubble structures were the result of ruptured, nonmyelinated structures showing damage similar to that seen in Fig. 5.26.

In Fig. 5.26 also note the wide range of altered states displayed by the mitochondria, nonmyelinated structures, and synapses in the tissue surrounding the blood vessel.

5.8.6. Nonmyelinated Structures

These structures exhibited increased degrees of swelling, and their internal organelles displayed the altered states described above for the neurons and mitochondria. The delimiting membranes of many of these structures showed the membrane degeneration described for the synapses, and shown in Fig. 5.22.

5.8.7. Myelinated Axons

More mitochondria within the myelinated axons exhibited the earliest stages of swelling that were described for stage 4. The asymmetry between the number of altered mitochondria and the degree of the alterations observed within the myelinated and nonmyelinated structures persisted.

5.9. Stage 6

If neurons were present within the tissue region under consideration it was an easy matter to score the tissue as stage 6 using LM. Between 25 - 100% of the neurons had shrunken and now stained a very dark, blue-purple color with the toluidine blue. It was difficult to distinguish the nucleus from the cytoplasm, for it too was shrunken and dark staining. The nucleolus did, however, stand out very clearly, as it appeared to stain almost black in color. Transparent vacuoles were observed in these cells, particularly along their perimeter. Other dark staining structures besides the neuron cell bodies were also present in the tissue. Serial sectioning demonstrated that these were dendrites and dendritic thorns from the shrunken neurons.

Transparent voids larger than 2 - 3 μm were easily observed with LM in the stage 6 tissue. Such voids were most prominent in

the GM and GWGM and absent in WM. Electron microscopy revealed a grainy texture to the substance within many of these voids, and the presence of amorphous, membranous debris.

The axoplasm and its contents very distinctly displayed signs of altered morphology. A significant fraction (10% - 75%) of the mitochondria within these axons exhibited the range of altered states described in stage 4. The axoplasm itself appeared less dense with both TEM and LM observation. Microtubules and intermediate filaments were more widely spaced from one another. This observation, together with the decreased density of the axoplasm, strongly suggested that the axons themselves were swelling.

5.9.1. Synapses

The wide range of altered states observed within the synaptic population is illustrated in Fig. 5.27. Note that when the synapses occurred along the perimeter of the transparent voids (double arrowheads) their synaptic membranes often bulged into these voids, and that the membrane at such points displayed the degeneration described in state 5 and pictured in Fig. 5.22.

5.9.2. Mitochondria

Figure 5.27 also shows that the mitochondria exhibited a wide range of altered states throughout the population, from the near normal appearing mitochondria (0) to the very swollen (3 and 4).

5.9.3. Neurons

A shrunken neuron is illustrated in Fig. 5.28. The electron density of both the cytoplasm and the nucleoplasm is markedly

increased over that presented in Figs. 5.14 - 5.16 and 5.14, and the nucleolus is also very electron dense. The transparent regions observed in these cells with LM were clearly the more swollen segments of the endoplasmic reticulum and the swollen mitochondria. There is also a preponderance of smaller, electron transparent, membrane-bound vesicles, v, along the shrunken cells' perimeter. The origin of these vesicles could not be determined. From the morphological point of view, the lysosomes remained unaltered.

The origin of the electron transparent space that surrounds much of the neuron in Fig. 5.28 can only be speculated upon. Some, if not most of the space, is volume that was formally occupied by the neuron cell body. When the cell contracted, this volume was left unoccupied and hence, electron transparent. Electron dense trailers, or threads of the neuron run from the shrunken cell to the outer perimeter of the transparent space in support of the contention that the cell formerly occupied this space (arrowheads). Some of these trailers appear to be stressing the membrane-bound structures along the perimeter of the transparent space to which they are still attached, *. The presence of mitochondria and other ultrastructural features indicates that such structures were indeed separate membrane-bound regions and not just space encircled by membranous fingers spreading out from the neuronal trailers. Perhaps the force exerted by the contracting cell ruptured some of the surrounding, membrane-bound structures releasing their contents into the newly vacated volume.

5.9.4. Glial Cells

No shrinking of the glial cells similar to that described for the neurons was observed. Instead, a slight increase in the cells' swelling was noted.

5.9.5. Voids

Large, transparent voids were observed within the tissue, as shown in Fig. 5.27. These were most prevalent in the GM and GWGM tissue and completely absent in the WM. Many of these voids were truly transparent even at the TEM level, and just contained fragments of membranous debris (V in Fig. 5.27). Others had a mottled appearance to their interiors, along with the debris. Both types of voids were also observed within the transparent regions surrounding the shrunken neurons (Fig. 5.28). It is likely that the voids with the mottled interiors resulted when the shrinking force of the cell ruptured some of the surrounding nonmyelinated structures, and the lightly staining background material and the debris are, respectively, the remnants from the interiors and membranes of these structures. Also the presence of subcellular organelles such as mitochondria and synaptic vesicles would be explained by such a mechanism. Serial sectioning showed that many of the voids like those observed in Fig. 5.27 were indeed cross sections of the transparent space surrounding a shrunken neuron taken through a plane that did not contain the cell body.

Another possible origin for the voids would be the superswelling of dendrites of nonmyelinated axons. Although many of the neurons were shrunken in the stage 6 tissue, there were

some neurons that were even more swollen than in stage 3 - 6. Perhaps the cell bodies for such swollen neuron-related structures were located in another portion of the irradiated volume that was scored as an earlier stage in the sequence, hence the neurons had not yet begun to exhibit signs of necrosis.

5.9.6 Nonmyelinated Structures

The electron density of the cytoplasm within the nonmyelinated structures ranged from being very electron transparent for the most swollen synapses, dendrites and axons, to very electron dense for those dendrites and dendritic thorns associated with the shrunken neurons (Figs. 5.27, 5.28 and 5.29). The variety of the electron density observed was likely related to the varied degrees of collapse observed for the neurons. The more collapsed the neuron, the darker the cytoplasm of the associated cell processes. The cytoplasm of nonmyelinated axons and synapses never exhibited the increased electron density displayed by some of the dendritic processes (Fig. 5.29.).

Unlike the more electron dense neuron cell bodies, which appeared shrunken, and lost contact with the surrounding tissue structures, the smaller dendritic thorns still maintained contact with their adjacent tissue structures even though they appeared markedly more electron dense, Fig. 5.29. There are several possible explanations for this phenomenon. Perhaps, as the cell body collapsed some of the cytoplasm, now more electron dense, was forced into some of the dendrites and dendritic thorns. This prevented them from shrinking and also would explain their increased electron density. Another explanation lies in the fact

that the dendrites and dendritic thorns branched out profusely from the neuron cell body. As the cell body contracted, the force of contraction could not dislodge the dendrites and thorns from their adjacent structures. In this instance, the outlying dendrites and thorns might even become pinched off from the cell body. Before such a pinching-off could occur, some of the more electron dense cytoplasm from the shrinking neuron could be perfused through these structures.

This neuron necrosis resulting in darker staining neurons and neuron processes was also observed by Barnard et al [1956], and was used as a tool for quantitatively mapping the extent of the neuronal process of neurons located within the mammillary nuclei of the cat brain by W. J. Fry et al. [1964]. They centered the focal volume within this region of the brain and the exposure was chosen such that the neurons became necrotic. Serial sectioning through this volume and the surrounding tissue demonstrated the distribution and extent of the neuronal processes from the necrotic neurons as they would now stain darker than the surrounding material. Such serial sectioning was used to trace back and locate the neuron from which the thorns in Fig. 5.29 originated. When stage 6 damage was present somewhere within the lesion volume, the electron dense thorns and dendrites were observed in tissue regions exhibiting a lesser degree of damage since these appendages from the shrunken reurons extended beyond the stage 6 tissue.

The thorns in Fig. 5.29 exhibited the membrane-bound, electron transparent vacuoles so commonly observed along the perimeter of shrunken neurons (Fig. 5.28) and within their

dendrites and thorns. It was not possible to determine their origin, which may have been as remnants of the endoplasmic reticulum. If so, it is not known why they were so uniform in size and located predominantly along the cells' perimeter. Perhaps they were secretion vesicles from the golgi trying to release built up toxins or waste. On the other hand, they may have been pinocytotic vesicles trying to bring in essential nutrients or other substances in an attempt to save a dying cell.

5.9.7. Myelinated Axons

The axoplasm of many axons was now slightly less electron dense, and the spacing between adjacent microtubules and neurofilaments appeared greater (Fig. 5.30). In many of the axons, the microtubules and neurofilaments no longer paralleled each other along the axons axis, but displayed a more disordered and random arrangement. A significant fraction (greater than (10 - 50%) of the mitochondria now exhibited swollen morphology like that described for the nonmyelinated structures in stage 4. The degree of damage sometimes exceeded that displayed by the mitochondrion labeled 4 in Fig. 5.18, but no ring-like structures such as those in Fig. 5.23 were observed.

Curiously, the degree of demyelination had not increased over that observed in stage 5, which now appeared to be less apparent in the smaller axons. It is likely that the decreased electron density of the axoplasm and the disarray of the microtubules and neurofilaments were indicative of axonal swelling. As the axons swelled they would then put stress on their surrounding myelin sheath and hence tighten up some of the looseness resulting from

demyelination. Because any volume increase due to swelling would be a more significant fraction of the smaller axons' volume than that of the larger axons, any tightening up of previously unraveled myelin would be more noticeable in the smaller axons.

5.10. Stage 7

The tissue was now markedly lighter staining when observed with LM, and transparent regions were observed between many of the tissue structures. The same tissue also had a bleached-out appearance when observed with TEM. Because of the spaces between the membrane-bound structures it was apparent that fluid was accumulating within portions of the irradiated volume. The staining density of the myelin sheaths remained unaltered, and so the sharp contrast between the dense staining myelin and the electron transparent regions separating the axons made this effect most pronounced in the WWGM and WM. In the GM and GWGM, the interstructural swelling tended to isolate clusters of membrane-bound structures from one another making the tissue appear like the lake filled with numerous, various sized, closely spaced islands. Swelling was still clearly observed within the membrane-bound structures themselves, and as before, this swelling was more pronounced in the nonmyelinated structures.

The mitochondria within the myelinated axons now displayed the full range of altered stages described earlier for the nonmyelinated structures. A greater percentage of these mitochondria displayed these altered states, and only 10 - 30% presented the normal morphology. The axoplasm appeared less electron dense and there was a marked reduction in the number of

neurofilaments. The number of microtubules within the axons was also less, and, probably due to the swelling, the microtubules were spaced further apart from one another. It was also noted that many of the microtubules themselves appeared more diffuse and less electron dense.

There was a wide range in the degree to which the different axons were demyelinated within the WM, WWGM and WGM. Some axons had myelin sheaths that were still tightly wound about the axons, showing no signs of demyelination. Others appeared as almost bare axons surrounded by a diffuse cloud of myelin. The degree of demyelination did not always coincide with the degree of the altered morphology within an axon. There were severely demyelinated axons that showed very little swelling of the contents, while others that had unaltered myelin sheaths contained markedly swollen mitochondria and electron transparent axoplasm. Frequently, serial sectioning revealed positions along the length of such axons where the demyelination was more substantial. However, just as often no such demyelination was observed.

The membranes of more nonmyelinated structures exhibited the diffuse, degenerative state described earlier. There was an increase in the amount of membranous debris within the spaces between the membrane-bound structures, together with an increase in the observed number of membrane-bound voids. This was accompanied by a concomitant decrease in the number of nonmyelinated structures that could be identified positively as synapses, axons, etc. Many of the nonidentifiable, membranous structures also exhibited the degenerative membrane morphology observed in the membranes of the identifiable, membrane-bound

structures. The voids were larger than the swollen mitochondria and probably were the remains of very swollen, nonmyelinated structures such as synapses and dendritic thorns. Some of these voids indeed had electron dense material where two such structures came into opposition. This density may have been the remains of a synapse's junctional density, implicating a synaptic origin for these structures. Synaptic vesicles were rarely observed in such structures, but when present they did confirm a synapse origin.

Further swelling was observed in the glial cells, and the degree of damage to the subcellular organelles was similar to that described for the neurons in stage 5. The number of collapsed neurons was increased over that observed in stage 6, and only 0 - 30% of the neurons were not collapsed. At this stage there were no unaltered neurons or glial cells.

The blood vessel cuffing became more extensive and pronounced, and many vessels, including some of the larger ones, were now completely surrounded by a transparent cuff which frequently contained membranous debris and fragments of membranous structures. The endothelial cells were very light staining when observed with both LM and TEM, and TEM revealed damage to the subcellular structures similar to that observed in the neurons and glial cells in stage 5. Within irradiated volumes where the greatest degree of tissue damage was scored as stage 7, vessel cuffing was observed in surrounding tissue regions that were scored as stages 1 - 3. The degree of cuffing decreased with increasing distance from the point of greatest damage in the lesion. Since vessel cuffing was not observed in tissue scored as stages 1 - 3 unless the lesion contained some region exhibiting

stage 7 damage, it was assumed that the degree of blood vessel damage present at stage 7 somehow affected other portions of the altered blood vessels that traversed the lesser damaged regions of the lesion.

5.10.1. Synapses

There were no unaltered synapses but there were still some that exhibited only the earliest stages of altered morphology. Fewer structures recognizable as synapses were observed within the tissue. Because the increase in the number of small, membrane bound voids, whose delimiting membranes usually exhibited the degeneration discussed earlier, paralleled the decrease in the number of synapses and other nonmyelinted structures, it is believed that such voids were the remains of superswollen, nonmyelinated structures. This conjecture was made more plausible because two adjacent voids often had electron dense material at the point of closest approach. Although the material was less electron dense than the junctional densities observed at the earlier stages, it was likely that such structures were the remains of synapses. The very rare presence of a synaptic vesicle or two supported such an origin. In these structures the cleft distance was increased by 100 - 250% over that observed in the nonirradiated synapses.

5.10.2. Mitochondria

Fewer mitochondria, or objects identifiable as mitochondria, were observed within the nonmyelinated structures. Only a small fraction of the remaining mitochondria appeared unaltered, usually

less than 10 - 15% of the population, and most of the mitochondria exhibited the more advanced stages of swelling.

Mitochondrial damage was now more prevalent within the myelinated axons (Fig. 5.31), and only 10 - 30% of the population exhibited no indications of altered morphology. The ring-like structures were now also observed within the myelinated axons.

5.10.3. Nonmyelinated Structures

The large transparent voids present in stage 6 became larger and smaller, transparent regions developed between the nonmyelinated structures, were apparently the result of swelling induced by an accumulation of body fluids. Single membrane-bound voids, V (Fig. 5.31), were observed within these transparent regions. Their delimiting membranes were frequently irregular in shape and displayed the diffuse degenerative morphology described in stage 5. The remnants of swollen mitochondria and microtubules were sometimes observed within these voids suggesting that they were the final stages of swollen nonmyelinated axons, dendrites and dendritic thorns.

5.10.4. Neurons

No neurons within the tissue scored as stage 7 exhibited the normal morphology displayed by the nonirradiated neurons. Only 0 - 30% of the observed neurons were not in some stage of collapse.

5.10.5. Glial Cells

Swelling was more pronounced within both the cytoplasm and nucleoplasm of the glial cells (Fig. 5.30). It was only rarely

(less than 5% of the glial cells) that any glial cells showed signs of shrinkage and collapse.

5.10.6. Blood Vessels

Some of the blood vessels were now completely surrounded by a large transparent cuff, as shown in Fig. 5.32. Membranous debris and fragments of myelin were present within the cuff region. The endothelial cells forming the blood vessels stained much lighter than in the earlier stages. Swelling was observed in all of their subcellular organelles, including the lysosomes. Despite the massive internal damage, the endothelial cell membranes were not ruptured.

Minor cuffing was now observed in regions within the irradiated volume that were scored as stages 1 - 3 when they were located at greater radial distances from a region scored as stage 7. Serial LM sections demonstrated that the blood vessel cross sections seen within the stage 1 - 3 tissue were part of the same vessels present within the stage 7 tissue. It therefore appears that the degree of blood vessel damage present at stage 7 somehow affected the morphology and function of other portions of the damaged blood vessels that were present in tissue regions scored as stages 1 - 3. Blood vessel damage was never observed in tissue scored as these earlier stages unless stage 7 or greater damage was present within the irradiated volume.

5.10.7. Myelinated Axons

Figure 5.31 is a low magnification, electron micrograph of a white matter region scored as stage 7. The swelling of the interaxon space is evident and indicated by the asterisks. In

some places the fluid-filled regions contain an electron dense, granular substance which has no structure, as can be seen with the higher magnification of Fig. 5.33 (asterisk).

The wide range of altered states displayed by the mitochondria within the myelinated axons is illustrated in Fig. 5.31. There were still a small number of mitochondria that exhibited normal morphology, but this was never more than 30% of the observed population and usually less than 15%. The majority of the observed mitochondria were in various stages of swelling. Figure 5.33 shows a closeup of one such swollen mitochondrion. The matrix is electron transparent except for a few regions along the perimeter. Cristae are absent from the central region of the mitochondrion, although membranous debris, possibly arising from damaged cristae, was sometimes observed in the central region. The arrowheads in Fig. 5.33 indicate points where it is easy to see that the inner mitochondrial membrane and the cristae are continuous.

A comparison of Fig. 5.31 with Fig. 5.1 clearly shows a decreased electron density of the axoplasm within most of the axons in Fig. 5.31. In general, the axoplasm of the axons in Fig. 5.30 have a more mottled appearance. There is also a drastic decrease in the number of neurofilaments and a less substantial decrease in the population of microtubules, while the remaining microtubules in Fig. 5.31 appear less electron dense and more diffuse. The more swollen mitochondria were found within the axons that displayed the more electron transparent axoplasms.

5.11. Stage 8

No structures exhibited normal morphology in any of the tissue scored as stage 8 (Fig. 5.34). The interstructure swelling described in stage 7 became more pronounced and with LM, the stage 8 tissue resembled the more damaged sections of Fig. 4.3.

Many of the nonmyelinated structures in the GM and GWGM were swollen beyond the point where the nature of the structure could be identified. Other nonmyelinated structures were shrunken and electron dense. Identification of the nature of individual structures was difficult or impossible in this contracted state.

In all tissue types the axoplasm of the myelinated axons exhibited an even further decrease in its electron density, but still had a mottled texture. No neurofilaments could be observed in 50 - 100% of the axons. Microtubules were still present, but in markedly reduced numbers. The myelin sheath was now demyelinating such that some of the unfolding myelin projected inward towards the center of the axon whereas the unfolded myelin always expanded away from the axon in all earlier stages.

In the WM, WWGM, and WGM most of the nonmyelinated structures were more swollen than the myelinated axons. The only exceptions were the small dendrites and dendritic thorns which were identifiable because their cytoplasms were electron dense. The remaining nonmyelinated structures were present as electron transparent, membrane-bound voids, many of which contained the single, membrane-bound ring form of swollen mitochondria.

5.11.1. Nonmyelinated Structures

No nonmyelinated structures displayed normal morphology. In the WM, WWGM, and GWM most of the myelinated structures were now so swollen that they appeared as electron transparent, single membrane-bound voids (Fig. 5.34). Such voids often contained severely swollen mitochondria, particularly the ring-like form. There were no mitochondria exhibiting the earliest stages of swelling. The only structures that could be identified positively were small dendrites and dendritic thorns because their cytoplasms still stained very electron dense.

The nonmyelinated structures in the GM and GWGM were of two forms. Most were swollen like those in the WM, WWGM and GWM. The remainder were electron dense. It is likely that the electron dense structures were the remains of dendrites, dendritic thorns and synapses that were directly associated with collapsed neurons.

5.11.2. Glial Cells

The plasma membranes on some of the glial cells had ruptured, but the nuclear membranes remained intact. Less than 5% of the observed glial cells were shrunken while the remainder appeared very swollen and turgid.

5.11.3. Myelinated Axons

Figure 5.34 shows a further decrease in the electron density of the axoplasms. They still displayed the mottled texture described in stage 7, but it was now less distinct. No neurofilaments were observed within 50 - 100% of the axons. Some of the electron dense material giving the axoplasm its mottled appearance had a filament-like texture and may have been the

remnants of disassociated or swollen neurofilaments. Microtubules were still observed within many axons, but in further reduced numbers. Most of the remaining microtubules had low electron densities.

In the earlier stages of the temporal sequence, the demyelinated portions of the myelin sheath always unfurled outward from the axon. Now, some of the demyelinated sheath projected in towards the axon and distorted the biological membrane of the axon itself (Fig. 5.34).

The interstructure swelling was markedly increased over that in stage 7. In many WM, WWGM and WGM regions, the interstructure space had a mottled appearance similar to that of the axons (Fig. 5.34). The electron transparent material was somewhat less dense than its counterpart in the axons and had a finer texture. The origin of this electron dense material was unknown.

Mitochondria within the axons still exhibited a range of altered states, but none were normal. Fewer mitochondria were observed, and the remaining population was further shifted towards the more damaged states. There were still mitochondria exhibiting early stages of swelling while these earlier stages were absent in mitochondria within the nonmyelinated structures.

5.12. Stage 9

The LM appearance of tissue at this stage was similar to that illustrated within the lesion in Fig. 4.4. Both Figs. 4.4 and 5.35 have large transparent regions between the tissue structures, which were most certainly occupied by body fluids, and as discussed in Chapter 4, the increased fluid content of the lesion

volume was considered responsible for a decrease in the measured absorption coefficient for the tissue.

In GM, GWGM, and WGM the only recognizable structures were the myelinated axons, neurons and glial cells. All of the neurons were collapsed, and the plasma membrane and nucleus of every glial cell in all stage 9 tissue was ruptured, and appeared similar to the glial cells in Fig. 5.35.

In the WGM, WWGM, and WM the myelinated axons were the most prominent structures (Fig. 5.35). The myelin sheaths displayed varying degrees of demyelination, including the inward demyelination discussed in stage 8. The axoplasms all had the mottled texture described in stage 8, and no neurofilaments were observed. Only a small number of microtubules were still present, all of which were diffuse and had a low electron density.

The total number of mitochondria observed in the stage 9 tissue was further reduced and there were only 10 - 30% of the mitochondrial numbers observed in the nonirradiated tissues. A small fraction of the remaining mitochondria still displayed the earliest stages of mitochondria swelling, but most of them exhibited the latter stages of swelling and the ring morphology.

Lysosomes now began to show signs of altered morphology. Their membranes still appeared intact, but their contents were noticeable less electron dense (arrowheads in Fig. 5.35).

5.13. Friable Tissue

Ultrasonic exposures of 3.5 sec and longer usually rendered the tissue at the lesion center friable. This tissue was difficult to handle as it often crumbled when the tissue disks

were being cut from the main cores for TEM processing. The tissue was most susceptible to crumbling after it had been post fixed with the 1% osmium tetroxide solution. Once the friable tissue had been embedded it was more difficult to section than the other tissues. The resultant sections frequently had knife and chatter marks. These could be reduced by slowing the cutting speed, but they could not be eliminated completely. The friable tissue took the toluidine blue stain as well as any of the other tissue but required longer staining periods with the uranyl acetate and lead citrate. Increasing the staining times in both these stains by 50 - 100% resulted in well stained sections.

When examined with LM and magnifications less than 200X, the friable tissue resembled the nonirradiated tissue with respect to morphological appearance and staining density. With LM magnifications of 400X or more, the friable tissue showed a grainy or ricey texture. The morphologic features such as cells and myelinated axons could still be discerned, but their borders were not sharp. It appeared that the tissue was slightly out of focus, even when the microscope focus was properly adjusted.

When examined with TEM the abnormalities of the tissue became more apparent, particularly in the WM. The nucleus and cytoplasm of the oligodendrocyte in Fig. 5.36 are clearly discernible, but neither shows much internal detail. The nuclear membranes appear as dark lines separating the nucleus and the cytoplasm, and small, dark bodies, probably mitochondria, can just be distinguished within the cytoplasm. An arrowhead indicates a lysosome which is identifiable by the electron transparent band across the otherwise electron dense organelle. No endoplasmic reticulum, golgi, etc.,

could be distinguished. The myelin sheaths appeared swollen and now stained lighter than the axons which were collapsed and electron dense. Also, the multilayered nature of the myelin was masked by the swelling and was only barely evident even at the higher magnifications. More subcellular structures could be distinguished in the friable GM, particularly within the neurons, probably because the nucleoplasm and cytoplasm of the neurons stained much lighter than those of the oligodendrocytes. Small pieces of mouse brain tissue that were heated for several seconds in 60^{o}C physiological saline displayed morphology similar to that observed in the friable tissue and also had a friable texture. This supports the view that the friable tissue was heat fixed by the ultrasonic exposure.

5.14. The 0.42 Sec Threshold Exposure

The shortest exposure with the 300 W/cm^2 intensity ultrasound that produced observable changes in the tissue ultrastructure was 0.42 sec. Only WWGM and WM tissue sites responded to this exposure, and a 24 hr post irradiation period was required before the tissue damage could be observed, as seen in Fig. 5.37. The damage was scored as stage 1 even though a few swollen mitochondria were present. The most prominent damage was the vesicle clumping in the presynaptic elements and the presence of membranous debris within some nonmyelinated structures. Demyelination was also observed but it was scarcely more prominent and prevelent than in the nonirradiated tissue. This would have made the determination of stage 1 damage questionable in the WM site were it not for the presence of a small number of synapses.

5.15. Tabulation of the Temporal Development of the Tissue Morphology in the Ultrasonically Irradiated Cat Brains

The only report that has related the temporal development of ultrasonically-induced morphological changes to the ultrasonic dosage was that of Barnard et. al. [1956] where in LM was employed. Their experimental tissue was also the adult female cat brain, and they used focused ultrasound with SPTA acoustic intensities between 730 - 870 W/cm^2 with exposure times of 1.0 - 3.0 sec. Using these intensities in Equation 1.3, the exposure times used by Barnard et al. [1956] were 13 - 33 times longer than the threshold exposure times. The longest exposures used in this present study (4 - 5 sec) were 9 - 11 times longer than the threshold exposure time for 300 W/cm^2 as calculated by Equation 1.3, while the majority of the exposures used were less than 3 - 5 times longer than this threshold value. Consequently, the lesions presented by Barnard et al. [1956] were very severe in comparison to those produced for this present study. By their standards, the lesion presented in Fig. 4.4 would be classified as light, and those lesions exhibiting the island-moat effect would be classified as moderate. Only those lesions resulting from exposures in excess of 4.5 sec would be classified as severe, while most of the lesions observed in this study would not have been classified as lesions by Barnard et al. since an electron microscope was required to observe the altered tissue morphology.

Table 5.1 illustrates the temporal development of the ultrasonically-induced tissue damage observed in the cat brains as a function of exposure time and the WM and GM content of the tissue. The data are representative of the variations in the

degree of damage induced by the various exposure times, the effect of the WM and GM content of the irradiated tissue volume on the degree of damage and the rate at which the tissue progressed through the temporal sequence, together with the variations observed in the lesion development among identically irradiated animals. The scoring system of stages 1 - 9 as described above is used to indicate the degree of damage present within the irrdiated tissue. Since the degree of tissue damage depended upon its position within the focal volume, the damage scored in Table 5.1 is that observed at the position of the focal point.

For many of the animals of this study, the focal point was located at an interface between a region of WM and GM permitting altered morphology to be studied in tissue structures that were found in both the WM and GM. Also, the relative responses of the WM and GM to a given acoustic exposure could be studied simultaneously. Within 2 - 7 min post irradiation the tissue on the WM side of the WGM border usually exhibited damage that was scored as 0 - 1 stage more severe than the WGM, while the GM side of the border was 0 - 1 stages less severe. With longer post irradiation times the WM side exhibited 1 - 2 stages (and occasionally 3 - 4 stages) more severe damage than at the interface. The variations were due to the amount of WM and GM on either side of the interface and the dimensions of the transition zone between the WM and GM.

The left most column in Table 5.1 lists the specimen number of the cat (1 - 38) from which the data in that row is being taken. The next four columns are labeled 1 - 4 repesenting the irradiated site number in the given animals from which the data in

that column is taken. When more than four irradiated sites were placed in a given animal, the subsequent row will be used to report the data from sites 5 - n which will fall under the columns 1 - 4 in that second row. The data for each irradiated site will be reported in the manner illustrated by the following sample entry;

exposure time (sec); post irradiation time (h.min)
tissue type (WM, GM, etc.), peak temperature (^{o}C)

The peak temperatures reported are not those recorded within these irradiated sites, but are the values taken from Table 4.4.

CHAPTER 6

HIGH VOLTAGE ELECTRON MICROSCOPY OBSERVATIONS OF THE NONIRRADIATED AND IRRADIATED CAT BRAIN TISSUE

A request was made to study the ultrasonically-induced morphological changes in the chemical synapses of the cat brain, and three days of observation time were granted on the AEIEM-7 high voltage electron microscope, HVEM, at the University of Wisconsin, Madison campus. Most of the observation time was spent in becoming familiar with the operation of the AEIEM-7, and in studying the morphology of normal and irradiated synapses. Major emphasis was placed on studying both the pre- and postsynaptic elements to determine if any changes in the cytoskeletal morphology accompanied the shift towards more flat and positively curved synaptic junctions within the population of ultrasonically altered synapses.

Figure 6.1 is a stereo electron micrograph of a synapse from the nonirradiated tissue. The presynaptic element is filled with synaptic vesicles which obscure most other morphological features. A mitochondrion is visible within the presynaptic element and, between the vesicles, a gray, mottled background material can be seen throughout the presynaptic element. The postsynaptic element also contains mottled gray material that has a somewhat filamentous look about it. It is very probable that it is this material that gives the synaptic elements' cytoplasm their mottled appearance as observed in the ultrathin sections using a standard TEM (Section 5.1.2). The ultrathin sections were too thin for showing anything other than the mottled pattern of mildly electron

dense material. The sections used for HVEM were 10 - 20 times thicker than those used for TEM. This demonstrated that the electron dense material pervaded both synaptic elements and that it had an appearance suggesting a filamentous nature.

A synapse from a WGM region scored as stage 2 (cat #16, site 1) is presented in Fig. 6.2. The presynaptic element shows the reduction of synaptic vesicles and the aggregation of the remaining vesicles described in Chapter 5. Just as noted in the TEM observations, an electron dense material is associated with the aggregated vesicles. This material appears identical in nature to the electron dense material observed throughout the entire presynaptic element of Fig. 6.1. Here it is found almost entirely within the synaptic vesicle aggregates. Strands of materials, St, are seen coursing from the walls of the presynaptic element to the vesicle aggregate at the cleft, which is the largest aggregate in this figure. Most of the electron dense material is associated with the cleft vesicle aggregate and has a very filamentous appearance which may be the remmants of the presynaptic element's cytoskeleton which became enmeshed with the vesicles when the aggregates formed. Alternatively, it may have been that the ultrasound altered the synapse in a manner that forced a contracture of the presynaptic element cytoskeleton which enmeshed the synaptic vesicles and gathered them into the aggregates. Aside from the vesicle aggregates, a few filaments, and some membranous debris, the presynaptic element in Fig. 6.2 is devoid of material and is very electron transparent. The junction curvature is very positive and, just as in the sections

examined with TEM, over 95% of the junctions of the altered synapses were either positively curved or flat.

There are no significant differences between the morphology of the postsynaptic elements in Figs. 6.1 and 6.2, which is in agreement with the observations described in Chapter 5 where altered morphology was not observed in the postsynaptic elements until stage 3 or 4. Gulley and Reese [1981] suggested that the cytoskeleton within the synaptic elements was responsible for maintaining or changing the synaptic curvature, and their data suggested that the postsynaptic element cytoskleton performed this function. The data presented in this chapter demonstrates clearly that a shift in the distribution of synaptic curvatures occurred in the absence of any discernible changes in the cytoskeleton of the postsynaptic element.

Altered morphology was initially observed only within the presynaptic elements Comparisons between the cytoskeleton in the normal and altered presynaptic elements could not be made because of the obscuring effect of the synaptic vesicles in the normal, presynaptic elements. Studies of the cytoskelton in cultured cells [Ris, 1980; Heuser and Kirschner, 1980; Wolosewick and Porter, 1976] and intact tissues [Hirokawa, 1982] indicate that the cytoskeleton pervades the cell and cellular processes. Assuming this is also true for the presynaptic elements, the cytoskeleton in the altered synapses somehow became disrupted and or condensed, implying that an intact, cytoskeleton in the presynaptic element is required for the synaptic cleft to attain and maintain a negative curvature.

CHAPTER 7

NEONATAL MOUSE IRRADIATIONS: RESULTS

A brief summary of recently obtained threshold data for ultrasonically-induced hind limb paralysis in neonatal mice, together with the harmonic analysis of the acoustic energy within the irradiation chamber is presented herein to indicate how the ultrasonic exposures used for the morphology study related to the various threshold level exposures, and whether or not static pressure-induced changes in the harmonic content of the measured acoustic energy were accompanied by changes in the nature of the observed ultrasonically-induced tissue damage. As in the earlier studies of W. J. Fry and Dunn [1956], Frizzell et al. [1983] obtained a sigmoid curve, for each acoustic intensity used when the incidence of paralysis among the irradiated mice was plotted versus the inverse of the exposure time (Fig. 7.1). Table 7.1 lists the exposure times resulting in a 10%, 50%, and 90% paralysis incidence rate among the irradiated animals, respectively t_{10}, t_{50}, and t_{90}, for each of the acoustic intensities used.

The signal levels for the subharmonic and superharmonic frequencies, together with the anahrmonic noise levels of the acoustic energy within the irradiation chamber, recorded at atmospheric pressure, are presented in Tables 7.2 and 7.3. Measurements were made within the irradiation chamber both with and without the mouse in its holder. Table 7.2 shows that the half harmonic amplitude recorded in the irradiation chamber was 12 - 26 dB greater when the specimen was present. The data in

Table 7.3 indicate that the difference between the second and third harmonic amplitude levels, with and without the specimen present, decreased with increasing intensity. The broadband noise level increased with intensity, with the exception of the 289 W/cm^2 irradiations.

The narrowband 0.5 MHz monitor observations of the subharmonic and anharmonic signal levels were barely detectable at 16 atm. Pressurizing the irradiation chamber reduced the subharmonic signal by 30 - 40 dB for all the acoustic intensities. Measurements were not made with the broadband monitor at 16 atm for fear of damaging the transducer. Also, the t_{90} threshold exposure time at 289 W/cm^2 was increased by a factor of 4.16, to 1.54 sec.

Irradiated specimens were routinely tested for paralysis 4 min post irradiation, to provide data for the threshold curves, after which the animals were sacrificed. Mice used for the morphology study were frequently maintained alive beyond this 4 min test time in order to examine the manner in which the ultrasonically-induced morphological changes developed as a function of increasing post irradiation time, and were tested a second time for paralysis just prior to being sacrificed. As a result of this protocol, it was discovered that some of the initially paralyzed animals recovered hind limb function. This recovery was not instantaneous. The recovering mice initially responded sluggishly to the stimulating pinch, and hind limb movement very gradually returned to normal. Recovery of hind limb function always occurred witin 25 min post irradiation. A plot of the exposure time and intensity parameters for producing 50%

reversible and irreversible paralysis at 1 atm is presented in Fig. 7.2.

The phenomenon of reversible paralysis has been studied most extensively in the mice irradiated with 289 W/cm^2. At this intensity the t_{10}, t_{50}, and t_{90} exposure times listed in Table 7.1 always resulted in some percentage of the initially paralyzed mice recovering hind limb function after 4 min post irradiation. It was obvious that the incidence of reversible paralysis decreased with increasing exposure time. Many of the mice irradiated with 289 W/cm^2 were retested 25 min post irradiation to determine the exposure times required to produce 10%, 50%, and 90% irreversible paralysis, viz., t'_{10}, t'_{50}, and t'_{90}, and the results were t_{10}" = 0.27, t'_{50} = 0.33, and t'_{90} = 0.43 sec.

Some of the paralyzed mice were able to sense the stimulating pinch, and responded by emitting a vocal squeeking sound and/or by moving their forelimbs. Other paralyzed mice did not respond in any way indicating that the stimulating pinch was sensed. This observation raised the possibility of a mouse being classified as paralyzed as a result of not responding to the stimulus because of neuro-sensory and not neuro-motor damage. This possibility was eliminated by two observations. Control mice demonstrated spontaneous, unprovoked movements of both their hind and forlimbs. Also, pinching the animals' forelimbs resulted in their rapidly moving both sets of limbs in response to the stimulus. Both sham irradiated and irradiated, non-paralyzed animals exhibited identical spontaneous limb movements and responses to forelimb stimulation. Irradiated mice classified as paralyzed exhibited spontaneous forelimb movement, but not hind limb movement. It was

therefore concluded that hind limb paralysis can occur in the absence of sensory loss, while the opposite does not occur.

It was observed that the concomitant incidence of sensory loss in the paralyzed animals depended upon the acoustic intensity and exposure times used. Animals chosen for the morphology study, which were paralyzed with 289 W/cm^2 and exposure times of t'_{90} and shorter, never exhibited sensory loss. Approximately 60% of the paralyzed animals exposed to 192 W/cm^2 for t_{90} experienced sensory loss. The incidence was much lower for t_{50} exposures and never observed following t_{10} exposures. Most animals paralyzed with t_{50} and t_{90} exposures using acoustic intensities lower than 192 W/cm^2 experienced sensory loss, while no sensory loss was observed following the t_{10} exposures.

7.1. Observations of the Control and Sham Irradiated Spinal Cord Tissue

An entire epoxy-embedded, transverse section of sham irradiated spinal cord is shown in Fig. 7.3a. The large, dorsal and ventral blood vessels were sometimes absent from such sections (as illustrated in Fig. 7.3a), but sections containing one or both vessels were frequently encountered. Dark staining cells clearly delineate the spinal canal, Sc, and since this structure lies closer to the ventral border of the spinal cord it was useful in orientating the sections properly. There were two distinct tissue regions in the spinal cords, as seen in Figs. 7.3a,b. The thin band of tissue along the perimeter of the spinal cord corresponded to the white matter in the adult spinal cords, and the central region corresponded to the gray matter. Although

myelination of the axons had not yet begun, the classic H-shaped region of gray matter was distinguishable from the surrounding peripheral tissue.

The peripheral band of tissue in each section contained far fewer cell bodies than the gray matter regions. A series of dark staining cells was commonly observed along the sections' perimeter (7.3a, b). The higher magnification in Fig. 7.3b reveals a thin membrane interconnecting these cells, finger-like projections of which frequently invaded the peripheral tissue region, together with some of the dark staining cells. When the membrane and dark cells were missing or detached from portions of a spinal cord sections (Fig. 7.3a) the morphological appearance of the underlying tissue was unaffected.

A variety of cell bodies were observed within the gray matter regions. It has been suggested that the largest cells in the ventral half of the sections were most likely the motoneurons [Pappas, 1982; Wehenmeyer, 1982; Ralston, 1983], some of which may regulate hind limb function. A positive identification of those motoneurons innervating the hind limb muscles could not be made using the data from this study. One future approach towards making such an identification would be to inject horseradish peroxidase into the hind limb muscles, which would then enter the neuronal axons via the neuromusclar junctions, migrate to the neuronal perikaryon, and hence positively identify the motoneurons innervating these muscles by rendering their cytoplasms electron dense [Ralston, 1983].

Electron microscopy revealed a large number of nonmyelinated axons, Ax, in the peripheral regions of the spinal cord (Figs.

7.4 and 7.5). The axoplasm had a mottled appearance and contained microtubules, Mt, smaller diameter, filamentous structures that were most likely neurofilaments, nf, and mitochondria, m. The axons exhibited a wide range of dimensions, and essentially every axon appeared in cross section within these transverse spinal cord sections, as evidenced by their circular shapes and the circular shapes of the microtubule and neurofilament cross sections within them. Few longitudinal axonal sections appeared in this region of the spinal cord.

Although the axons themselves were not myelinated, myelin-like structures, MyL, were commonly observed amongst them (Fig. 7.4). Serial sectioning did not demonstrate an association of these myelin-like structures with any cell such as an oligodendrocyte or Schwann cell that resembled myelin. Hence, it could not be determined whether or not these sructures represented the beginnings of axon myelination or were simply electron dense, membranous debris.

Large, membrane-bound, often irregularly shaped regions were observed among the axons (Figs. 7.4 and 7.5), most of which were probably dendrites and dendritic thorns from the neuronal cells in the GM portion of the spinal cord. Other cells besides the neurons had dendrite-like processes, including some of the glial cells and the cells associated with the membranes that surrounded the spinal cord. Since the distinction between the different cellular processes was not easily made in the peripheral tissue; all such structures in this region of the spinal cord are referred to as dendrite-like structures, DyL. Although not universally true, the mitochondria in such structures often possessed less

electron dense matrices than the axonal mitochondria. Synapses were also observed in this region of the spinal cord (Fig. 7.5). The electron density of the junctional density, Jd, varied significantly among the many synapses observed. There were also variations in the number, electron density, and distribution of the synaptic vesicles, Sv, observed within the presynaptic element, Pre, or bouton. The synaptic vesicles were less electron dense and distinct than those contained within the cat brain synapses.

The small nonmyelinated axons became less numerous as one moved radially in towards the central regions of the sections. Larger axons and other cellular processes, viz., synapses, dendrites, etc., became more prevalent, together with an increased number of cell bodies (Fig. 7.6). A variety of cells were observed within the gray matter regions of the spinal cords differing in size, shape, electron density, and the appearance and distribution of their subcellular organelles. The regions between the cell bodies were filled with synapses, nonmyelinated axons, dendrites, dendritic thorns, glial processes, etc., (Fig. 7.7), and was similar in appearance to the gray matter, GM, regions of the cat brain.

Using the electron micrographs and morphological descriptions of both spinal cord and brain tissue, prepared by Peters et al. [1976] as a guide, the cell bodies observed in the neonatal mouse spinal cord were separated into two classes, viz., neuronal and nonneuronal cells, with a good degree of confidence. The cells were not subclassified further as specific classification was not required for the purposes of this study.

Figure 7.8 shows a low magnification electron micrograph of several neuronal cells. Note the rounded nuclei with their homogeneously distributed chromatin and conspicuous nucleolus. The cytoplasm contains a large number of subcellular organnelles including mitochondria, golgi, and both rough and smooth endroplasmic reticulum. Nissel bodies which were so prominent in the cat brain neurons were less so in the spinal cord neurons. A higher magnification of the cytoplasm (Fig. 7.9) revealed numerous ribosomes both free and attached to the rough endoplasmic reticulum. Most of the free ribosomes were found in groups forming the distinct patterns of rosettes, lines and spirals as described by Peters et al. [1976].

A noneuronal cell, most likely a glial cell, is shown in Fig. 7.10. The nucleus is more irregular in shape than that of the neurons as is the cell body itself. The subcellular organelles in such cells were similar in nature to those found in the neurons, but were fewer in number and more sparsly distributed throughout a less electron dense cytoplasm. Fewer free ribosomes were observed in the nonneuronal cells, though those that were observed exhibited patterns similar to those found in the neuron (Fig. 7.11).

The control and sham irradiated tissues were indistinguishable at both the LM and TEM levels. Although the various membrane-bound structures were clearly delineated and partitioned from one another, close examination revealed that they were often discontinuous, as illustrated in Fig. 7.7. Such discontinuities were most likely the result of nonoptimal chemical fixation. In support of this conjecture, the membranes were better preserved in

the spinal cords fixed via the heart puncture perfusion, while diffusion fixed spinal cords that were not removed from the spinal column exhibited even less optimal preservation. Increasing the fixation time or aldehyde concentration made no improvement in membrane preservation. Ralston et al. [1982] improved membrane preservation in mammalian, fetal spinal cords by adding 4M sucrose to the buffered fixative. Attempts at adding this sucrose concentration to the fixative used herein improved membrane preservation, but resulted in shrinkage of the membrane bound structures. However, 1M sucrose reduced the shrinkage while enhancing membrane preservation. Further experimentation is required to determine the optimal fixative for preserving the ultrastructure in the neonatal mouse spinal cord. Because the present study was nearly completed before it became known that fixation improvements were possible, by using sucrose in the fixative, the histology and cytology discussed herein did not so benefit. The nonoptimal preservation, however, did not hinder structure identification or identification of ultrasonically induced morphological changes.

7.2. Observations of the Morphology in Ultrasonically Irradiated Spinal Cords

No ultrasonically-induced morphological changes were ever observed in the spinal cords of irradiated, nonparalyzed animals. The tissue obtained from these specimens was morphologically indistinguishable from that of the control and sham irradiated specimens. Tissue taken from reversibly paralyzed mice also lacked any abnormal morphology. No exposure conditions, viz.,

exposure time and intensity, were found to yield 100% reversible paralysis. Hence, the mice had first to recover hind limb function prior to being sacrificed before they could be positively identified as being reversibly paralyzed. It was noted that using ultrasonic exposures which yielded a higher percentage of reversibly paralyzed mice resulted in lower incidence of abnormal spinal cord morphology in specimens sacrificed within 25 min post irradiation. This evidence suggests that reversibly paralyzed mice did not have ultrasonically-induced morphological changes.

The spinal cord tissue from irreversibly paralyzed mice always exhibited some degree of ultrasonically induced morphological changes. The degree to which the tissue morphology was affected, together with the manner in which the altered morphology was distributed throughout the irradiated segment of the spinal cord, depended upon the acoustic intensity and exposure time used and the post irradiation time after which the specimen was sacrificed. However, the spinal cord tissue from two identically irradiated and sacrificed mice did not necessarily exhibit the same degree of ultrasonically induced morphological damage. This result was anticipated. As described earlier, any given ultrasonic exposure resulted in only a certain percentage of the irradiated mice becoming irreversibly paralyzed. The remainder were either nonparalyzed or reversibly paralyzed. As there was a range of functional effects among the identically treated mice, so too was there a range in the nature of the ultrasonically induced morphological changes. In identically treated specimens the morphological changes were clearly visible

with LM in some spinal cords while in others the higher resolution of TEM was required for detection.

Some general trends concerning the ultrasonic exposure parameters and post irradiation treatment of the specimens, and their effects on the resultant morphological changes induced in irreversibly paralyzed mice have been observed. Increasing the exposure time with a given acoustic intensity produced a greater degree of morphological alteration, a larger percentage of the irradiated mice exhibited the increased levels of tissue damage, and there was less diversity in the nature of the damage within the population of identically irradiated mice.

In each spinal cord the degree of tissue damage decreased in a gradual manner within those sections both anterior and posterior to that section containing the maximum degree of damage. Although the mice were positioned such that the acoustic beam would be centered on the third lumbar vertebra, the maximum damage was usually, but not always, found in this portion of the spinal cord. When the maximally damaged region was located within the second or fourth lumbar segment of the spinal cord, it was usually anticipated because a post irradiation examination of the mouse in its holder demonstrated that it had moved slightly in a direction parallel to the body axis, either prior to or during the irradiation. The direction of the animals displacement corresponded to that of the shift in the location of the maximally damaged spinal cord segment. There were, however, a few instances where such a shift in the tissue damage occurred in the absence of any perceptible specimen movement. It is possible that the

specimen moved during the irradiation, but then returned to its original position, and this event would go unnoticed.

There were instances where only one leg was paralyzed, and in all such cases, altered morphology was observed in only one half, i.e., the left or right half, of the spinal cord. Figures 7.12a,b illustrate an asymmetrical distribution of the ultrasonically-induced tissue damage. Although this particular section comes from an animal that had both legs paralyzed, and mild morphological changes can be seen in the right half of the section, this particular micrograph was used because it best illustrates asymmetrical damage distrubtion in a whole, transverse, spinal cord section. Marking the spinal cord sections for proper left, right orientation after sectioning was difficult and could not always be successfully accomplished. In those cases where the marking was successfully performed, the damaged side of the spinal cord, i.e., left or right half, was on the same side of the body as the paralized leg. Oftentimes, specimen movement perpendicular to the spinal axis was observed and could thus explain the single leg paralysis.

Unlike the cat brain experiments where mutliple ultrasonic exposures could be placed in a single animal and temporally spaced to study the development of the ultrasonically-induced morphological changes as a function of increasing post irradiation time, only one exposure could be placed in each individual mouse. Hence, any study of the temporal development in the ultrasonically-altered tissue morphology had to be made using different, but identically irradiated mice that were sacrificed at progressively later post irradiation times.

The distribution of altered morphology throughout the transverse spinal cord sections depended upon the acoustic intensity and exposure time, with the intensity having the more significant effect. Low magnification, light micrographs are best suited for illustrating the distribution of damaged tissue within the spinal cord sections. In order to illustrate clearly the affected region, sections exhibiting gross LM visible damage are presented, and exposure times of t_{90} or longer were used at each intensity. The micrographs presented were chosen because they are representative of the tissue damage distributions produced by the various acoustic intensities, even in those sections where TEM was required to visualize the morphological changes.

In every irradiated spinal cord taken from the irreversibly paralyzed mice, the tissue damage was greatest along the cord's perimeter, and was most prominent in the ventral-most portion of each section. The degree of damage decreased gradually along a radial direction towards the spinal cord center. The longer exposure times with each acoustic intensity resulted in a larger volume of each spinal cord exhibiting altered morphology. A quantitative value for the tissue volume damaged as a result of each dosage was not determined because of the variability in specimen response, as discussed above.

In every spinal cord from irreversibly paralyzed mice irradiated with 289 W/cm^2 using exposure times of t'_{90} and less, the tissue damage was restricted to the ventral half of the spinal cord (Figs. 7.13a, b), and every specimen was capable of sensing the stimulating pinch. The damage resulting from t_{10} exposures always required TEM to be observed, even following post

irradiation times in excess of 4 hr. Exposures of t_{90} and t'_{90} induced LM obserable damage within 0 - 30 min post irradiation in approximately 80% of the specimens. Frequently, the ventral, peripheral tissue receiving the longer exposures was friable, and portions of this tissue were absent from the sections (Figs. 7.13a, b). They crumbled away from the spinal cord during removal from the spinal column or processing of the tissue for TEM, particularly following osmium post fixation.

Exposures of t_{90}, or longer with acoustic intensities of 144 W/cm^2, or lower, induced tissue damage in both the dorsal and ventral halves of the spinal cords from over 90% of the irreversibly paralyzed mice (Figs. 7.14a, b). Damage was usually visible with LM between 0 - 40 min post irradiation. The entire perimeter of these sections was involved, and the specimens did not respond to the stimulating pinch. The remaining 10% or so of these mice exhibited damage in the ventral and lower dorsal portions of the spinal cord sections. No abnormalities were observed in the upper dorsal region of the sections and the mice responded to the stimulating pinch. Tissue along the perimeter was frequently friable, and some of the tissue was lost during processing, as was the case with the 289 W/cm^2 exposures. The t_{10} exposures resulted in tissue damage in only the ventral half of the spinal cords, and the animals responded to the stimulating pinch. Mild damage was observed with LM in some of these specimens within 1.5 - 3 hr post irradiation, but TEM was required in most cases.

The distribution of ultrasonically induced damage produced with 192 W/cm^2 exposures was intermediate between that described

for the 289 W/cm^2, and 144 W/cm^2 and lower intensities. Most of the animals exposed for t_{90} had the majority of the tissue damage within the ventral half of the spinal cord with some present along the perimeter in the lower portion of the dorsal half. No damage was present in the upper dorsal region and these mice responded to the stimulating pinch. Some of the t_{90} exposures, and a larger percentage of the t'_{90} exposures also induced damage along the dorsal perimeter, and these specimens did not respond to the stimulating pinch. The t_{10} exposures induced damage only in the ventral half of the spinal cord, and almost always required TEM to observe, except in a small number of animals sacrificed later than 1 hr post irradiation.

Increasing the exposure times slightly beyond t_{90} (or t'_{90}) often produced results similar to that presented in Fig. 7.15a. Here it appears that the dorsal half of the section is more damaged than the ventral half. Actually, the entire ventral half and a portion of the dorsal half was friable, as evidenced by the missing tissue in the lower right portion of the section. Although the friable tissue stained like control tissue and appeared similar to the control tissue at low LM magnifications, higher magnifications demonstrated that the friable tissue had a granular or ricey appearance (Fig. 7.15b). The electron microscope clearly demonstrated the abnormality of this friable tissue (Fig. 7.16). Small, electron dense blotches peppered the section, while the remainder of the tissue was electron transparent. Membranes were still discernable, but often appeared fragmented and distorted.

A further increase of the exposure time made the entire irradiated spinal cord segment friable, frequently to the point where it could not be removed from the spinal column without crumbling into tiny pieces. A 2.3 sec exposure with 289 W/cm^2, for example, reduced the irradiated segment to a state having a powder-like consistency.

The increase in the threshold exposures for each intensity produced by pressurizing the irradiation chamber was paralleled by a decrease in the degree of tissue damage induced by a given exposure. Also affected was the distribution of damage throughout the spinal cord sections, viz., the asymmetry between the damage in the dorsal and ventral halves of the spinal cords was less pronounced. Pressurization produced significant changes in the mice irradiated with 289 W/cm^2, viz., damage was now sometimes observed in the lower dorsal half of the sections following an exposure at the new t_{90}.

7.3 Ultrasonically-Induced Changes in the Fine Structure of the Spinal Cords

The ultrasonically-induced ultrastructural changes observed within the spinal cords of irreversibly paralyzed mice, together with the manner in which the degree of the ultrastructural alterations depended upon the exposure time, i.e., t_{10}, t_{50}, and t_{90}, and post irradiation time, were similar for all of the acoustic intensities used. The major effect of changing the intensity was to alter the distribution of the damaged tissue throughout the spinal cords. Because of this observation, it is only necessary to present a detailed description of TEM

observations of the tissue obtained from one intensity of irradiation. Tissue obtained from the mice irradiated with 289 W/cm^2 is chosen for this purpose since more specimens were obtained for the study. Reference is made to the tissue irradiated with the lower intensities when pertinent.

In order to describe the nature and degree of the ultrasonically-induced tissue damage in the mouse spinal cord sections, a scoring system utilizing six distinct states was devised. As it was with the nine stage system employed for the cat brain tissue, the six states are distinguished by significant changes in the observed altered morphology. The term "states" is used since there was no direct proof that the tissue passed through the lower numbered "states" to achieve a higher damaged state, as in the case of the cat brain tissue. A temporal association between the six states can only be implied, as discussed earlier. Unlike the cat brain scoring system in which different regions within a lesion cross section could be scored as a different stage, the system described below pertains to the entire, transverse, spinal cord section. The reasons for this will become obvious. Scoring designations are based on the portion of the sections that exhibited the greatest degree of tissue damage, and this was always the ventral most portion of each section. Since the animals irradiated with intensities other than 289 W/cm^2 frequently displayed tissue damage in both the dorsal and ventral halves of the section, the dorsal and ventral halves were scored separately. Sections anterior or posterior to that displaying the greatest degree of damage, e.g., state n, displayed decreased degrees of tissue damage that changed in a

gradual manner from state n to state 1 before sections containing normal morphology were encountered.

7.3.1. State 1

The minimum degree of ultrasoncally induced changes within the spinal cord ultrastructure associated with irreversible hind limb paralysis is illustrated in Figs. 7.17 and 7.18. Both the electron density and contrast of the morphological features in the affected portions of the spinal cords were noticably decreased in comparison to that found in identical regions of the control spinal cords. Most of the mitochondria appeared slightly swollen. They had less electron dense matrices which contained small, electron transparent regions. A smaller number of mitochondria were more substantially swollen, had completely electron transparent matrices, and their cristae were displaced towards the periphery of the organelle (Fig. 7.17). Both mitochondrial membranes remained intact despite swelling. The asymmetry between the electron density of the matrices of axonal and nonaxonal mitochondria was less obvious.

Many of the dendrite-like processes displayed rounded shapes and appeared more turgid than in the control tissue. Their cytoplasm was less electron dense and lacked the mottled appearance characteristic of the cytoplasm of control tissue. A similar change was observed within some of the axons, but the decrease in electron density of the axoplasm was less pronounced. Most of the axons remained unaltered. An aggregation of the synaptic vesicles within the vicinity of the synaptic cleft, together with an overall reduction in the number of synaptic

vesicles within the presynaptic element, similar to that observed by Borrelli et al. [1980] in ultrasonically irradiated cat brain, was observed in some of the synapses (Fig. 7.18). The cytoplasm within the presynaptic element was less electron dense. Membranous debris was more prevalent in the affected synapses and dendrite-like structures, while only a small fraction of the affected, nonmyelinated axons contained such debris.

Tissue damage of this nature was typical of the maximum damage observed in irreversibly paralyzed mice irradiated with t_{10} exposures at 289 W/cm^2 and sacrificed within 4 - 45 min post irradiation. Such minimal damage was also observed following t_{50} and t_{90} exposures, but rarely following the t_{90} exposures. Altered ultrastructure was observed only along the ventral perimeter of the sections, within the band of tissue that would have become the white matter following axon myelination. Abnormal morphology was not detected with the LM examinations of the 1μm sections scored as state 1.

Ultrastructural changes like those described above were also observed following the shorter exposures, viz., t_{10} and t_{20}, using the lower acoustic intensities. The damage was also restricted to the ventral perimeter, but frequently involved a larger portion of the section, than with the t_{10} and t_{20} exposures with 289 W/cm^2. As mentioned earlier, the longer exposures at the lower intensities often induced damage in the dorsal half of the spinal cord together with a concomitant loss of hind limb pain sensation. The minimum ultrastructural damage observed in conjunction with this sensory loss was the same as that described above for hind limb paralysis.

7.3.2 State 2

The affected portion of the spinal cord remained restricted to the ventral, peripheral tissue, and TEM was still required to detect the altered morphology. The ultrastructural changes described in state 1 were more pronounced and prevalent (Fig. 7.19). Most of the mitochondria displayed some degree of swelling, ranging from a mild decrease in matrix electron density to structures barely recognizable as mitochondria. Ring-like structures like those in Fig. 5.23 were also observed, although infrequently.

Most of the dendrite-like structures were swollen to some degree, and many more swollen than in state 1. A larger percentage of the axons were swollen, but most remained normal in appearance. A reduced number of neurofilaments were observed in the more swollen axons. Microtubules, although not significantly reduced in numbers, appeared more diffuse and less electron dense. The majority of the axons appeared to be in clusters that were isolated by the swollen dendrite-like structures (Fig. 7.19). An increase in the number of altered synapses was also observed. More membranous debris was observed in the tissue, particularly in the dendrite-like processes.

Some of the cell bodies observed in the peripheral region exhibited a mild decrease in the electron density of both their cytoplasm and nucleoplasm. The endoplasmic reticulum and golgi in such cells was mildly swollen, and the free ribosomes appeared less organized.

7.3.3. State 3

Tissue damage was clearly visible within the peripheral region using LM. The tissue stained lighter with the toluidine blue, and this effect was enhanced with the ethanol differentiation. Small, transparent voids were the main features that stood out during the LM observations in addition to the lighter staining of the tissue. The TEM revealed that these transparent voids were grossly swollen dendrite-like structures (Fig. 7.20), which were now extremely electron transparent and exhibited only traces of the electron dense material that gave the mottled appearance in the normal tissue. They contained membranous debris together with altered, but recognizable, organelles such as mitochondria and endoplasmic reticulum. The ring form of the swollen mitochondria was common in the dendrite-like structures (Fig. 7.20).

The cell bodies in the peripheral region displayed a wide range of altered states from the mild damage, described for state 2, to cells with very electron transparent cytoplasms with swollen nuclei having large patches of condensed chromatin (Fig. 7.20). There were no unaltered cell bodies in the peripheral tissue.

More axons were swollen, some to the point where their delimiting membranes ruptured. However, most axons still maintained a rather normal morphology. The increased swelling of the dendrite-like structures tended further to isolate the axon clusters (Fig. 7.20).

Essentially every synapse showed some degree of altered morphology. The membranes had ruptured in the more severely damaged synapses. In such cases all that remained to identify

positively the structure was the junctional density and a few associated synaptic vesicles.

As in the cat brain tissue, the mitochondria displayed a wide range of altered states. Figure 7.20 shows that there were normal appearing mitochondria together with the very swollen, ring-like forms. The degree of swelling of the structure occupied by the mitochondria did not seem to correlate with the degree of swelling presented by the mitochondria. Also, the various mitochondria occupying a given membrane bound structure did not necessarily display similar degrees of swelling.

Tissue damage was observed in the GM tissue using TEM. Near the interface between the peripheral tissue and the GM, the axons, synapses, dendrites, and mitochondria exhibited the altered states described in state 1. Some of the neurons, particularly the largest ones in the interface region, exhibited an effect unique to the 289 W/cm^2 irradiations (Fig. 7.21). Numerous, single membrane-bound, electron transparent vacuoles were observed within the cytoplasm. These vacuoles were most common in regions where there were high concentrations of smooth endoplasmic reticulum and golgi. Both the nearby endoplasmic reticulum and golgi often appeared swollen, and serial sectioning frequently demonstrated a continuity between the vacuoles and the structures which strongly suggested that these vacuoles were grossly swollen portions of the endoplasmic reticulum and golgi. Only a mild swelling was observed in portions of the rough endoplasmic reticulum, most of which appeared normal. Except for a few swollen mitochondria, the remainder of these cells appeared unaltered.

State 3 damage was typical of that observed 4 - 25 min following a t_{90}, 289 W/cm^2 exposure. Similar damage was observed 10 - 30 min following a t_{50} exposure with 105 W/cm^2.

7.3.4. State 4

Tissue damage in the GM regions was visible with LM, and very similar to that scored as stages 3 and 4 in the irradiated cat brain tissue. The most prominent features were the swollen cytoplasms and nucleoplasms of the neurons (Figs. 7.22 and 7.23). Condensed chromatin was observed in the nuclei, but these condensations did not tend to favor a central location as they did in the cat brain neurons. When present, the nucleolus was prominent (Fig. 7.23), but only appeared slightly more condensed than in the normal neurons. The rough and smooth endoplasmic reticulum were swollen in most of the affected neurons (Fig. 7.22). No Nissl bodies remained and there was a decrease in the free ribosome patterns. Golgi bodies also exhibited signs of swelling, but less than that observed for the endoplasmic reticulum.

Some of the swollen neurons displayed a juxtanuclear condensation of their internal organelles. In such cases the rough endoplasmic reticulum showed little sign of swelling. Just as in the cat brain tissue, this effect was most common in the larger neurons. Note the similarities between Figs. 7.22 and 7.23, and Figs. 5.14 and 5.15. Dendrites displayed decreased electron densities, and the altered forms of their subcellular organelles were as described above for the neurons (Fig. 7.23).

The mitochondria in both the neurons and the intervening tissue structures displayed a wide range of altered states (Figs. 7.22 and 7.23). The ring-like structures were, however, not commonly observed. A larger number of synapses were altered than in the state 3 GM.

Glial cells also exhibited some of the altered morphology described above for the neurons, but to a lesser degree.

The section in Figs. 7.13a and b was scored as state 4. A t_{90} exposure with 289 W/cm^2 was used and the animal was sacrificed 35 min after being irradiated. The ventral most portion of the peripheral tissue was often friable and fell away from the section during processing. This friable tissue was different than that pictured in Figs. 7.15 and 7.16. The friable nature of the tissue appeared to be more the result of extensive vacuolization and swelling than heat fixation.

7.3.5. State 5

The peripheral tissue appeared like that of Fig. 7.24. Most of the axons were now swollen and contained no neurofilaments and a markedly reduced number of microtubules. This tissue was often friable, and large pieces of the peripheral tissue were sometimes missing from the sections. The section in Figs. 7.14a and b was scored as state 5. It was irradiated with a t_{90} exposure and intensity of 86 W/cm^2, and sacrificed 5.5 min post irradiation. State 5 was also obtained with a t'_{90} exposure with 289 W/cm^2 and a 10 - 30 min post irradiation time, a t_{90} exposure with 289 W/cm^2 and a 25 - 45 min post irradiation time, and a t_{90} exposure with 105 W/cm^2 and a 5 - 20 min post irradiation time.

Figure 7.14b shows some very large, dark staining cells that appear to be neurons. TEM indeed confirmed they were neurons, based on their nucleoli and the presence of an axon hillock, AH, (Fig. 7.25). As illustrated by Fig. 7.25, the endoplasmic reticulum, golgi, and mitochondria in these cells were grossly swollen. The nucleus and the cell itself appear to be condensed, which probably explains the increased electron density of the cytoplasm and nucleoplasm. Although there are some similarities beween the neurons in Figs. 5.28 and 5.25, there was no electron transparent space surrounding the dark neurons observed in the spinal cord. A few dark neurons such as that in Fig. 7.25 were observed in the nonirradiated spinal cords. Ralston [1983] has suggested that in the still developing, neonatal spinal cord some of the neurons that may not be essential for the tissue's function die and become necrotic. It is in tissue in this state that the number of these dark neurons increased significantly over that found in the control tissue. It is most likely that some of the more severely affected neurons became necrotic and indistinguishable from a dead cell.

Some of the cells in Fig. 7.14b appeared as light staining nuclei surrounded by an electron transparent space. These are nonneuronal cells, and were similar to Fig. 7.26 when examined with TEM. The cytoplasm is almost devoid of any structure, and most of the remaining organelles are near the nucleus. The nucleus itself is very swollen and contains condensed chromatin.

Figures 7.27 and 7.28 are representative of the most damaged portion of the GM in state 5 tissue. Most tissue structures were swollen except for the dark neurons and their processes.

7.3.6. State 6

State 6 tissue can be seen in the left ventral region of Figs. 7.12a and b, and the dorsal region of Figs. 7.15a and b. Portions of both the peripheral and GM tissue were highly vacuolized and fragmented. There is some similarity between stage 9 tissue in the cat brain and the state 6 tissue. An electron micrograph of state 6 tissue is presented in Fig. 7.29.

CHAPTER 8

RESULTS OF THE FREEZE FRACTURE STUDY

Freeze-fracture replicas made from both the cat brain and neonatal mouse spinal cord tissues were examined during the course of this study, however, only micrographs from the cat brain tissue are discussed in the chapter. The reasons for this are that more replicas were obtained from both the nonirradiated and irradiated cat brain tissue, the cat brain replicas were of a higher quality, and finally, both the cat brain and mouse spinal cord replicas exhibited the same type of altered ultrastructure.

In order to aid readers inexperienced in viewing freeze-fracture micrographs to understand the features they will view, the following comments are made. There are two ways in which the biological tissue can fracture [Stolinski and Breathnack, 1975]. The fracture plane can pass through a structure perpendicular to its biological membrane, revealing the structure's internal contents. This is known as a cross-fracture, and is illustrated in Fig. 8.1 where the synaptic vessicles within the presynaptic element are revealed. The fracture plane can also run parallel to the structures biological membrane. This type of fracture is of the greatest value as it reveals the ultrastructure of the biological membranes which cannot be observed in the sectioned tissue.

The fracture plane runs through the hydrophobic region between the two leaflets of the protein-lipid bilayer of the membrane. Hence, the only two membrane surfaces revealed by the fracture are the inward-facing surface of the outer leaflet and

the outward-facing surface of the inner membrane leaflet, which are referred to respectively, as the internally facing, Int, and externally facing, Ext, surfaces, or more simply the internal or external surfaces [Stolinski and Breathnack, 1975]. The distinguishing characteristics between the two membrane surfaces is that the external surface contains more membrane associated particles, mp, than the internal surface, as illustrated in Fig. 8.1.

Frequently, an internal and external membrane surface are observed next to each other with a step, St, forming the border between them. These two membrane surfaces are not from the same structure but are separate membrane fracture faces from two separate, adjacent structures (Fig. 8.1). The only exceptions to this rule are the multi membrane-bound structures such as the mitochondria, the myelin sheath, and the nuclei. In such cases, the internal and external membrane surfaces from the same structure can be observed, but each surface comes from a different one of two separate membranes.

8.1. Replicas of the Nonirradiated Cat Brain Tissue

8.1.1. The Myelinated Axons

A typical white matter field is shown in Fig. 8.2. The smooth, featureless internally-facing surface of the myelin membrane was the most commonly observed membrane surface in the WM replicas. Both the internal membrane surface and the less commonly observed external surface are shown in Figs. 8.2 and 8.3. The multilayered nature of the myelin sheath could be observed in axons running parallel to the fracture plane when the

fracture plane shifted from one level to the next forming a series of step interfaces (Fig. 8.2), but was best seen in the cross fractured axons (Fig. 8.3). Particles were observed between the myelin layers of the cross-fractured axons, and these were probably the membrane particles from the external membrane surface.

Mitochondria, microtubules, neurofilaments, and other structures were observed within the cross-fractured axoplasms. Cristae could be observed in the cross-fractured mitochondria (Fig. 8.3) which were studded with particles. Some investigators have suggested that these cristae particles are the mitochondrial ATP-ase [Smith, 1963]. However, the manner in which the membranes fracture precludes this possibility since the ATP-ase molecules lie on a membrane surface that is never seen. That surface may be revealed by etching but, as mentioned in Chapter 3, the cryoprotected tissue used in this study could not be etched. There were other structures observed in the axoplasms that were not positively identified, which may have been fragments of the endoplasmic reticulum or other membranous structures that were observed in the sectioned axons (Fig. 8.3).

8.1.2. The Nonmyelinated Structures

The membrane ultrastructure of all the nonmyelinated structures, e.g., synapses, dendrites, cell plasma membrane, etc., was very similar, and so the normal and altered morphology exhibited by these structures can be illustrated with examples from just some of these structures. Figure 8.4 shows a synapse where portions of both the pre- and postsynaptic elements have

been cross-fractured to reveal the internal structure. The external membrane surfaces of both these synapse structures can be seen, and portions of the internal membrane surface from an adjacent structure cover part of the presynaptic element. The axon which developed into the presynaptic element can also be seen in the upper right portion of Fig. 8.4.

Synaptic vesicles are the most prominent structure within the presynaptic element cytoplasm of Fig. 8.4., while mitochondria are most prominent within the postsynaptic elements. A series of particles borders the cleft region on the postsynaptic side (arrowheads). Stolinski and Breathnack [1975] indicate that such a structure is common in replicas of gap junctions and tight junctions, and Peters, et al. [1976] state that these particles are only found on the internal face of the postsynaptic membrane. It is not known whether or not these particles are the freeze-fracture manifestation of the junctional density. Smaller particles can be seen in the cytoplasm of both synaptic elements. As discussed below, these may be cross-fractured filaments of the cytoskeleton.

In order to have been positively identified as a synapse, a portion of the presynaptic element had to be crossfractured to reveal the synaptic vesicles. Observations of the morphology of many such positively identified synapses enabled structures like that in Fig. 8.5, where no vessicles can be seen, to be identified as synapses. Neither the pre- or postsynaptic elements are identifiable, but as the narrowing structure leading into the upper element appears to be an axon, this seems to indicate that it is most likely the presynaptic element.

8.2. Replicas of the Irradiated Cat Brain Tissue

8.2.1. The Myelinated Axons

A replica from a WWGM region scored as stage 1 is shown in Fig. 8.6. The myelin here and in other such regions appeared slightly more ruffled and irregular about the axons, possibly indicative of the mild demyelination observed in the sectioned tissue. All other aspects of the myelin and the axons appeared unaltered. No changes in the myelin membrane ultrastructure were ever observed in stage 1 tissue or in any of the latter stages. There were no signs of tears or pores in the myelin, and the particle distribution of the external face was unaltered.

An increased degree of demyelinaton was noted in the replicas rich in myelinated axons and scored as the later stages. This trend is illustrated by Figs. 8.7, 8.8, and 8.9, which were scored respectively as stages 3, 5, and 6 - 7. As the demyelination increased, fewer cross-fractured axons were observed. It appears that the unravelled myelin controlled the direction of the fracture plane in the latter stages, reducing the occurrence of cross-fractures. Some of the featureless regions in Fig. 8.9 are probably the interstructure spaces resulting from the tissue edema.

8.2.2. Nonmyelinated Structures

The morphological features observed within the cross-fractured, membrane-bound structures in replicas of irradiated tissues reflected the altered morphological states observed in the sectioned material, as illustrated by the synapse

with aggregated vesicles in Fig. 8.10. The tissue used to make this replica was scored as stage 2 - 3.

No tears or pores are evident in the membranes in Fig. 8.10 or in any of the replicas (no matter what stage the tissue was scored as) observed during this study, though there were changes in the membrane ultrastructure. Note that on the external membrane surfaces in Fig. 8.10 the surface density of the membrane particles is less than that observed in the nonirradiated membranes (see Figs. 8.4 and 8.5). Although the particles are more sparsely distributed throughout the membranes, the particles tended to form aggregates, Ag, of 2 - 15 particles. Single particles were observed, though they were few in number.

The particles observed within the cytoplasm of many structures, particularly the synapses, were more sparsely distributed and also tended to form aggregates (Fig. 8.10). In the presynaptic elements, these cytoplasmic particle aggregates were concentrated within the aggregated synaptic vesicles. This observation strengthens the arguement that these cytoplasmic particles are related to the electron dense material observed in the sectional tissue, and represents portions of the cytoskeleton.

In Fig. 8.11, the swollen mitochondria identify this tissue region as stage 4. The external membrane surfaces still display the sparser and patchy distribution of the membrane particles. The cross fractured synapse shows a further reduction and aggregation of the cytoplasmic particles in both synaptic elements. In the presynaptic element, the localization of the cytoplasmic particles within the synaptic vesicle aggregates is

more pronounced. There is still a concentration of particles along the postsynaptic side of the synaptic cleft.

Figure 8.12 shows a replica from tissue scored as stage 5 - 6. The altered morphology illustrated in Figs. 8.10 and 8.11 is more pronounced, particularly the distribution of particles on the external membrane surface of the presynaptic element. Also note the further concentration of the cytoplasmic particles within the synaptic vesicle aggregates.

The decreased surface density and concomitant aggregation of the membrane particles is probably related to the swelling of the membrane-bound structures that was observed in the sectioned tissue. As the membranes became more swollen and turgid, the surface area of the membranes increases. Since the number of particles remained constant, it also was necessary that they became more sparsely distributed. The tendency towards particle aggregation is not easy to explain. These membrane particles are believed to be aggregates of proteins, lipids and lipid-proteins. Perhaps these particles formed integral associations in the normal membranes, but they were masked by the higher particle density. When the tissue swelled, these associations were maintained and became evident as the particles moved away from one another, much like spots painted on the surface of a deflated balloon that is then inflated.

CHAPTER 9

RESULTS OF THE BHK CELL HYPERTHERMIA STUDY

9.1. Observations of the Control and Sham Heated Cells

Representative micrographs of the control and sham heated ultrathin-sectioned cells are presented in Figs. 9.1, 9.2, and 9.3. The most prominent structure in each cell was the centrally situated nucleus. Smooth and rough endoplasmic reticulum, together with free ribosomes, were observed throughout the cells, but there were no associations of free ribosomes and the rough endoplasmic reticulum, analogous to the Nissl bodies observed in the neurons. Mitochondria were often observed in small, loose clusters, which were randomly scattered throughout the cytoplasm.

The nuclei generally exhibited one or more nucleoli (Fig. 9.1). Most of the chromatin appeared to be uniformly distributed throughout the nucleoplasm, but localized chromatin condensations were also observed. An irregular, oftentimes discontinuous, narrow band of electron dense material bordered the nucleoplasmic side of the inner nuclear membrane (Fig. 9.1 and 9.2). In some nuclei, portions of this band were associated with chromatin condensations, or even one or more of the nucleoli.

Higher magnifications (Fig. 9.2 and 9.3) showed that most of the free ribosomes were in small aggregates, forming patterns similar to those observed in the neuron cells (see Chapters 5 and 7). Cytoskeletal filaments were observed among the ribosomes, but it was not possible to determine whether the two structures were intimately associated. Most of the endoplasmic reticulae observed within these cells was studded with ribosomes, and hence

classified as rough endoplasmic reticulum. Very few ribosome-free segments that could be classified as smooth endoplasmic reticulum were observed.

Small patches of lower electron density were observed within the matrices of some mitochondria, togehter with a small number of electron dense granules, Dg (Figs. 9.2 and 9.3). Both mitochondrial membranes were clearly visible, and the intracristal space was very uniform among the observed mitochondria, approximately 200 - 250 Å, as measured in both transverse and longitudinal mitochondrial sections. A small number of swollen and distorted mitochondria were observed in a few cells, but this was never more than 10% of the total number of mitochondria in an individual cell, and usually less than 5%. It may be that these swollen mitochondria were simply indicative of normal turnover of the organelle in these cultured cells.

Light staining spherical bodies were also observed within the cell cytolasm, as shown in Fig. 9.3. They did not appear to be delineated by a biological membrane, and the interiors were homogeneous and featureless. The exact biochemical nature of these structures is unknown, but morphologically, they most closely resemble lipid granules.

Figure 9.4 is representative of the morphology observed in a low magnification micrograph of all extacted, control and sham heated cells. Stress fibers, sf, parallel bundles of microtubules and other filaments, were observed in these preparations, particularly near the cell perimeters. Examination of this micrograph reveals an inhomogeneously distributed, filamentous network pervading the cells. Nuclei appeared as electron dense,

"honeycombed" structures situated near the center of each cell, and often contained one or more electron dense structures which were most likely the nucleoli. The density of the filamentous network varied from cell to cell, being least dense in the larger, more spread-out cells. There always appeared to be a halo region, H, of lower filament density surrounding the nuclei together with a denser annulus of filaments directly attached to the nucleus itself. Small, electron dense spherical bodies, Sb, were scattered throughout the cells, together with membranous-like debris. The size distribution and shape of these spherical bodies was similar to the spherical bodies observed in the sectioned materials. In fact, sections taken from epoxy-embedded, extracted cells contained spherical structures very much the same as those found in the sectioned, nonextracted cells, suggesting that they represented the same feature. The fact that the spherical bodies were osmophillic suggests that they were proteinacious or lipid in nature. Since these bodies did not disperse when the membrane was solubilized is indicative that at least the outer layers are hydrophobic. Electron dense material of varying dimension was observed on the formvar substrate. This material may have been residue from the extracted cells that was not rinsed away during processing.

A higher magnification (Fig. 9.5) revealed three distinct filament populations having diameters of 6, 12, and 24 nm. Based on the results of the immunolabeling experiments of Heuser and Kirschner [1980], these filaments were identified as actin microfilaments (6 nm), intermediate filaments (12 nm), and microtubules (24 nm). Each individual filament maintained a very

uniform diameter along its length. Although the filaments crossed over one another, intertwined, and actually touched and ran parallel for several microns, the individuality of the filaments was always discernable.

The small, electron dense particles attached to the micro- and intermediate filaments in Fig. 9.5 were identified as ribosomes, based on the observations of earlier investigators [Cevera et al., 1981; Heuser and Kirschner, 1980; Ris, 1980]. They were either attached individually to the filaments or found in grape-like clusters. However, even with microscope magnifications in excess of 100,000X, no means of attachment between the ribosomes and cytoskeleton filaments was observed. Fewer ribosomes appeared to be associated with the microtubules.

The cytoskeleton morphology shown in Fig. 9.6 is very different from that in Fig. 9.5. This type of morphology resulted when the extracted cells were critical point dried, using ethanol which was not treated with molecular sieve, and unfiltered carbon dioxide transition fluid. Cytoskeletons similar to that in Fig. 9.6 have been presented by other investigators using both extracted [Webster et al., 1978; Cevera et al., 1980] and nonextracted cells [Wolosewick and Porter, 1976]. It has been suggested that failure to remove even trace amounts of residual water produces a surface tension across the filaments as the carbon dioxide becomes gaseous at its critical point but that water does not [Ris, 1980; Borrelli et al., 1983]. The surface tension from the remaining water provides a force which fuses the cytoskeleton filaments, like those in Fig. 9.5, to form the web-like structure in Fig. 9.6.

9.2. Observations of the Hyperthermia Treated Cells

The morphological appearance of the heated cells depended upon the treatment parameters, viz., temperature, heating time, and the post heating incubation period at 37°C. Following many of the treatments used, some of the examined cells exhibited morphological appearances indistinguishable from that presented by the control and sham heated cells, and the population of altered cells displayed a range of altered morphological states. Increasing the temperature, heating time, or post heating incubation period, or any combination thereof, resulted in a decrease in the number of normal appearing cells and shifted the population of altered cells to those in states with an increased degree of altered morphology.

The following discussion centers on a detailed description of the altered morphological states observed in the heated cells, and relates qualitatively the trends observed by changing the treatment parameters. Comparisons can then be made to the altered, cellular morphology resulting from ultrasonic irradiations, as discussed in Chapters 5 and 7.

With increasing post heating time following each hyperthermia treatment, the population of heated cells as a whole displayed a shift towards states having a greater degree of altered morphology. By recording the order in which new altered states appeared within the heated cell population, a temporal sequence for the morphological changes resulting from each hyperthermia treatment was established. It was noted that the nature of the hyperthermia-induced, morphological changes, together with the temporal sequence in which these changes occurred, was the same

irrespective of the temperature and heating time used. Increasing either the temperature or heating time, or both, increased the number of cells exhibiting altered morphology and the time rate at which the affected cells progressed through the temporal sequence. This was evidenced by a larger proportion of the cells exhibiting the more altered morphological states at a given post heating incubation time following a longer exposure at a given temperature, or a given exposure at a higher temperature.

The temporal sequence of morphological changes determined from observations of the heated cells is presented in five stages. Each stage is characterized by a significant change in morphology from that described in the previous stage. Remarks of comparison are made with reference to the previous stage unless otherwise noted. In some instances, a percentage range is given for the altered structures. These numbers were obtained from counts made with at least 10 cells classified as belonging to the stage under consideration. These semi-quantitative approximations are intended to provide some feeling for the degree of damage observed in these cells, and to provide an estimate for what might be expected should these experiments be repeated.

Not all of the hyperthermia treatments that produced altered cellular morphology yielded cells that proceed through all five stages of the temporal sequence, even following post heating times of 6 hr. However, for each hyperthermia treatment, the cell population progressed to the point of greatest observed altered morphology along the sequence of stages described below.

9.2.1. Stage 1

9.2.1.1. Sectioned Cells

The amount of electron dense, condensed chromatin in the nucleus was significantly greater than that observed within the control and sham heated cells (Fig. 9.7), and the electron dense band along the nucleoplasmic side of the inner nuclear membrane was more irregularly distributed (Fig. 9.7 and 9.8). Electron transparent regions within the cells were now more numerous, but there was no apparent change in the electron density of the cytoplasm or nucleoplasm.

Essentially all of the mitochondria in the hyperthermia altered cells contained electron dense granules (Figs. 9.7 - 9.9) which were now more numerous and more electron dense than those observed in the control and sham heated cells. No significant changes were observed in the electron density of the mitochondrial matrices or the dimensions of the intracristal spaces.

Most of the free ribosomes were no longer associated with the patterns that were so distinct in the control and sham heated cells, but were present as single, unassociated entities within the cytoplasm (Figs. 9.8 and 9.9). The remaining free ribosome associations formed looser patterns that were less prominent against the cytoplasm background. There appeared to be no change in the number of ribosomes attached to the rough endoplasmic reticulum. All of the observed golgi, g, exhibited some degree of altered morphology such as swelling or irregularly shaped membranes, (Fig. 9.9) and many of the electron transparent regions within the cytoplasm were located near the golgi and

smooth endoplasmic retiulum. Amorphous membranous debris, ?, was also present, with no clue as to its origin.

9.2.1.2. Extracted Cells

The appearance of the cytoskeletal filaments varied very little from those of the control and sham heated cells. There did appear to be a mild decrease in filament density, particularly in the number of action microfilaments in the peripheral regions of the cells. There was also a marked decrease in the number of ribosomes associated with the cytoskeletal filaments.

9.2.2. Stage 2

9.2.2.1. Sectioned Cells

Chromatin condensations became less prominent and fewer in number within the cell nuclei (Fig. 9.10), and the electron dense band along the inner nuclear membrane became less electron dense (Figs. 9.10 and 9.11). The mitochondria appeared condensed, more electron dense, and tended to occupy the region surrounding the nucleus, as shown in Figs. 9.10 and 9.11. Many cells with these characteristics had cytoplasms and nucleoplasms that appeared less electron dense (Figs. 9.10 and 9.11). This density decrease may have been the result of a mild cellular swelling or a result of the cells spreading out flatter on the substrate.

Figure 9.11 illustrates that the mitochondrial matrices were more electron dense while the intracristal spaces were widened and more electron transparent. Electron dense granules could still be observed in the mitochondria, but they appeared less prominent because of the increased matrix density.

The number of ribosomes attached to the rough endoplasmic reticulum was significantly reduced. No golgi were observed and sightings of smooth endoplasmic reticulae became rarer. The number of small, membrane bound vesicles observed within the cytoplasm increased, and amorphous, membranous structures were still present (Fig. 9.11).

9.2.2.2. Extracted Cells

The most prominent change in the cytoskeletal morphology was the formation of a juxtanuclear condensation, Jc, of filaments, accompanied by a marked reduction of the filament density in the peripheral regions of the cells (Fig. 9.12). The stress fibers were less distinct and the cell boundary was more irregular and less well defined. Many cells appeared to spread out, as if they were swollen.

Usually only one juxtanuclear condensation per cell was observed, but there were occasional sightings of multiple condensations. A higher magnification (Fig. 9.13) demonstrated that the juxtanuclear condensating consisted primarily of the action microfilaments and intermediate filaments. The peripheral regions were essentially devoid of microfilaments, and contained a reduced number of intermediate filaments (Fig. 9.14). There appeared to be no change in the number or distribution of the microtubules, other than in the stress fibers which exhibited a lower density of microtubules, and a marked reduction in their microfilament and intermediate filament content.

9.2.3. Stage 3

9.2.3.1. Sectioned Cells

The nucleus almost always contained one nucleolus but no other electron dense chromatin condensations (Fig. 9.15), and the electron dense band along the nuclear membrane was very thin and indistinct. There was no change in the distribution of the endoplasmic reticulum throughout the cell, although the amount of endoplasmic reticulum observed was reduced. The remainder of both the cytoplasm and nucleoplasm appeared very homogeneous in texture and electron density, and the electron denity was more like that observed in the control and sham heated cells than some of the cells in stage 2. This probably indicated that any swelling that may have occurred during stage 2 was reduced.

Most of the mitochondria displayed the morphological state described in stage 2, while from 10 - 40% of them were in various stages of swelling (Fig. 9.16). In some cases the swelling was too pronounced to identify the structure as a mitochondrion. Electron dense granules were rarely observed within the swollen mitochondria, but were still commonly found in the condensed mitochondria.

9.2.3.2. Extracted Cells

The most striking change in the cytoskeleton morphology was the increased prominence and localization of the juxtanuclear condensation, as seen in Fig. 9.17. Ribosomes, spherical bodies, and membranous debris were concentrated within the region of the juxtanuclear condensation, and were only sparsely distributed elsewhere within the cells. Hirokawa [1982] and Wolosewick and

Porter [1976] demonstrated that the cytoskeletal filaments were attached to the subcellular organelles such as the mitochondria, endoplasmic reticulum, etc. As the juxtanuclear condensation became more concentrated, the filaments apparently pulled their attached subcellular organelles into that portion of the cell. This would explain the movement of the mitochondria towards the nucleus, as illustrated in Fig. 9.15. The membranous debris observed within the juxtanuclear condensation in Fig. 9.17 may be the remnants of extracted mitochondria.

The reduction in filament density in the peripheral regions of the cells was more pronounced (Fig. 9.17). Stress fibers were absent, and the perimeter of the cells appeared more irregular and ill defined. As in stage 3, the majority of filaments remaining at the cell periphery were microtubules and intermediate filaments. Microfilaments were further reduced in the periphery, as one would expect since the juxtanuclear cap was now more prominent.

9.2.4. Stage 4

Both the cell and the nucleus exhibited irregular shapes (Fig. 9.18), suggesting a collapse of the cells. Chromatin condensations were once again observed in increased numbers, and the electron dense band along the inner nuclear membrane became more prominent than that in stage 2 and 3. However, it was still distributed more irregularly than in the control and sham heated cells.

Mitochrondrial numbers were reduced by approximately 30 - 70% from those observed in the control and sham heated cells.

Remaining mitochonria were still concentrated near the nucleus and exhibited the condensed morphology described in stages 3 and 4. Electron transparent regions were observed among the mitochondria and were possibly the remnants of swollen mitochondria.

9.2.4.1. Extracted Cells

Figure 9.19 shows that the extracted cells also displayed the irregular cell and nuclear shapes. The cells appeared more rounded along portions of their perimeters, and were smaller in their lateral extant. The juxtanuclear condensations were still present, but appeared less prominent.

9.2.5. Stage 5

The cells now had a more rounded and condensed shape as evidenced by Figs. 9.20 and 9.21. The most prominent features in the sectioned cell of Fig. 9.20 are the electron transparent voids, V, particularly the smaller ones distributed along the cell perimeter. In most cases, the voids were delineated by a membrane, probably indicating that their origin may have been with swollen organelles, such as mitochondria for the larger voids and the golgi and endoplasmic reticulum for the smaller ones.

Mitochondria in various stages of swelling are seen in Fig. 9.20. Note here that the swollen mitochondria often possessed electron dense granules whereas these were rarely present in swollen mitochondria in stages 3 and 4. Both rough and smooth endoplasmic reticulum were present in these cells. Free ribosomes were found throughout the cells but only as individual organelles and not as part of any patterns.

Little or no detail was observed within the internal regions of the rounded, extracted cells (Fig. 9.21). Filamentous trailers, T, were seen eminating from the cell body and attached to the substrate some distance away. Other, shorter filaments were seen protruding from the cell body. These were not attached to the substrate and could be made to move across the substrate by slightly increasing the electron beam intensity.

Prior to fixing or extracting the heated cells, light microscopy revealed that some of the rounded cells became detached from their substrates. More became detached during the extraction procedure.

The cytoskeletal morphology of the cells which attained a rounded shape as a result of the hyperthermia treatmens was very different than that dispayed by the rounded shaped cells which were in the process of mitosis, as can be seen by comparing Figs. 9.21 and 9.22. Mitotic cells were larger and less tightly rounded than the heated cells. The trailers did not extend as far from the cell body, and both the chromasomes, Chr, and mitotic spindle, Sp, were observed. The cell in Fig. 9.22 is in metaphase.

9.2.6. The Temporal Sequence as a Function of the Hyperthermia Teatements

Table 9.1 indicates when the morphology typical of each of the five stages was first observed among the population of cells receiving each of the different hyperthermia treatments. The first column lists the hyperthermia treatment used, and the entry in each of the remaining columns indicates the post heating time after which the altered morphology characteristic of each stage

was first observed in approximately 25% of the examined cells. In column 1, a range of heating times is given for each temperature, demonstrating that there was some variation in the cells' response from one experiment to the next.

CHAPTER 10

DISCUSSION

10.1. The Thermocouple Measurements

Although using a 13 μm diameter thermocouple minimized the viscoelastic heating associated with the oscillating thermocouple wires, its contribution to the thermocouple recorded temperature rises reported in Chapter 4 was nonzero. Just how accurately do these reported temperature rises represent the bulk heating properties of the tissue in the absence of the thermocouples? Frizzell [1983] developed a computer model that calculates the bulk and viscoelastic heating contributions to the recordings of tissue embedded, ultrasonically irradiated thermocouples. Factors affecting the calculated output are thermocouple junction size, viscosity, absorption coefficient, and thermal diffusivity of the medium.

Figure 10.1 shows the calculated response of a 13 μm diameter thermocouple to a 1.5 sec exposure in a medium having an absorption coefficient of 0.057 Np/cm, a viscosity of 0.05 poise and a thermal diffusivity of 0.0014 cm^2/sec, parameters which are similar to those of the brain white matter. The peak temperature calculated by the model for the thermocouple response is 6% greater than that predicted for the bulk tissue absorption. Hence, the peak temperatures reported in Chapter 4 can be taken to represent an upper limit to the peak temperature rises resulting from the ultrasonic exposures in the absence of the thermocouple. The slopes of both the total and bulk heating curves are essentially identical at 0.5 sec into the exposure, supporting the

choice of this point for calculating the tissue absorption coefficient.

Inserting thermocouple wires into the brain produced localized tissue damage and edema, and it is a point of concern that these changes affected the tissue absorption coefficient such that the thermocouple recorded a reduced temperature rise. Figures 4.3 and 4.4 illustrate that a degree of tissue damage much more severe than that resulting from the thermocouple insertion is required to affect the thermocouple's response, so that the latter is probably negligable.

The measured absorption coefficients were found to be independent of the acoustic intensity over the intensity range of 10 - 600 W/cm^2. Goss and Fry [1981], however, demonstrated absorption coefficient increases of nearly 400% over this same intensity range in nonnervous mouse tissue. They argued that the nonlinear acoustic properties of the medium distorted the focused ultrasonic wave and generated higher harmonic frequency components which, since the absorption coefficient is frequency dependent, have higher absorption coefficients.

There are, however, several differences between the experimental protocols utilized by Goss and Fry [1981] and those of the present study which may account for the different results. Goss and Fry used nonnervous murine tissue, e.g., muslce, which may have different nonlinear properties than does cat brain. Variability in the nonlinear properties among different tissue types does exist, as illustrated by Goss and Fry where murine muscle tissue exhibited a stronger dependence on the acoustic intensity than does murine testes. Also, the thermocouples used

in the present study were typically embedded 4 - 10 mm deep into the tissue compared to 2 - 3 mm the Goss and Fry work. Therefore, the higher frequency components would be more significantly attenuated for the more deeply embedded thermocouples, reducing significantly any intensity related increase in the absorption coefficient [Carstensen et al., 1983].

Probably the most significant difference between the two experiments was that of the focal lengths of the transducers employed. Goss and Fry [1981] used a focal length of 17 cm compared to 7.5 cm for this study. Muir and Carstensen [1980] present a theoretical treatment of harmonic generation in focused acoustic fields, and show that the dependence upon the transducer focal length, r_o, is

$$r = r_o \exp\left(\frac{-\sigma}{Cr_o}\right) \quad , \tag{10.1}$$

where r is the field point distance measured from the focal point back towards the transducer and parallel to the beam axis, and σ is the shock parameter which is proportional to the degree of wave distortion and harmonic development. The term C in Equation 10.1 is,

$$C = \left(1 + \frac{B}{A}\right) k \left(\frac{2I_o \cdot 10^7}{\rho_o C_o^3}\right)^{1/2} \tag{10.2}$$

where B/A is the nonlineariy parameter of the medium, I_o is the source intensity in watts per square centimeter, and ρ_o and C_o are in cgs units. For a given source intensity and distance r, the shock parameter will be greater in the 17 cm focal length field than in the 7.5 cm field. The sound field from the longer focal

length transducer is richer in harmonics, and thus any nonlinear phenomena would be more accentuated. F. J. Fry [1983] has compared the harmonic contents of a 17 cm and 8 cm focal length transducer in water, and observed that the longer focal length transducer had more significant harmonic development.

10.2. Factors Affecting the Degree and Temporal Development of Ultrasonically-Induced Tissue Damage

Increasing the ultrasonic dosage increased the degree and rate of development of induced tissue damage in both the cat brain and the neonatal mouse spinal cord. The effect of dosage was not only illustrated by comparisons between different lesions, but also within each individual lesion since the acoustic intensity varied according to the tissue's position within the acoustic field.

The different absorption properties of the WM and GM in the cat brain determined the development of tissue damage by influencing the ultrasonically induced temperature rise. This was most dramatically illustrated when the focal point was centered on an interface between WM and GM tissue regions. Although the acoustic field was symmetrical about the focal point as illustrated in Figs. 4.1 and 4.2, the tissue damage was asymmetrically distributed about this point being greater in the WM where the temperature rise was greater.

There was no WM in the neonatal mouse spinal cords, and no temperature measurements were made within the irradiated tissue. However, the effect of temperature upon tissue damage development can be deduced from the distribution of damage within each spinal

cord section. Tissue damage was always greater along the spinal cord perimeter where it bordered the spinal column. This was particularly evident along the ventral perimeter even though the ultrasound was incident upon the dorsal side of the animal. Bone tissue has an attenuation and absorption coefficient much greater than that of nervous tissue [Goss et al., 1978]. Assuming that the attenuation coefficient of spinal cord is similar to that of brain, and that the absorption coefficient of bone is a substantial portion of the attenuation coefficient, it may be assumed that the temperature at the spinal cord periphery would be greater as a result of absorbed heat conducted from the spinal column. The ventral portion of the spinal column is more massive than the dorsal portion, and would be expected to absorb more acoustic energy and to serve as a larger and hotter heat source. Also, the ventral portion of the spinal column is ossified to a greater degree than the dorsal portion [W. J. Fry and Dunn, 1956], which may further contribute to the absorption coefficient.

The increased tissue damage along the spinal cord perimeter may not only be the result of heat conducted from the spinal column. Longley and O'Brien [1982] have modeled acoustic wave interactions with tissue-like spheres and infinite cylinders, and predicted nonuniform temperature and intensity distributions arising from perturbations of the incident wave. In several instances, a hot spot is generated in the half of the object opposite to that where the sound wave is incident. The spinal cord and column form a cylinder with a 0.65 mm average radius whose major axis is much greater than the acoustic wavelength and beam width. The spinal cord also lies very close to the animal's

dorsal surface, thus minimizing any wave distortions by intervening tissue. Though the spinal cord system is different from that modeled by Longley and O'Brien in many ways, including materials of differing attenuation and acoustic impedance, their results suggest that the spatial nonuniformity of intensity and temperature, together with peak temperatures generated, increased with increasing impedance mismatch. It is thus considered possible that the spinal cord and column perturbed the acoustic field in a manner that would result in an asymmetrical distribution of tissue damage.

10.3. Interpretations of the Ultrasonically-Induced Morphological Changes

Relationships are often established between physiological or biochemical activity and the morphological state of the cell or cellular components. Since no physiological or biochemical analyses were done on the irradiated tissue, results from other studies will be used to interpet the ultrasonically-induced changes in cell function that accompanied the observed morphological changes and the effects on subsequent cellular activity.

10.3.1. Chemical Synapses

Synaptic transmission requires an influx of calcium ions into the presynaptic element [Dodge and Rahaminoff, 1967], which triggers a movement of synaptic vesicles toward the synaptic complex where the vesicles fuse with the presynaptic membrane and release transmitter into the cleft. After diffusing across the cleft, the chemical transmitter binds to receptor sites on the

postsynaptic membrane, affecting ionic currents in the postsynaptic membrane such that an action potential is initiated. Whether or not the synapses assume an active curvature prior to or proceding these events is unknown, as is the mechanism by which the curvature change is achieved.

Synaptic vesicle depletion, aggregation, and synaptic curvature changes identical to those present in the ultrasonically irradiated tissue were observed within ischemic cat brain by Williams and Grossman [1970] and Kalimo et al. [1977]. Williams and Grossman [1970] further demonstrated that these morphological changes were coincident with a failure in synaptic transmission, indicating that such altered synapses are nonfunctional. Further evidence supporting the results of Williams and Grossman can be found in the data presented in Chapters 5 and 7. The minimum tissue damage required to induce hind limb paralysis or loss of pain sensation in the neonatal mouse spinal cord was the altered synaptic morphology. Altered synapses were also the first structures affected in the cat brain, observable with TEM in tissue scored as normal using LM. In view of this it seems likely that the synapses were the affected structures that resulted in the cessation of light stimulated, evoked potentials when F. J. Fry et al. [1958] irradiated the lateral geniculate nuclei, regions of synaptic coupling between the optic nerve and the visual cortex of the brain [Gray, 1980].

The depletion of synaptic vesicles in the irradiated tissue may have resulted in the loss of synaptic transmission, i.e., no vesicles present means, no transmitter available for stimulating the postsynaptic membrane. The small amount of membranous debris

within the presynaptic elements suggests that the vesicles were not lost as a result of being ruptured. Since the altered synapses had active curvatures, it is suggested that the vesicles were depleted by a massive transmitter release. Assuming that the same mechanism of transmitter release existed as in the nonirradiated tissue, the mass release of vesicles would require triggering by a large influx of calcium ions. Harris et al. [1981] recorded a massive influx of calcium into the brain tissue upon the onset of ischemia, which they believe resulted from an ischemia-induced change in membrane permeability. It is therefore suggested that the ischemia related vesicle depletion resulted from a calcium-induced, massive transmitter release. Since the ischemia and ultrasound induced synaptic morphology changes were identical, it is probable that the ultrasound affected membrane permeabilities, and a large calcium influx caused the depletion of synaptic vesicles. Since the altered synapses were never repopulated with vesicles nor shifted to an inactive curvature, it is implied that the mechanisms for these two processes were inactivated, perhaps by the presence of excess calcium. It is also likely that such processes require energy in the form of ATP, and that the inability to replenish the vesicles or change the synaptic curvature may also have been linked to a decrease in endogenous ATP levels. Lipton and Whittingham [1981] recorded a large decrease in ATP concentrations concomitant with synaptic failure in hypoxic brain slice preparations. Synaptic failure and ATP level decreases were delayed in preparations loaded with creatine phosphate, which can transfer its high energy phosphate group to ADP and buffer the cellular ATP levels. This observation

indicates that loss of endogenous ATP is related to synaptic failure and to the accompanying morphological changes.

10.3.2. Mitochondria

Ultrasonically-induced mitochondrial swelling has been observed in muscle tissue [Ravitz and Schnitzler, 1970], in mouse uterus [ter Haar et al., 1979], and in mouse liver [Stephens et al., 1980]. Stephens et al. [1980] also reported the formation of electron dense granules within the mitochondrial matrix. They further suggested that both the size and extent of these granules could be used as indicators of the degree of ultrasonically-induced damage, and whether or not the damage was reversible.

The data reported in Chapter 5 shows that mitochondrial swelling in the irradiated cat brain was preceded by a mitochondrial condensation; this effect was noticed to a lesser extent in the irradiated spinal cord tissue. Hackenbrach et al. [1971] demonstrated that a shift from the normal in situ mitochondrial morphology, or orthodox state, to a condensed state identical to that seen in Figs. 5.12 and 5.13 occurred in response to decreased levels of endogenous ATP. They also determined that the condensed state was accompanied by increased respiration and oxidative posphorylation rates. Rydzynski induced a condensed mitochondrial state with DNP, an oxidative phosphorylation uncoupler, and Kalimo et al. [1977] observed mitochondrial condensation followed by swelling in ischemic cat brain. One of the results of ischemia is hypoxia, a condition

under which Lipton and Whittingham [1981] measured decreased ATP levels.

The subsequent mitochrondrial swelling may have resulted from one of many different causes, as they swell in response to changes in the osmotic content of their surroundings [Lehninger, 1984; Munn, 1974] or after exhausting their supply of ATP because they can no longer control their volume [Rydzynski, 1978; Lehninger, 1964]. Swelling can also be induced by an energy dependent uptake of calcium ions and the co-transport of phosphate ions [Greenawalt et al, 1964; Hackenbrach and Caplan, 1969]. This possibility must be considered in light of the evidence suggesting a calcium influx into the damaged brain tissue. However, calcium and phosphate sequestering does not induce mitochondrial condensation, though it does result in the formation of electron dense, calcium phosphate granules when sufficient quantities of calcium (40 - 190 nM calcium/mg mitochondrial protein [Hackenbrack and Calan, 1969]) and phosphate have been sequestered. No electron dense granules were observed in the altered neonatal mouse mitochondria. Granules were infrequently observed in severely swollen cat brain mitochondria, but these more closely resembled the granules observed by Stephens et al. [1980] which were not considered to be calcium phosphate deposits.

10.3.3. Neurons and Glial Cells

The greater sensitivity of the neurons to ultrasonic irradiation may reflect differences in the function, plasma membrane, and metabolic activity among the neurons and the glial cells. For example, since the neurons are continually involved in

transmitting electrical and chemical signals, they may require, on the average, more energy than the glial cells. Another indication of cell differences is that neurons initially swelled then collapsed while the glial cells continued to swell. It is interesting to note that the same order of cell sensitivity was observed in ischemic brain tissue [Kalimo et al., 1977; Garcia et al., 1977].

10.3.4. Ribosomes, Endoplasmic Reticulum, and Golgi

Ribosomes, endoplasmic reticulum, and Golgi are involved in the synthesis, transport, and secretion of proteins. The results reported in Chapter 9 and those of other investigators [Wolosewick and Porter, 1976; Lenk et al., 1977; Heuser and Kirschner, 1980] demonstrate that the polyribosomes are intimately associated with the cytoskeleton filaments. The free ribosome patterns seen in sectioned cells are probably a two dimensional representation of the swirls and spirals of ribosome-laden filaments seen in the extracted cells in Chapter 9. Cevera et al. [1981] present data indicating that the cytoskeleton-ribosome association is obligatory for protein synthesis. They also present evidence that the ribosomes on the rough endoplasmic reticulum are attached via cytoskeletal filaments.

The data of Chapter 9 indicates that the loss of polysome patterns in the ultrasonically irradiated cells results from the dissociation of the ribosomes from the cytoskeleton, while the results of Cevera et al. [1981] suggest that these cells have reduced, or no, protein synthesis capabilities.

Endoplasmic reticulum and golgi swelling were always observed in cells showing other signs of swelling, e.g., swollen nuclei, electron lucent cytoplasms, swollen mitochondria, etc, which suggests that the swelling in these two organelles resulted from osmotic imbalances within the cells. The effect of the swelling on their function is unknown.

10.3.5. The Cytoskeleton

Dissolution of the cytoskeleton filaments, similar to that described in Chapter 9, was observed in the irradiated tissue. The 6 nm filaments and the neurofilaments were affected more than the microtubules, which did not show signs of degredation until the later stages of tissue damage.

As the cytoskeleton responded to the ultrasonic irradiation, it appeared capable of rearranging subcellular structures such as the synaptic vesicles and the mitochondria. In fact, the condensation of the subcellular organelles about the cell nuclei in Figs. 5.15 and 7.22 is reminiscent of the mitochondria condensation around the nuclei of heated BHK cells (Figs. 9.11 and 9.15) which appears to be related to the formation of a juxtanuclear filament condensation. Hirokawa [1982] demonstrated that the cytoskeletal filaments form intimate associations with subcellular organelles, such that any rearrangement of the filaments would tend to drag the organelles with them. Although a juxtanuclear condensation was not observable in the TEM sections of the irradiated tissue, the peripheral regions of cells, like those in Figs. 5.15 and 7.22 exhibited decreased filament numbers. This fact, together with the juxtanuclear position of

the organelles, suggests the presence of a juxtanuclear filament condensation. Cytoskeletal rearrangement also appears to be involved in producing the synaptic vesicle aggregates and in the changing of the curvature of altered synapses. The cytoskeletal elements appear as filamentous condensation within vesicle aggregates, in Fig. 6.2, and as the cytoplasmic particles associated with vesicle aggregates in the freeze fractured synapses.

10.3.6. Myelin

Demyelination similar to that observed in the irradiated cat brain can be induced by concussions [Bakay et al., 1977] and ischemia [Garcia et al., 1979]. The actual cause of the demyelination is unknown, but may be related to damage in the oligodendrocyte cells which produce the myelin sheaths.

It is clear that even in the presence of mild demyelination, the myelin sheath seems to protect the axons from the morphological changes so distinct in surrounding nonmyelinated structures, as illustrated in Chapter 5 (see Figs. 5.13 and 5.18). The presence of a significant absorption across the expanse of the myelin sheath surrounding an axon is not a realistic possibility. In Fig. 5.18, the largest myelin sheath is less than 0.5 μm thick. Using Equation 1.1 and an attenuation coefficient of 0.1 Np/cm, the acoustic intensity attenuation across such a myelin sheath is less than one part in a million, i.e., negligible. Therefore, the acoustic intensity present within the myelinated axons in Fig. 5.18 was identical to that in the adjacent, nonmyelinated structures. Because of their close

proximity, the temperature within the myelinated and nonmyelinated structures of Fig. 5.18 is assumed to be the same. The only difference between these two types of structures is the presence of the myelin sheath, which somehow protected the organelles within the myelinated axons from the ultrasonically induced morphological changes observed in the nonmyelinated structures. It is suggested that the myelin protected the axons by serving as an osmotic barrier. Osmotically active substances need only penetrate one membrane in nonmyelinated structures compared to the multiple membranes about the myelinated axons.

10.4. A Hypothesis Concerning the Production of the Ultrasonically-Induced Morphological Changes

Based on the data in Chapters 5 and 7, and the discussion of the previous section, the following sequence of events is proposed to explain the development of tissue damage in response to ultrasonic irradiation. The ultrasound alters the selective permeability of the biological membranes, and membrane permeable species move across the biological membranes in a direction dictated by the free energy gradients established by the concentration differences across the membranes. The degree and development rate of tissue damage are then proportional to the extent of the membrane damage. The synapse is the first structure to exhibit altered morphology because increased calcium influx triggers a sustained release of transmitter. The change in ion distribution also affects the cytoskelton which alters the synaptic curvature and aggregates synaptic vesicles.

In an attempt to reestablish homeostatic ion concentrations, the membrane pumps increase their rate of activity, requiring a greater supply of ATP, so that endogenous ATP levels fall. The mitochondria respond to the decreased ATP levels by transforming to the condensed state and increasing their rates of respiration and oxidative phosphorylation to supply the increased demand for ATP. Mitochondrial swelling then ensues either because they no longer have sufficient ATP to maintain their volume, or swell in response to the change in osmotic pressure. Eventually all structures swell and distort since the ion pumps can no longer maintain the required ion gradients and osmotic balance.

According to this model, it is expected that the most metabolically active portions of the brain are first to show signs of altered morphology since these are the sites of early and rapid ATP depletion. The synapses and neurons are believed to have the highest metabolic rates in the nervous tissue [Mountcastle, 1974], and indeed they are the first structures to respond. Subsequently morphological changes proceed similarly to that described for nervous tissue dying from ischemia, anoxia, toxins, etc.

In the sequence of events just described, the biological membrane is the initial target for the ultrasonically induced damage. However, the same sequence of events could take place if the mitochondria were the initial targets, and their ability to produce ATP was fully or partially interrupted. If the mitochondria were the primary target, one would expect to observe similar mitochondrial changes simultaneously in both myelinated and nonmyelinated structures. The appearance of damage within the myelinated axons is delayed, indicating that the myelin protects

the axonal contents, most probably by acting as an osmotic barrier, and this is in agreement with the proposal that the membranes are the primary sites of induced damage.

Membrane damage must occur on a level smaller than 20Å since no altered membrane morphology could be observed on the freeze fractured replicas until stages 3 and 4. At that point the ultrastructural changes are those expected on a membrane being distended as the enclosed structure begins to swell.

10.5. Mechanisms by which Ultrasound May Have Induced the Observed Morphological Changes

10.5.1. Ultrasonically-Induced Anoxia

The arguement of Lele and Pierce [1971] concerning an ultrasonically-induced, localized hypoxia bears further consideration in light of the similarities between the ultrasound and ischemia induced morphological changes in nervous tissue. They argued that elevated temperatures resulting from acoustic absorption increase the metabolic rate and oxygen demands of the irradiated tissue. Kalimo et al. [1977] and Garcia et al. [1977] have clearly demonstrated that even under conditions of global ischemia, tissue damage does not appear for up to 10 min. The data in Chapter 4 shows that even with 300 W/cm^2 exposures of up to 3 - 4 sec, the tissue temperature returns to normal in under 1 min, demonstrating that a temperature related anoxic state is not involved in producing the ultrasonically-induced tissue damage.

Ultrasound could conceivably also induce an anoxic state by interrupting the delivery of oxygen to the irradiated tissue.

Oxygen moves across the capillary walls into the tissue by passive diffusion [Vander et al., 1975]. Hence, the only way for the tissue's oxygen supply to be cut off is for blood flow into the irradiated region to be interrupted for a significant period of time. Since the irradiated volume perfused well and no thrombi were observed, it is considered that blood flow was unimpeded. Dyson et al. [1974] did demonstrate an ultrasonically-induced cessation of blood flow which lasted only while the sound wave was present. Normal blood flow resumed once the sound was terminated.

Even after extensive blood vessel cuffing developed, evidence suggests that blood flow through the irradiated volume was maintained. The endothelial vessel walls remained intact, and all cuffed vessels perfused cleanly. The large degree of tissue swelling was another indicator of unobstructed blood flow. Garcia et al. [1977] and Kalimo et al. [1977] demonstrated that permanently ischemic tissue did not exhibit significant swelling. Reperfusing the tissue was required to carry additional water and ions to the ischemic tissue to maintain an osmotic gradient between the interstitial fluids and the now permeable tissue structures.

Although the ultrasound apparently does not induce an anoxic state, it does not follow that anoxia cannot serve as an adjunct to ultrasound for inducing tissue damage. Taylor [1970] demonstrated the anoxia decreased the threshold dosage required to produce damage in ultrasonically irradiated mouse spinal cord. Hence, the anoxia may have decreased the tissue ATP levels prior to the irradiation. If the ATP levels following an ultrasonic irradiation are a factor in determining whether or not tissue

damage develops, it would be expected that the anoxic tissue would be more sensitive and exhibit a lower threshold.

10.5.2. Ultrasonically-Induced Hyperthermia

The temperatures chosen for the BHK hyperthermia study were similar to the peak temperatures recorded in cat brain tissue receiving ultrasonic exposures known to produce tissue damage. The data in Chapter 4 demonstrates that for all damage producing exposures, the tissue was maintained for only a brief time at the elevated temperature. A significantly longer exposure time was required to induce morphological changes in heated BHK cells using temperatures less than 57°C. This indicates that tissue damage produced by ultrasonic exposures failing to raise the tissue tempeature to 57°C was not the result of the ultrasonically-induced hyperthermia. Ultrasonic exposures with 300 W/cm^2 for 3 sec or longer did result in temperature rises exceeding 57°C, and it is likely that hyperthermia was a major or sole cause of that resultant tissue damage.

Lele [1979] has presented a graph of temperature versus the exposure time at each temperature required to produce altered morphology within whole tissue *in vivo*, due to exposures to ultrasound, microwaves, or water bath produced hyperthermia. The BHK study data agrees with Lele's graph in that both indicate temperatures near 60°C are required for exposures on the order of 1 - 5 sec to produce morphological changes. Altered BHK morphology was observed following exposure to 50, 46, and 43.5°C for times shorter than those reported by Lele [1979]. This most likely was because the increased resolution of TEM permitted an

earlier detection of altered morphology in BHK cells than Lele could observe in tissue using LM.

It is interesting to note the similarities in the sequence of morphological changes induced by ultrasound in the nervous tissue and by hyperthermia in the BHK cells. Although the mechanisms eliciting the responses appear to be different in these two instances, the same target structures, e.g., biological membranes, mitochondria, etc., may be altered in a similar manner.

10.5.3. Ultrasonic Cavitation

It is clear that ultrasonically-induced temperature increases play a role in determining the degree of any resultant tissue damage, even when the heat alone is incapable of affecting the tissue. The heat may modify the tissue, e.g., by causing a phase or fluidity change within the biological membranes such that the tissue is more susceptible to damage from another mechanism. The tissue damaging mechanism may also be a function of temperature such that it is more damaging at higher temperatures. One such mechanism was discussed in Chapter 2, viz., acoustic cavitation. Cavitation would also produce more pronounced effects with increasing dosage as the magnitude of nuclei oscillation increases with the acoustic intensity [Beyer, 1974] and the duration of the phenomenon increases with longer exposure times.

Cavitation was implicated in the production of tissue damage in the neonatal mouse spinal cord, as discussed in Chapter 7. Unfortunately, similar tests could not be effectively performed with the cat brain system to detect the presence of cavitation. However, the presence of cavitation may be implied from the

temperature dependence of the induced tissue damage, and the similarities in the nature and temporal development of the morphological changes to those observed in the neonatal mouse spinal cord.

How can cavitation exert its effect on the tissue? The freeze fracture data clearly shows that the membranes were not torn, ruptured, or punctured. Hence, any shock waves, microstreaming, or secondary sound fields apparently did no gross structural damage to the membranes like that observed by F. J. Fry et al. [1970]. Any membrane damage must have occurred to features smaller than the electron microscope resolution limit, e.g., the consitituent lipid and protein molecules.

Cavitation also induces localized temperature increases and chemical reactions such as free radical production. Temperature rises in the vicinity of oscillating nuclei may produce hot spots within the tissue. The total integrated contribuion of such hot spots to the bulk tissue heating may be such as not to be recorded by a thermocouple, though temperatures near the cavitating nuclei may reach levels capable of affecting adjacent tissue structures, possibly by making their membranes leaky.

Fu et al. [1979] and Armour and Corry [1982] observed a cavitation-induced loss of reproductive integrity in intact cultured cells that was inhibited by the presence of free radical scavengers. Armour and Corry [1982] also demonstrated a change in membrane permeability because the affected cells no longer excluded the dye trypan blue. The inability to exclude trypan blue was immediately manifest after the ultrasonic irradiation and not at some later time as observed in cell death from ionizing

radiation. Hence, the permeability change was an immediate result of the ultrasound and not a delayed effect resulting from another form of tissue damage. How the free radicals are involved in producing such a permeability change is unknown. Perhaps they poisoned the cells, or reduced or oxidized functional portions of membrane associated proteins or lipids that are normally required to maintain proper ionic and osmotic gradients.

Although gross mechanical damage to the membranes was not observed except for the highest dosages used in this study, this does not mean that the bubble motion itself had no effect on the tissue. El'piner et al. [1965] produced tissue damage in the cat brain similar to that described for stages 1 and 2 in Chapter 5 using a vibrating needle. This system models a stable, oscillating bubble and sets up a pattern of microstreaming in the medium [Nyborg, 1968; El'piner et al., 1965]. El'piner et al. [1965] argued that the microstreaming induced the tissue damage. However, since there was no cell disruption as observed accompanying microstreaming <u>in vitro</u> [Hughes and Nyborg, 1962; Rooney 1970], the microstreaming would have to affect the tissue in a more subtle manner. Perhaps the microcurrents against the tissue membranes resulted in a frictional heating or a membrane stress altering selective permeability.

The acoustic intensities used in this study were probably incapable of fracturing the tissue to create cavities [Flynn, 1964; Flynn, 1982]. Hence, the cavitation nuclei must either have been already present in the tissue or formed rapidly from the dissolved gases upon irradiation.

Much has been written concerning the formation and stability of cavitation nuclei [Crum, 1982a, 1982b). There is one mechanism of nuceli formation that is not discussed that may be involved in the irradiation tissue, which was mentioned briefly in Chapter 2. The ultrasonically-induced temperature rise occurred only in a small volume of the cat brain and the mouse spinal cord. As the temperature increased, the solubility of the dissolved gases in both the blood and interstitial fluids of the irradiated volume decreased [CRC Handbook, 1974], particularly for the carbon dioxide. Some of the now released gas is, of course, carried away by the blood flow, but blood flow also brings in fresh blood to the heated volume so that more gas is released. As the tissue temperature continues to rise even more gas comes out of solution. The released gas may provide the nuclei required for cavitation. Nuclei smaller than resonant size may grow via rectified diffusion.

10.6. Concluding Remarks

The results of this study suggest topics for further experimentation concerning the effects of ultrasound on biological tissue. One study would be to quantitate the ultrasonically induced damage in the cat brain or neonatal mouse spinal cord, viz., for each dosage score the percentage of the morphological features according to the degree to which they are altered, and record how this distribution changes as a function of post irradiation time. The experimental results might be made more consistent in the cat brain by removing the brain meninges prior to irradiation. The experiments might also be designed to include

irradiations with intensities both higher and lower than 300 W/cm^2.

A concerted effort should be made to detect cavitation in the cat brain, either by direct measurement of subharmonic signals or varying physical parameters known to affect cavitation, e.g., temperature, ambient pressure, and acoustic frequency to see how they affect the resultant tissue damage. The role of free radical formation should also be investigated, possibly by perfusing free radical quenchers through the animals.

An attempt should be made to measure any ultrasonically induced changes in the ionic content of both the extracellular and intracellular compartments. This can be accomplished using ion sensitive microelectrodes similar to those employed by Harris et al. [1981]. Experiments along this line are already being performed by the author at Stanford University using ultrasonically irradiated or hyperthermia treated cultured neurons. Preliminary results indicate a reduction in the intracellular potassium concentration in a response to both the ultrasound and the hyperthermia treatments.

CHAPTER 11

SUMMARY

Multiple sites in the cat brain were irradiated with high intensity, focused ultrasound. Both light and electron microscopy were used to observe the tissue, and a scoring system utilizing nine stages was used to describe the resultant tissue damage. The increasing degrees of damage presented in stages one through nine represent the temporal order in which the altered morphology developed in the irradiated tissues. Chemical synapses were always the first structures affected by the ultrasound, followed by the mitochondria, neurons, glial cells, and the myelinated axons. The rate at which the morphological changes progressed in a lesion increased with increasing ultrasonic dosage, as indicated in Table 5.1. Tissue damage decreased with increasing distance from the center of the focal lesions, and the spatial gradient of altered morphology was identical to that described for the temporal sequence, with stage 1 tissue damage present at the lesion perimeter.

Tissue with a higher white matter content required a lower dosage to induce tissue damage. Recordings from embedded thermocouples demonstrated that this resulted because higher temperatures were generated in irradiated white matter than gray matter, as illustrated in Table 4.1. However, in a given lesion, the nonmyelinated structures developed altered morphology before the adjacent myelinated structures, suggesting that the myelin protected the contents of the axons.

Ultrasonically irradiated spinal cord tissue from neonatal mice was examined with both light and electron microscopy. Nonparalyzed and temporarily paralyzed specimens showed no signs of altered spinal cord morphology. Paralyzed animals exhibited altered spinal cord morphology similar to that observed in the irradiated cat brains. Tissue damage was greatest along the regions where the spinal cord bordered the spinal column, particularly in the ventral portion of the spinal cord. This observation suggested that heat conducted from the more highly absorbing spinal column tissue into the spinal cord enhanced the effect of the ultrasound.

Pressurizing the irradiation chamber to 16 atm reduced the magnitude of the altered morphology produced by a given ultrasonic dosage. This result, together with the data of Frizzell et al. [1983], suggests that acoustic cavitation was involved in producing the tissue damage.

Freeze-fracture replicas made from both the irradiated cat brain and mouse spinal cord tissue showed no initial signs of algered membrane ultrastructure. When swelling of the tissue structures became evident, the surface density of the membrane particles was decreased, and the particles tended to form aggregates upon the membrane surface.

Cultured BHK cells were heated for various times at temperatures similar to the peak temperatures recorded by the cat brain embedded thermocouples. Temperatures less than 57^{o}C required exposure times much longer than the ultrasonic exposure times to produce altered morphology in the BHK cells (see Table 9.1). This observation suggests that the ultrasonically-induced

hyperthermia was not responsible for the resultant tissue damage unless the peak temperatures exceeded 57°C.

Extraction of the BHK membrane revealed cytoskeletal morphology which changed in response to the hyperthermia treatments. Reduction of the cytoskeleton filament population and the formation of a juxtanuclear filament condensation were responsible for some morphological changes in other subcellular structures, e.g., the loss of free ribosomal patterns and a condensation of the subcellular organelles towards the cell nucleus. Similar changes were observed in the brain and spinal cord following ultrasonic irradiation, suggesting that the cytoskeleton may also be responsible for these changes in the irradiated tissue.

Using the results of studies linking changes in tissue morphology to tissue function, it is suggested that the primary site of ultrasonic damage is in the selective permeability of the biological membranes. Since no membrane ultrastructural changes were observed initially, the damage must have occurred on the macromolecular level. The changing ionic content of the tissue structure, such as an influx of calcium ions, is known to trigger morphological changes similar to those observed in the ultrasonically irradiated tissues.

ABBREVIATIONS

Å - Angstrom unit

AH - Axon hillock

Ax - Nonmyelinated axon

BHK - Baby hamster kidney

cp - Cytoplasmic particle

CPD - Critical point dried

Cr - Chromosome

cr - Chromatin

crs - Crista

Dy - Dendrite

DyL - Dendrite-like structure

EM - Electron microscopy

er - Endoplasmic reticulum

EW - Endothelial wall

Ext - Externally facing membrane

g - Golgi apparatus

GM - Gray matter

GWGM - Gray-white gray matter

H - Halo region

HVEM - High voltage electron microscopy

IF - Intermediate filament

Int - Internal facing membrane surface

Jc - Juxtanucleas condensation

Jd - Junctional density

LM - Light microscopy

Lu - Lumen

Ly - Lysosome

m - Mitochondrion

Ma - Myelinated axon

Mf - Microfilament

mp - Membrane particle

Mt - Microtubule

mvb - Multivesicular body

My - Myelin

MyL - Myelin-like structure

N - Neuron

Nb - Nissl body

nf - Neurofilament

np - Nuclear pore

nu - Nucleolus

Od - Oligodendrocyte

p - Pore

Po - Postsynaptic element

Pre - Presynaptic element

r - Ribosome

rer - Rough endoplasmic reticulum

Sb - Spherical body

ser - Smooth endoplasmic reticulum

Sf - Stress fiber

St - Membrane step

Sv - Synaptic vesicle

Sy - Synapse

T - Trailer

TEM - Transmission electron microscopy

th - Dendritic thorn

V - Void

v - Vesicle

WM - White matter

WWGM - White-white gray matter

Figure 1.1. Threshold ultrasonic dosage curve for lesion production in cat brain white matter (after F. J. Fry et. al., 1970).

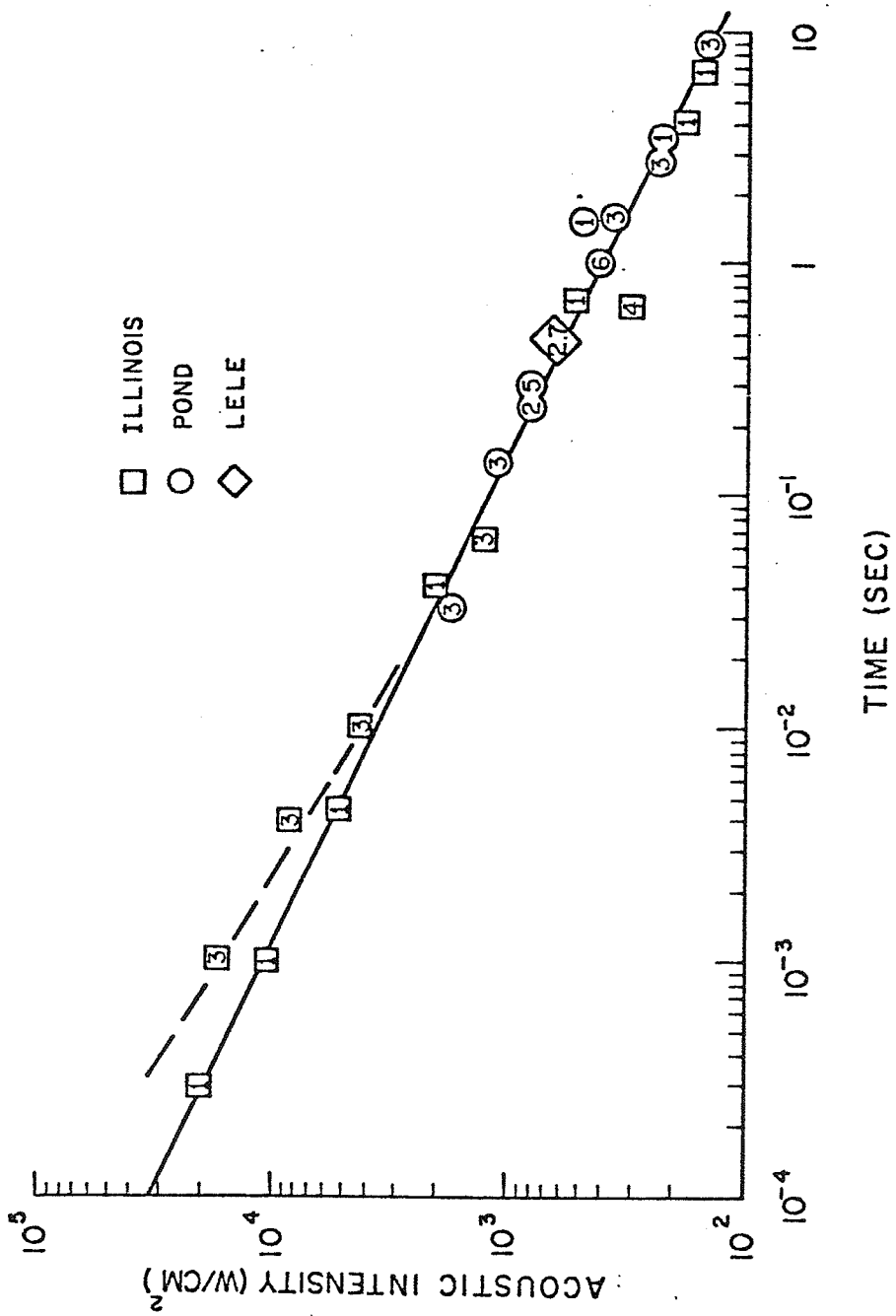
ILLINOIS
POND
LELE
ACOUSTIC INTENSITY (W/CM²)
TIME (SEC)
10⁵
10⁴
10³
10²
10⁻⁴
10⁻³
10⁻²
10⁻¹
1
10

Figure 1.2. Threshold dosage region for ultrasonically-induced hind limb paralysis in the mouse neonate at 10°C. The temperatures indicated in the graph are temperature rises measured by embedded thermocouples (after W. J. Fry and Dunn, 1956).

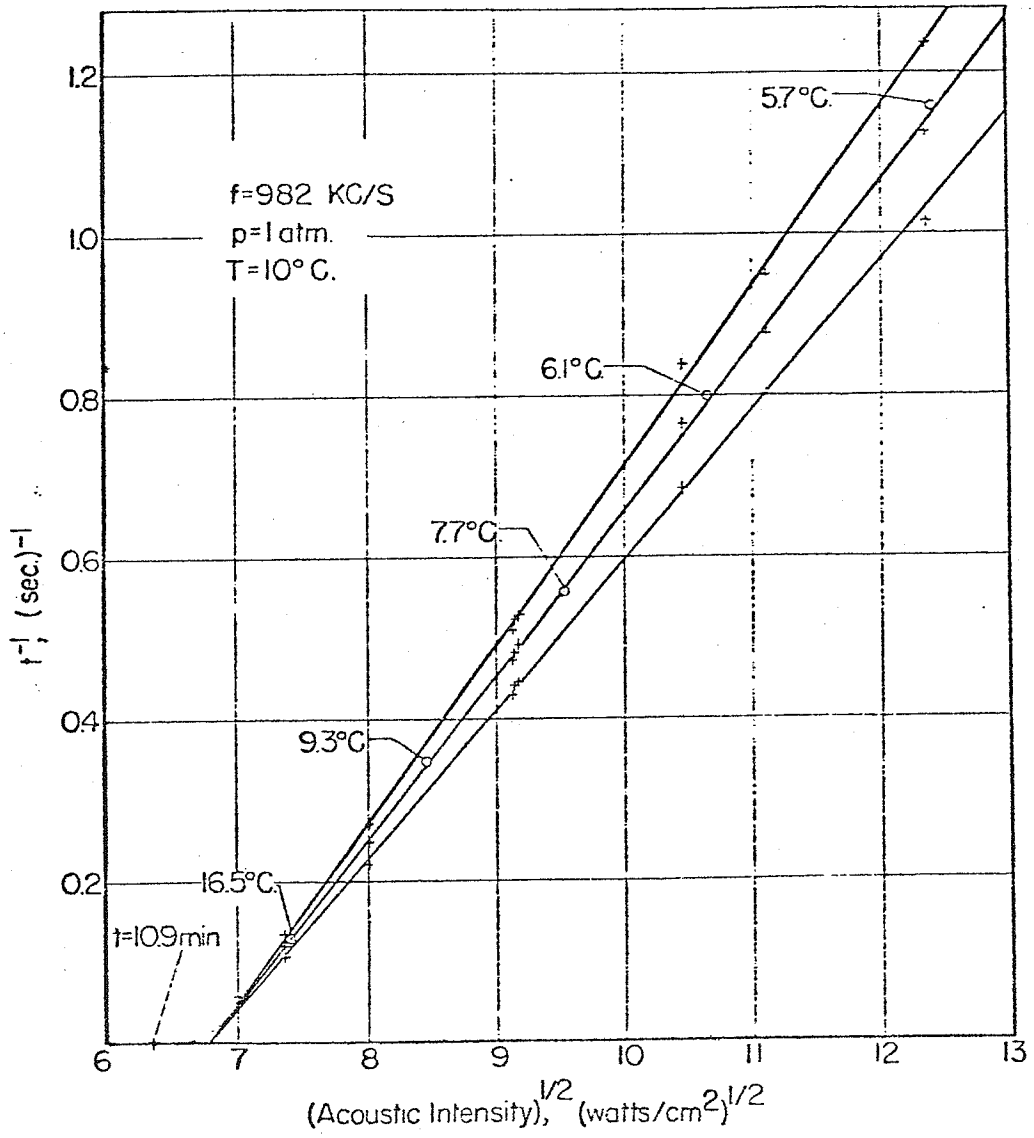
f=982 KC/S
p=1 atm.
T=10° C.
5.7°C.
6.1°C.
7.7°C.
9.3°C.
16.5°C.
t=10.9min
1.2
1.0
0.8
0.6
0.4
0.2
6
7
8
9
10
11
12
13
t^{-1}; (sec.)$^{-1}$
(Acoustic Intensity)$^{1/2}$ (watts/cm^2)$^{1/2}$

Figure 1.3. Sigmoidal distribution of percentage of mouse neonates paralyzed verses the reciprocal of the exposure time with an acoustic intensity of 83 W/cm2 (after F. J. Fry and Dunn, 1956).

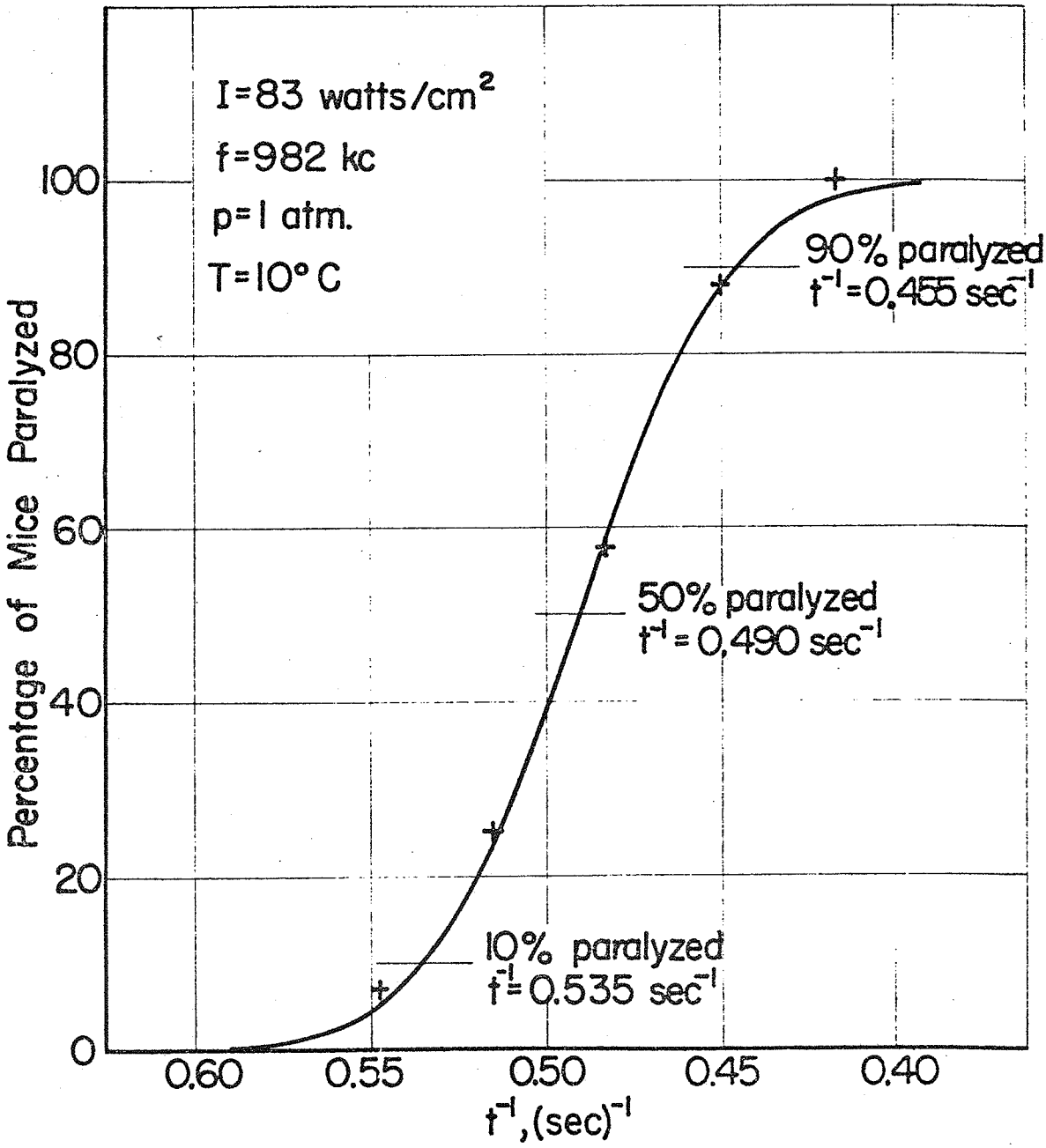
I=83 watts/cm²
f=982 kc
p=1 atm.
T=10° C
90% paralyzed
t⁻¹=0.455 sec⁻¹
50% paralyzed
t⁻¹=0.490 sec⁻¹
10% paralyzed
t⁻¹=0.535 sec⁻¹
Percentage of Mice Paralyzed
100
80
60
40
20
0
0.60
0.55
0.50
0.45
0.40
t⁻¹,(sec)⁻¹

Figure 1.4. The 50% paralysis curves for mouse neonates irradiated at ambient temperatures of 2, 10, and 20°C. Thermocouple recorded temperature rises are also shown (after Dunn, 1958).

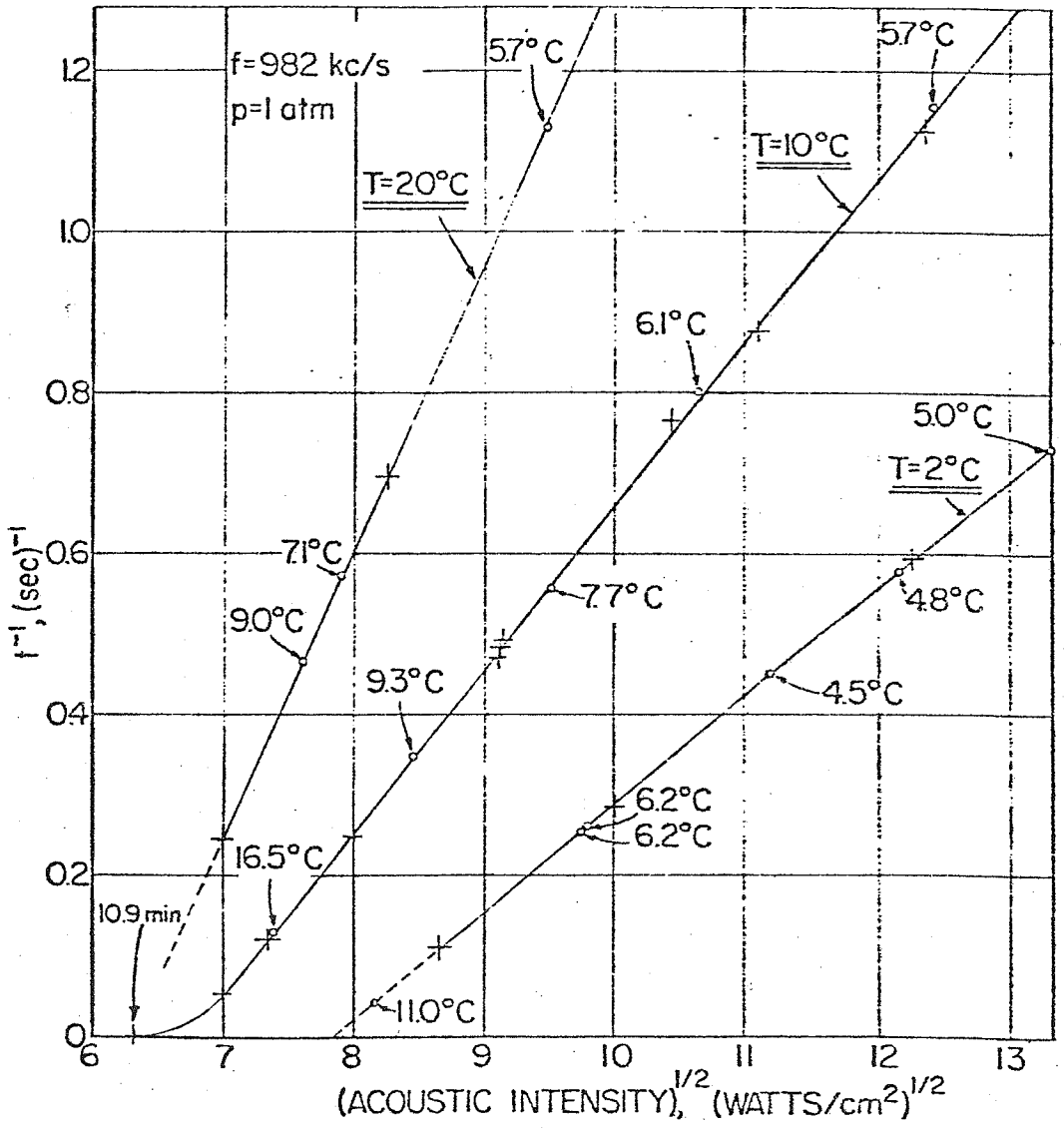
f=982 kc/s
p=1 atm
T=20°C
T=10°C
T=2°C
5.7°C
5.7°C
6.1°C
5.0°C
7.1°C
7.7°C
4.8°C
9.0°C
9.3°C
4.5°C
6.2°C
6.2°C
16.5°C
10.9 min
11.0°C
τ⁻¹, (sec)⁻¹
(ACOUSTIC INTENSITY)^1/2 (WATTS/cm²)^1/2
0
0.2
0.4
0.6
0.8
1.0
1.2
6
7
8
9
10
11
12
13

Figure 2.1. Record from cat brain embedded thermocouple exposed for 1.5 sec with 300 W/cm^2 intensity ultrasound. The rate of temperature rise in phase 1 contains a viscoelastic contribution resulting from relative motion between the thermocouple wires and the tissue. Phase 2 exhibits a nearly linear temperature rise, and the slope at 0.5 sec into the exposure is used to calculate . Phase 3 shows a deviation from linearity as heat is conducted away from the thermocouple. The rapid temperature drop from the peak temperature rise seen in phase 4 results from the loss of the viscoelastic component when the sound was turned off. Phase 5 shows the gradual cooling of the tissue surrounding the thermocouple as heat is conducted away.

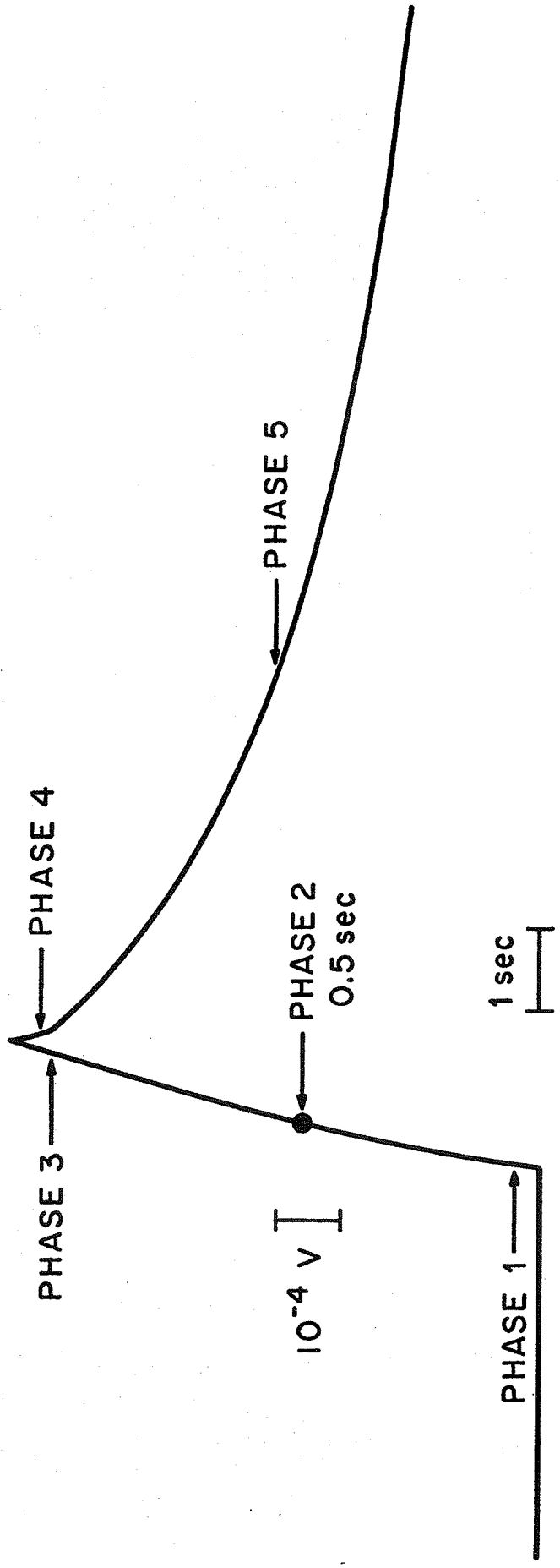
PHASE 5
PHASE 4
PHASE 2
0.5 sec
1 sec
PHASE 3
10^{-4} V
PHASE 1

Figure 2.2. Pressure verses volume graph illustrating that acoustic energy is lost to the medium if the medium condensation is out of phase with the changing acoustic pressure. The area enclosed by the curve 1-4-3-5-1 represents the energy lost by the acoustic wave.

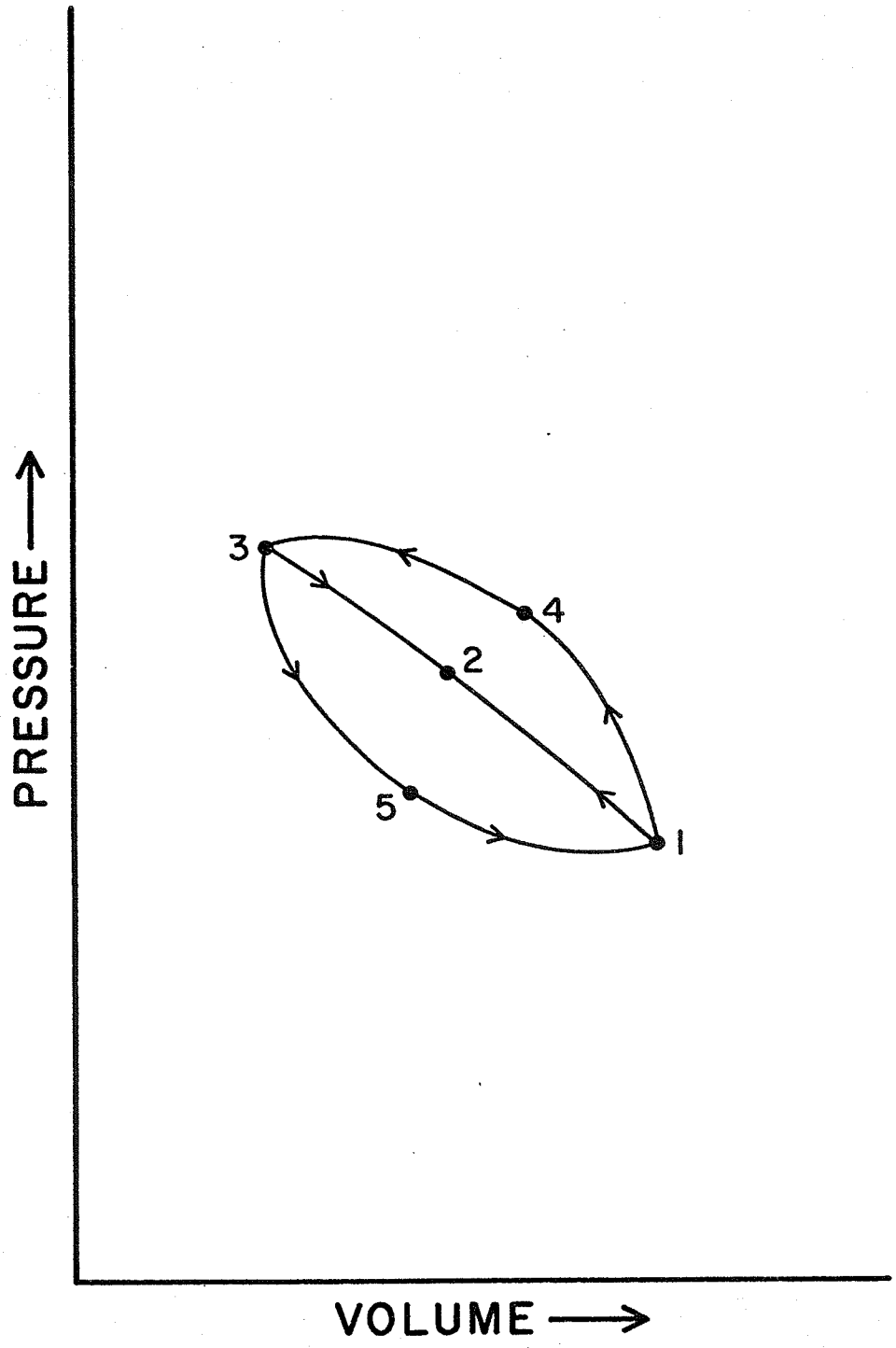
PRESSURE
VOLUME
3
4
2
5
1

Figure 2.3. This freeze-fracture micrograph of a normal cat brain cell demonstrates that the golgi, g, and the endoplasmic reticulum, er, (both the tubular, er_t, and sheet forms, er_s,) are intimately associated with the nuclear membranes (double arrowheads). Note the nuclear pores, np, and the fenestrations, f, in the endoplasmic reticulum.

Figure 2.4. Cytoskeleton of a BHK (baby hamster kidney) cell.

Figure 2.5. Radiation force, Fr, on a suspended steel sphere. In the formula for Fr, m is the mass of the sphere, I is the acoustic intensity and Y is the acoustic radiation factor which depends upon the material and dimensions of the sphere.

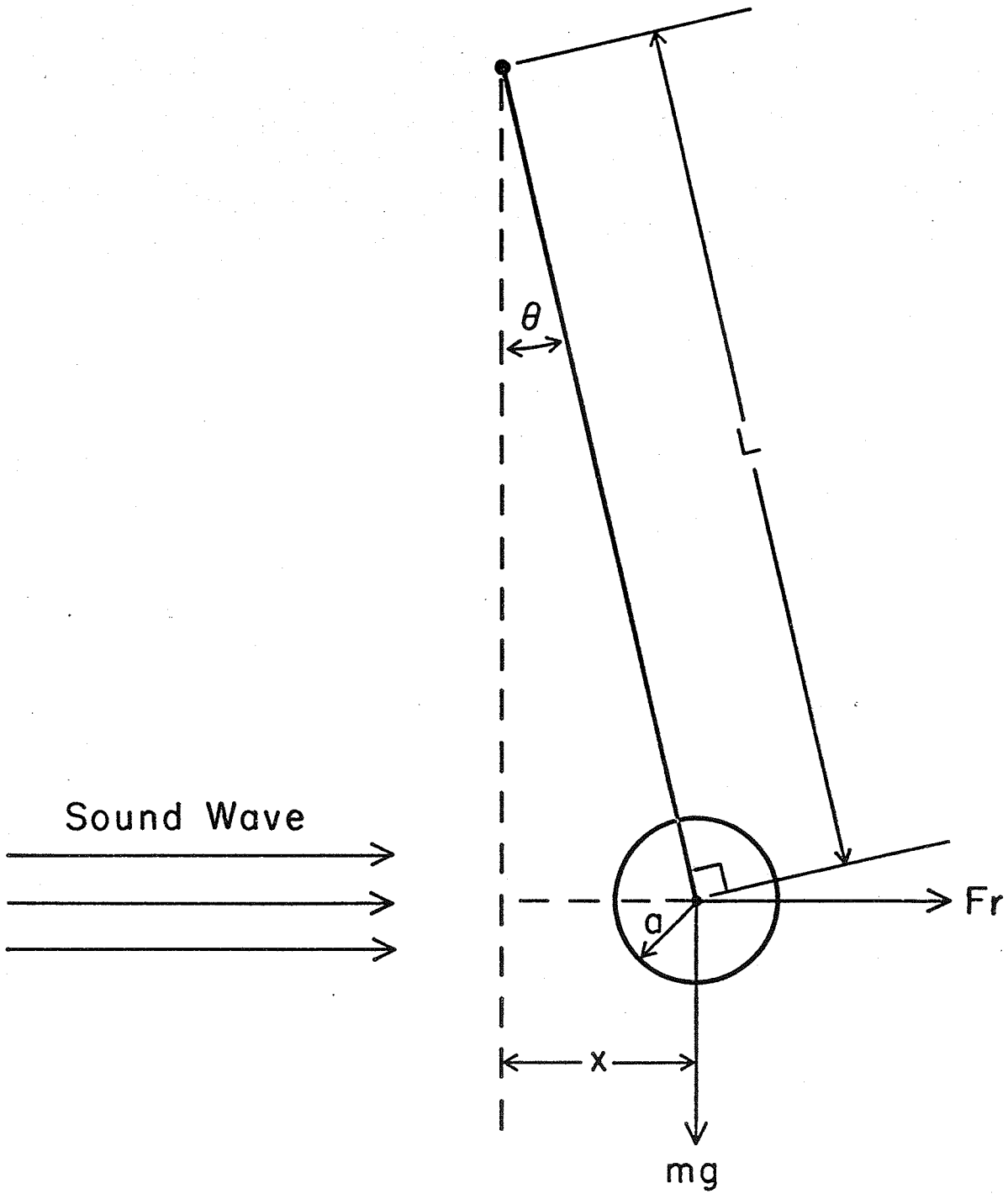

$$Fr = mg \tan\theta = \frac{mgx}{(L^2 - x^2)^{1/2}} = \frac{Y I \pi a^2}{c}$$

Figure 3.1. Transverse beam plots of the transducer used for the cat brain irradiations. Measurements were made in water, and in the plane transverse to the beam axis containing the focal point. Plot A was made along the length of the thermocouple wires. Plot B made along a line perpendicular to the wires. Note that Plot A is broader than Plot B. This results from thermal conduction along the wire.

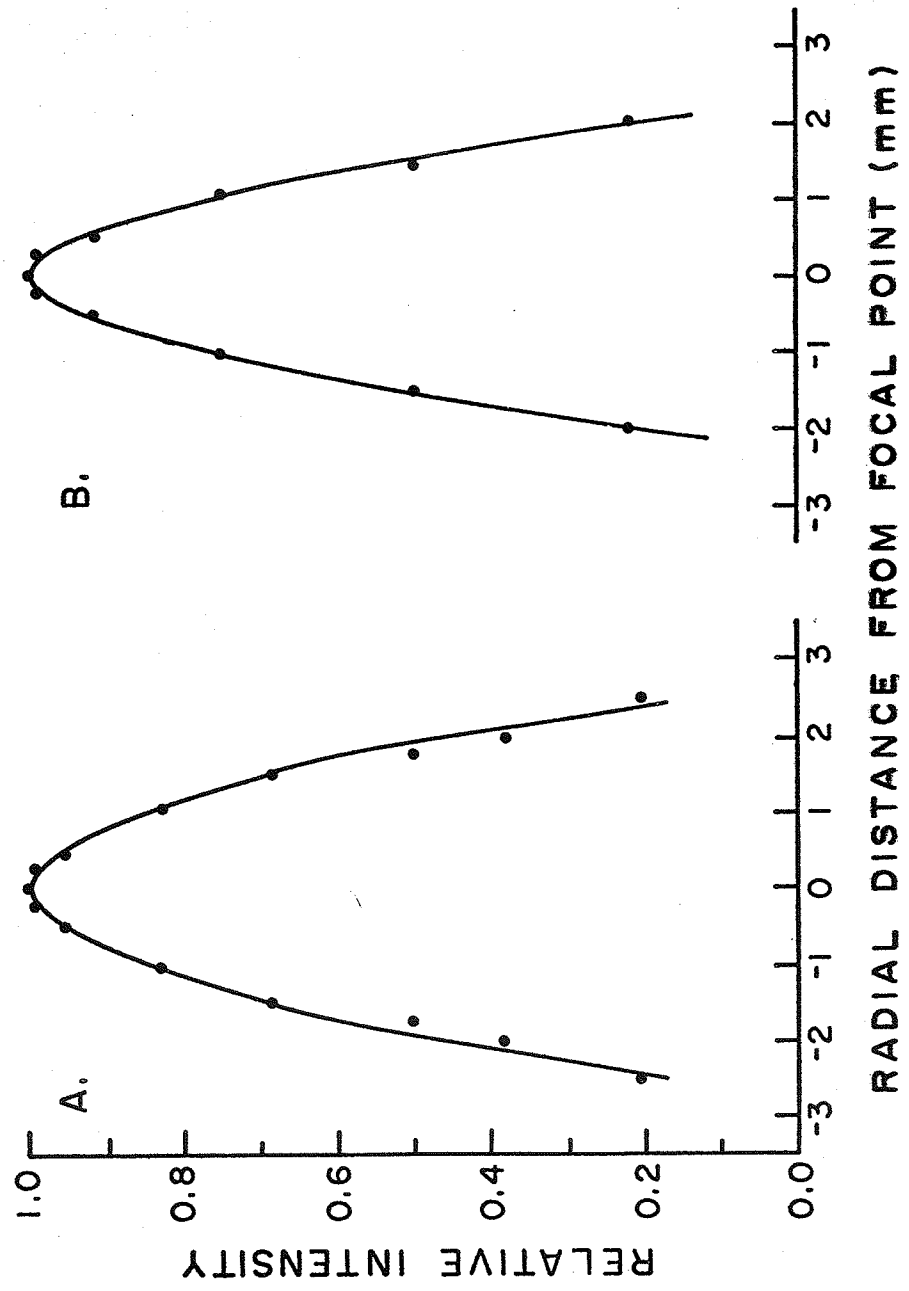
A.
B.
RELATIVE INTENSITY
1.0
0.8
0.6
0.4
0.2
0.0
-3
-2
-1
0
1
2
3
RADIAL DISTANCE FROM FOCAL POINT (mm)

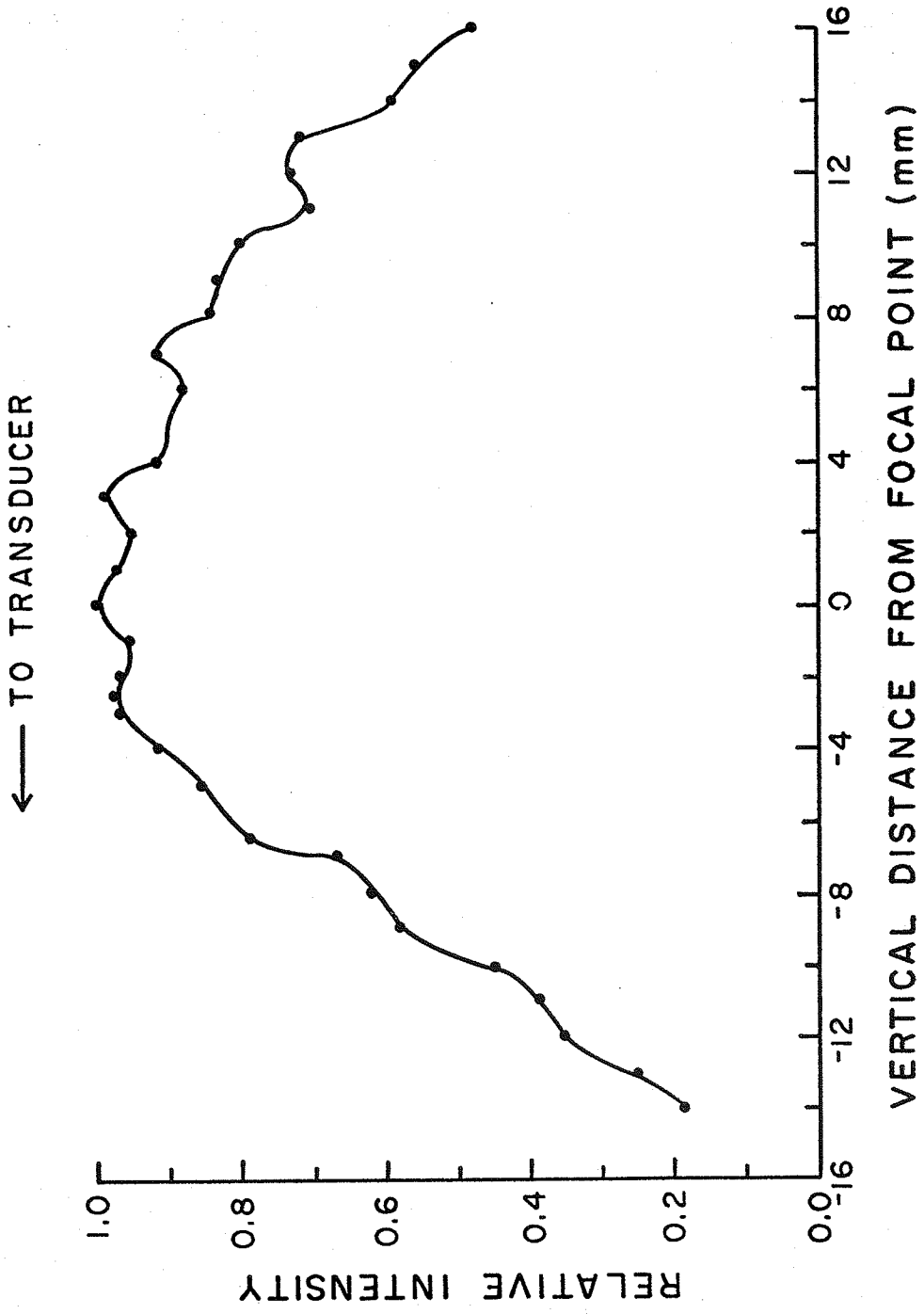
TO TRANSDUCER
RELATIVE INTENSITY
1.0
0.8
0.6
0.4
0.2
0.0
-16
-12
-8
-4
0
4
8
12
16
VERTICAL DISTANCE FROM FOCAL POINT (mm)

Figure 3.3. Scheme for locaing the thermocouple junction in the cat brain. The coordinates of the two points where the thermocouple wires enter the brain, viz., (A_1, B_1, C_1) and $A_2, B_2, C_2)$ are measured, and they are used to define a line vector a, where $a = (a_1, a_2, a_3) = (A_1 - A_2, B_1 - B_2, C_1 - C_2)$. The point (X,Y,Z) is at position ta where $X = ta_1 + A_2$, $Y = ta_2 + B_2$, and $Z = ta_3$. The parameter t is related to the length of the vector a and the distance of the junction from point (A_2, B_2, C_2), viz., D, as $t = D/ a$. The marker on the thermocouple corresponding to the distance D is then located at position (A_2, B_2, C_2). Since the line equation is known, adjustments in the position of the junction can be made accurately.

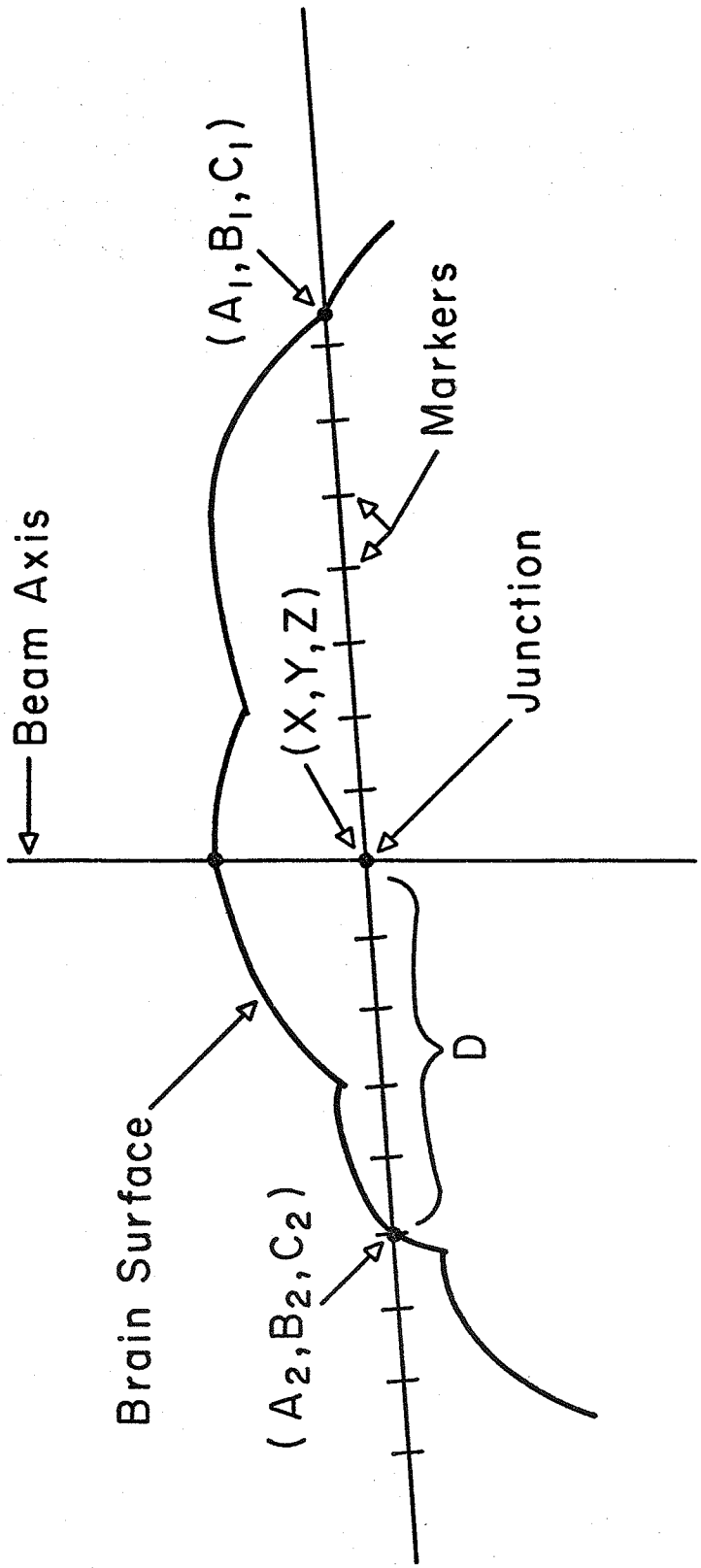
Beam Axis
(A_1, B_1, C_1)
Markers
(X, Y, Z)
Junction
D
Brain Surface
(A_2, B_2, C_2)

Figure 3.4. Scheme used to disect the brain tissue core and identify the subsequent tissue pieces.

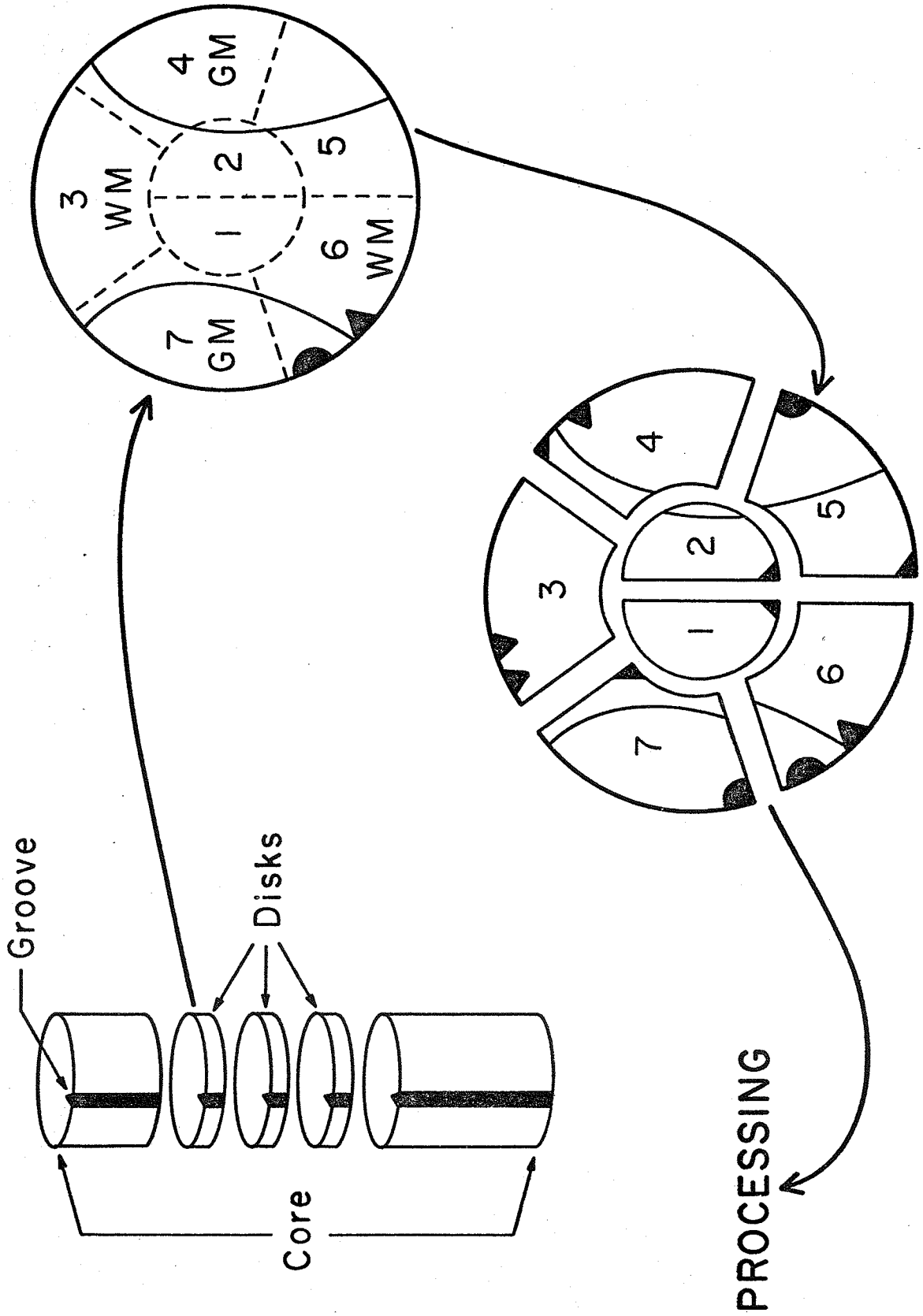
4
GM
5
3
WM
2
1
6
WM
7
GM
4
5
3
2
1
6
7
Groove
Disks
Core
PROCESSING

Figure 3.5. Freeze-fracture micrograph showing artifact produced when attempting to etch cryo-protected tissue.

Figure 4.1. Transverse beam plot of the transducer used for the cat brain irradiations. Measurements were made in the cat brain, in the plane containing the focal point. The scatter in the data points resulted from the transducer movement not always being exactly perpendicular to the thermocouple wires.

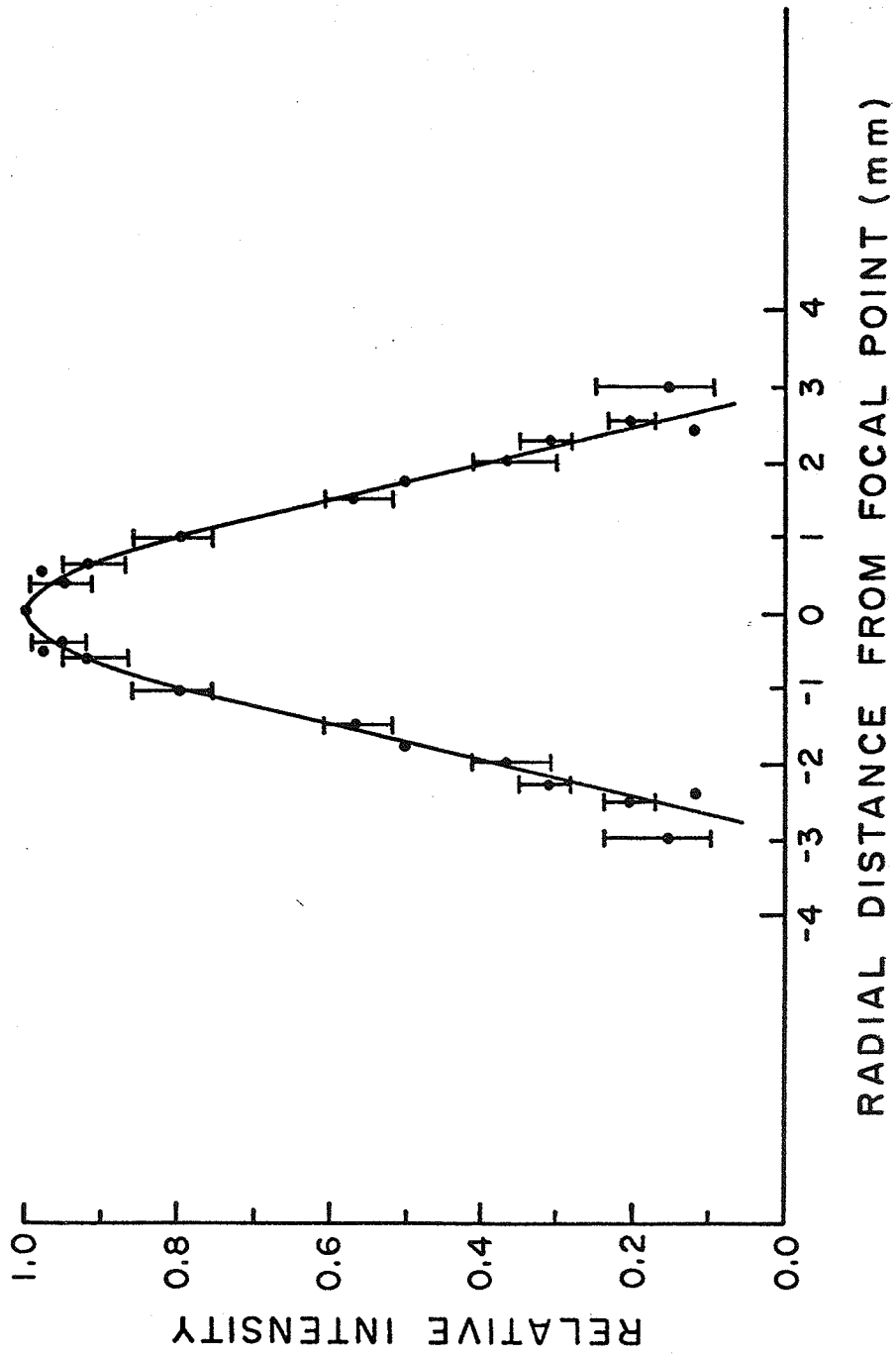
RELATIVE INTENSITY
1.0
0.8
0.6
0.4
0.2
0.0
-4
-3
-2
-1
0
1
2
3
4
RADIAL DISTANCE FROM FOCAL POINT (mm)

Figure 4.2. Axial beam plot of the transducer used for the cat brain irradiations, measured in the cat brain. The only significant deviation from the plot obtained in water is the section between -3 and -7 mm from the focal point. The dotted line averages out this sinusoid-like region.

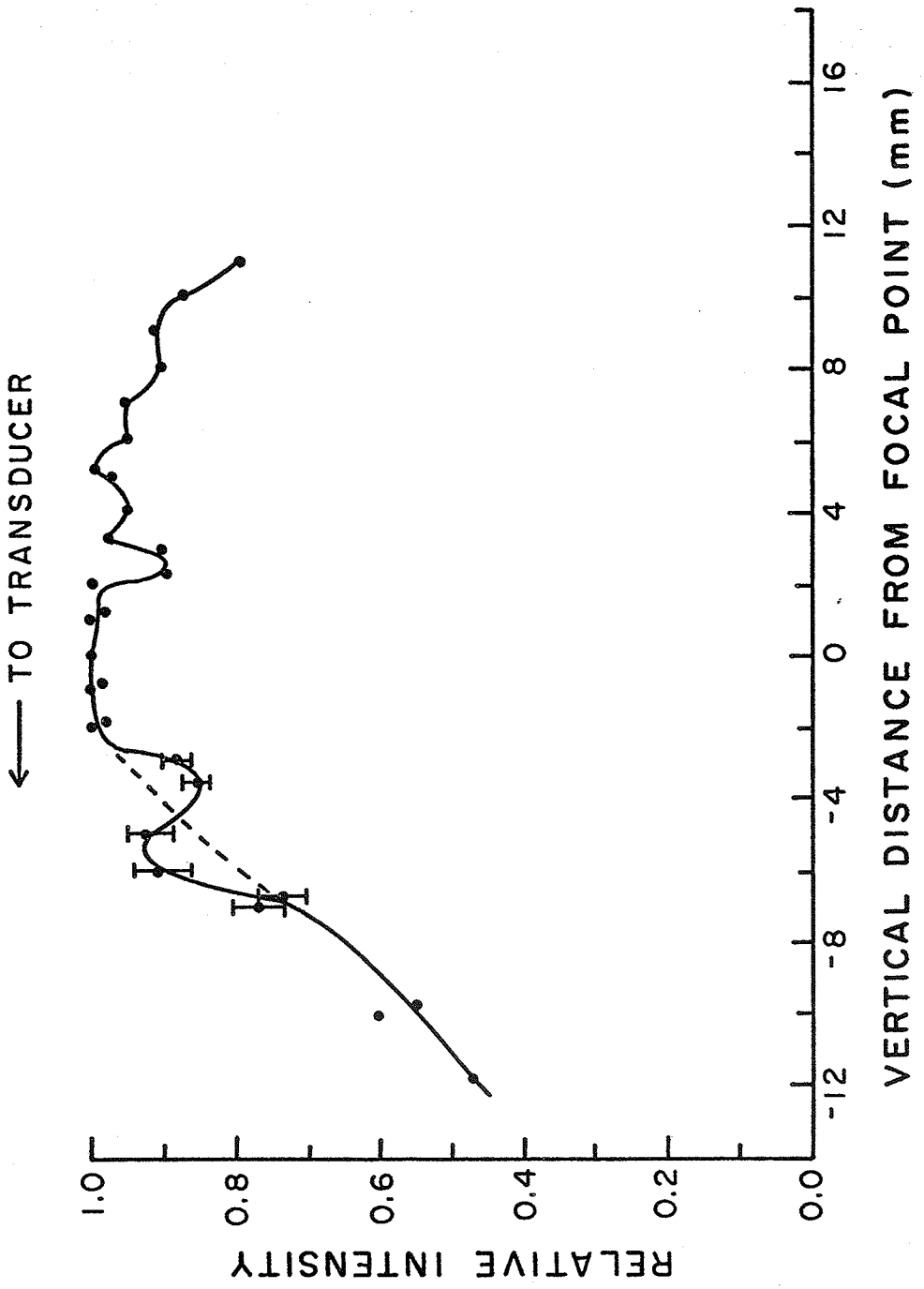
TO TRANSDUCER
RELATIVE INTENSITY
1.0
0.8
0.6
0.4
0.2
0.0
-12
-8
-4
0
4
8
12
16
VERTICAL DISTANCE FROM FOCAL POINT (mm)

Figure 4.3. Thermocouple recording in plane of focal point with the junction located 2.25 mm away from the focal point. The response was induced by a 1 sec expsoure with 300 W/cm^2. Note that the secondary temperature rise, resulting from heat conducted away from tissue nearer the focal point, is greater than that resulting from the energy absorption at that particular point, viz., the initial temperature rise.

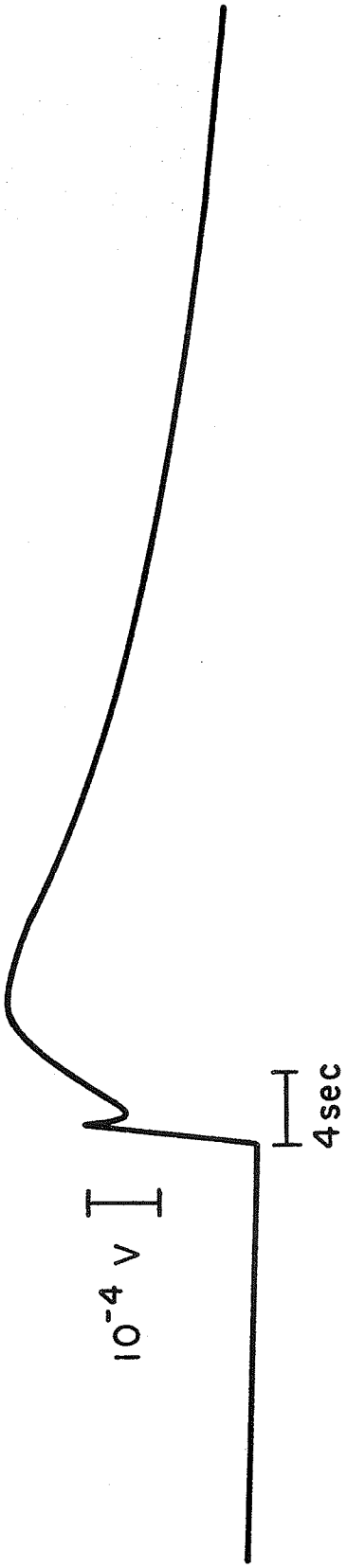
4sec
10^{-4} v

Figure 4.4a. Thermocouple track through cat brain section. The arrowhead marks the position of the thermocouple junction.

Figure 4.4b. Higher magnification of Fig. 4.3a showing the tissue damage induced by the ultrasonic irradiations.

Figure 4.5a. Thermocouple track through cat brain receiving identical ultrasonic exposures as sectioned in Fig. 4.3a, but sacrificied 5 hr later following the exposures.

Figure 4.5b. Higher magnification of Fig. 4.4a showing the tissue damage induced by the ultrasonic irradiations. Note that the damage is much greater than that seen in Fig. 4.3b.

Figure 5.1. Normal WM field showing myelinated axons, Ma, myelin sheath, My, and an oligodendrocyte, Od.

Figure 5.2a. Longitudinal section through a myelinated axon showing the mitochondria, m, and the microtubules, mt, in the axoplasm.

Figure 5.2b. Transverse section of a myelinated axon. The dark, dense line and lighter intraperiod line are evident in the myelin sheath, My. Both microtubules, mt, and neurofilaments, nf, are seen in the axoplasm, and more details of the mitochondria are evident, including the cristae, crs.

Figure 5.3. Normal oligodendrocyte cell showing the dark staining nucleus, N, mitochondria, m, golgi, g, lysosomes, Ly, Note the patterns of the free ribosomes. Filament bundles, f, from an adjacent astrocyte are also visible.

Figure 5.4. Normal GM field showing nonmyelinated, Ax, and some myelinated, Ma, axons, dendrites, Dy, dendritic thorns, th, and synapses, Sy.

Figure 5.5. Normal neuron with the characteristic large, light staining nucleus, and large, dark staining nucleolus.

Figure 5.6. Higher magnification micrograph of a neuron clearly showing the Nissl bodies, Nb. Note that the free ribosomes both in the Nissl bodies and in the rest of the cytoplasm exhibit distinct patterns, identical to those observed within the oligodendrocyte in Fig. 5.3. Besides the mitochondria and lysosomes, another membrane-bound organelle, the multivesicular body, mvb, was observed within the neuronal cytoplasm. This figure also illustrates the fine structure of the nuclear membranes, including the pores, p.

Figure 5.7. Synapses with three different cleft curvatures, viz., positive, 1, flat, 2, and negative, 3, are present. The electron dense junctional density, Jd, is associated with the synaptic cleft which represents the tight junction formed between the pre-, Pre, and postsynaptic, Po, elements. Note the distribution of the synaptic vesicles, Sv.

Figure 5.8. Micrograph of a normal WWGM region.

Figure 5.9. Micrograph of a normal GWGM region.

Figure 5.10. A LM micrograph of a lesion cross section in WM. Note the transparent regions surrounding some of the blood vessels, arrowheads, even around vessels in otherwise normal appearing tissue.

Figure 5.11. Stage 1 tissue showing the synaptic vesicle aggregates of both synaptic complex associated vesicles, Sv, and nonassociated aggregates, *. Membranous debris, Md, was common in the presynaptic elements, some of which resembled swollen vesicles, [ ]. Note the electron dense material associated with the vesicle aggregates, and the decreased electron density of the altered presynaptic elements' cytoplasm.

Figure 5.12. Stage 2 WGM showing increased swelling of the presynaptic elements, Pre, and mild demyelination of some axons.

Figure 5.13. Higher magnification of stage 2 tissue. Synaptic vesicle numbers are further reduced and the cytoplasm in the presynaptic element is less than that observed in stage 1. Many mitochondria showed a mild condensation evidenced by an increase in matrix density and swelling of the intracristal spaces (arrowhead).

Figure 5.14. A stage 3 neuron with swollen nucleus, N, and condensed chromatin, cr. Both the golgi, g, and the endoplasmic reticulum, er, are swollen, and the mitochondria, m, in both the neurons and surrounding structures exhibit the altered morphology described in stage 2.

Figure 5.15. Stage 3 neuron with the intracellular organelles concentrated in the region surrounding the nucleus.

Figure 5.16. Stage 3 neuron with a condensed nucleolus, nu, in addition to the condensed chromatin, cr.

Figure 5.17. Higher magnification of Fig. 5.16 for comparison to Fig. 5.6. Nissl bodies no longer exist in the stage 3 neurons. Both the smooth, ser, and rough, rer, endoplasmic reticula are swollen, and fewer ribosomes are attached to the rough engoplasmic reticulum. Fewer free ribosomes display the patterns seen in Fig. 5.6. Golgi, g, also exhibit swelling, particularly near the terminal regions forming the secretory vesicles, *. The structure indicated by the question marks may be an altered multivesiculas body.

Figure 5.18. Stage 4 WGM. Varied degrees of altered mitochondrial morphology are seen in the nonmyelinated structures (numbers 1 - 4), but the mitochondria within the myelinated axons appear unaltered. Membranous whorls of unraveled myelin, *, are present near several myelinated axons.

Figure 5.19. Stage 4 oligodendrocyte with both cytoplasm and nucleoplasm being less electron dense. The remaining organelles exhibit altered state identical to those described for the neurons in stage 3 and illustrated in Figs. 5.14 - 5.17.

Figure 5.20. Normal capillary in GM. Note the clear lumen, Lu, indicating a good perfusion, and the relationship between the endothelia wall, Ew, and the surrounding structures.

Figure 5.21. Stage 4 capillary. Electron transparent vacuoles, v, are present within the endothelia cells. The structures bordering the capillary are less electron dense and swollen.

Figure 5.22. Stage 5 synapse. Both the pre- and postsynaptic elements were less electron dense and swollen. Only a few vesicles remain in the presynaptic element, and those are near the junctional density. Microtubules, mt, can still be seen together with membranous debris, Md. The presynaptic element membrane is severely distorted and swollen at the points indicated by the arrowheads. One mitochondria is in the process of losing its outer membrane (double arrowheads), while several others, *, appear to have already done so.

Figure 5.23. Various forms of the ring-like structure of mitochondria that have lost their outer membranes (numbers 1 - 4).

Figure 5.24. Stage 5 neuron. See description Section 5.8.3.

Figure 5.25. Stage 5 oligodendrocyte. Although no cristae are present, the swollen structures designated as mitochondria, m, are identified by means of their double membranes (double arrowheads).

Figure 5.26. Stage 5 capillary. The structures bordering the capillary have ruptured forming an electron transparent void or cuff surrounding the capillary. The endothelial cells of the capillary itself appear less electron dense, probably also the result of swelling.

Figure 5.27. Stage 6 GM showing the large, transparent voids and the varied degrees of altered mitochondria, m (numbers 1 - 4), synapses, Sy, and other structures.

Figure 5.28. Stage 6 shrunken neuron with small vesicles, v, along its perimeter. Trailers (arrowheads) from the cell apprear to be attached to surrounding structures, and some of these structures appear distorted by the shrunken neuron.

Figure 5.29. Electron dense thorns, th, from a shrunken neuron. Note the small, transparent vesicles, v.

Figure 5.30. Stage 6 WM. The mitochondria in myelinated axons exhibited a wide range of altered morphology. Microtubules and neurofilaments exhibited a less ordered arrangement in the axons, and the axoplasm is less electron dense.

Figure 5.31. Stage 7 WM. A wide range of altered mitochondrial morphology represent (numbers 0 - 5), and there is an increased degree of demyelination. The electron transparent spaces between the axons may be the remnants of swollen, nonmyelinated structures, or fluid-filled spaces resulting from edema.

Figure 5.32. Stage 7 capillary showing extensive cuffing about the capillary and gross damage to the endothelial cells.

Figure 5.33. Stage 7 WM. Grossly damaged mitochondrion, m, shows that the cristae, crs, are still continuous with the inner mitochondrial membrane. The asterisk indicates an inter-axon space.

Figure 5.34. Stage 8 WM. Note the wide range of altered mitochondrial morphology (numbers 1 - 4) and the intraverted myelin whorls.

Figure 5.35. Stage 9 WM. Note the still intact lysosomes (arrowheads) in an otherwise dessimated oligodendrocyte, Od.

Figure 5.36. Friable WM showing myelin, My, myelinated axon, Ax, and oligodendrocyte, Od.

Figure 5.37. Section from tissue exposed for 0.42 sec with 300 W/cm^2 and sacrificed 24 hr later. The synapses, Sy, mitochondria, m, and other tissue structures show the mild damage described for stages 1 and 2.

Figure 6.1. HVEM stero micrograph of normal synapse. The cytoplasm of both the pre-, Pre, and postsynaptic, Po, elements is electron dense. Other synapse features, viz., the synaptic vesicles, Sv, junctional density, Jd, and mitochondria, m, are clearly visible.

Figure 6.2. HVEM stero micrograph of synapse from stage 2 cat brain tissue. The most obvious differences from Fig. 6.1 are the decreased electron density of the presynaptic element, Pre, and a reduction in the number of synaptic vesicles, Sv. Most of the remaining vesicles are aggregated near he junctional density, Jd, and have an electron dense material associated with them. Filamentous strands, St, are seen connecting the vesicle aggregate to The delimiting membrane of the presynaptic membrane. No changes are observable in the postsynaptic element.

Figure 7.1. Threshold exposure curve for mouse neonate hind limb paralysis induced by 144 W/cm^2 ultrasound (after Frizzell et al., 1983).

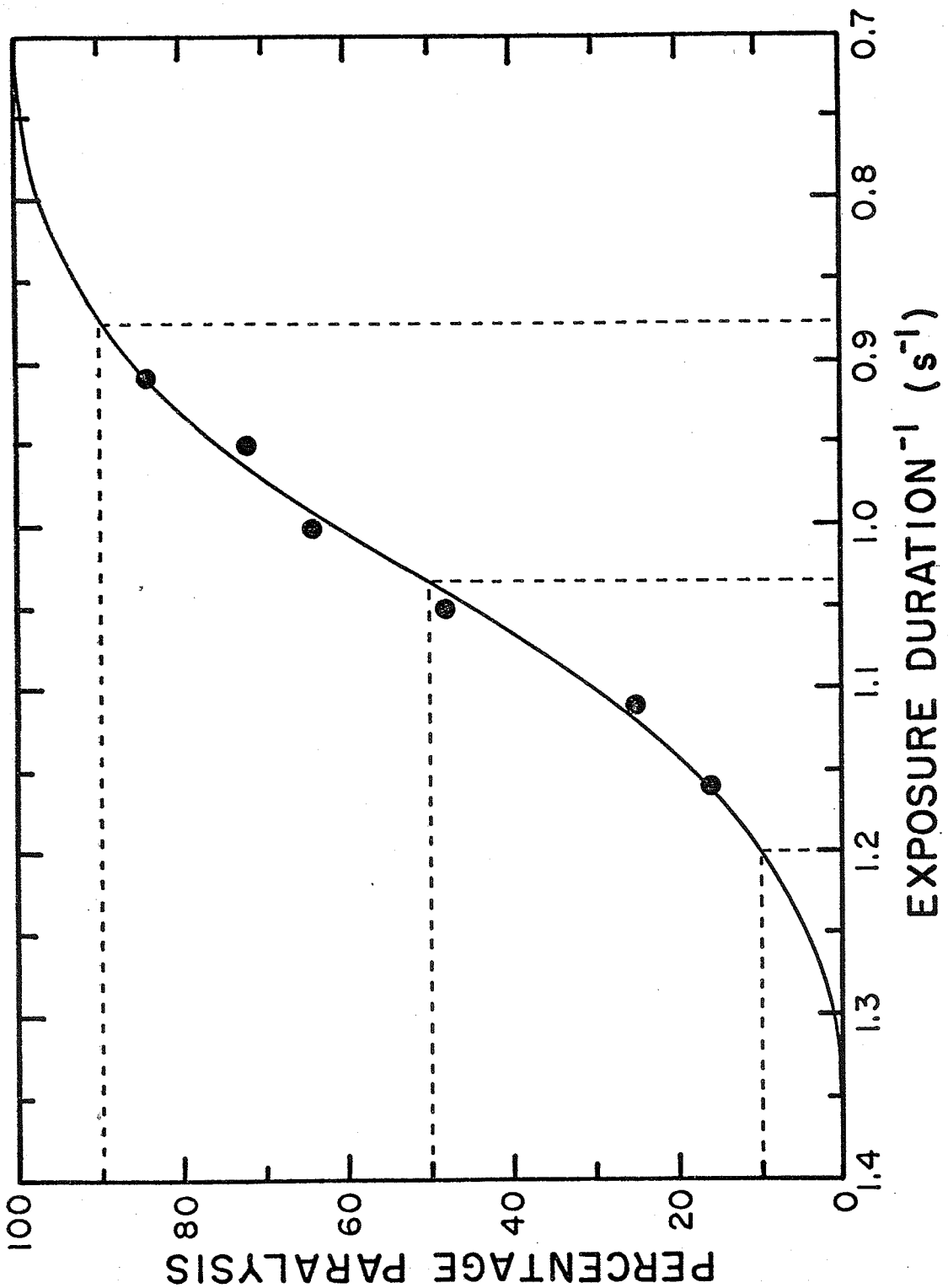
PERCENTAGE PARALYSIS
100
80
60
40
20
0
0.7
0.8
0.9
1.0
1.1
1.2
1.3
1.4
EXPOSURE DURATION^{-1} (s^{-1})

Figure 7.2. Plot of acoustic intensity verses exposure time required to produce 50% paralysis in mouse nenonates. Note the effect of increasing the irradiation chamber pressure to 16 atm for the 289 W/cm^2 exposures.

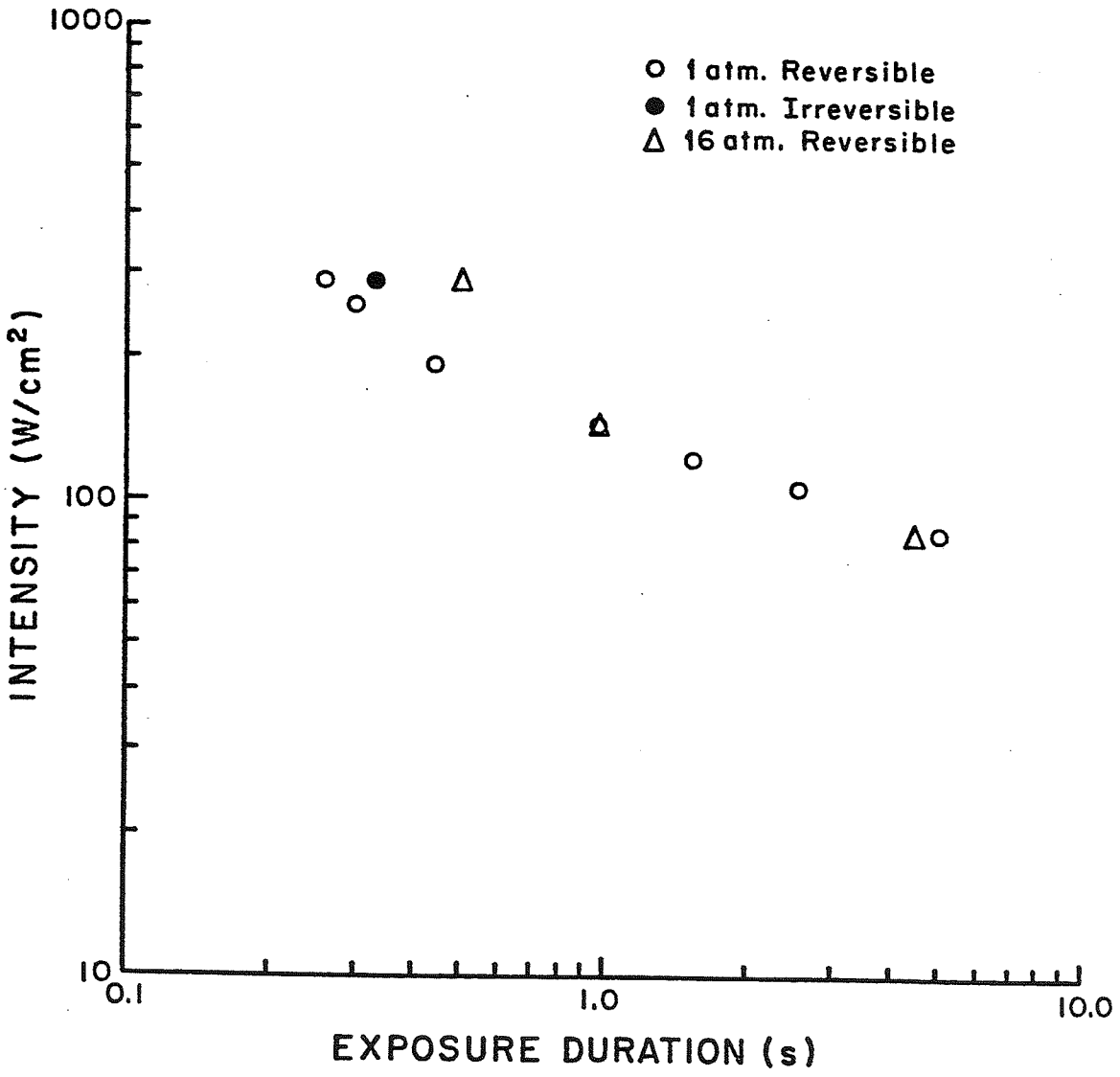
1000
100
10
INTENSITY (W/cm²)
0.1
1.0
10.0
EXPOSURE DURATION (s)
1 atm. Reversible
1 atm. Irreversible
16 atm. Reversible

Figure 7.3a. Normal spinal cord section. The V indicates the ventral half.

Figure 7.3b. Higher magnification of Fig. 7.3a. The asterisk marks the corresponding position in the two micrographs.

Figure 7.4. Micrograph of the peripheral region of a normal spinal cord. Nonmyelinated axons, Ax, predominate in this tissue. Dendrite-like structures, DyL, and myelin-like structures can also be observed. Note the difference in the electron density of the mitochondria located in the axons compared to those in the other structures.

Figure 7.5. Higher magnification of Fig. 7.4. Cross sections of microtubules, Mt, and neurofilaments, nf, can be seen in the nonmyelinated axons, Ax. The fine structures of a normal spinal cord synapse is also seen.

Figure 7.6. Low magnification field of normal tissue from the central region (or GM) of the spinal cord.

Figure 7.7. Higher magnification of central region tissue showing synapses, Sy, axons, Ax, dendrites, Dy, dentritic thorns, th, and mitochondria.

Figure 7.8. Normal spinal cord neuron. Note the prominent nucleolus, nu, within the large rounded nucleus, N.

Figure 7.9. Higher magnification of Fig. 7.8 showing the rough, rer, and smooth, ser, endoplasmic reticulum, golgi, g, and the distinct patterns of the free ribosomes, r.

Figure 7.10. Normal nonneuronal cell. Note the irregularly shaped, multinucleolated nucleus, N, and the lower number of intracellular organelles compared to the neurons (Fig. 7.8).

Figure 7.11. Higher magnification of Fig. 7.10 showing the rough, rer, and smooth, ser, endoplasmic reticulum, golgi, g, and the free ribosomes, r. Note that the free ribosome patterns are less distinct than in the neurons.

Figure 7.12a. Spinal cord section illustrating asymmethrical ultrasonically-induced tissue damage. The V marks the ventral half.

Figure 7.12b. Higher magnification of Fig. 7.12a.

Figure 7.13a. Spinal cord exposed for t_{90} with 289 W/cm^2. Note that the tissue damage is restricted to the ventral, V, half of the spinal cord.

Figure 7.13b. Higher magnification of Fig. 7.13a. Note the electron transparent regions in the damaged position of the tissue.

Figure 7.14a. Spinal cord exposed for t_{90} with 144 W/cm^2. Tissue damage can be seen everywhere except for the central region of the section.

Figure 7.14b. Higher magnification of Fig. 7.14a. The asterik marks the corresponding position in the two micrographs. Several dark neurons, DN, are seen within the section.

Figure 7.15a. Spinal cord exposed for t'_{90} with 105 W/cm^2. The dorsal half of the spinal cord is vacuolated while the ventral half, V, is friable, as evidenced by the missing portions of the section.

Figure 7.15b. Higher magnification of Fig. 7.15a showing the grainy texture of the friable tissue.

Figure 7.16. Electron micrograph of friable tissue. Membrane-bound structures are still discernable, but the membranes appear fragmented and distorted. The section is peppered by electron dense blotches.

Figure 7.17. State 1 peripheral tissue. The electron density of the cytoplasm in the tissue structures is decreased in comparison to the control tissue, many structures appear more turgid than in the control tissue, and contain membranous debris, Md. Altered mitochondria, m, and synapses, Sy, can be seen.

Figure 7.18. State 1 tissue region adjacent to that in Fig. 7.19 which better illustrates the altered synapse morphology (see Section 7.3.1). Note that the nonmyelinated axons are the least affected structures.

Figure 7.19. State 2 peripheral tissue. A marked increase in the degree of altered mitochondrial morphology is evident. Both the dendrite like, DyL, structures and the axons appear more swollen than in state 1. The axons also contain fewer neurofilaments than in the control and state 1 tissue, and the remaining neurofilaments and microtubules appear less distinct.

Figure 7.20. State 3 peripheral tissue. The most prominent features are the swollen and electron transparent dendrite-like structures, DyL. Although some axons were swollen and had ruptured membranes, most of the axons still appeared similar to those in state 2. Mitochondria exhibit a wide range of altered states from normal morphology to the ring-like structure seen in the stage 5 cat brain tissue.

Figure 7.21. State 3 neuron containing the membrane bound vacuoles, V,. These appear to be associated with the smooth endoplasmic reticulum, ser, and golgi, g, and are probably swollen portions of these organelles.

Figure 7.22. State 4 neurons exhibiting altered morphology very similar to that described for stage 3 neurons in the cat brain, viz., swollen nucleus, N, condensed chromatin, cr, loss of free ribosome patterns, and swollen rough, rer, and smooth, ser, endoplasmic reticulum. Unlike the stage 3 cat brain neurons, the state 4 spinal cord neurons had the condensed chromatin distributed throughout the nucleus instead of concentrated at its center.

Figure 7.23. State 4 neuron showing condensation of its internal organelles near the nucleus. Note that the nucleolus, nu, is not condensed. The dendrites, Dy, exhibit the same altered morphology as observed in the neuronal eytoplasm.

Figure 7.24. State 5 peripheral tissue.

Figure 7.25. Dark neuron. The nucleus, N, is necrotic and the mitochondria, m, golgi, g, and endoplasmic reticulum, er, are swollen.

Figure 7.26. State 5 nonneuronal cell showing a swollen nucleus, N, containing condensed chromatin, cr. The damage to the remaining structures is similar to that observed in the state 4 neurons.

Figure 7.27. State 5 central region or GM tissue.

Figure 7.28. State 5 central region or GM tissue.

Figure 7.29. State 6 tissue. The tissue structures are vacuolized and fragmented.

Figure 8.1. The internal, Int, and external, Ext, membrane surfaces of synapse and surrounding structures are illustrated in this freeze-fracture micrograph of normal cat brain GM. The presynaptic element is identified by the synaptic vesicles, Sv. Note that the external surface contains more membrane particles than the internal surface, and that there is a step, St, at the border between adjacent internal and external surfaces.

Figure 8.2. Normal cat brain WM. The field is dominated by axons, Ax, and their surrounding myelin sheaths, My. Both the internal, Int, and external, Ext, suraces of the myelin can be seen, and a step, St, can be seen between successive myelin layers.

Figure 8.3. This higher magnification of Fig. 8.1 shows the microtubules, Mt, neurofilaments, nf, smooth endoplasmic reticulum, ser, and mitochondria within the axoplasm. The cristae, crs, within the cross fractured mitochondrian are easily distinguished.

Figure 8.4. Normal synapse. Cytoplasmic particles, cp, are present in both the pre-, Pre, and postsynaptic, Po, elements. They are probably cross fractured cytoskeletal filaments. A series of particles is also seen along the postsynaptic side of the cleft (arrowheads).

Figure 8.5. Normal synapse. Arrowheads indicate the tight junction between the synaptic elements.

Figure 8.6. Stage 1 WM. The myelin was frequently observed to bulge out from the axons (double arrowheads).

Figure 8.7. Stage 3 WM. Demyelination is clearly evident. The asterisks indicate the surface or the axolemma.

Figure 8.8. Stage 5 WM. Many tissue structures are obscured by unraveled myelin.

Figure 8.9. Stage 6 - 7 WM.

Figure 8.10. Stage 2 - 3 synapse. The vesicles, Sv, aggregated near the cleft have a large number of cytoplasmic particles, cp, associated with them. The surface density of the membrane particles is reduced, and most of the particles are found in small aggregates, Ag. the arrowheads indicate the tight junction.

Figure 8.11. Stage 4 - 5 GM. Both the cytoplasmic particles, cp, and membrane particles form tighter aggregates. The particles associated with the cleft (arrowheads) appear unaffected. This tissue is identified as being at least stage 4, by the swollen mitochondria, m.

Figure 8.12. Stage 5 - 6 GM. The morphological alterations shown in Fig. 8.11 are more pronounced.

Figure 9.1. Normal BHK cell. Several nucleoli, nu, can be seen within the nucleus, N. Electron transparent voids, V, were some times observed in the cytoplasm. Note the uniform distribution of the mitochondria, m, throughout the cytoplasm.

Figure 9.2. Higher magnification of BHK cell showing greater detail of the mitochondria, m, endoplasmic reticulum, rer, and the free ribosome patterns, r. The double arrowheads indicate the electron dense band of material along the nucleus perimeter.

Figure 9.3. Similar to Fig. 9.2 but also shows the spherical bodies, Sb. Note that the spherical bodies have no internal structures.

Figure 9.4. Extracted BHK cytoskeleton. The nucleus, N, nucleonlus, nu, stress fibers, sf, and spherical bodies are clearly visible. A halo region, H, of lower filament density surrounds the nucleus.

Figure 9.5. Cytoskelton of extracted BHK cell dehydrated with molecular sieve treated ethanol and CPD using filtered carbon dioxide. Three distinct filament populations can be observed; the 6 mm actin microfilaments, Mf, the 12 mm intermediate filaments, If, and the 24 mm microtubules Mt. Ribosomes, r, are attched to the filaments.

Figure 9.6. Cytoskeletal morphology of cells dehydrated in untreated ethanol and CPD with unfiltered carbon dioxide. Filament fusion is evident.

Figure 9.7. Stage 1 BHK cell. The nucleoli appear more prominent and there is a greater abundance of condensed chromatin.

Figure 9.8. Stage BHK cell. The free ribosome paterns so prominent in the normal cells are dissociated. A marked increase in the number of mitochondrial dense granules, Dg, is evident, and the electron dense band in the nucleus (arrowheads) shows a more irregular distribution.

Figure 9.9. Stage 2 BHK cell. Unidentifiable membranous debris, ?, and damage to the golgi can be seen.

Figure 9.10. Stage 2 BHK cells. The nucleoli and chromatin condensations are less prominent. The cytoplasm is less electron dense, and the mitochondria, m, tend to occupy the regions closer to the nucleus, N. Note that the mitochondria also appear more electron dense.

Figure 9.11. Stage 2 BHK cell. The cytoplasm exhibits a reduced electron density and the free ribosome patterns are completely dissociated. Fewer ribosomes are attached to the rough endoplasmic reticulum, rer. The mitochondrial matrices are very electron dense and the intracristal spaces are swollen. The electron dense nuclear band is almost nonexistent (double arrowheads).

Figure 9.12. Extracted stage 2 BHK cell. The filament density at the cell perimeter is reduced, and a juxtanuclear filament condensation has formed.

Figure 9.13. Peripheral region of Fig. 9.13 illustrating the reduction in cytoskeletal filaments, particularly the microfilaments.

Figure 9.14. The juxtanuclear condensation of Fig. 9.12 consisting of mostly the microfilaments and intermediate filaments.

Figure 9.15. Stage 3 cell showing the more pronounced juxta-nuclear condensation of the mitochondria.

Figure 9.16. Higher magnification showing the swollen mitochondrial in Fig. 9.15.

Figure 9.17. Stage 3 BHK cytoskeleton. The juxtanuclear condensation is more pronounced. Note that the spherical bodies and membranous debris appear to be concentrated in the juxtanuclear condensation.

Figure 9.18. Stage 4 BHK cells. Note the irregular shape of both the cell membranes and the nuclei. The number of mitochondria per cell is reduced and those remaining are more tightly associated with the nucleus.

Figure 9.19. Stage 4 cytoskeleton. The cell and nuclei shapes reflect those seen in Fig. 9.18. Note the reduced prominence of the juxtanuclear condensations.

Figure 9.20. Stage 5 BHK cell. The cell is very rounded and contains swollen mitochondria, m, and electron transparent voids, V. A series of small electron transparent vacuoles lines the cell perimeter.

Figure 9.21. Stage 5 cytoskeleton. The cell is rounded up with trailers, T, extending to points on the substrate formerly occupied by the cell perimeter.

Figure 9.22. Normal cytoskeleton of cell in metaphase. Note the spindle, Sp, and chromosomes, Cr.

Figure 10.1. Computer generated thermocouple response showing the contributions from bulk tissue heating and the viscous heating generated by the relative motion between the tissue and the thermocouple wires. The slopes of the bulk and total heating curves are identical at 0.5 sec into the exposure.

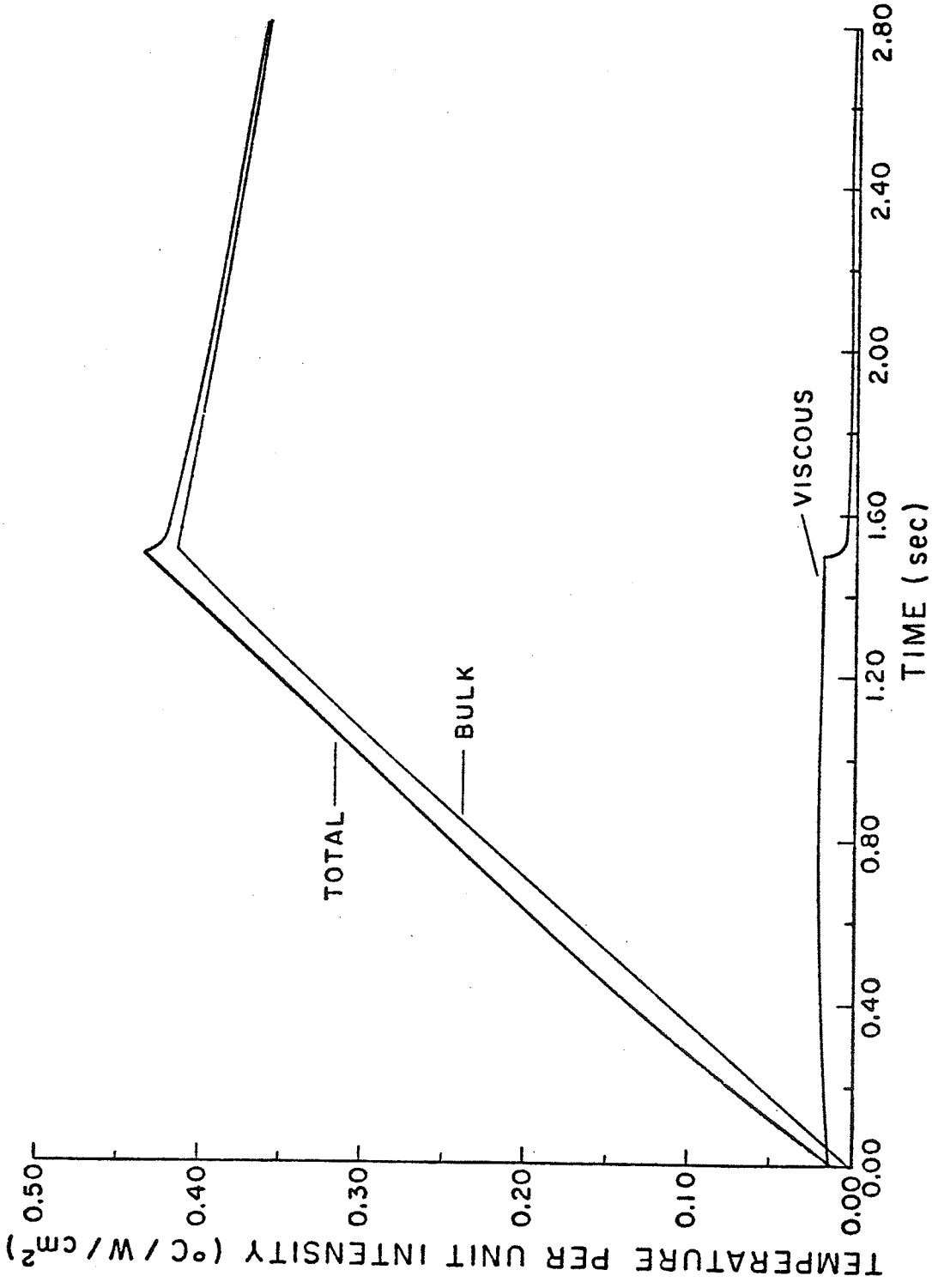
TEMPERATURE PER UNIT INTENSITY (°C / W / cm²)
0.00
0.10
0.20
0.30
0.40
0.50
TIME (sec)
0.00
0.40
0.80
1.20
1.60
2.00
2.40
2.80
TOTAL
BULK
VISCOUS

Table 4.1. Initial and secondary peak temperature as a function of radial distance from the beam axis in the plane of the focal point resulting from a 1 second exposure at 300 W/cm^2.

Radial Distance (mm)	Primary Peak Temperature (^oC)	Secondary Peak Temperature (^oC)	I_r/I_o	$t2^o$ (sec)
0.00	10.73	----	1	----
0.25	10.65	----	0.99	----
0.50	10.00	----	0.93	----
0.75	8.95	4.78	0.83	2.6
1.00	7.58	5.24	0.71	3.4
1.25	6.77	4.84	0.63	3.9
1.75	3.95	3.63	0.47	5.8
2.25	1.94	2.82	0.25	7.0
2.75	0.81	1.77	0.08	8.2
3.25	0.73	1.45	0.07	11.0
3.75	0.70	1.13	0.05	10.8

I_r/I_o = ratio of acoustic intensity at a given radial distance to that at the focal point.

$t2^o$ = time following termination of the acoustic exposure when the secondary peak temperature appeared.

Table 4.2. Peak temperature developed by 300 W/cm^2 irradiations, measured at the focal center.

Exposure Time (sec)	GM (°C)	WGM (°C)	WM (°C)
0.42	--------	$4.8^{+0.3}_{-0.2}$	$5.5^{+0.6}_{-0.3}$
0.50	$3.9^{+0.3}_{-0.5}$	$5.0^{+0.4}_{-0.4}$	$6.3^{+0.6}_{-0.4}$
1.00	$5.8^{+1.6}_{-0.7}$	$7.6^{+0.8}_{-0.4}$	$10.4^{+0.4}_{-0.5}$
1.50	-------	$10.4^{+1.3}_{-0.6}$	$13.1^{+0.7}_{-0.9}$
2.00	$8.9^{+1.2}_{-1.6}$	$13.6^{+1.2}_{-0.9}$	$16.2^{+0.8}_{-0.7}$
3.00	$9.7^{+1.7}_{-1.1}$	$14.7^{+1.3}_{+1.6}$	$20.2^{+2.2}_{-3.1}$

Table 4.3. Decay time to 1/e of the peak temperature.

Exposure Time (sec)	GM (sec)	WGM (sec)	WM (sec)
0.42	----	$4.2^{+0.6}_{-0.3}$	$4.8^{+0.4}_{-0.6}$
0.50	$2.7^{+1.5}_{-1.1}$	$5.0^{+1.3}_{-0.8}$	$4.3^{+0.4}_{-1.1}$
1.00	$2.2^{+2.3}_{-1.1}$	$5.2^{+0.6}_{-0.3}$	$8.1^{+1.5}_{-0.6}$
1.50	----	$5.4^{+1.1}_{-0.8}$	$10.6^{+4.1}_{-1.8}$
2.00	$3.6^{+0.9}_{-1.3}$	$7.4^{+1.2}_{-2.5}$	$11.2^{+3.1}_{-2.2}$
3.00	$3.8^{+1.1}_{-0.8}$	$7.6^{+2.0}_{-2.1}$	$11.4^{+2.8}_{-1.4}$

Table 4.4. Absorption coefficients measured at 300 W/cm^2.

GM (Np/cm)	WGM (Np/cm)	WM (Np/cm)
$0.034\ ^{+0.008}_{-0.006}$	$0.045\ ^{+0.006}_{-0.007}$	$0.056\ ^{+0.007}_{-0.008}$
$0.038\ ^{+0.004}_{-0.007}$*		

*Omitting data from thermocouples less than 3 mm deep into the brain tissue.

Table 5.1. Scoring of lesion damage in irradiated cat brains.

Animal #	Site 1	Site 2	Site 3	Site 4
34	0.42; 24.0 WM; 42.5 1	0.42; 24.0 WGM; 41.8 1	0.50; 24.0 WM; 43.3 3-4	0.50; 24.0 WGM; 42.0 2-3
25	0.5; 24.0 GM; 40.9 NORM	0.65; 24.0 GM; ---- NORM	0.70; 24.0 GM; 41.5 1	0.80; 24.0 GM; ---- 2-3
12	0.50; 1.0 GM; 40.9 NORM	0.50; 0.50 WM; 43.3 NORM	0.50; 0.45 GM; 40.9 NORM	
13	0.50; 1.0 GM; 40.9 NORM	0.50; 0.55 WM; 43.3 1(?)	0.50; 0.50 GM; 40.9 NORM	
33	0.50; 6.00 WGM; 42.0 1-2	0.50; 5.00 WGM; 42.0 1	0.50; 3.20 WGM; 42.0 1(?)	0.50; 2.07 WGM; 42.0 NORM
28	0.55; 1.00 WGM; ----- 1	0.55; 0.45 WGM; ----- 1(?)	0.55; 0.30 WGM; ----- NORM	
15	0.7; 0.13 WM; 44.7 1-2	0.7; 0.08 WM; 44.7 1	0.7 0.03 WM; 44.7 1(?)	
11	1.0; 0.55 WGM; 44.6 2	1.0; 0.50 WGM; 44.6 2	1.0; 0.45 WGM; 44.6 1	
24	1.0; 3.00 WGM; 44.6 4	1.0; 2.00 WGM; 44.6 2-3	1.0; 1.00 WGM; 44.6 2	

27	1.0; 0.15 WGM; 44.6 4	1.0; 0.07 WGM; 44.6 2-3	1.0; 0.03 WGM; 44.6 1	
30	1.0; 3.20 WGM; 44.6 3	1.0; 2.50 WGM; 44.6 2	1.0; 2.20 GM; 42.8 NORM	1.0; 1.50 WGM; 44.6 1
16	1.2; 0.25 WGM; ---- 3	1.2; 0.12 GM; ---- 1-2	1.2; 0.02 GM; ---- 1	
17	1.2; 0.18 GM; ----- 1(?)	1.2; 0.08 GM; ----- NORM	1.2; 0.02 GM; ----- NORM	
19	1.5; 0.45 WGM; 47.4 4	1.5; 0.05 WGM; 47.4 3	1.5; 0.15 WGM; 47.4 1	
21	1.5 1.50 GM; ----- 4-5	3.0; 1.00 WGM; 51.7 7	1.5; 0.34 GM; ----- 3	1.5; 0.04 GM; ----- 1
23	1.5; 2.00 WGM; 47.4 6	1.5; 1.50 WGM; 47.4 3-4	1.5; 1.00 WGM; 47.4 5	
26	1.5; 0.03 WGM; 47.4 2-3	1.5; 0.15 WGM; 47.4 1	1.5; 0.02 WGM; 47.4 1(?)	
29	1.5; 1.30 WGM; 47.4 4	1.5; 0.50 WGM; 47.4 2-3	1.5; 0.25 WGM; 47.4 2	1.5; 0.03 WGM; 47.4 1
18	2.0; 0.20 GM; 45.9 2	2.0; 0.18 WGM; 50.6 3	20.; 0.15 WM; 53.2 4-5	

20	2.0; 0.25 GM; 45.9 4-5	2.0; 0.10 GM; 45.9 3	2.0; 0.02 GM; 45.9 1	
31	2.0; 1.43 WM; 53.2 9	2.0; 1.00 WM; 53.2 6-7	2.0; 0.25 WM; 53.2 4	2.0; 0.03 WM; 53.2 1
38	2.0; 1.04 WM; 53.2 7-8	2.5; 1.01 WGM; ----- 6	2.0; 0.32 WM; 53.2 5	2.5; 0.30 GM; ----- 4
38	2.5; 0.17 GM; ----- 3	2.0; 0.15 WM; 53.2 4	2.5; 0.3 GM; ----- 1	2.0; 0.2 WM; 53.2 2
8	2.5; 0.50 GM; ----- 5	4.0; 0.47 WGM; >53.3 9	1.5; 0.44 GM; ----- 2-3	
9	2.5; 0.50 WM; 53.2 9	4.0; 0.48 WM; >60.3 Friable	1.5; 0.47 WM; 50.1 5	
10	2.5; 1.20 WM; ----- 9	2.5; 0.55 WM; ----- 8	4.0; 0.50 WM; >60.3 Friable	
5	2.0; 0.45 WGM; 50.6 4-5	3.0; 0.42 WGM; 51.7 6-7	1.0; 0.38 WGM; 44.6 3	
4	5.0; 0.45 WM; >60.3 Friable	3.0; 0.40 WM; 57.2 7-8		
2	5.0; 0.45 GM; >48.0 Friable	3.0; 0.42 GM; 46.7 5		
3	6.0; 0.15 WM; >60.3 Friable	4.0; 0.02 WM; >60.3 Friable		

Table 7.1. Exposure conditions for 10, 50, and 90% of the specimens developing hind limb paralysis at 1 MHz and 10°C. I is the ultrasonic intensity, P is the hydrostatic pressure, and t_n are the exposure durations where n is the percentage of specimens paralyzed.

I (W/cm^2)	P (atm)	t_{10} (s)	t_{50} (s)	t_{90} (s)
86	1	3.44	5.04	9.40
86	16	2.59	4.50	18.70
105	1	2.01	2.56	3.53
122	1	1.37	1.53	1.72
144	1	0.84	0.97	1.14
144	16	0.85	0.97	1.12
192	1	0.36	0.44	0.58
256	1	0.23	0.30	0.45
289	1	0.20	0.26	0.37
289	16	0.30	0.50	1.54

Table 7.2. Comparison of monitored half harmonic signal levels with, and without, the specimen and holder present in the irradiation chamber, at the exposure conditions for 90% reversible paralysis and at 1 atm.

0.5 MHz Signal Level

Intensity (W/cm^2)	Specimen Present (dB)	Specimen Absent (dB)	Difference (dB)
86	-30	-42	12
105	-22	-40	18
122	-20	-37	17
144	-18	-37	19
192	-16	-42	26
256	-18	-37	19
289	-22	-38	16

Table 7.3. Harmonic and noise signal levels, referenced to the fundamental, as a function of the incident intensity with (W) and without (WO) the specimen and holder present. Exposures are for the 50% paralysis level.

Intensity (W/cm^2)	2nd Harmonic (dB)			3rd Harmonic (dB)			Broadband Noise (dB)		
	WO	W	Diff	WO	W	Diff	WO	W	Diff
86	---	-20	----	---	-17	----	---	-62	----
105	-30	-21	9	-48	-15	33	-60	-57	3
122	---	-23	----	---	-11	----	---	-62	----
144	-30	-21	9	-48	-13	35	-60	-55	5
192	---	-20	----	---	-12	----	---	-50	----
256	-22	-15	7	- 8	- 8	0	-65	-50	15
289	-16	-20	-4	---	- 8	----	-60	-50	10

Table 9.1. Development of morphological changes as a function of hyperthermia treatment and post heating time for BHK cells.

Hyperthermia Treatment (°C; Heating time)	Stage 1	Stage 2	Stage 3	Stage 4	Stage 5
43.5°C; 4 min	-----	------	-------	-------	-------
43.5°C; 7-10 min	0 sec	10 - 20 min	No Data	No Data	No Data
43.5°C; 20 min	0 sec	0 sec	5 - 10 min	10 - 20 min	No Data
43.5°C; 40 min	0 sec	0 sec	0 sec	5 - 10 min	10 - 25 min
46°C; 1 min	-----	-------	-------	-------	-------
46°C; 2-4 min	0 sec	10 - 25 min	2 hr	No Data	No Data
46°C; 10 min	0 sec	0 sec	5 - 10 min	10 - 30 min	> 2 hr
46°C; 15 min	0 sec	0 sec	0 sec	0 sec	0 sec
50°C; 5 sec	-----	-------	-------	-------	-------
50°C; 20 sec	-----	-------	-------	-------	-------
50°C; 25-30 sec	0 sec	5 - 10 min	10 - 20 min	30 - 40 min	45 min-1 hr
50°C; 1 min	0 sec	0 sec	5 - 15 min	15 - 25 min	20 - 40 min
57°C; 1 sec	-----	-------	-------	-------	-------
57°C; 3-5 sec	0 sec	0 sec	0 sec	0 sec	0 sec

REFERENCES

1. Bakay, L., Lee, J. C., Lee, G. C., and Peng, J. R. (1977), "Experimental Cerebral Concussion Part I: An Electron Microscope Study," J. Neurosurg., 47, 525-531.
2. Barnard, J. W., Fry, W. J., Fry, F. J., and Brennan, J. F. (1956), "Small Localized Ultrasonic Lesions in the White and Gray Matter of the Cat Brain," AMA Arch. Neurol. and Physch., 75, 15-35.
3. Basauri, L. and Lele, P. P. (1962), "A Simple Method for Production of Trackless Focal Lesions with Focused Ultrasound," J. Physiol., 160, 513-534.
4. Beyer, R. T. (1974), Nonlinear Acoustics (Naval Ship Systems Command, Department of the Navy, N00024-72-C-1397).
5. Beyer, R. T. and Letcher, S. V. (1969), Physical Ultrasonics (Academic Press, New York), Chap. 1.
6. Borrelli, M. J., Bailey, K. I., and Dunn, F. (1981), "Early Ultrasonic Effects Upon Mammalian CNS Structures (Chemical Synapses)," J. Acoust. Soc. Am., 69, 1514-1516.
7. Borrelli, M. J., Koehm, S., Tompkins, W. A. F., and Cain, C. A. (1983), "The Morphology of the Cytoskeletal System: Normal and Hyperthermia Treated BHK Cells," in press.
8. Bradford, H. F. (1977), "The Metabolic and Transmitter-Releasing Properties of Isolated Nerve-Terminals," in Synapses, edited by G. A. Cottrell and P. N. R. Usherwood (Academic Press, New York), pp. 21-39.

9. Carstensen, E. L. and Schwan, H. P. (1959a), "Absorption of Sound Arising from the Presence of Intact Cells in Blood," J. Acoust. Soc. Am., 31, 185-189.

10. Carstensen, E. L. and Schwan, H. P. (1959b), "Acoustic Propeties of Hemoglobin Solutions," J. Acoust. Soc. Am., 31, 305-311.

11. Carstensen, E. L., McKay, N. D., Delecki, D., and Muir, T. G. (1983), "Absorption of Finite Amplitude Ultrasound in Tissue," in press.

12. Cevera, M., Dreyfuss, G., and Penman, S. (1981), "Messenger RNA is Translated when Associated with the Cytoskeletal Framework in Normal and VSV-Infected HeLa Cells," Cell, 23, 113-120.

13. Coakley, W. T. and Nyborg, W. L. (1978), "Cavitation; Dynamics of Gas Bubbles; Applications," in Ultrasound: Its Applications in Medicine and Biology Part I, edited by F. J. Fry (Elsevier Scientific Publishing Co., Amsterdam).

14. Cook, C. T., Nolan, T. M., Dyson, S. E., and Jones, D. G. (1974), "Pentobarbitol-Induced Configurational Changes at the Synapse," Brain Res., 76, 330-335.

15. Costello, M. J., Felter, R., and Hochli, M. (1982), "Simple Procedures for Evaluating the Cryofixation of Biological Samples," J. Microsc., 125, 125-136.

16. CRC Handbook of Chemistry and Physics (1974), edited by R. C. Weast (CRC Press, Cleveland).

17. Crum, L. A. (1980a), "Measurements of the Growth of Air Bubbles by Rectified Diffusion," J. Acoust. Soc. Am., 68, 203-211.

18. Crum, L. A. (1980b), "Acoustic Cavitation Thresholds in Water," in Cavitation and Inhomogeneities in Underwater Acoustics, edited by W. Lauteborn (Springer-Verlag, New York), pp. 84-89.

19. Crum, L. A. (1982a), Personal Communication.

20. Crum, L. A. (1982b), "Nucleation and Stabilization of Microbubbles in Liquids," Applied Sci. Res., 38, 101-115.

21. Davson, H. and Segal, M. B. (1975), Introduction To Physiology Vol. I (Greene and Stratton Pub., New York).

22. Dodge, F. A. and Rahaminoff, R. (1967), "Co-Operative Action of Calcium Ions in Transmitter Release at the Neuromuscular Junction," J. Physiol., 193, 419-432.

23. Duffy, C. J. and Tyler, T. J. (1975), "A Simple Tissue Slicer," Physiol. and Behavior, 14, 525-526.

24. Dunn, F. (1958), "Physical Mechanisms of the Action of Intense Ultrasound on Tissue," Am. J. Phys. Med., 37, 148-151.

25. Dunn, F. Lohnes, J. E., and Fry, F. J. (1975), "Frequency Dependence of Threshold Ultrasonic Dosages for Irreversible Structural Changes in Mammalian Brain," J. Acoust. Soc. Am., 58, 512-514.

26. Dunn, F. (1977), Personal Communication.

27. Dunn, F. Averbuch, A. J., and O'Brien, W. D. (1977), "A Primary Method for the Determination of Ultrasonic Intensity with the Elastic Sphere Radiometer," Acoustica, 38, 58-61.

28. Dunn, F. and Pond, J. B. (1978), "Selected Non-Thermal Mechanisms of Interaction of Ultrasound and Biological Materials," in Ultrasound: Its Applications In Medicine and Biology Part II, edited by F. J. Fry (Elsevier Scientific Publishing Co., Amsterdam).

29. Dyson, M., Pond, J. B., Woodward, B., and Broadent, J. (1974), "The Production of Blood Cell Stasis and Endothelial Damage in the Blood Vessels of Chick Embryos Treated with Ultrasound in a Stationary Wave Field," Ultrasound Med. Biol., 1, 133-148.

30. Dyson, S. E. and Jones, D. G. (1980), "Quantitation of Terminal Parameters and Their Interrelationships in Maturing Central Synapses: A Perspective for Experimental Studies," Brain Res., 183, 43-59.

31. Eigen, M. and Hammes, G. G. (1963), "Elementary Steps in Enzyme Reactions," in Advances in Enzymology Vol. 25 (Interscience Publishers, New York), pp. 21-39.

32. El' Pinear, I. E., Faiken, I. M., and Basurmanova, O. K. (1965), "Intracellular Microcurrents Caused by Ultrasound Waves," Biofizika, 10, 805-809.

33. Falkner, F. G., Saumweber, H., and Biessman, H. (1981), "Two Drosophila Melanogaster Proteins Related to Intermediate Filament Proteins of Vertebrate Cells," J. Cell Biol., 91, 175-183.

34. Flynn, H. G. (1964), "Physics of Acoustic Cavitation in Liquids," in Physical Acoustics Vol. IB, edited by W. P. Mason (Academic Press, New York).

35. Flynn, H. G. (1975a), "Cavitation Dynamics. I. A Mathematical Formulation," J. Acoust. Soc. Am., 57, 1379-1396.

36. Flynn, H. G. (1975b), "Cavitation Dynamics. II. Free Pulsations and Models for Cavitation Bubbles," J. Acoust. Soc. Am., 58, 1160-1170.

37. Flynn, H. G. (1982), Personal Communication.

38. Freese, M. and Lyons, E. A. (1979), "Dependence of Ultrasound Backscatter from Human Liver Tissue on Frequency and Protein/Lipid Composition," in Ultrasonic Tissue Characterization, edited by M. Linzer, National Bureau of Standards Publication 525 (U.S. Government Printing Office, Washington, DC), pp. 157-163.

39. Frizzell, L. A., Carstensen, E. L., and Dyro, J. F. (1976), "Shear Properties of Mammalian Tissues at Low Megahertz Frequencies," J. Acoust. Soc. Am., 60, 1409-1411.

40. Frizzell, L. A., Lee, C. S., Aschenbach, P. D., Borrelli, M. J., Morimoto, R. S., and Dunn, F. (1983), "Involvement of Ultrasonically Induced Cavitation in Hind Limb Paralysis of the Mouse Neonate," J. Acoust. Soc. Am., 74, 1062-1065.

41. Frizzell, L. A. (1983), Personal Communication.

42. Fry, F. J., Kosoff, G., Eggleton, R. C., and Dunn, F. (1970), "Threshold Ultrasonic Dosages for Structural Changes in the Mammalian Brain," J. Acoust. Soc. Am., 48, 1413-1417.

43. Fry, F. J. (1983), Personal Communication.

44. Fry, W. J. (1952), "Mechanisms of Acoustic Absorption in Tissue," J. Acoust. Soc. Am., 24, 412-415.

45. Fry, W. J., Barnard, J. W., Fry, F. J., Ksumis, R. F., and Brennan, J. F. (1955), "Ultrasonic Lesions in the Mammalian Central Nervous System," Science, 122, 517-518.

46. Fry, W. J. and Dunn, F. (1956), "Ultrasound Irradiation of the Central Nervous System at High Sound Levels," J. Acoust. Soc. Am., 28, 129-131.

47. Fry, W. J. (1958), "Intense Ultrasound in Investigations of the Nervous System," in Advances in Biology and Medical Physics Vol. VI, edited by J. M. Lawrence and C. A. Tobias (Academic Press, New York).

48. Fry, W. J. and Dunn, F. (1962), "Ultrasound: Analysis and Experimental Methods in Biological Research," in Physical Techniques in Biological Research, edited by W. L. Nastuck (Academic Press, New York).

49. Fry, W. J., Fry, F. J., Malek, R., and Pankau, J. W. (1964), "Quantitative Studies Implemented by Ultrasonic Lesions-Mammalian Nuclei and Associated Complex of Cat Brain," J. Acoust. Soc. Am., 36, 1795-1935.

50. Fu, Y., Kaufman, G. E., Miller, M. M., Griffiths, T. D., and Lange, C. S. (1979), "Modification by Cyteamine of Ultrasound Lethality to Chinese Hamster V-79 Cells," Radiat. Res., 80, 575-580.

51. Garcia, J. H., Kalimo, H. K., Kamjyo, Y., and Trump, B. F. (1977), "Cellular Events During Partial Cerebral Ischemia: I. Electron Microscopy of Feline Cerebral Cortex after Middle-Cerebral-Artery Occlusion," Virchows Arch. B. Cell Path., 25, 191-206.

52. Garcia, J. H., Lossinsky, A. S., Conger, K., and Kauffman, F. C. (1979), "The Interpretation of Ultrastructural Abnormalities in Ischemia," in Proc. of International Symposium on Pathophysology of Cerebral Energy Metabolism (Plenum Press, New York).

53. Gershoy, A. and Nyborg, W. L. (1973), "Perturbation of Plant-Cell Contents by Ultrasonic Micro-Irradiation," J. Acoust. Soc. Am., 54, 1356-1367.

54. Goss, S. A. and Dunn, F. (1974), "Concentration Dependence of Ultrasonic Absorption in Aqueous Solutions of Bovine Serum Albumin," 1974 Ultrasonic Symposium Proceedings, IEEE Cat. #74CHO 896-1SU, pp. 65-68.

55. Goss, S. A., Cobb, J. W., and Frizzell, L. A. (1977), "Effect of Beam Width and Thermocouple Size on the Measurement of Ultrasonic Absorption Using the Thermoelectric Technique," in 1977 Ultrasonic Symposium Proceedings, IEEE Cat. #77CH 1264-1SU, pp. 206-211.

56. Goss, S. A., Johnston, R. L., and Dunn, F. (1978), "Comprehensive Compilation of Empirical Ultrasonic Properties of Mammalian Tissues," J. Acoust. Soc. Am., 64, 423-457.

57. Goss, S. A., Frizzell, L. A., and Dunn, F. (1979), "Ultrasonic Absorption and Attenuation in Mammalian Tissues," Ultrasound Med. Biol., 5, 181-186.

58. Goss, S. A. and Fry, F. J. (1981), "Nonlinear Acoustic Behavior in Focused Ultrasonic Fields: Observations of Intensity Dependent Absorption in Biological Tissue," IEEE Trans. Sonics and Ultrasonics, SU-28, 21-26.

59. Goss, S. A. (1983), Personal Communication.

60. Gould, R. K. and Coakley, W. T. (1974), "The Effects of Acoustic Forces on Small Particles in Suspension," in Finite Amplitude Wave Effects In Fluids, edited by L. Bjorno (IPC Science and Technology Press).

61. Gray, E. G. (1976), "Problems of Understanding the Substructure of Synapses," Prog. Brain Res., 45, 207-234.

62. Gray H. (1980), Anatomy: Descriptive and Applied, edited by R. Warwick and P. L. Williams (W. B. Saunders, Philadelphia) 36th British Edition, pp. 826-833.

63. Greenough, W. (1983), Personal Communication.

64. Gude, W. D., Cosgrove, G. E., and Hirsch, G. P. (1982), Histological Atlas of the Laboratory Mouse (Plenum Press, New York), pp. 42-43.

65. Gulley, R. L. and Reese, T. S. (1981), "Cytoskeletal Organization at the Postsynaptic Complex," J. Cell Biol., 91, 298-302.

66. Hackenbrach, C. R. and Caplan, A. I. (1969), "Ion-Induced Ultrastructural Transformations in Isolated Mitochondria," J. Cell Biol., 42, 221-234.

67. Hackenbrach, C. R., Rehn, T. G., Weinbach, E. C., and Lemaster, J. J. (1971), "Ultrastructural Transformations in Mitochondria in the Intact Acites Tumor Cell," J. Cell Biol., 51, 123-137.

68. Harris, R. J., Syman, L., Branston, N. W., and Bayhan, M. (1981), "Changes in Extracellular Calcium Activity in Cerebral Ischemia," J. Cereb. Blood Flow Metabol., 1, 203-209.

69. Heuser, J. E. and Kirschner, M. W. (1980), "Filament Organization Revealed in Platinum Replicas of Freeze-Dried Cytoskeletons," J. Cell Biol., 86, 212-234.

71. Hirokawa, N. (1982), "Cross-Linker System between Neurofilaments, Microtubules, and Membranous Organelles in Frog Axons Revealed by the Quick-Freeze, Deep-Etching Method," J. Cell. Biol., 94, 129-142.

70. Hoak, R. A., Kleinhaus, F. W., and Ochs, S. (1976), "The Viscosity of Mammalian Nerve Axoplasm Measured by Electron Spin Resonance," J. Physiol., 263, 115-137.

72. Hudson, C. S., Rash, J. E., and Graham, W. F. (1979), "Introduction to Sample Preparation for Freeze Fracture," in Freeze Fracture: Methods Artifacts and Interpretations, edited by J. E. Rash and C. S. Hudson (Raven Press, New York) pp. 1-10.

73. Hughes, D. E. and Nyborg, W. L. (1962), "Cell Disruption by Ultrasound," Science, 138, 108-114.

74. Humason, G. L. (1962), Animal Tissue Techniques (W. H. Freeman and Co., San Francisco), pp. 282.

75. Jehl, B., Bauer, R. Dorge, A., and Rick, R. (1981), "Use of Propane/Isopentane Mixtures for Rapid Freezing of Biological Specimens," J. Microsc., 123, 307-309.

76. Johnston, I. R. (1972), "The Biochemical Properties of Nuclei Fractioned by Zonal Centrifugation," in Subcellular Compartments, edited by G. D. Birney (University Park Press, Baltimore).

77. Johnston, R. L. and Dunn, F. (1976a), "Ultrasonic Absorbed Dose, Dose Rate, and Produced Lesion Volume," Ultrasonics, July 1976, 153-155.

78. Johnston, R. L. and Dunn, F. (1976b), "Influence of Subarachnoid Structures on Transmeningial Ultrasonic Propagation," J. Acoust. Soc. Am., 60, 1225-1227.

79. Johnston, R. L., Goss, S. A., Maynard, V., Brady, J. K., Frizzell, L. A., O'Brien, W. D., and Dunn, F. (1979), "Elements of Tissue Characterization: Part I. Ultrasonic Propagation Properties," in Ultrasonic Tissue Characterization II, edited by M. Linzer, National Bureau of Standards, Spec. Publ. 525 (U.S. Government Printing Office, Washington, DC).

80. Johnston, R. L. and Dunn, F. (1981), "Ultrasonic Hysterisis in Biological Media," Radiat. Environ. Biophysics, 19, 137-148.

81. Johnston, R. L. (1982), Personal Communication.

82. Jones, D. G. and Devon, R. M. (1977), "The Influence of Pentobarbitane on the Distribution of Membrane in Cortical Synapses," Neurosci. Lett., 6, 177-182.

83. Jones, D. G. and Devon, R. M. (1978), "An Ultrastructural Study into the Effects of Pentobarbitone on Synaptic Organization," Brain Res., 147, 47-63.

84. Kalimo, H., Garcia, J. H., Kamijyo, Y., Tanaka, J., and Trump, B. F. (1977), "The Ultrastructure of Brain Death: II Electron Microscopy of Feline Cortex after Complete Ischemia," Virchows Arch. B Cell Path., 25, 207-220.

85. Kass, I. S. and Lipton, P. (1982), "Mechanisism Involved in Irreversible Anoxic Damage to In Vitro Rat Hippocampal Slice," J. Physiol., 332, 459-472.

86. Kato, S., Suzuki, T., Nomura, H., and Miyahara, Y. (1979), "Ultrasonic Relaxation in Aqueous Solutions of Dextran," Macromolecules, 13, 889-892.

87. Kessler, L. W. and Dunn, F. (1969), "Ultrasonic Investigation of the Conformal Changes of Bovine Serum Albumin in Aqueous Solution," J. Phys. Chem., 73, 4256-4263.

88. Kinsler, L. E. and Fry, A. R. (1962), Fundamentals of Acoustics (John Wiley and Sons, New York), Chaps. 5 and 6.

89. Lehninger, A. L. (1964), The Mitochondrion, (W. A. Benjamin Inc., New York), pp. 181.

90. Lele, P. P. and Pierce, A. D. (1971), "The Thermal Hypothesis of the Mechanism of Ultrasonic Focal Destruction in Organized Tissues," in Interaction of Ultrasound and Biological Tissues, edited by J. Reid and M. Sikov, DHEW Publication (FDA) 73-8008 BRH/DBE, 121-128.

91. Lele, P. P. (1978), Personal Communication.

92. Lele, P. P. (1979), "Safety and Potential Hazards in the Current Applications of Ultrasound in Obstetrics and Gynecology," Ultrasound Med. Biol., 5, 307-320.

93. Lenk, R., Ransom, L., Kaufman, Y., and Penman, S. (1979), "A Cytoskeletal Structure with Associated Polyribosomes Obtained from He-La Cells," Cell, 10, 67-78.

94. Lipton, P. (1981), Personal Communication.

95. Lipton, P. and Whittingham, T. S. (1982), "Reduced ATP Concentration as a Basis for Synaptic Transmission Failure During Hypoxia in the In Vitro Guinea Pig Hippocampus," J. Physiol., 325, 51-56.

96. Longley, L. A. and O'Brien, W. D. (1982), "Ultrasonic Heating Distribution in Lossy Cylinders and Spheres," IEEE Trans. Sonics and Ultrasonics, SU-29, 69-78.

97. Margaritis, L. H., Elgsaeter, A., and Branton, D. (1977), "Rotary Replication for Freeze Fracture," J. Cell Biol., 72, 47-56.

98. Mazia, D., Schatlen, G., and Sale, W. (1975), "Adhesion of Cells to Surfaces Coated with Polylysine," J. Cell Biol., 66, 198-200.

99. Miller, D. L. (1977), "Stable Arrays of Resonant Bubbles in a 1 MHz Standing-Wave Acoustic Field," J. Acoust. Soc. Am., 62, 12-19.

100. Miller, D. L., Nyborg, W. L., and Whitcomb, C. C. (1978), "In Vitro Clumping of Platlets Exposed to Low Intensity Ultrasound," in Ultrasound in Medicine, Vol. 4, edited by D. N. White and E. A. Lyons (Plenum Press, New York), pp. 545-553.

101. Muir, T. G. and Carstensen, E. L. (1980), "Predictions of Nonlinear Effects at Biomedical Frequencies and Intensities," Ultrasound Med. Biol., 6, 345-357.

102. Munn, E. A. (1974), The Structure of Mitochondria (Academic Press, London), pp. 116-117.

103. Nyborg, W. L. (1968), "Mechanisms for Nonthermal Effects of Sound," J. Acoust. Soc. Am., 44, 1302-1309.

104. Nyborg, W. L. (1983), Personal Communication.

105. O'Brien, W. D. and Dunn, F. (1972), "Ultrasonic Absorption Mechanisms in Aqueous Solutions of Bovine Hemoglobin," J. Phys. Chem., 76, 528-533.

106. O'Donnell, M. and Miller, J. G. (1975), "Mechanisms of Ultrasonic Attenuation in Soft Tissue," in Ultrasonic Tissue Characterization II, edited by M. Linzer, National Bureau of Standards Publication 525 (U.S. Government Printing Office, Washington, DC).

107. Papas, G. (1982), Personal Communication.

108. Parker, K. (1982), Personal Communication.

109. Pauly, H. and Schwan, H. P. (1971), "Mechanisms of Absorption of Ultrasound in Liver Tissue," J. Acoust. Soc. Am., 50, 692-699.

110. Peters, A., Palay, S. L., and de F. Webster, H. (1976), The Fine Structure of the Nervous System: The Neurons and Supporting Cells (W. B. Saunders Co., Philadelphia).

111. Pond, J. (1968), "A Study of the Biological Action of Focused Mechanical Waves," Ph.D. Thesis, University of London.

112. Pond, J. B. (1970), "The Role of Heat in the Production of Ultrasonic Focal Lesions," J. Acoust. Soc. Am., 47, 1607-1611.

113. Ralston, H. J. (1979), "The Fine Structure of Laminae I, II, and III of the Macaque Spinal Cord," J. Comp. Neur., 184, 619-642.

114. Ralston, H. J. (1982), Personal Communication.

115. Rash, J. E. (1981), Personal Communication.

116. Ravitz, M. J. and Schnitzler, R. M. (1970), "Morphological Changes Induced in the Frog Semitendinorus Muscle Fiber by Localized Ultrasound," Expt. Cell Res., 60, 78-85.

117. Reid, J. M. and Shung, K. K. (1979), "Quantatitive Measurements of Scattering of Ultrasound by Heart and Liver," in Ultrasonic Tissue Characterization II, edited by M. Linzer, National Bureau of Standards Publication 525 (U.S. Governmet Printing Office, Washington, DC), pp. 153-156.

118. Reid, N. (1962), Ultramicrotomy, in Practical Methods in Electron Microscopy, II, edited by A. M. Glauert (American Elsevier Publishing Co., New York).

119. Repocholi, M. H. (1981), Ultrasound: Characteristics and Biological Action, (National Research Council of Canada).

120. Reynolds, E. S. (1963), "The Use of Lead Citrate at High pH as an Electron-Opaque Stain in Electron Microscopy," J. Cell Biol., 17, 208-210.

121. Ris, H. (1980), "The Cytoplasmic Microtrabecular Lattice-Reality or Artifact," 38th Ann. Proc. Electron Microsco. Soc. Am., 812-813.

122. Robinson, T. C. and Lele, P. P. (1972), "An Analysis of Lesion Development in the Brain and in Plastics by High-Intensity Ultrasound at Low Megahertz Frequencies," J. Acoust. Soc. Am., 51, 1333-1351.

123. Rooney, J. A. (1970), "Hemolysis Near and Ultrasonically Pulsating Gas Bubble," Science, 169, 869-871.

124. Rydzynski, K. (1978), "An Attempt to Modify the Configurational States of Mitochondria from the Ependyma of the Choroid Plexus In Vivo," Ninth Intlt. Cong. Elect. Micros., 2, 254-255.

125. Sacks, P. G., Miller, M. W., and Church, C. C. (1982), "The Exposure Vessel as a Factor in Ultrasonically-Induced Mammalian Cell Lysis-I: A Comparison of Tube and Chamber Systems," Ultrasound Med. Biol., 8, 289-298.

126. Selman, G. G. and Jurand, A. (1964), "An Electron Microscope Study of the Endoplasmic Reticulum in Newt Notochord Cells after Disturbance with Ultrasonic Treatment and Subsequent Regeneration," J. Cell Biol., 20, 175-183.

127. Slutsky, L. J., Madsen, L., White, R. K., and Harkness, J. (1980), "Kinetics of the Exchange of Protons between Hydrogen Phosphate Ions and a Histadyl Residue," J. Phys. Chem., 84, 1325-1329.

128. Small, J. V. (1981), "Organization of Actin in the Leading Edge of Cultured Cells: Influence of Osmium Tetroxide and Dehydraion on the Ultrastructure of Actin Meshworks," J. Cell Biol., 91, 695-705.

129. Smith, D. S., Jarlfors, U., and Baremek, R. (1970), "The Organization of Synaptic Axoplasm in the Lamprey (Petromyzon Marinus) Central Nervous System," J. Cell Biol., 46, 199-218.

130. Snider, R. S. and Neiman (1964), A Stereotoxic Atlas of the Brain (University of Chicago Press, Chicago).

131. Stephens, R. J. Hart, C. P., Torbet, C. A., and Edmonds, P. D. (1980), "Reproducible Subcellular Alterations in Hepatocytes Resulting from Ultrasound," Ultrasound Med. Biol., 6, 239-249.

132. Stolinski, C. and Breathnack, A. S. (1975), Freeze-Fracture Replication of Biological Tissues (Academic Press, London).

133. Tanford, C. (1961), The Physical Properties of Macromolecules (John Wiley and Sons).

134. Taylor, K. J. W. (1970), "Ultrasonic Damage to Spinal Cord and the Synergistic Effect of Hypoxia," J. Pathology, 102, 41-47.

135. Taylor, K. J. W. and Pond, J. B. (1972), "A Study of the Production of Haemorrhagic Injury and Paraplegia in Rat Spinal Cord by Pulsed Ultrasound of Low Megahertz Frequencies in the Context of the Safety for Clinical Usage," Brit. J. Radiol., 45, 343-353.

136. ter Haar, G., Dyson, M., and Smith, S. P. (1979), "Ultrastructure Changes in the Mouse Uterus Brought About by Ultrasonic Irradiation at Therapeutic Intensities in Standing Wave Fields," Ultrasound Med. Biol., 5, 167-179.

137. ter Haar, G., Daniels, S., Eastough, K. C., and Hill, C. R. (1982), "Ultrasonically Induced Cavitation In Vivo," Br. J. Cancer, 45, 151-155.

138. Vander, A. J., Sherman, J. H., and Luciano, D. S. (1975), Human Physilogy--The Mechanisms of Body Function (McGraw-Hill, New York), pp. 296-297.

139. Waag, R. C., Lee, P. P. K., Lerner, R. M., Hunter, L. P., Gramiak, R. G., and Shenk, E. A. (1979), "Angle Scan and Frequency-Swept Ultrasonic Scattering Characterization of Tissue," in Ultrasonic Tissue Characterization II, edited by M. Linzer, National Bureau of Standards Publication 525 (U.S. Government Printing Office, Washington, DC), pp. 143-152.

140. Webster, R. E., Henderson, K., Osborn, M., and Webster, K. (1978), "Three-Dimensional Electron Microscopical Visualization of the Cytoskelton of Animal Cells: Immunoferriten Identification of Actin- and Tublin-Containing Structures," Proc. Natl. Acad. Sci. USA, 75, 5511-5515.

141. Wehenmeyer, J. (1982), Personal Communication.

142. White, R. D. and Slutsky, L. J. (1972), "Ultrasonic Absorption and Relaxation Spectra in Aqueous Bovine Hemoglobin," Biopolymers, 11, 1973-1984.

143. Williams, V. and Grossman, G. (1970), "Ultrastructure of Cortical Synapses after Failure of Presynaptic Activity in Ischemia," Anat. Rec., 166, 131-142.

144. Wolosewick, J. J. and Porter, K. R. (1976), "Stereo High-Voltage Electron Microscopy of Whole Cells of the Human Diploid Line, WI-38," Am. J. Anat., 147, 303-324.

145. Yamada, H. (1970), Biological Materials (Williams and Wilkins, Co., Baltimore).

VITA

Michael Jude Borrelli was born on December 26, 1953 in Jersey City, New Jersey. He attended Cherry Hill High School West, Cherry Hill, New Jersey, graduating with high honors in 1972. In the fall of 1972 he enrolled in the University of Illinois at Urbana-Champaign graduating in 1977 with Bachelor of Science degrees in Astronomy and Physics, and Biology, with highest distinction in Astronomy. Later that year Mr. Borrelli entered the graduate program in Biophysics at the University of Illinois. During his graduate studies Mr. Borrelli was a Radiation Oncology Trainee with support from the National Institute of Health, a Teaching Assistant in the Departments of Physiology and Biophysics and Biology, and a Research Assistant in the Department of Electrical Engineering. Mr. Borrelli is a member of Phi Eta Sigma, Ph Kappa Phi, and the Acoustical Society of America. He is also a member of the Electron Microscopy Society of America where he was one of the 1980 recipients of the President's Award for excellence in electron microscopy.